

University of Strathclyde

Department of Naval Architecture, Ocean and
Marine Engineering

**THE DEVELOPMENT OF TIME-
DEPENDENT BIOFOULING MODEL FOR
SHIPS**

Dogancan Uzun

A thesis presented in fulfilment of the
requirements for the degree of Doctor of
Philosophy

2019

This thesis is the result of the author's original research. It has been composed by the author and has not been previously submitted for the examination which has led to the award of a degree.

The copyright belongs to the author under the terms of the United Kingdom Copyright Acts as qualified by University of Strathclyde Regulation 3.50. The due acknowledgement must always be made of the use of any material contained in, or derived from, this thesis.

Signed:

Date:

Acknowledgements

My PhD journey came to an end after a 4 year of challenging, constructive and enjoyable period. It has been an exciting journey starting in a new country full of surprises, marvellous people and challenges. I would like to thank everyone who contributed to this journey.

First of all, I would like to express my most profound appreciation to my first supervisor Professor Osman Turan not only for giving me the opportunity of doing my PhD but also sharing his wisdom, motivation, curiosity and tenacious effort towards to achieve this research. I would like to acknowledge my second supervisor Dr Yigit Kemal Demirel, for being in my research from beginning to the end, sharing his experiences and critical answers. I am grateful for the interesting discussions with him, his mentoring and valuable contribution to each chapter of this study.

I would like to also express my gratitude to Dr Nermin Tekogul and Professor Sander Calisal, who were my lecturers and mentors from Piri Reis University for encouraging me to study a PhD. I would like to thank them for extending my vision and showing me the opportunities to continue my professional and personal progress.

I feel blessed to share the same house with Margaret Anderson (Maggie), Louise Anderson and David Babb who make me feel like I am in my home in Scotland. A special thanks goes to Maggie for proofreading my texts and always supporting me.

I would like to thank my colleagues and friends for their encouragements and support in alphabetical order; Dr Batuhan Aktas, Ece Dirik, Dr Elif Oguz, Emin Ozturk, Kaan Iltter, Dr Naz Yilmaz, Dr Olgun Guven Hizir, Onder Canbulat, Refik Ozyurt, Savas Sezen, Seda Ozaydin, Dr Sefer Anil Gunbeyaz, Soonseok Song, Dr Tong Cui, Dr Volkan Aslan, Dr Yansheng Zhang, Yildirim Dirik, Zeynep Gunbeyaz and Zeynep Iltter.

Last but not least, my deepest appreciation to my precious family members; my father Senturk Uzun, my mother Inci Uzun and my sister Bengu Uzun for always believing in me, supporting and encouraging me.

Contents

List of Figures	vii
List of Tables.....	xii
Abstract	xiv
1 Introduction.....	1
1.1 Introduction	1
1.2 General Perspectives	1
1.3 Motivations behind this Work.....	5
1.4 Research Aims and Objectives.....	8
1.5 Structure of this Thesis.....	10
1.6 Chapter Summary.....	11
2 Literature Review.....	12
2.1 Introduction	12
2.2 Marine Biofouling	12
2.2.1 Types of Marine Fouling	14
2.3 Factors Influencing Marine Biofouling.....	16
2.3.1 Seawater Temperature	17
2.3.2 Salinity.....	17
2.3.3 pH value.....	19
2.3.4 Water Depth, Nutrient Abundance and Light.....	21
2.3.5 Water Current and Velocity of Flow	22
2.3.6 Surface Factors	23
2.4 Antifouling Methods and Technologies.....	26
2.4.1 Physical Methods.....	27

2.4.2	Biological Methods-The Answer in Nature.....	28
2.4.3	Chemical Methods – Antifouling Coatings	31
2.5	Antifouling Coatings Performance Tests	39
2.5.1	Field Tests.....	39
2.5.2	Laboratory setups	45
2.5.3	Other Setups	47
2.6	Effect of Biofouling on Ships.....	50
2.7	Theoretical backgrounds – Roughness and Turbulent Boundary Layer	53
2.7.1	The velocity Profile in The Boundary Layer	53
2.7.2	The Effect of Surface Roughness on Boundary Layers	57
2.7.3	Determination of Roughness Functions	59
2.7.4	Identified Gaps and Conclusions	60
3	Methodology	62
3.1	Introduction	62
3.2	Methodology	62
4	Effect of Barnacle Fouling on Ship Resistance and Powering	65
4.1	Introduction	65
4.2	Manufacturing of Artificial Barnacles	66
4.3	Experimental Facilities.....	68
4.4	Plate Preparations	72
4.5	Test Methodology	77
4.6	Repeatability and Uncertainty Estimates	80
4.7	Results	92
4.7.1	Total Resistance Coefficients	92
4.7.2	Frictional Resistance Coefficients	96
4.8	Determination of Roughness Functions	111

4.9	Chapter Summary and Conclusions	118
5	Granville’s Similarity Law Scaling Procedure	120
5.1	Introduction	120
5.2	Methodology	121
5.3	Prediction of the Roughness Effects of Biofouling on Ship Resistance and Powering	124
5.3.1	Added Resistance and Effective Power of Ships.....	124
5.4	Discussion of the Results and Conclusions.....	138
6	Time-Dependent Biofouling Growth Model.....	141
6.1	Introduction	141
6.2	Modelling Approach	144
6.2.1	General Perspective	144
6.2.2	Ideal Biofouling Growth Model	144
6.2.3	Development of a Time-Dependent Model for an SPC type antifouling coating	150
6.2.4	Added Resistance and Powering Prediction Tool	159
6.3	Validation	165
6.3.1	A real ship application.....	165
6.3.2	Comparison of the results with power measurements	170
6.4	Case Study.....	183
6.4.1	Ship description and operation data.....	183
6.4.2	Results	185
6.5	Discussion and Conclusion	186
7	Discussion	191
7.1	Introduction	191
7.2	Achievement of Research Aims and Objectives	191

7.3	Novelties and Contributions to the Field.....	194
7.4	General Discussion.....	195
7.5	Chapter Summary.....	197
8	Conclusions and Recommendations	198
8.1	Introduction	198
8.2	Conclusions	198
8.3	Summary of Conclusions	200
8.4	Recommendations for Future Research	201
	References	204
	Research Outputs	219

List of Figures

Figure 2-1: Temporal sequence of biofouling with reaction types (Rosenhahn et al. 2010)	14
Figure 2-2: Microscopic organisms, including diatoms (top left pictures), bacteria (bottom left) and <i>Ulva zoospores</i> (bottom right). A <i>Balanus amphitrite</i> cyprid larva (about 300-500 μm in size) is also shown (top right) (Lejars et al. 2012).....	15
Figure 2-3: Categorization and characteristics of marine macro-organisms (Almeida et al. 2007).....	16
Figure 2-4: Annual mean of the sea surface salinity distribution in PSU (World Ocean Atlas 2005-2012, counter interval =0.5)	19
Figure 2-5: Estimated annual sea surface pH for the present day (the 1990s) (World Ocean atlas 2005).....	20
Figure 2-6: Photos of droplet regimes and contact angle range between different wettability surfaces (Bixler and Bhushan 2012).	24
Figure 2-7 An illustration of attachment point theory on cases of (a) diatom on smooth surface-multiple attachments (b) diatom small enough to fit between 2mm ripples-multiple attachments (c) diatom settled on 2 mm ripples - 3 attachment points (d) diatom settled on 4mm ripples-2 attachment points (Scardino et al. 2006).....	25
Figure 2-8: Categorization of antifouling methods drawn according to Cao et al., (2011)	26
Figure 2-9: Working principle of insoluble (above) and soluble (under) matrix paints and comparison of biocide release rate in time with minimum biocide release rate (adapted from Yebra et al., 2004).	34
Figure 2-10: Performance and Cost Comparison of Antifouling Technologies (from Lejars et al. 2012).....	38
Figure 2-11 Timeline for the experimental procedure for new antifouling technology	39
Figure 2-12: Comparison of 16 weeks AF coating field test results in temperate waters (the Mediterranean Sea, left) and warm waters (Tropical area in the Indic Ocean, right) adapted from Sanchez and Yebra (2009).	41

Figure 2-13 Polycarbonate coated panels with foul-release silicone (SIL), polyurethane (PU) and an acrylic commercial (Olympic+) based marine paints exposed on a raft in Singapore (1°23'33 N, 103°58'34E) for 24 weeks, started in June 2014 taken from Silva et al.,(2019).....	43
Figure 2-14 Front views of the dynamic rotor setup adapted from (Lindholdt 2015)	44
Figure 2-15 Schematic drawing and the picture of Couette-type rotary set-up adapted from Sanchez and Yebra (2009)	45
Figure 2-16 Picture of the Turbo Eroder apparatus Sanchez and Yebra (2009).....	46
Figure 2-17 Top views of dynamic test tank adapted from Swain et al., (2007).....	48
Figure 2-18 General arrangement of a slime growth farm device (view from top) (Atlas et al.).....	48
Figure 2-20 Diagram of a high-speed seawater flow channel (top view) adapted from Sanchez and Yebra (2009)	49
Figure 2-21 Workflow for an efficient antifouling paint design and optimisation adapted from Sanchez and Yebra (2009).....	50
Figure 2-22 Law of the wall plot for a turbulent boundary layer adapted from Schultz and Swain (2000)	54
Figure 2-23 Turbulent boundary layer shear stress profile adapted from Ligrani (1989)	57
Figure 3-1 The general methodology followed in this thesis.....	62
Figure 4-1: The picture of Amphibalanus Improvisus.....	66
Figure 4-2: The Picture of 3D Scanned Barnacle Model.....	66
Figure 4-3: Picture of a Mixed type barnacle bundle.....	67
Figure 4-4: KHL towing tank and carriage	68
Figure 4-5 LVDT transducers	69
Figure 4-6: Calibration process	70
Figure 4-7: Calibration line for Lift Transducer.	71
Figure 4-8: Calibration line for Drag Transducer.	71
Figure 4-9: Schematic of the flat plate test fixture.....	72
Figure 4-10: 10% of barnacle coverage on the flat plate	73
Figure 4-11: 20% of barnacle coverage on the flat plate	73
Figure 4-12: 40% of Barnacle coverage on a Flat Plate.....	74

Figure 4-13: 50% Percentage of Barnacle Coverage on a Flat Plate	74
Figure 4-14 NS Mixed 10% barnacle coverage on a flat plate	75
Figure 4-15 NS Mixed 20% barnacle coverage on the flat plate	76
Figure 4-16 NS Mixed 40% barnacle coverage on a flat plate	76
Figure 4-17 NS Mixed 50% barnacle coverage on a flat plate	77
Figure 4-18 C_T values of test surfaces	95
Figure 4-19 C_F values of all test surfaces.....	98
Figure 4-20: C_F comparison for 10% coverage area.....	99
Figure 4-21 C_F comparison for 20% coverage area.	100
Figure 4-22 C_F comparison for 40% coverage area.	101
Figure 4-23 C_F comparison for 50% coverage area.....	102
Figure 4-24 C_F comparison for the biggest type configurations	103
Figure 4-25 C_F comparison for the middle type configurations	104
Figure 4-26 C_F comparison for the smallest type configurations.	105
Figure 4-27 C_F comparison for the Mixed type configurations.	106
Figure 4-28 C_F comparison for the NS Mixed type configurations.	107
Figure 4-29 C_F comparison of mixed and natural settlement mixed configurations.	110
Figure 4-30: The roughness functions for all of the test surfaces.....	111
Figure 4-31: The roughness functions for all of the test surfaces together with the roughness function model of Grigson (1992).	112
Figure 4-32: The roughness functions for all test surface, using corresponding k_G values together with the roughness function of Grigson (1992).....	113
Figure 5-1: C_{FS} and shifted the frictional line for C_{FR}	121
Figure 5-2: The third step of the Granville scale up.	122
Figure 5-3: Granville scale-up procedure.	123
Figure 5-4 Added frictional resistance diagram for a 230 m container ship with different barnacle fouling conditions	126
Figure 5-5 Added frictional resistance diagram for a 230 m container ship with different barnacle fouling conditions	126
Figure 5-6 Added frictional resistance diagram for a 180 m bulk-carrier with different barnacle fouling conditions	127

Figure 5-7 Added frictional resistance diagram for a 180 m bulk-carrier with different barnacle fouling conditions	127
Figure 5-8 Added frictional resistance diagram for a 270 m LNG carrier with different barnacle fouling conditions	128
Figure 5-9 Added frictional resistance diagram for a 270 m LNG carrier with different barnacle fouling conditions	128
Figure 5-10 Added frictional resistance diagram for a 250 m tanker with different barnacle fouling conditions	129
Figure 5-11 Added frictional resistance diagram for a 250 m tanker with different barnacle fouling conditions	129
Figure 5-12 Added frictional resistance diagram for a 120 m special purpose vessel with different barnacle fouling conditions	130
Figure 5-13 Added frictional resistance diagram for a 120 m special purpose vessel with different barnacle fouling conditions	130
Figure 5-14 Added frictional resistance diagram for a 60 m special purpose vessel with different barnacle fouling conditions	131
Figure 5-15 Added frictional resistance diagram for a 60 m special purpose vessel with different barnacle fouling conditions	131
Figure 6-1 Illustration of a downward shift in log-law velocity profile due to the roughness effect (adapted Schultz and Swain 2000).....	161
Figure 6-2 Relative frequency of idle time occurrence according to latitude.....	166
Figure 6-3 Propulsion plan layout.....	168
Figure 6-4 Estimation of the fouling ratings, percentage of surface coverage for calcareous type fouling, percentage of increases in the frictional resistance in respect to time.	169
Figure 6-5 Estimated delivered-power-modelling flowchart.....	173
Figure 6-6 Time periods for delivered power comparison.....	174
Figure 6-7 First Period - 17/05/12-24/05/12	175
Figure 6-8 Second period – 22/02/13-26/03/13	175
Figure 6-9 P_{DM} and P_{DE} comparisons at various ship speeds – CASE A.....	176
Figure 6-10 GH model scatterplot – CASE A	177

Figure 6-11 Relative frequencies of relative error percentage distribution – CASE A 177

Figure 6-12 P_{DM} and P_{DE} comparisons at various ship speeds – CASE B..... 178

Figure 6-13 GH model scatterplot – CASE B..... 179

Figure 6-14 Relative frequencies of relative error percentage distribution – CASE B 179

Figure 6-15 P_{DM} and P_{DE} comparisons at various ship speeds – CASE C..... 180

Figure 6-16 GH model scatterplot – CASE C..... 181

Figure 6-17 Relative frequencies of relative error percentage distribution – CASE C 181

Figure 6-18 Illustration of the ship route 184

Figure 6-19 Idle times for each latitude degree (% of total idle time)..... 184

Figure 6-20 Estimation of the fouling ratings, percentage of surface coverage for calcareous type fouling, increase in the frictional resistance and percentage increase in effective power with respect to time 186

List of Tables

Table 2-1 Advantages and drawbacks of the Turbo Eroder in comparison with traditional, in situ dynamic drum apparatus	47
Table 4-1 Configuration table	67
Table 4-2: Uncertainty limits in C_T	83
Table 4-3 Uncertainty limits in C_F	86
Table 4-4: Uncertainty limits in ΔU^+	89
Table 4-5 Percentage increase in the C_T values of test surfaces with respect to reference plate (Smallest, Middle and Biggest)	94
Table 4-6 Percentage increase in the C_T values of test surfaces with respect to reference plate (Mixed and N_s Mixed)	94
Table 4-7 Percentage increase in the C_F values of test surfaces with respect to reference plate (Smallest, Middle and Biggest)	97
Table 4-8 Percentage increase in the C_F values of test surfaces with respect to reference plate (Mixed and N_s Mixed)	97
Table 4-9 Change in the C_F values of the test plates with respect to the reference plate	106
Table 4-10 Change in C_F values of the test plates with respect to the reference plate	106
Table 4-11 ΔU^+ and k^+ values of test surfaces for $k = 0.059 h$ (coverage %) ^{0.5} (Biggest and Smallest).....	115
Table 4-12 ΔU^+ and k^+ values of test surfaces for $k = 0.059 h$ (coverage %) ^{0.5} (Middle and Mixed)	115
Table 4-13 ΔU^+ and k^+ values of test surfaces for $k = 0.059 h$ (coverage %) ^{0.5} (Mixed and NS Mixed)	116
Table 4-14 ΔU^+ and k^+ values of test surfaces for k_G (Biggest and Smallest).....	116
Table 4-15 ΔU^+ and k^+ values of test surfaces for k_G (Middle and Mixed).....	117
Table 4-16 ΔU^+ and k^+ values of test surfaces for k_G (Mixed and NS Mixed).....	117
Table 5-1 Increases in frictional resistance and powering compared to smooth conditions	132

Table 5-2 Speed reductions in fouled conditions for ships compared to smooth conditions	133
Table 5-3 Speed reductions in fouled conditions for ships compared to smooth conditions	134
Table 6-1 The coverage ratings with an equivalent covered surface adapted from (Silva et al., 2019).....	151
Table 6-2 Antifouling coating performance parameters for each type of fouling ...	155
Table 6-3 Constants of logistic curves	157
Table 6-4 A ranges of representative coating and fouling conditions. The values of equivalent sand roughness heights and average coating roughness are based on the measurements of Schultz (2004) adapted from Schultz (2007).....	162
Table 6-5 Fouling descriptions in relation with coverage ratings, percentage of coverage and equivalent sand roughness heights in conformity with roughness functions provided in Schultz (2007) and Uzun et al. (2017).....	163
Table 6-6 Ship profile	165
Table 6-7 Measured values available from the continuous monitoring system (Coraddu et al., 2017).....	167
Table 6-8 Data filtering.....	170
Table 6-9 Time periods for delivered power comparison.....	174
Table 6-10 Summary of case results	182
Table 6-11 Ship profile	183

Abstract

Despite a large amount of research, the effect of barnacle fouling on the frictional resistance has a lack of systematical experimental investigation focussing on parameters such as size, coverage area and settlement pattern. Limited roughness functions data about barnacle fouling is available in the literature. Moreover, although a large number of the study has been carried out on the effect of roughness on the frictional resistance, only the limited lab-based results were extrapolated to the full-scale ship results (Schultz et al.,2011).

In addition, antifouling precautions cost 5% of the total fuel-oil cost of world fleet for a year, and to the best of the author's knowledge,there is no scientifically settled approach for selecting the best antifouling coating for the ship in question. This situation forced vessel owners/responsible person have their particular strategy to deal with marine fouling based on personal experience or negotiating with the sales personnel of the paint company.

Based on the background given above, an extensive and systematic experimental study was carried out for investigating the effect of barnacle fouling on ship resistance and powering. One of the most common barnacle geometry was produced on bundles through a 3D technology and attached on the flat plates for towing tank experiments at Kelvin Hydrodynamics Laboratory in the University of Strathclyde. Eighteen different configurations varying in terms of size, coverage area and settlement pattern were tested. Drag characterisations, determination of roughness functions and full-scale extrapolations were performed.

A simplified time-dependent biofouling prediction model for ships was developed in order to be used as a decision support tool, regarding the effect of biofouling on ship resistance due to the performance of the antifouling coating. First, a growth prediction model was developed based on the antifouling field test data (fouling ratings in time) and then time parameter of this model was assigned to the idle times of ships coming from ship operational data. The fouling ratings were predicted in time according to this data, and then these fouling ratings were converted into the sand roughness height in

accordance with the roughness data provided in the literature and this PhD thesis. Predicted equivalent sand roughness heights were then employed in the Granville similarity law scaling process to predict the increase in the ship frictional resistance and powering. Finally, the results were compared with real-world operation data and ship performance report provided by a ship performance analysis company. The results of the comparison showed that there is a good agreement between the predictions and real-world operation data as well as the company report.

Acronyms and Abbreviations

GHG	Green House Gases
EEDI	Energy Efficiency Design Index
IMO	International Maritime Organisation
NIS	Non-indigenous species
SEEMP	Ship Energy Efficiency Management Plan
EPS	Extracellular polymeric substances
ERI	Engineered roughness index
SEA	Surface energetic attachment
TBT	Tributyltin
TBT-SPC	Tributyltin Self-Polishing Copolymer Paints
CDP	Controlled depletion systems
AF	Antifouling
CFD	Computational Fluid Dynamics
MPF	Multipurpose Flume
S	Smallest type configuration
M	Middle type configuration
B	Biggest type configuration
NS	Natural settlement
Mix	Mixed type configuration
CAD	Computer-aided design
KHL	Kelvin Hydrodynamics Laboratory
LVDT	Linear variable differential transformer
SC	Surface coverage
BG	Biofouling growth
PSU	Practical salinity unit
API	Antifouling performance index
FR	Fouling Rating
GH	Guldhammer & Harvald method

Nomenclature

psu	Unit Of Salinity
v	Water Flow Velocity (m/s)
I	Light Intensity (cd)
S	Concentration Of Nutrients ($\mu\text{mol kg}^{-1}$)
m_t	Microtexture
σ	Surface Potential (C. m^{-2})
θ_c	Contact Angle Of Surface (degree)
R_t	Surface Roughness (μm)
η_c	Antifouling Coating Performance Parameter
μ	Specific Growth Rate
η_{cx}	Antifouling Coating Performance Parameter At The Field Test Location X
η_{cy}	Antifouling Coating Performance Parameter At The Field Test Location Y
η_{ca}	Antifouling Coating Performance Parameter At An Arbitrary Location
b and f	Logistic Curve Regression Parameters For SC Of Calcareous Type Fouling
SC	Surface Coverage (%)
BG	Biofouling Growth
API	Antifouling Performance Index
FR	Fouling Rating
t_0 and τ	Antifouling Coating Regression Parameters
L	Ship Design Length (m)
B	Ship Design Breadth (m)
T	Ship Design Draft (m)
Δ	Ship Design Displacement(tonnes)
V	Ship Design Speed (knot)
a	Regression Upper Limit
t	Idle Time Length (Hour/Day)
SST	Sea Surface Temperature ($^{\circ}\text{C}$)
SST_y	The Sea Surface Temperature At The Location Y ($^{\circ}\text{C}$)
SST_x	The Sea Surface Temperature At The Location X ($^{\circ}\text{C}$)
SST_a	The Sea Surface Temperature At An Arbitrary Location ($^{\circ}\text{C}$)
t_{01} - t_{E1}	Database First Period
t_{01} - t_{E2}	Database Second Period
REP	Relative Error Percentage
k_s	Equivalent Sand Roughness Height (μm)
k	Roughness Length Scale (μm)

k^+	Roughness Reynolds Number
ΔU^+	Roughness Function
U^+	Non-Dimensional Velocity
y^+	Non-Dimensional Normal Distance From The Wall
Rt_{50}	Highest Peak To Lowest Valley Roughness Height For A 50mm Cut-Off Length (μm)
R_T	Ship Total Resistance (N)
P_E	Effective Power (kW)
P_{DE}	Estimated Delivered Power (kW)
P_{DM}	Measured Delivered Power (kW)
ρ	Density (kg/m^3)
S	Wetted Surface Area (m^2)
C_F	Frictional Resistance Coefficient
C_R	Residual Resistance Coefficient
C_{AA}	Air Drag Coefficient
$I+k_0$	Form Factor
C_T	Total Resistance Coefficient
C_{TR}	Total Resistance Coefficient In Rough Condition
C_{TS}	Total Resistance Coefficient In Smooth Condition
ΔC_F	Increase In Frictional Resistance
ΔP_E	Increase In Effective Power
$t_{01}-t_{E1}$	Database First Period
$t_{01}-t_{E2}$	Database Second Period
C_{FR}	Frictional resistance coefficient in rough condition
C_{FS}	Frictional resistance coefficient in smooth condition
C_{RR}	Residuary resistance coefficient in rough condition
C_{RS}	Residuary resistance coefficient in smooth condition
C_D	Drag coefficient
C_F	Frictional resistance coefficient
C_k	Roughness coefficient
C_L	Lift coefficient
h	The highest roughness height
k_G	Experimentally obtained equivalent roughness length scale
Re	Reynolds number

1 Introduction

"As you start to walk on the way, the way appears."

Rumi

1.1 Introduction

This chapter will start by providing general perspectives in Section 1.2 about the topics studied in this thesis. Following that, motivations behind each chapter of the thesis will be presented in Section 1.3. After that, the main research aims and objectives will be stated in section 1.4. In Section 1.5 gives the structure of this thesis. Finally, the Chapter is summarised in Section 1.6.

1.2 General Perspectives

Shipping is significant for world trade as over 80 per cent of global trade by volume is being carried by ships. Importance of shipping and world trade demand drastically increased from 1965 to 2017, and as anticipated, it will increase in the future. Moreover, this increase is not only for the cargo weight in tons but also for the length of the route in miles with the shifting of trade growth to Asian countries. When statistics are compared, it can be seen that the world seaborne trade in a unit of billion-ton miles was around 6000 in 1965 however within 52 years with over 830% increase it became around 56000 billion ton-miles in 2017 (Branch 2008) (UNCTAD 2017).

Today shipping is more competitive and intricate than ever it was with the added effect of active integration with other transport modes. Within this framework, the main focus on improvement for ships should propose larger carriage capacity, higher speeds, lower capital and operating costs, better manoeuvrability, reliability, safety and reduced environmental impact such as Green House Emissions (GHG). Nowadays, many scenarios were outlined for future fuel trends such as Status Quo, Global Commons and Competing Nations assessing the possible trend in usage of HFO, MDO/MGO, LSHFO, LNG, Hydrogen, and Methanol by 2030 (Hirdaris 2014).

No matter which fuel will be used in future, as it will be an energy source and will be limited in any case, ships must be improved in terms of efficiency in order to decrease operating costs and environmental impacts. Indeed this is not a new effort. In the beginning, the importance of GHG emissions was brought to attention in the Kyoto Protocol in Japan in 1997 to reduce six primary GHG emissions. Then the first legally binding climate change treaty was adopted with the mandatory of The Energy Efficiency Design Index (EEDI) and Ship Energy Efficiency Management Plan (SEEMP) for ships in 2011 (IMO 2011)

After the implementation of these regulations, a need for ship efficiency solutions was revealed in the marine world, and possible solutions were started to be assessed for reducing GHG emissions and having more energy-efficient shipping. Some example of these solutions can be listed as stated below:

- Reducing air resistance; Superstructure streamlining
- Using wind power; Wind engines, Wind kite, Sails
- Solar power integration; Solar panels
- Air lubrication
- Trim and Ballast optimization
- Pod usage; Wing pods, Podded propulsor
- Propeller design upgrades; Contra-rotating propellers, Ducted propellers
- Hull protection (hydrodynamic resistance); Biocide based coatings, Foul-release coatings, hull cleaning, and propeller polishing.

This thesis is focused on the benefits of the hull protection option, and it shows the detrimental effects of marine biofouling on full-scale ship resistance and power. Marine fouling is a significant problem since it increases hull roughness and hence it has effects such as increased ship resistance and power requirements, reductions in ship speed and consequently increased GHG emissions. Moreover, due to ballast water exchange operations and biofouling on the various parts of the vessel, ships pose severe risks for the world's marine biosecurity. The IMO published a guideline for the control and management of ship's biofouling to minimize the transfer of invasive aquatic species (IMO 2011).

Hull resistance is a vital parameter for ships since it affects power requirements and thereby fuel consumption. Although it may change from a ship –to –ship according to their operation characteristics, general intent in ship design is to design a hull form with lower hull resistance.

Ship resistance mainly consists of two principal components: frictional and residual resistance. Results of a resistance experiment conducted on destroyer Yudachi revealed that at low speeds, the frictional resistance amounts to 87% of the total resistance (Woods Hole Oceanographic Institute 1952) However, as ship speed increases the importance of frictional resistance diminishes and frictional resistance amounts to around 40% of the total resistance (Woods Hole Oceanographic Institute 1952). It is important to note that frictional resistance is the dominant component of ship total resistance for ships, especially at low speed.

According to the review of marine transport of UNCTAD (2017) high-speed cargo transport takes around 16% share in total world seaborne trade in cargo ton-miles which can be interpreted as 84% of total cargo ton-miles are carried by slow speed ships. For this reason, any improvement in frictional resistance would have a significant influence on world fleet fuel consumption.

Marine biofouling, which is the main problem addressed in this thesis, on the other hand, causes significant increases in ship resistance and power due to the accumulation of marine species on ship hull. Schultz et al. (2011) showed that fouling conditions from light slime to heavy calcareous fouling might change required shaft power of ship from 9% to 76% for an Arleigh Burke-class destroyer at a speed of 15 knots. Furthermore, because of the increased power requirements, ship operators may either burn more fuel oil, to maintain their cruise speeds or decrease cruise speed to prevent extra fuel consumption.

For the reasons outlined above, keeping ship hulls smooth is vital in terms of both the economic and the environmental point of view. The ways of protecting ship hulls are called fouling control methods, and they can be grouped into three according to the working principles as chemical, physical, and biological (Cao et al.,2011). Although

many options are available within these groups, marine antifouling paints are the most effective way to protect ship hulls from fouling accumulation.

The two main points that need to be taken into consideration critically in terms of energy efficiency for antifouling coatings are shown below:

- Initial drag efficiency of an antifouling product when it is applied
- Time-dependent drag profile of antifouling product during its life cycle

Both points are vital and have to be assessed when an antifouling paint selection is made. Towing tank tests for flat plates coated with an antifouling coating (Demirel 2015) in question are one of the popular ways to measure initial drag efficiency of newly applied antifouling coatings. The ways to measure the performance of newly applied coatings can be extended with rotational disk/cylinder setups (Weinell et al. 2003), water tunnels, fully turbulent flow channel, multipurpose flume facility (Candries and Atlar, 2005; Yeginbayeva et al., 2018) and static and dynamic panel exposure tests on boats (Swain et al. 2007). Whereas there is a solid settled physical ground to measure the initial performance of newly applied antifouling coatings, but it is not easy to measure or predict the time-dependent operational performance of antifouling for a large time scale. Time-dependent performance of antifouling coatings is tested mostly in laboratory environments, field tests, and via limited ship tests. However, there is no study connecting these paint test results to full-scale ship resistance in order to understand the time-dependent drag profile of the antifouling coatings.

Ship performance monitoring via on-board measurement devices can give an idea of the performance of antifouling coatings (Armstrong 2013), but there are also problems in this such as low frequency of data sampling from on-board devices and lack of utilization since a minimal number of ships have these monitoring devices on board.

In a relatively short time, after ships are launched, biofouling starts and ship hulls are exposed to numerous marine organisms of which there are more than 4000 species according to Crisp (1973) and Callow and Callow (2002). With regards to microorganisms, which are classified under the common name of slime, main macro-organisms can be listed as shown below, according to Almeida (2007).

- Algae (plants)
 - Green (Enteromorpha, Ulva, and Cladophora)
 - Brown (Ectocarpus and Fucus)
 - Red (Ceraminum)
- Invertebrates (animals)
 - Hardshell organisms (Balanus, Barnacles, Molluscs, Bryozoans)
 - Grass-type organisms (Hydroids or bryozoans)
 - Small bush organisms (Hydroids or bryozoans)
 - Spineless organisms (Ascidians and sea anemones)

A growing body of literature has investigated the effects of a wide variety of biofouling conditions on ship resistance. Watanabe et al. (1969) indicated that added frictional resistance due to slime formation was 8-14% whereas Haslbeck and Bohlander (1992) reported that a frigate hull covered with fairly substantial slime film with little to no calcareous biofouling showed 8-18% difference in shaft power. Schultz (2007) stated that increases in shaft power were 21% for heavy slime, 35% for small calcareous fouling or weeds, 54% for medium calcareous fouling and 86% for heavy calcareous fouling.

Despite this interest, as far as the author knows, no one has systematically studied the effects of particular fouling species with regards to fouling conditions such as having different dimensions, coverage areas, and settlement patterns.

Therefore, this thesis mainly focused on the investigation of barnacle fouling on ship resistance by using 3D printing technology and the overall (towed plate) method. Also, it focuses on developing a decision-support tool which bridges antifouling field tests and ship operation profiles in order to make time-based assessments for the performance of antifouling coatings.

1.3 Motivations behind this Work

This section gives the main motivations behind the study and a brief description of how the chapters in this study challenge against gaps in the literature described as follows:

- It is brought to attention by ITTC (2011) that there is a lack of roughness database for biofouling surfaces and testing rough surfaces representing different fouling conditions is encouraged. To develop a scientific and practical approach for predicting the effect of biofouling on added resistance, and hence the increase in power requirements, this study presents a systematic experimental approach. (i.e. using 3-D printed artificial barnacles in order to systematically determine the effects of different levels of fouling growth and coverage on the hydrodynamic resistance of plates) (Chapter 4).
- As stated in Demirel (2015), “a future work may be the determination of the roughness functions of surfaces covered with fouling, by conducting further experiments. Naturally fouled surfaces, or surfaces covered with artificial fouling organisms, such as barnacles or slime, could be used for the experiments”. To the best of this author’s knowledge, there is no systematic study on a particular biofouling species regarding effects of dimensions, coverage rates, and settlement pattern on full-scale ship resistance (Chapter 3 & 4).
- ASTM is the well-known and appropriate standard to be used in biofouling studies, and it proposes a standard settlement configuration for biofouling accumulations. However, to the best of the author’s knowledge, this settlement was not tested for consistency with natural conditions Therefore it is essential to conduct a study in order to investigate how settlement pattern affects full-scale ship resistance. Moreover, it also testifies ASTM standards and gives feedback about the applicability of their settlement configuration compared to the so-called natural settlement. (Chapter 3 & 4)
- The ITTC Resistance and Propulsion Committee decided that there is a need for investigation of change of standard hull and propeller roughness and develop and propose new roughness correction methods for both hull and propeller. Therefore the roughness functions and their extrapolations results to

full-scale produced in this study can be used to predict ship hull efficiency in the fouled situation. Moreover, this roughness functions can be implemented for propeller and rudder to be able to understand the effect of fouling on propulsion and manoeuvring (Chapter 3 & 4).

- In spite of some research conducted on new generation coating systems by some leading coating manufacturers, e.g. in Candries (2001), as Swain (2007) indicated, there are no standards, tests, or models with which to predict antifouling coating performance under ship operating conditions. Therefore, antifouling coatings are selected according to the information supplied by the manufacturer, by word of mouth, and negotiations with a salesperson with the economic aspects of the antifouling coating. This situation, without doubt, causes detrimental effects on ship performance, reduction in ship speed, or increase in required ship power. Due to contractual restrictions, ships have to maintain their operation speed and hence increased power causes fuel consumption above the anticipated amount. Therefore, it is essential to develop a decision-support model that correlates biocide based antifouling coating performances and ship operations in order to make the most effective choice of antifouling coating for any particular ship in question (Chapter 6).
- The selection of the appropriate biocide based antifouling coating is not only crucial for preventing extra fuel consumption and thereby extra GHG emissions but also for preventing unscheduled maintenance operations (dry-docking or underwater cleaning) which leaves significant losses in company revenues. For this reason, a model predicting possible fouling conditions on ship and its effect on ship resistance for the specific ship route planned would be very beneficial in terms of economic and environmental concerns (Chapter 6).
- Moreover, biofouling causes spread of some marine organisms called non-indigenous species (NIS) which is now recognized by IMO as one of the greatest threats to ecological and the economic well-being of the planet. This

undesired transportation of invasive aquatic species directly affects aquaculture and fisheries, tourism, and infrastructures in coastal areas. Biofouling was first brought to IMO's attention in 2006 and after following studies in this area, IMO published guidance as MEPC.1/Circ.811 for minimizing the transfer of invasive species in May 2013. Implementation is planned from September 2018 for five years period. For the reasons outlined above, a developed decision-support model, capable of selecting the most appropriate antifouling coating is also essential for minimizing the transportation of NIS by preventing fouling accumulation on ship hulls to some extent (Chapter 6).

- Effective biofouling management is also critical for the Guidelines for the development of a Ship Energy Efficiency Management Plan (SEEMP) (resolution MEPC.282 (70)) implemented by IMO in 2016. Therefore, it is fundamental to produce data in order to point out the effect of the extensive range of fouling conditions considering parameters such as coverage rate and roughness height on ship resistance. In addition to that, developing a model for predicting the performance of antifouling coating before its application on ship hull would, therefore, be of great benefit. (Chapter 3&4&5).

1.4 Research Aims and Objectives

The main aims of this PhD thesis are to enhance the existing biofouling roughness database, particularly on barnacle fouling and to develop a time-dependent biofouling model that predicts added frictional resistance due to biofouling while the ship is in operation. The specific objectives in detail were listed below to support the realisation of the motivations behind this study, as stated in the previous section:

- To review the existing literature on biofouling, essential factors of biofouling growth, antifouling coatings and testing methodologies, modelling the roughness effects of different fouling conditions on ship resistance and powering.

- To manufacture the selected barnacle species by using 3D printing technology in order to conduct a systematic study and to create an extensive biofouling roughness database by making variations on coverage rates, dimensions and settlement pattern.
- To verify the settlement pattern in ASTM standards by proposing a new chaotic settlement pattern in order to investigate differences in frictional resistance between two different settlement patterns.
- To extrapolate the experimental roughness data on full-scale ships through similarity law scaling to show increases in frictional resistance and required ship power or to show reductions in ship design speed through added resistance diagrams and tables
- To investigate and show usability antifouling field tests in correlation with real ship operations for antifouling coating selection for the ship in question.
- To develop a time-based model that predicts the effect of biofouling on ship resistance combining antifouling coating field tests with ship operation data including ship speed, idle time-frequency, and ship route.
- To test and validate this developed model by performing it on one year of a real ship operation data and then comparing the results with data analysis tool for ship operation data collected via on-board measurement devices.

1.5 Structure of this Thesis

The structure of this thesis is briefly summarised, as stated below:

- Chapter 2 (Literature Review) presents a detailed literature survey on the biofouling phenomenon and its effects on ships in an engineering point of view. It lists conducted research to date on the effects of biofouling conditions on ship resistance and powering. Moreover, general information on antifouling technologies, mainly on coatings and their performance testing methods are presented. The gaps in the literature are also noted.
- Chapter 3 presents the general methodology followed in this thesis.
- Chapter 4 (Effect of Barnacle Fouling on Ship Resistance) presents an experimental determination of the roughness functions of flat plates covered with artificially printed barnacle tiles. Details of the 3D printed barnacle tiles and test configurations were presented. Results of towing tank experiments for each test surface were given, including drag coefficients, roughness functions, and uncertainty estimations.
- Chapter 5 (Granville's Similarity Law Scaling Procedure) presents predictions of increases in the frictional resistance and effective power of ships due to fouling conditions tested in Chapter 4. Details of Granville's similarity law scaling procedure are provided. Six ships in different lengths and operating at varying speeds were used as case studies. Full-scale predictions of increases in the frictional resistance are illustrated by means of diagrams, whereas predictions of increases in the effective power and decreases in the ship speed are given in the form of tables.
- Chapter 6 (Time-Dependent Biofouling Growth Model) proposes a time-dependent biofouling model that enables prediction of the effect of biofouling conditions occurring during ship operation on ship resistance and powering. The model was developed by correlating antifouling field performance test and

ship operation data to predict biofouling growth in real ship operation. The developed model then was tested on one year of ship operation data collected via onboard devices from a ship coated with an antifouling coating for which field performance test data is available. Validation for the model was made based on comparisons in power requirements after one year over a data analysis tool presented in Coraddu et al. (2017).

- Chapter 7 (Discussion) provides a broad discussion on how the research study conducted in this thesis contributed to existing literature and to point out clearly how the designated aims and objectives were achieved.
- Chapter 8 (Conclusion and Recommendations) presents the concluding remarks and recommendations for further work.

1.6 Chapter Summary

This chapter introduced the framework of the study conducted in this thesis. The general perspectives, motivations behind this work, research aims and objectives and structure of the thesis were presented in this chapter.

2 Literature Review

2.1 Introduction

The aim of this Chapter is to identify current gaps in the state-of-the-art literature regarding the research study presented in this thesis in order to make a novel contribution to the field. For this reason, an extensive literature review was performed to justify the aim and objectives of this thesis and to determine literature gaps and to support research motivations behind this thesis.

In order to achieve the chapter objectives, Section 2.2 provides information on marine biofouling explaining the biofouling stages along with the types of biofouling. In Section 2.3, an extensive assessment of the factors influencing marine biofouling was introduced, whereas in Section 2.4, antifouling methods and technologies were reviewed. This followed by a review of state-of-art experimental methods for testing antifouling coating performances in Section 2.5. The previous studies on the effect of biofouling on ship resistance and powering were shown in Section 2.6. In Section 2.7, the turbulent boundary layer and the effect of roughness on the turbulent boundary layer were presented. Finally, the concluding remarks of the literature review are listed as well as providing the identified gaps in the literature.

2.2 Marine Biofouling

Biological fouling, commonly called biofouling, is the undesired accumulation of biological matters on a surface that and it is mainly divided into two major groups as micro and macro fouling. Although biofouling may pose various problems in different areas such as medical (only micro fouling), industrial and marine, this study will be focusing on only marine biofouling.

Once a structure comes into contact with seawater, the biofouling process starts immediately from micro-scale to macro-scale in time. Without a doubt, any structure

such as ships, offshore structures, buoys, underwater cables, etc. which is in contact with seawater is an object for biofouling (Bixler and Bhushan 2012).

There is a temporal sequence in the biofouling process, which is generally considered in four main stages. Marine biofouling on a substrate starts with adsorption of organic particles in seawater such as protein, polysaccharide, and proteoglycan. This adsorption is driven by physical forces such as Brownian motion, electrostatic interaction, gravity, and van der Waals forces, and it is the first stage of biofouling, which is called conditioning film or layer. The first stage takes place in a minute and makes the substrate surface suitable and attractive for microorganisms (Loeb and Neihof, 1975; Baier, 1984; Lewin, 1984; Abarzua and Jakubowski, 1995).

Then the process carries on with the formation of microbial biofilm within two inner stages. First one is reversible adsorption of pioneering microorganism on the modified surface; this process is also mainly governed by physical forces. The initial process is called reversible since there is no strong connection between microorganisms (bacteria and diatoms) and the surface during the first stage. Secondly, the adhesion takes place as these microorganisms adhere on the surface and form a microbial film by secreting extracellular polymeric substances (EPS) together with protozoa and rotifers within 1-24 hours. This specially created gel-like structure (EPS) provides microorganisms with protection from outside and helps to capture required nutrients from the water with also preventing loss of resources produced inside the structure (Donlan 2002; Yebra et al. 2004).

In a week after the formation of the microbial film, colonization gears up with adsorption of secondary colonizers including spores of macroalgae, protozoa, and dominantly diatoms. It is not easy to distinguish existing colonization in the third stage as it is the transition stage from micro fouling to macro fouling (Von Oertzen et al. 1989).

In the fourth stage, larvae of macro organisms, which are called tertiary colonizers, attach on the surface. Also, the existing macro-organisms that settled in the previous stage keep growing and reproduce in this stage. Finally, from the beginning within 2-

3 weeks, the target surface ends up with very complex and multi-dimensional biological community unless any precaution is taken (Cao et al. 2011).

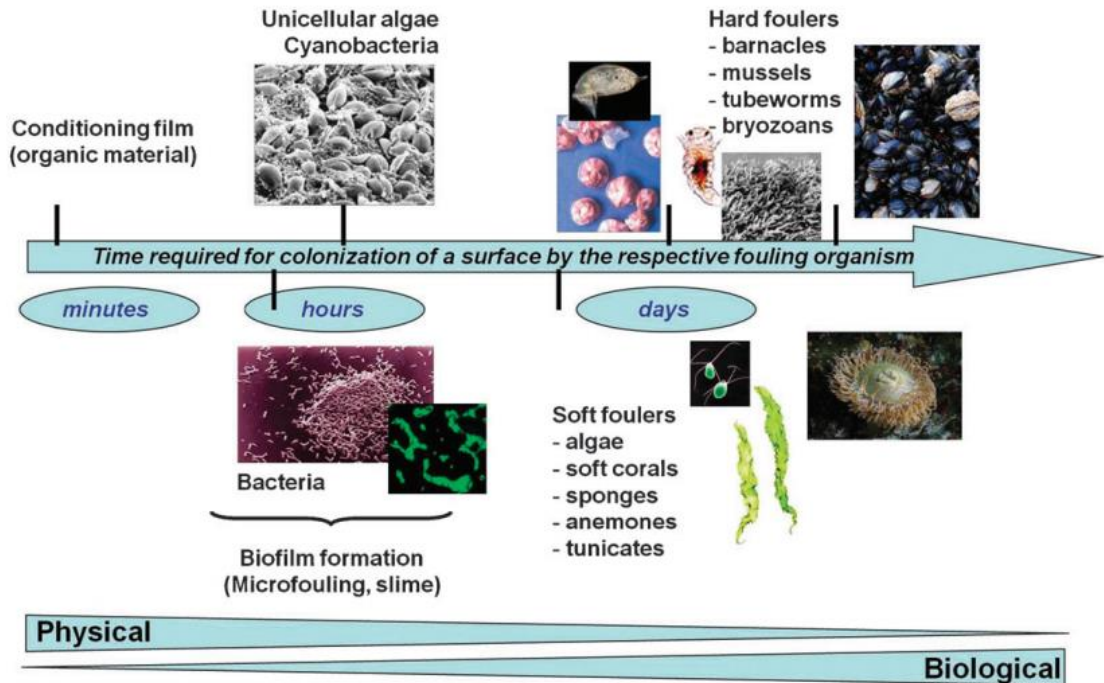


Figure 2-1:Temporal sequence of biofouling with reaction types (Rosenhahn et al. 2010)

Figure 2-1 summarizes biofouling accumulation stages, from micro fouling to macro fouling with the type of reactions take place during this process. Although this is not the exact sequence that has to be seen, biofouling formation usually follows this order (Yebra et al. 2004 ;Cao et al. 2011).

2.2.1 Types of Marine Fouling

As has already noted, there are more than 4000 marine fouling species which have intentions to attach human-made structures (Crisp 1973; Callow and Callow 2002). However, marine biofouling can be mainly divided into two groups as microfouling and macro fouling of which both parts of an involved living community. Micro fouling community, which is called slime in naval architecture literature, comprises diatoms, bacteria, protozoa, and spores of macroalgae. Figure 2-2 illustrates some captured figures of these microorganisms.

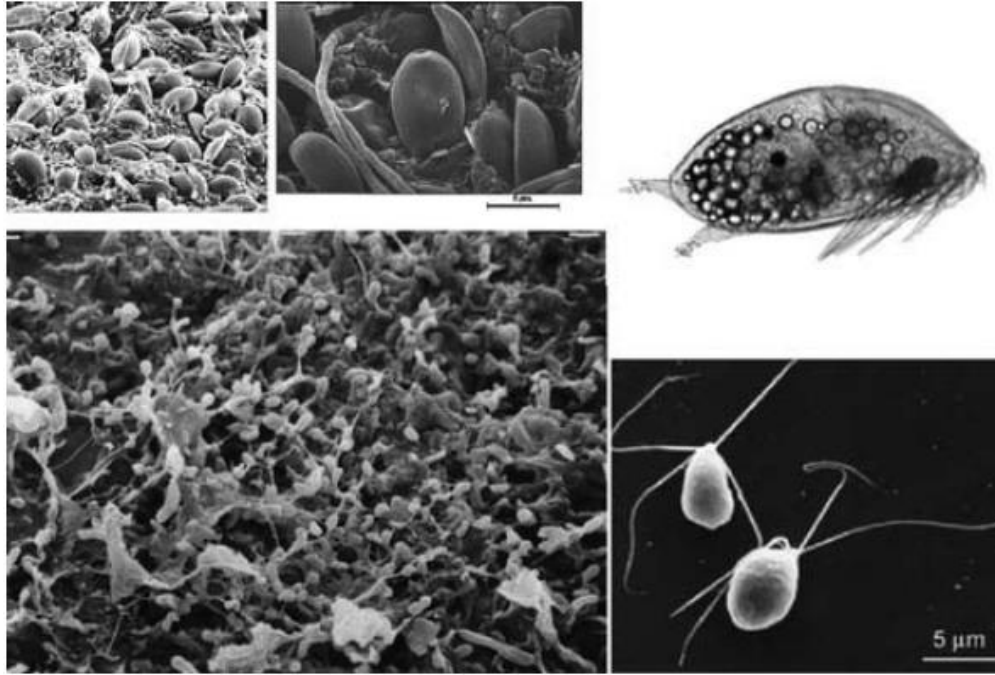


Figure 2-2: Microscopic organisms, including diatoms (top left pictures), bacteria (bottom left) and *Ulva* zoospores (bottom right). A *Balanus amphitrite* cyprid larva (about 300-500 μm in size) is also shown (top right) (Lejars et al. 2012).

As stated above, these organisms play an essential role in marine fouling accumulation process such as colonizing the substrate surface and making a significant contribution for start of macro fouling by secreting EPS in order to make the surface conditions suitable. Moreover, micro fouling is attractive for macro fouling as it can be a natural food resource for macro fouling organisms.

In the 1960s with attempts of Organisation for Economic Cooperation and Development (OECD), a study for classification of marine macro-organisms that attach to ship hulls was conducted by French Standardization Association (AFNOR) (Almeida et al. 2007). Figure 2-3 shows the categorization and characteristics of the main marine macro organism species.

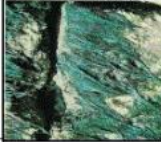

















Groups	Algae (plants)	Invertebrates (animals)								
Subgroups	(a) green, (b) brown and (c) red	Hard shell organisms				Grass type organisms	Small bush organisms	Spineless organisms		
Designation	(a) <i>Enteromorpha</i> , <i>Ulva</i> and <i>Cladophora</i> , (b) (<i>Ectocarpus</i> and <i>Fucus</i> , and (c) (<i>Ceramium</i>)	<i>Balanus</i>	<i>Barnacles</i>	<i>Molluscs</i>	<i>Fouling bryozoans</i>	<i>Hydroids or bryozoans</i>	<i>Hydroids or bryozoans</i>	<i>Ascidians</i>	<i>Sponges and sea anemones</i>	
Example of typical aspect										
Designation	<i>Green algae</i>	<i>Balanus</i>	<i>Calcareous polychaetes</i>	<i>Molluscs</i>	<i>Fouling bryozoans</i>	<i>Bryozoans</i>	<i>Ascidians</i>			
Example of typical aspect										
Short description	Only plants that become attached to immersed surface: a) close to surface; b) at mid depth; and c) at depth	Attached trunco-conical or cylindrical crustaceans	Barnacles are Balanus that are fixed to surfaces via a stem	Bivalves containing a spineless animal in their interior	Calcareous incrustations that multiply from a central individual	Organisms that cover surfaces with an open grass or fur	Like bushes of several centimetres and with branches	Constituted by a spineless bag with two tubular openings or starry plates	Spineless and spongy aspect (sponges) and sea anemones	

Figure 2-3: Categorization and characteristics of marine macro-organisms (Almeida et al. 2007)

As shown in Figure 2-3, macro fouling is divided into two groups, such as algae (plants) and invertebrates (animals). Algae group comprises three types of marine species including green (*Enteromorpha*, *Ulva* and *Cladophora*), brown (*Ectocarpus* and *Fucus*) and red (*Ceramium*). Invertebrates (animals) on the other side are separated into four sub-groups as a hard shell, Grass-type, Small bush, and Spineless organisms. While hardshell organisms refer to; *Balanus*, *Barnacles*, *Mollusks* and *Bryozoans*, grass type and Small bush groups; *Hydroids* or *Bryozoans* species and Spineless organisms; *Ascidians*, *Sponges* and *sea anemones* (Almeida et al. 2007).

2.3 Factors Influencing Marine Biofouling

Biofouling adhesion and growth are affected by many parameters since the process includes physical, chemical, and biological processes. These parameters can be summarized as:

- Seawater temperature
- Salinity (organic material content in seawater)
- pH, Water depth, Nutrients abundance, Light
- Water current and velocity of flow
- Surface factors

2.3.1 Seawater Temperature

Seawater temperature plays a catalyzer role in biofouling accumulation as it affects breeding and growth rate of these marine organisms. Although each species has different temperature tolerances, it is well-known that rising temperature generally has positive effects on marine organisms' breeding and growth rates (Woods Hole Oceanographic Institute 1952). Depending on the temperature, different regions in world seas pose a variety of fouling risks and are categorized as tropical, subtropical, temperate, cold, and Polar Regions.

In temperate waters, biofouling growth profile may change due to seasonal effects, whereas tropical and sub-tropical region does not show vast differences due to the consistency of seawater temperature during the year (Hellio and Yebra 2009).

Villanueva et al. (2011) indicated that biofilm formation was faster and microbial colonization of the substratum occurred earlier under increased water temperature conditions. An experimental study on several tunicate and bryozoan species, conducted in 18 marinas from 5 countries, highlighted seawater temperature has a substantial impact on growth, recruitment, and trade-offs for each species (Lord 2016). Koopmans and Wijffels (2008) stated that the volumetric growth rate of *Haliclona oculata* (sponge species) increased with increasing temperature values. Stachowicz et al. (2002) and Dean and Hurd (1980) showed a similar positive relationship between growth rate and seawater temperature for ascidians (sea squirt) and *B. Improvisus* (barnacle) and *Mytilus edulis* (mussel) respectively.

2.3.2 Salinity

Salinity is an important parameter that affects the life stages of organisms from the larval stage to the adult stage (Thiyagarajan 2003). Although it is well-known salinity affects marine organisms, it is not possible to generalize the effect of salinity on the organism as each organism has a different range of salinity tolerance.

Salinity tolerances of marine organisms are investigated through salinity treatments. Generally, low salinity conditions are applied on marine organisms, and their survivorship under this condition is assessed. Qui and Qian (1999) conducted an

experiment in which a range of S (salinity) treatments was applied to *Balanus amphitrite* in order to investigate the salinity tolerance of this organism. Results indicated that all adults died at 5‰ S treatment, low survivorship was observed at 10‰ S treatment, and at 10-35‰ S treatment adults had high survivorship and a high percentage of reproducing. Moreover, results in early stages organisms also indicated that embryos and larvae had lower survivorship and growth speed at 10‰, but ≥ 15 ‰ S treatments did not affect early stages of this species.

De Castro et al. (2018) conducted a study with immersed static panels in a marina in Plymouth, UK, for two years. Highly diverse biofouling community (25 different taxa) occurred on test panel during two-year seawater exposure, and these test panels were exposed to 33‰ S, 20‰ S, and 7‰ S treatments respectively. The results of the experiment indicated that 7‰ S treatment killed most of the macro benthos on the panels, whereas panels which are exposed to 20‰ S, 33‰ S treatments did not show considerable changes.

In a nutshell, marine biofouling is affected by salinity depends on the species' salinity tolerance. However, it is essential to note that the effect of salinity was seen in the conditions which salinity rates stayed under 10‰. Although changing salinity can be an effective way to mitigate biofouling accumulation in sea chest or closed areas with applying desalinated liquid, as the world sea salinity values do not reduce to this extent, it has no substantial influence on biofouling on ship hulls.

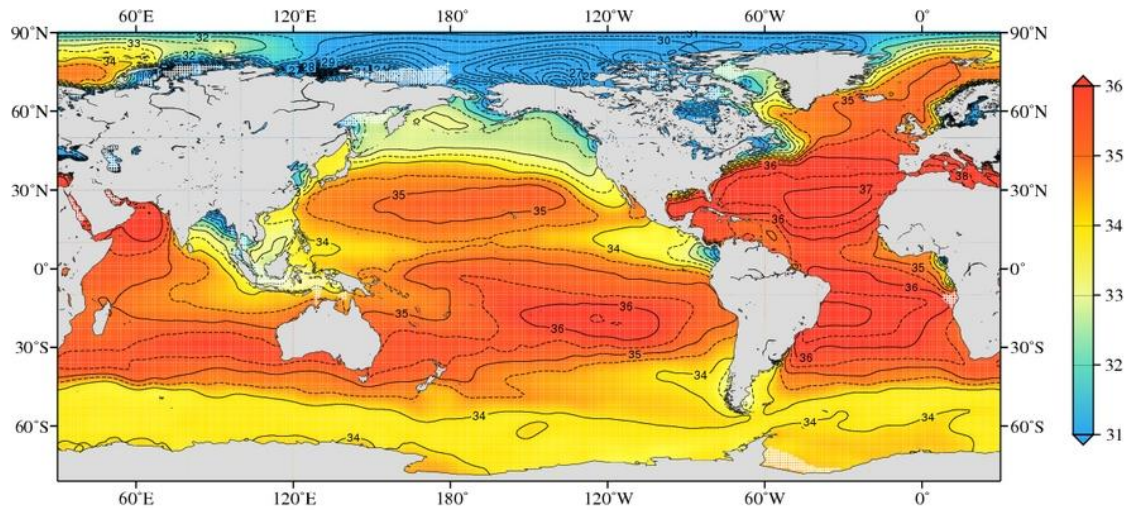


Figure 2-4: Annual mean of the sea surface salinity distribution in PSU (World Ocean Atlas 2005-2012, counter interval =0.5)

Some areas do not comply with the general salinity trend due to specific physical and chemical conditions of the region, as seen in Figure 2-4. The existence of these areas can be negligible as they are constrained; therefore, it is possible to state that world seas salinity values range between 30-36‰.

2.3.3 pH value

With day by day growing influence of climate change, marine life is under a threat of pH reduction due primarily to the increasing adsorption of CO₂ from the atmosphere by oceans. When CO₂ dissolves in seawater, chemical reaction of carbon dioxide and water forms carbonic acid (H₂CO₃). Then some of the carbonic acid molecules dissociate into a bicarbonate ion (HCO₃⁻) and a hydrogen ion (H⁺) thus this increases the acidity of seawater. This acidification has severe effects on a wide range of marine organisms in various ways.

Cullimore (1999) stated that polymeric structures in the biofilm have a buffer role against pH shifts in the water and pH range of 6 to 9 represents the most suitable conditions for biofilm. Kroeker et al. (2013) indicated that calcified algae, corals, molluscs, and larval stages of echinoderms are negatively affected due to ocean acidification. On the other hand, a decrease in pH does not significantly damage crustaceans, fish, fleshy algae, seagrasses, and diatoms. Moreover, some fleshy algae

and diatoms even benefit from acidification. Effects of ocean acidification on early life stages of *Amphibalanus Improvisus* (bay barnacle) was investigated using pH treatments down to 7.6 (equivalent to the estimated scenario for the year 2250). As the results show, pH treatments did not change survival and development rate of larvae (Pansch et al. 2013). Also, McDonald et al. (2009) showed that barnacle species of *Amphibalanus Amphitrite* has the same tolerance against the variations in pH in its early life stages. It is interesting to note that although there is no significant change in the growth rate of this species, the adhesion strength of barnacles was comparatively higher for the barnacles raised at acidic condition (pH 7.4 compared to pH 8.2).

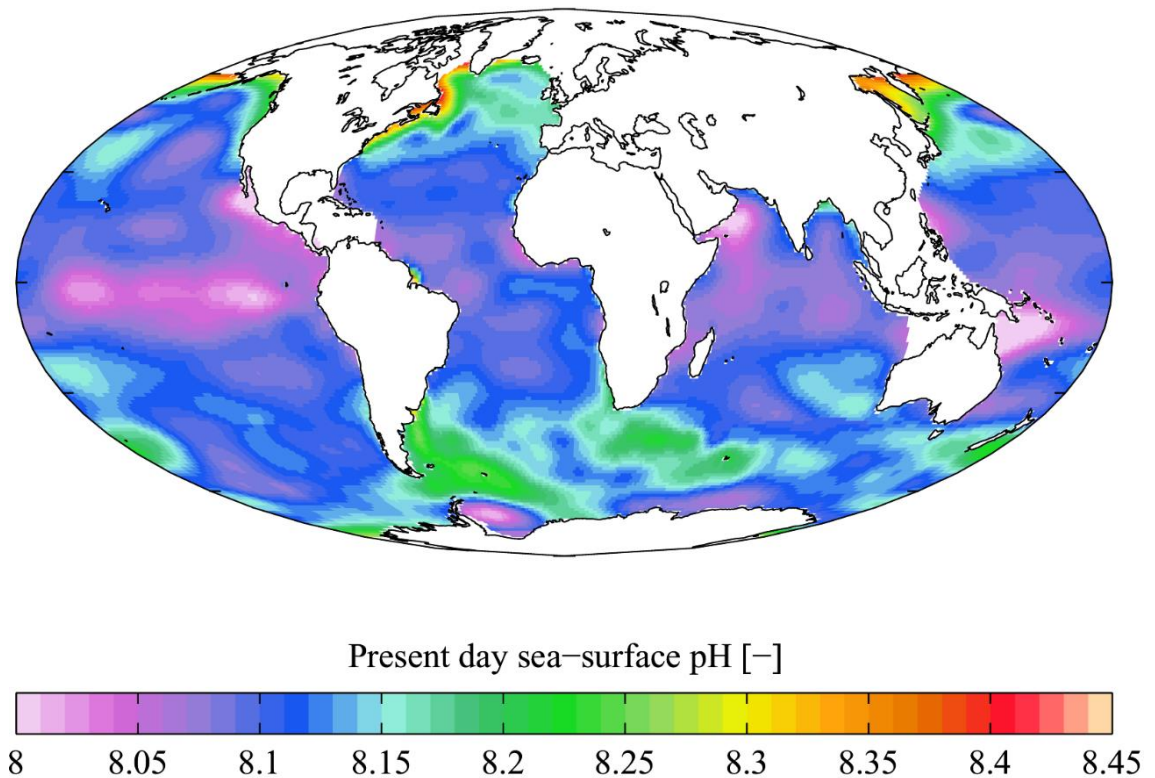


Figure 2-5: Estimated annual sea surface pH for the present day (the 1990s) (World Ocean atlas 2005)

Although pH value plays a significant role on marine life in world seas a wide range of influence area depending on organisms' life stages, Figure 2-5 shows that pH values of world seas do not change in an extensive range that will affect fouling accumulation on ship surfaces as aforementioned above. It is important to note that pH can be used as biofouling control treatment in closed areas since it can mitigate biofouling accumulation to some extent as salinity does.

2.3.4 Water Depth, Nutrient Abundance and Light

Physio-chemical features of sea-water, which has an influence on biofouling, vary a lot depending on water depth. Common sense is in a way that fouling communities tend to decrease in biomass and diversity in deep waters (Cronin et al. 1999) (Guenther et al. 2010).

A study, investigating the effect of water depth on biofouling accumulated on offshore gas platforms in the southern North Sea, showed that diversity of biofouling species increased with depth, but then decreased when seawater depth reached to 15-20m. Also, it was overserved that richness of fouling species was higher on platforms which are located close to shore (van der Stap et al. 2016).

An interesting study called ANTARES project investigated the effect of water depth on micro fouling via glass plates immersed at shallow water and 2400 m depth. More interestingly, results showed that the density of bacteria levels on glass plates was similar to each other. The only difference that reported was bacteria observed in the deep sea was comparatively smaller, and accumulation seemed to have less exopolymeric material (Amran et al. 2002).

Most of the species in the plant group as a part of macro fouling are photosynthetic, and thus their lives strictly depended on having an adequate light level. On the other hand, mussels, barnacles, tubeworms, ascidians, and hydrozoans rely on nutrients in the surrounding environment rather than light abundance. Therefore, these organisms can cause fouling at even great depths (Lehaitre et al. 2008).

Nutrient abundance is critical for marine fouling from biofilm formation to the feeding of macro fouling as all living organisms need food to sustain their lives. At this point nutrient abundance is also connected with seawater flow rate and closeness of location to shore. Even weak seawater flow supports biofilm formation at initial stages, but it causes a slower growth. Due to having high shear stress on the surface, the strong flow may slow down bacterial adhesion however it helps to biofilm to grow fast via a substantial amount of nutrients come with high seawater flow rate (Lehaitre et al. 2008).

Length of ship's idle times at port is also critical since coastal waters generally are more abundant than oceanic waters in terms of nutrient abundance due to domestic and human-based reasons. Therefore, as the ship is closer to shores, biofouling growth accelerates. It is of note that coastal waters also contain a great community of larvae of macro fouling compares to ocean waters.

2.3.5 Water Current and Velocity of Flow

Marine organisms tend to colonize themselves at a perpendicular position to water flow in order to get benefit from oxygen and nutrients as much as possible. On the other hand, water currents may restrict biofouling attachment and growth by exerting pressure and shear forces on the surface.

Bott and Pinheiro (1977) showed that an increase in flow velocity decreases the thickness of biofilm. Melo and Bott (1997) stated that biofilm that formed under a 2 m/s water flow was ten times thinner than the biofilm that formed under a 0.54 m/s water flow by keeping other conditions same.

The biofilm incubated at lower shear force conditions causes a higher frictional resistance (Cowle et al. 2017). Smith (1946) used the glass tubes of different diameters in order to investigate the effect of flow speed on biofouling. Results indicated that barnacles (*Balanus Improvisus*) were successful in attaching up to 0.5 knots, whereas the tubeworms (*Dasychone Conspersa*) could manage to attach up to 1 knot (Smith 1946).

McDougall (1943) expressed that the growth profile of biofouling organisms may change under the varying velocity of flow up to 1 knot. The result of the study revealed that *Bugula* and *Balanus* grew at slow speed, whereas *Tubularia* and the worms, *Hydroides*, and *Sabellaria* were observed intensely at a higher speed. Moreover, sponges (*Reniera*), oysters, and tunicates (*Phallusia*) preferred medium speed among these flows.

A study, conducted via buoys located on Atlantic Coast, pointed out strong tidal currents supported mussel fouling (*Mytilus edulis*) in a positive way when fouling rates

are compared to average tidal conditions (Woods Hole Oceanography Institution 1952)

2.3.6 Surface Factors

Surface properties such as micro-texture, surface charge, wettability, contour, and colour influence the diversity of biofouling species on the target surface (Bixler and Bhushan 2012). Gordon and Mawatari (1992) showed that bryozoan and mussel larvae tend to attach on hydrophobic surfaces whereas as stated in Railkin (2004), hydroids, bryozoans, and ascidians are prone to settle on microtextured surfaces. In addition, larvae, sponges, barnacles, ascidians and, go for light coloured surfaces, and barnacle larvae prefer to settle on convex contours while calcareous sponges prefer concave contours (Railkin 2004).

Surface wettability is a property of a surface that defines whether the surface in question can maintain contact with the liquid in terms of contact angle (θ). Surfaces thus are grouped according to their wettability. The surfaces which contact angle lies in a particular range are called super hydrophilic ($\theta \ll 10^\circ$), hydrophilic ($10^\circ < \theta < 90^\circ$), hydrophobic ($90^\circ < \theta < 150^\circ$) and superhydrophobic ($150^\circ < \theta < 180^\circ$). The interaction between a liquid and a surface can be classified under two regimes as Wenzel model (Wenzel 1936) and Cassie-Baxter model (Cassie and Baxter 1944). As water droplet interacts with the surface of lotus leaf, water droplet cannot spread out evenly on the surface and leaves a gap, which is called air pocket between solid-liquid interfaces (Xiao 2014). Figure 2-6 shows the contact angles for types of surface with illustrating the air pocket effect as well.

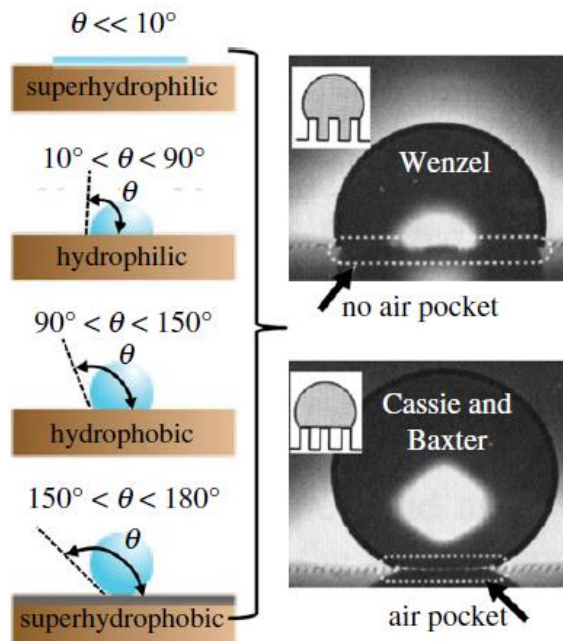


Figure 2-6: Photos of droplet regimes and contact angle range between different wettability surfaces (Bixler and Bhushan 2012).

Although the general perception is that micro fouling organisms face through challenges to locate on hydrophobic (low energy) surfaces, it is not possible to generalize this for all biofouling species. For example, *Enteromorpha* spores settled more easily on hydrophobic surfaces compare to hydrophilic surfaces. However, adhesion strength tests showed that attachment strength on the hydrophobic surface was weaker than the attachment on the hydrophilic surface (Callow et al. 2000)., It is reported that diatom slime attached to fouling release coating (hydrophobic surface) did not release as expected after even reaching 30 knots (Anderson et al. 2003).

A study, investigating attachment strength of cells of the diatom *Navicula* and sporelings of *Ulva* on hydrophobic and hydrophilic surfaces, indicated that *Navicula* performed a stronger attachment to the hydrophobic surface than to hydrophilic surface. However, *Ulva* sporelings were attached firmly to the hydrophilic surface (Krishnan 2006).

Several models, namely attachment point theory, engineered roughness index (ERI) model, surface energetic attachment (SEA) model were proposed to explain the relationship between the settlement of fouling organisms and surface topography.

In a study, four different diatom species with cell sizes ranging from 3 to 14 μm in length and 1 to 7 μm in width were tested on produced micro-textured polyimides surfaces in different surface pattern.

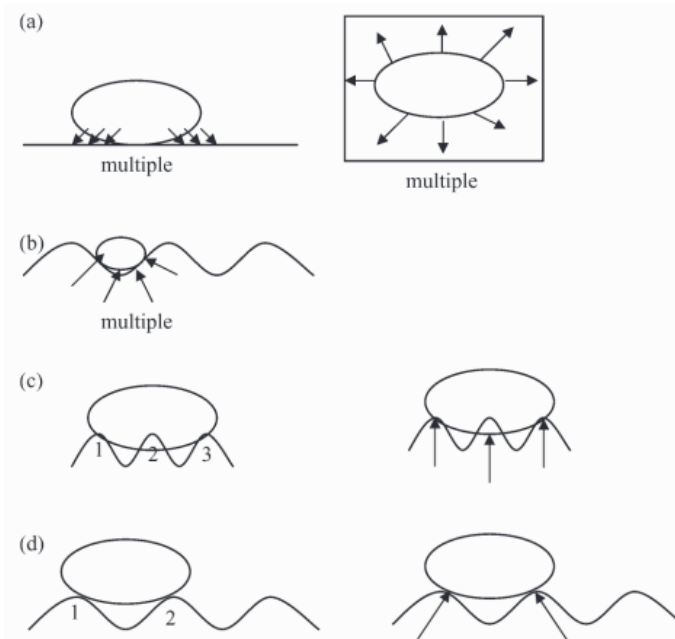


Figure 2-7 An illustration of attachment point theory on cases of (a) diatom on smooth surface-multiple attachments (b) diatom small enough to fit between 2mm ripples-multiple attachments (c) diatom settled on 2 mm ripples - 3 attachment points (d) diatom settled on 4mm ripples-2 attachment points (Scardino et al. 2006)

Scardino et al. (2006) stated that as the number of attachment point increase on the surface, it causes higher and stronger attachments for the diatom species. Moreover, a micro-textured surface either weakens or strengthens the attachment of microorganisms according to both wavelength of ripples and cell size of diatoms. Figure 2-7 gives an illustration of the attachment point theory in different cases.

Schumacher et al. (2007) introduced engineered roughness index (ERI) to characterize the surface topography. Four micro-textured surfaces with hexagonally packed circular pillars, triangle combined circular pillars, ridges channels, and Sharklet AFTM texture were tested based on their performance of preventing spores of the green alga *Ulva*. This study demonstrated that the Sharklet AFTM surface with highest ERI (9.5) has the lowest mean spore density. The surface with triangles/pillars topography was ranked by second-highest ERI (8.7) and showed the second-lowest micro

accumulation on the surface. Other two surfaces with the smaller ERI values (6.1 and 5.0) had higher mean spore densities.

A more recent study (Decker et al. 2013) developed a combined model based on two previous models (attachment point theory and ERI). The surface energetic attachment model (SEA) takes into account the properties of the cell-material interface and the size and configuration of the topography relative to the organism. The SEA model can also generate attachment maps for microorganisms by using Monte Carlo Simulation.

2.4 Antifouling Methods and Technologies

The history of the antifouling term and the need is as old as the history of navigation. The antifouling methodologies and technologies have been changing over the years to compensate the protection needs for ship hulls in each age with the help of floating technological developments.

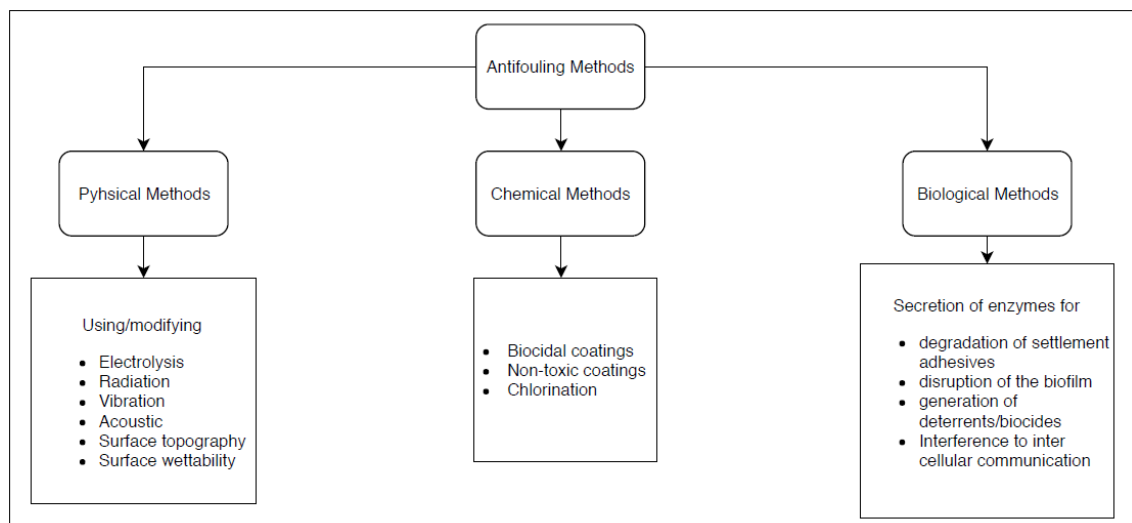


Figure 2-8: Categorization of antifouling methods drawn according to Cao et al., (2011)

Antifouling methods can be divided into three categories concerning their working principles such as chemical, physical, and biological methods, as shown in Figure 2-8. Chemical methods work based on by coating the target surface with a chemical compound containing various kind of biocides or providing a very smooth surface that allows removing attached fouling organisms while ship moving. Physical methods are focused on modification of surface physical properties like utilizing micro-textured surfaces, changing surface potential energy or using electrolysis, radiation, etc. to

mitigate biofouling accumulation. Lastly, biological methods work by secreting a variety of biodegradable enzymes or metabolites in order to stop or slow down biofouling accumulation in micro stage (Cao et al., 2011).

2.4.1 Physical Methods

Due to the problems with both insoluble and soluble matrix technology such as degradation and erosion rates and the environmental risk that these paints posed, there was always an intention to find alternative ways to prevent biofouling. The use of electric current over the ship hull was the most well-known method at the beginning of the 20th century (Bertram 2000). However, the first extensive study on the use of the electric current in antifouling systems, Castle (1951) reported that fouling organisms can easily stand against 15 minutes of 1,000,000 ma per square foot alternating current exposure. The effectiveness of these systems had been measured by means of formation of toxic chemicals on the ship surface (Woods Hole Oceanographic Institute 1952). These systems brought some problems such as inefficiencies because of non-homogenous voltage distribution across the ship hull, causing corrosion, cathodic chalk formation (Swain 1998) and early ageing of the coating (Anderson 1971). Electronically generated ozone bubble curtains, copper ions, H₂O₂, bromine, Pt complexes, and NH₃, are the other methods that have been proposed as antifouling methods (Yebra et al. 2004).

Although the many types of research have been conducted to improve these methods such as proposing ferrocene derivatives (Okochi and Matsunaga 1997) or carbon-chloroprene (Nakasono et al. 1993) sheet to prevent toxic chemical formation, results were not found satisfying enough. Most of the methods related to electric use were tested on a limited amount of marine organisms, so their efficiency on diverse biofouling accumulation has not been established well. Also, it has been found that these methods were not cost-wise when considering applying for large structures such as ships (Yebra et al. 2004).

Acoustic has been tried as an antifouling method utilizing an external vibration source (Taylor et al. 1983; Callow 1990; Marshall et al. 1998) or piezoelectric coatings (Murphy and Latour 1979 ;Rahmoune and Latour 1995). Gerliczy and Betz (1986)

stated that vibrating coatings are successful in sustaining the clean surface; however, these technologies are not a cost-wise solution for biofouling due to their high power requirements (Swain 1998). Moreover, magnetic fields, ultraviolet radiation, and radioactive coatings were tested, and it has been reported that these methods are not practical to use on ship protection (Yebra et al. 2004).

2.4.2 Biological Methods-The Answer in Nature

To protect themselves against fouling organisms, some marine organisms (especially marine invertebrates and micro-macro algae) secrete biogenic agents that inhibit the growth of biofouling organisms (Abarzua et al. 1999). Fungi, sponges, and some bacteria also have the capability of producing antifouling components as reported in Xiong et al. (2009) Limna et al. (2009), Fernando and Carlos (2008) and Burgess et al. (2003). The biogenic agents isolated from marine invertebrates and microalgae can be found in detail in Abarzua and Jakubowski (1995).

Recently, it has been reported that some enzymes have antifouling features, for instance, Oxidoreductases, Peroxidases, Transferases, Hydrolases, Hydrolysing O or S-glycosyl compounds, Endopeptidase, protease, Lyases, and Ligases. The enzymes in the same category can be found in detail in Kristen et al. (2008). Some of these enzymes are effective at protecting the surface against biofouling of any kind whereas some of them are successful at protecting against the only microfouling. By considering the biofouling process from initial settlement of micro fouling to macrofouling, the enzymes can be divided into four groups according to their way of effect on the process (Abarzua and Jakubowski 1995; Kristen et al. 2008; Cao et al. 2011).

1. Enzymes degrading adhesives substances used for settlement

It is known that proteins and proteoglycans play an essential role as adhesive compounds in settlement of macrofouling organisms. The enzymes which are called proteases hydrolyze peptide bonds and therefore degrade peptide-based adhesive materials. So this prevents the attachment of biofouling organisms. (Rawlings et al. 2006). It was reported that adhesion strength and settlement of *Ulva zoospores* was significantly reduced by serine-protease in Pettitt et al.,

(2004). In addition, proteases showed similar effects on the settlement of *Balanus Amphitrite* cyprid larvae and larval settlement of the bryozoan *Bulgularia neritina* (Pettitt et al., 2004; Dobretsov et al., 2007).

However, the process is more complicated for microfouling since polysaccharide-based adhesives as necessary as proteinaceous glue. Although polysaccharide degradation is executed by glycosylase, degradation of polysaccharides is quite tricky as a specific glycosylase is only valid on a limited range of bonds.

2. Enzymes disrupting the biofilm matrix

These enzymes aim to disintegrate the EPS structure in the biofilm matrix in order to inhibit microbial growth. However, this disintegration requires comprehensive combinations of hydrolases and lyases due to the complexity and variability of biofilm polymers in biofilm matrix (Manyak et al., 2005) (Kristensen et al., 2008). The known lyase enzyme for fouling protection is alginase, which is used for breaking the polysaccharide alginates (Moss, 2006).

Glycosylases are also known as one of the enzymes disturbing the biofilm matrix by targeting linkages in polysaccharides, but selecting the appropriate glycosylases is not as easy as the linkage types in mixed biofilm show considerable variability. In addition, the inhibition performance of glycosylases may exhibit differences according to the stage of biofouling. For instance, it was reported that glycosylases successfully reduced the adhesion of *Pseudoalteromonas* bacteria, whereas it could not detach the cells that had already attached on the surface (Leroy et al., 2008).

Proteins form a significant part of the biofilm matrix as polysaccharides. Leroy et al. (2008) reported that proteases are efficient in breaking the protein structures in biofilm. However, it is not feasible because of the structural stability of proteins in the biofilm matrix. Moreover, a protease type which

shows efficient performance in breaking a specific protein structure may not be sufficient for another.

It is important to note that a mixed biofilm structure is quite resilient against external influences. Degradation of a critical component of the biofilm does not destroy the biofilm as the alternative components exist in the biofilm, and they form new networks. Xavier et al. (2005) compared the rate of production of new EPS, and the rate of degradation and results showed that biofilm cells EPS production was faster than the degradation of EPS.

3. Enzymes generating deterrents/biocides

In recent years, there is an attention on extracting of metabolites from marine flora and fauna that show excellent performance at avoiding biofouling. Research on finding the antifouling compounds in these metabolites escalated during these days (Krug, 2006). These metabolites can be divided into two categories, such as polar and nonpolar metabolites.

Some of the enzymes mimic these metabolites by generating deterrents including glucose oxidase, hexose oxidase and haloperoxidase which all are sort of oxidases (Huijs and Klijnsstra.,2006;Johansen et al.,1997;Poulsen and Kragh, 2002;Wever and Dekker, 1995). The oxidates lead to hydrogen peroxide formation while haloperoxidase catalyzes the formation of hypohalogenic acids which are highly effective and are thus commonly used in water treatments.

Hydrogen peroxide's antifouling potential as an efficient non-ecotoxic biocide was tested in the study of Jacobi (2002). The results showed that hydrogen peroxide has a useful feature of antifouling as well as providing a cleaner way to do it compared to current antifouling biocide technologies. By considering the environmental effects, hypohalogenic acid usage is comparable to that of hydrogen peroxide (Wojtowicz, 2002; Wever and Dekker 1995).

4. Enzymes interfering with intercellular communication

Quorum sensing is the ability to detect and respond to fluctuations in cell-population density by regulating gene expression. Quorum sensing is used by Gram-positive and Gram-negative bacteria to sense communication circuits and regulate physiological activities (Miller and Bassler, 2001). It is reported that the existence of N-acyl homoserine lactones (AHL) is necessary for Gram-negative bacteria to use quorum sensing. Therefore, degradation of AHL through enzyme of AHL acylase inhibits microbial fouling (Reading and Sperandio, 2005; Waters and Bassler, 2005). Moreover, it was highlighted that AHLs might affect algal zoospore settlement by causing an increase in their settlement effort (Callow and Callow, 2006). Although it is possible to consider that AHL reduces extensive biofouling growth as it prevents microbial fouling, macrofouling can grow without biofilm formation (Kristensen et al., 2008).

Although many numbers of enzymes such as transferases, isomerases, and ligases are proposed to be used as antifouling, their effects and performances were not elucidated in detail.

Enzymes show advantageous characteristics of antifouling as stated above; however, there are also challenges for enzyme-based antifouling systems. The enzyme activities strongly influenced by temperature differences, for instance, they increase catalytic activity with increasing temperature, but they are also less stable in warm environments. It is a significant problem to find the right balance between activity and stability in a varying environment; therefore, producing enzyme-based antifouling coating is not feasible for now.

2.4.3 Chemical Methods – Antifouling Coatings

The initial antifouling paints were developed in the mid-19th century. The idea behind the working principle of the paints is releasing toxicant substrates which dissolve into water. While linseed oil, shellac varnish, tar and different kinds of resin were using as a binder, copper oxide, arsenic and mercury oxide were used as common antifoulants.

An antifouling paint containing toxic materials over a varnish layer was developed and patented by Mallet in 1841, but it was not a successful application because of abrasion and high solution rate (Woods Hole Oceanographic Institute, 1952). In 1847, William John Hay developed an efficient coating by using a non-conductive varnish to isolate iron hull from the copper powder in the coating based on the studies of Sir Humphrey Davy (Lunn 1974).

In 1860, James McInness patented a metallic soap composition which contains toxic copper sulphate as a biocide. It was applied hot over a quick-drying priming paint of rosin varnish and iron-oxide pigment. Then it was followed by similar paint known as Italian Moravian, which was claimed as the best at that time together with hot plastic paint (Woods Hole Oceanographic Institute, 1952). James Tarr and Augustus Wonson patented an antifouling paint using copper oxide in tar with naphtha or benzene in 1863 (Woods Hole Oceanographic Institute , 1952).

“Italian Moravian” and McInness’s ‘hot plastic paints’ shellac type paints were extensively popular paints at the end of the 19th century. In these paint applications, anticorrosive shellac, varnish or nontoxic coatings were missioned as a primer coating. However, these paints were not cost-effective, and their life span was not satisfactory (Woods Hole Oceanographic Institute, 1952).

In 1906, the US Navy performed a significant effort in finding the most appropriate coating for the US fleet. Hot plastic and other antifouling paints were tested at Norfolk Yard. Results of experiments showed that the spirit varnish paint was prosperous compared to other paints (Woods Hole Oceanographic Institute, 1952).

The red mercuric oxide as a toxic compound of antifouling paint was replaced with gum shellac, grain alcohol, turpentine, and pine tar oil. The life span of the paint was extended around nine months by incorporating zinc oxide, zinc dust, and Indian red into the paint formulation.

India was the source of high-grade shellac, but the supply was limited, and it started to be getting expensive. Because of the reasons indicated, the U.S. Navy started to conduct a set of experiments to find alternative substance instead of A-grade shellac and to enhance the efficacy of antifouling coating. Lower quality shellacs material had

adhesion problems; therefore, various potential substances were tried in experiments. Finally, rosin was evaluated as a substitute substance for high-grade gum shellacs. Coal-tar rosin paints were developed, and hot plastic ship bottom paint was improved by including toxics like cuprous oxide and mercuric oxide to make stronger the killing side of paint (Woods Hole Oceanographic Institute , 1952).

Although hot plastic antifouling paints were claimed as successful at that time, the difficulties of their application lead people to search for new practical paints that might be applicable with just a brush. Consequences of these problems lead to the development of various effective paints which dry by oneself via evaporation of the solvent. They are called cold plastic paint. These paints were capable of successfully protect ship hulls for up to 18 months between dry-dock periods (Graham, 1947)(Hole, 1952).

With the challenging effects of the Second World War on the industry and science after the Second World War new synthetic petroleum-based resins and organotins were introduced in the paint industry. Although new chemical substances improved paint's mechanical characteristics, frequency of dry dock need remain stable because of the release rate of biocides was uncontrolled, and their effects were decreasing by time. Between 12 and 24 months, paints were being useless when all biocides had leached to water (Milne, 1990). Organomercurials and Organoarsenicals were demonetized because of health and safety concerns (Milne, 1992).

2.4.3.1 Insoluble Matrix Paints

The paints which have polymer matrix that does not polish, erode or dissolve in the seawater are called insoluble matrix paints. Insoluble vinyl, epoxy, acrylic, or chlorinated rubber polymers can be given as examples of the commercial insoluble polymer matrix (Rascio, 2000). The embedded soluble toxic materials in an insoluble polymer matrix dissolve when contacts with the seawater by leaving a multi-porous structure in the matrix. Due to this porous structure, seawater goes into a polymer matrix and solves poisonous material in the deeper layers (Marson, 1969) (Cao et al., 2011). Although these kinds of paints are mechanically strong and durable against environmental conditions, the life span of these paints is around 12-18 months. The

reason is that as the toxic materials dissolve in time the porous structure gets deeper and water cannot reach to deeper layers so that leaching rate of this toxic material reduces the minimum required benchmark rate for antifouling as given in Figure 9 (Marson, 1969).

2.4.3.2 Soluble Matrix Paints

In order to increase the antifouling efficiency of paint matrix and lengthen the lifespan of the coatings, a binder which can be dissolved in the water was incorporated into the paint. Rosin which dissolves in the seawater is used in both toxic materials and matrix of these paints. For this reason, toxic materials in deeper layers can be exposed to water so that it increases antifouling efficiency and life span of the paints (Yebra et al., 2004). Besides, plasticizers and co-binders were included in the paint to be able to possess efficient film-forming and mechanical properties as well as suitable dissolution rate (Rascio 1988). The sailing speed of the ship plays an essential role in the release rate, so during the idle time, the release rate of toxic materials are minimal (Anderson 1995) (del Amo 1984). Another disadvantage of this condition is the exponentially increasing erosion rate of the paint, which increases with the vessel speed (Anderson 1995). The working principle of soluble matrix paints is also shown in Figure 2-9.

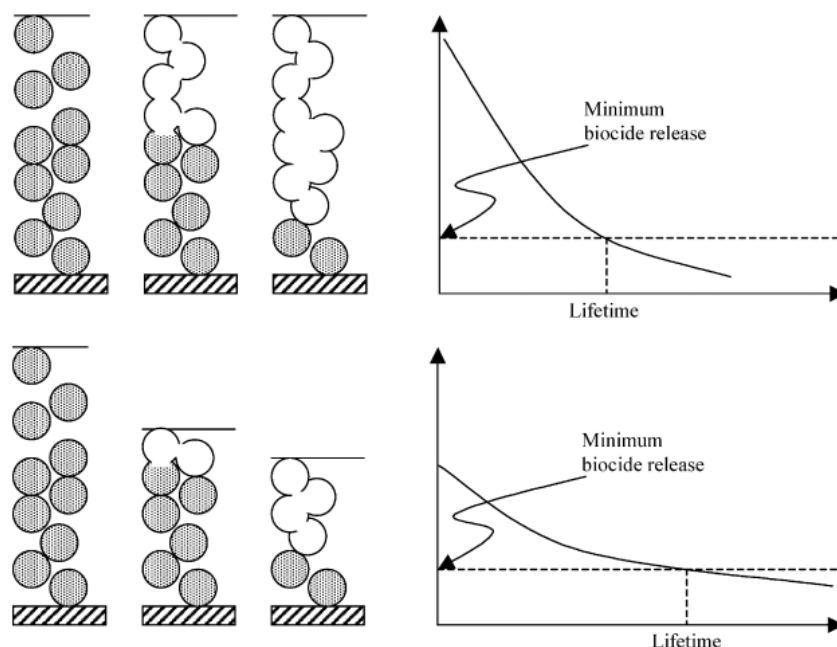


Figure 2-9: Working principle of insoluble (above) and soluble (under) matrix paints and comparison of biocide release rate in time with minimum biocide release rate (adapted from Yebra et al., 2004).

2.4.3.3 Tributyltin Self-Polishing Copolymer Paints (TBT-SPC)

TBT acrylate esters were first proposed to be used in antifouling coatings by Montermoso and co-workers in 1958 (Gitlitz 1981). After a short time, TBT acrylate and methyl methacrylate copolymers usage were patented by James (Ghiya 1987). In 1974, Milne and Hails developed the first TBT – SPC copolymer technology, which uses ZnO as a pigment in the coating to decrease the polishing rate (Milne 1977) (Milne 1991). With introducing the hydrophobic monomers, the polishing rate was controlled, and the most successful antifouling paint was developed in 1985. TBT-SPC paints consist of acrylic polymer and TBT groups linked on a polymer structure by ester links (Anderson 1995). The TBT copolymer methacrylate and methyl methacrylate behaves hydrophobic that does not allow seawater to solve paint film (Anderson 1995). Therefore, seawater penetrates the holes occurred due to dissolved soluble pigments. Also, the pH value of 7.5-8.5 (seawater condition) is suitable to hydrolyze the carboxyl–TBT linkage; therefore, TBT moiety is released slowly and in control from the copolymer (Iwao 2003). Once enough portion of TBT is released partially reacted brittle polymer backbone erodes due to effect of seawater flow, and this leads a new coating surface to appear which is called self-polishing effect (Kiil et al., 2001). It is possible to alter the polymer chemistry to modify the polishing rate, which is an advantageous feature for antifouling coatings. Because of this feature, the coatings can be designed according to the ship operating profile, such as the ratio of idle time to total operation duration and ship speed (Yebra et al., 2004). It was reported that the performance of the TBT-SPC coating during idle times is efficient as much as during the sailing times since the release rate of TBT almost does not show the difference with the sailing speed (Cao et al., 2011). Moreover, TBT-SPC paints satisfy many requirements expected from a successful coating such as having high mechanical strength, high stability to oxidation, short drying time as well as being easily maintainable and cost-friendly (Iwao 2003). Because of the advantageous features of TBT-SPC paints, it was commonly used in worldwide until it was banned.

2.4.3.4 Tin-Free Self-Polishing Technology

Although TBT-SPC paints were advantageous in many perspectives, severe effects of TBT on non-target organisms were reported at different places and dates around the

world. In the 1970s, marine scientist found that high mortalities of oysters' larvae and malformations of the shells of adults were caused because of high TBT contamination in Arcachon Bay in France. In the 1980s, studies showed that TBT caused a decrease in population of the dog whelk and TBT poisoning cause a change in their sex, which known as imposex condition for this species (IMO 2003). Due to the effects of TBT paints, the usage of TBT based paint was banned by the International Maritime Organization (IMO) in 2008.

Therefore, the research on antifouling coatings focused on the development of TBT – free systems which were aimed to produce a TBT- free antifouling coating as efficient as TBT-SPC coatings by using different toxic material rather than tin. As a result of this investment on antifouling coating research, several TBT-free coating products were produced and released to the market. These can be divided into two groups as below (Anderson 2000).

- Controlled depletion systems (CDPs)
Traditional soluble matrix technology was upgraded through reinforcing resins and designed to have the same reaction mechanisms with the conventional rosin-based antifouling paints.
- Tin-Free Self-Polishing Copolymers (tin-free SPCs)
It is designed to perform the same reaction mechanisms with TBT-SPC paints but using different toxic material than tin.

Today, it is possible to find a lot of these types of coatings that are produced by several companies around the world (Yebra et al., 2004). However, it was revealed that tin-free SPC paints were found more successful in many aspects of performance. Tin-free SPC paints works based on a mechanism similar to organic tin SPCs, but their matrix includes acrylic copolymer and metals such as copper, zinc, and silicon excluding tin. The chemical working mechanism and active toxic materials of these products from different companies can be found in detail in Yebra et al., (2004). As mentioned above, although several metal types are used in tin-free coatings, copper compounds are the most common materials used in these paints. However, copper can only affect a limited range of fouling organisms, unlike the broad range of TBT. The efficiency of copper against biofouling organism types can be listed in order like microorganisms >

invertebrates > fish > bivalves > macroalgae (Voulvoulis et al., 1999). In order to improve these coatings' protection efficiencies against macroalgae, barnacles, and bryozoans, booster biocides such as Irgarol 1051 and Diuron (Iwao 2003; Anita et al., 2009) copper pyrithione and isothiazolinone are included into the coating (Shtykova et al., 2009 ;Yebra et al., 2004).

2.4.3.5 Non-Stick Fouling Release Coatings

As severe effects of biocide based coatings are surfaced, research on antifouling technology has been urged to find an environmentally friendly way to prevent biofouling. Although foul-release coatings are not expected to be replaced by biocide based paints in the short term, a significant amount of investment is made on this technology to find an alternative way for biocide based coatings in the long term. A non-stick fouling release coating aims to provide low friction, ultra-smooth surface (CEPE 1999) (Champ 2003) which not only makes settlement difficult but also weakens adhesion strength of biofouling organisms. Thus, this feature of FR coatings provides an advantage in terms of releasing macro fouling organisms once the hydrodynamic conditions are satisfied (Yebra et al. 2004; Holland et al., 2004). It is found that the fluoropolymers and silicones are suitable compounds for the FR coatings (Yebra et al., 2004). Also, modified acrylic resin and nano-SiO₂ are used in the development of various foul-release antifouling coatings. However, it was realized that fouling release coatings are not able to release fouling organisms in a rate as expected (Holland et al., 2004).

Figure 2-10 shows the comparison of working principles, advantageous, disadvantageous, assumed paint lifetime as well as corresponding paint cost coefficients and overall paint application costs of leading antifouling technologies. As shown in the figure, antifouling technologies have different pros and cons varying according to the needs of the ship. Therefore, there is no single selection for all ships, the selection of the best antifouling coating should be tailored according to the needs of ship features such as ship speeds, ship operation profile, ship route, and foreseen maintenance schedule.

antifouling technology	mode of action	advantages	disadvantages	assumed paint lifetime (year)	relative paint cost (*)	estimated overall application cost (*)
contact leaching coatings	<ul style="list-style-type: none"> - high biocides content incorporated in high molecular weight insoluble matrices, low amount of rosin - rely on dissolution of water-soluble biocides 	<ul style="list-style-type: none"> - good mechanical strength 	<ul style="list-style-type: none"> - biocides release decreased with immersion time as did AF performance - biocides released into the environment - subjected to biocidal legislation 	1–2		
soluble matrix and controlled depletion polymer coatings	<ul style="list-style-type: none"> - biocides mixed with a soluble matrix based on high amounts of rosin. - rely on physical dissolution of the paint film to release biocides 	<ul style="list-style-type: none"> - relatively low cost/m² compared with SPC coatings 	<ul style="list-style-type: none"> - biocides release difficult to control, not constant. - low activity during idle periods 	≤3	1.5	50 \$/m ²
			<ul style="list-style-type: none"> - problems recoating at next dry-docking due to skeletal film left at surface - biocides released into the environment - subjected to biocidal legislation 			15.2 \$/m ² /year
tin-free SPC coatings	<ul style="list-style-type: none"> - hydrolyzable (meth)acrylate polymers combined with cobiocides - rely on chemical hydrolysis of matrix 	<ul style="list-style-type: none"> - constant biocide release rates over time (at fixed speed) - AF activity during idle periods 	<ul style="list-style-type: none"> - not as efficient as TBT-SPC coatings - biocides released into the environment - subjected to biocidal legislation 	5	2–3	75 \$/m ²
			<ul style="list-style-type: none"> - polishing leads to surface smoothing, reducing fuel consumption - long lifetime (5 years) 			15 \$/m ² /year
fouling release coatings	<ul style="list-style-type: none"> - low surface energy and minimally adhesive smooth surfaces 	<ul style="list-style-type: none"> - reduced adhesion strength of fouling organisms - no released biocides, so not affected by biocidal legislation - smooth surface leads to drag reduction and fuel saving - only 1 top-coat required compared to 2–3 coats for biocide-based AF coatings - low VOC - long life efficiency (5–10 years) 	<ul style="list-style-type: none"> - higher initial cost of paint and application - self-cleaning not efficient at speed lower than 8 knots - susceptible to mechanical damage - diatoms slimes difficult to remove even at high speed (30 knots) 	5–10	4–6	116 \$/m ²
						11.6 \$/m ² /year

Figure 2-10: Performance and Cost Comparison of Antifouling Technologies (from Lejars et al. 2012)

2.5 Antifouling Coatings Performance Tests

The design and development of antifouling coatings need a series experimental process. Every change in the chemical formulation of the antifouling coatings needs to be tested in experiments such as systematic raft (static) and dynamic tests carried out in the laboratory or sea sites. Periods of these experiments vary for the experiment type, but most of them last more than one year. The coatings which successfully pass these tests are used in 36-60 months real-life testing on the ship hulls to be sure that paint is useful in long terms before to be released to the market. All these time-consuming testing aims to investigate whether the designed antifouling coating shows sufficient efficiency in extended periods. Figure 2-11 illustrates the experimental procedure that antifouling coatings pass before going to market.

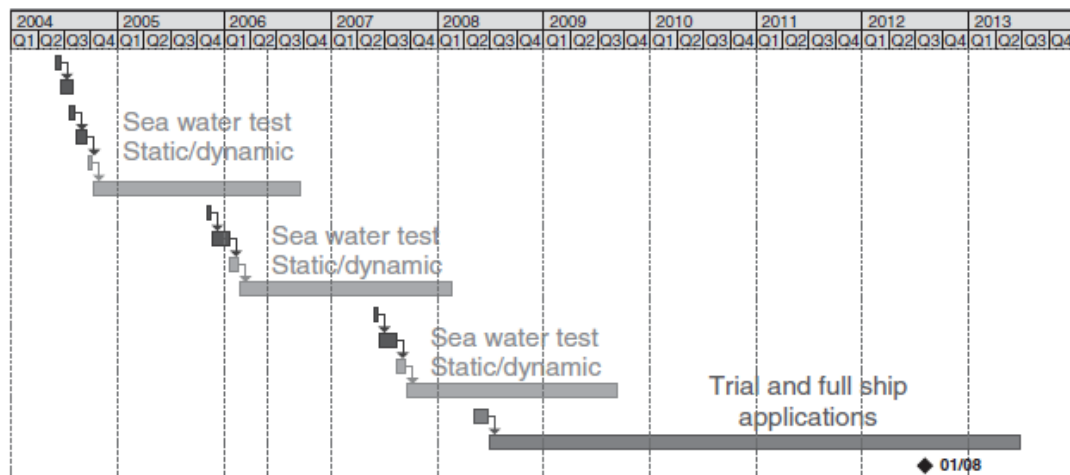


Figure 2-11 Timeline for the experimental procedure for new antifouling technology

2.5.1 Field Tests

Testing AF coating performances in the seawater conditions is significant as a part of their design and development process. Due to the working principles of AF coatings, their features change in time, for instance, chemical content, surface properties, and brittleness. Since it is not possible to estimate the effects of all these changes on the efficacy of the AF coatings, long term ageing tests are used to understand the coating's performance under the real conditions. There are two types of testing in AF coatings,

which are sea testing and ship trials. Although ship trials are the most reliable way to investigate the performance of the AF coatings through regular monitoring at ports, the application of AF coatings to the whole hull is not economically feasible. Therefore, ship trial tests are used for the AF coatings which are about to be sent to the market whereas laboratory tests and sea station tests are the main ways to test AF coating efficiency in the design and development stage.

2.5.1.1 Sea Station Tests

The AF coatings are applied to test materials and exposed to the seawater. The performance of AF coatings is continuously monitored in one or ideally more sea stations during 1 to 5 years period. The main aim of the new paint formulation testing is reducing test duration while increasing the number of different paint samples in the one test location. On the other hand, the paints which are closed to commercialization are tested with many replicates in different test locations as long as possible to investigate the limits of their performances. As the external conditions are not able to be controlled in these tests, each test may show varieties according to the term in which the experiment started. For example, comparatively slow biofouling growth can be observed in the experiments started in autumn compared to experiments settled up in spring.

For this reason, the experiments having different start-up times need to be analyzed by considering these effects. However, the author believes that an ideal experimental result dataset for an AF coating should be combined of replicates started in different seasons and last long five years to average these kinds of uncontrollable environmental effects. Although the seasonal effects on the performance of coatings are considered, these effects are comparatively small when differences are taken into account between the test setups at different test sites as illustrated in Figure 2-12 (Equatorial region and Mediaterrian region).

Biofouling growth depends on many factors, as explained in Section 2.3. It is well-known that temperature is a significant parameter that affects biofouling growth. Therefore, initial testings during the paint formulation developments are used to be conducted in warm waters where allows investigating small changes in the paint

performance. On the other hand, test stations in warm waters aim to provide extreme conditions for the coatings, which in their final development phases. It is important to note that station tests are supported with two types of field tests which are static and dynamic.

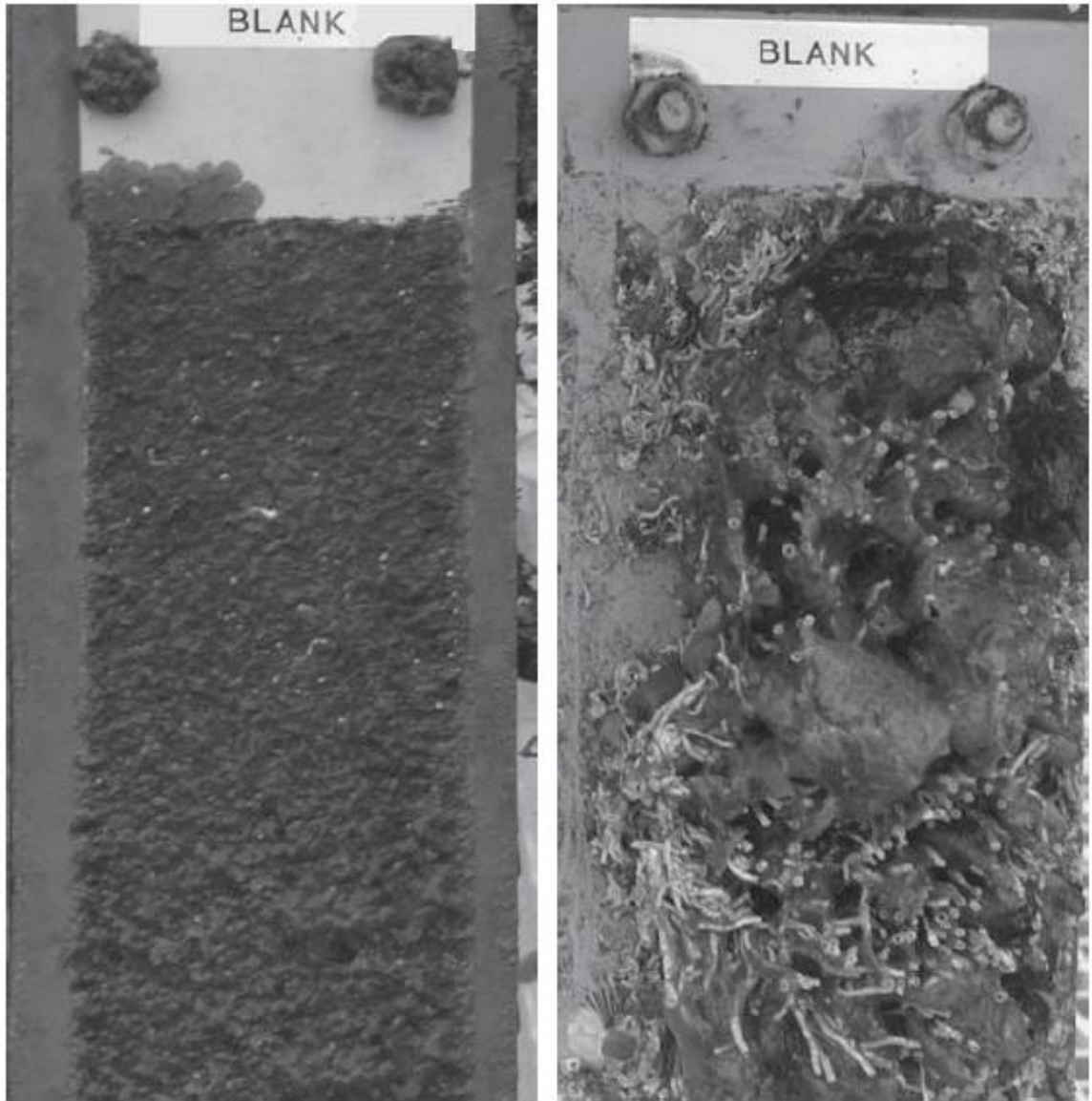


Figure 2-12: Comparison of 16 weeks AF coating field test results in temperate waters (the Mediterranean Sea, left) and warm waters (Tropical area in the Indic Ocean, right) adapted from Sanchez and Yebra (2009).

2.5.1.2 Static Tests

The static tests are conducted using coated surfaces which are immersed in seawater. Coating performances on these panels are continuously monitored in regular periods. Duration of these tests for biocide based paints is usually more than one year, but it usually lasts longer for antifouling release coatings as the aim is to test their self-cleaning performances. The materials of the panels may show varieties between metals and plastics according to the purpose of the experiment. Due to they are low-cost materials, plastics are commonly used in static tests if there is no intention to measure corrosion.

Coatings process for the panels starts with pre-coating to be sure that the coating will stay on the substrate. AF coatings are applied based on the procedure given by the manufacturer. According to the ASTM standards, the test substrate should be A569 type low-carbon steel with a minimum area of 465 cm². In addition, information about dimensions of the holes for plate handling can be found in the ASTM D3623-78a (2012). However, Sanchez and Yebra (2009) reported that a 100 cm² area is enough for typical AF coating comparison tests. For static tests setups, paint companies select different places in terms of hydro geographical features in order to investigate coating efficiencies under the different fouling pressures.

For this reason, at least three test locations from cold, sub-tropical and tropical waters are selected to test AF coating performance. Monitoring intervals depends on the coating features and region of the test set up. For instance, AF coating developed for cold waters are monitored in short terms at temperate or warm waters.

On the other hand, AF coatings developed for warm waters are inspected in long terms at temperate or cold waters. The inspections are made through visual assessment for fouling growth and mechanical conditions of the surface. Also, the adhesion strengths of fouling organisms are measured for fouling release coatings to investigate the required amount of shear stress to release attached organisms. Figure 2-13 shows an example of static test panels for a different type of coatings at two locations.

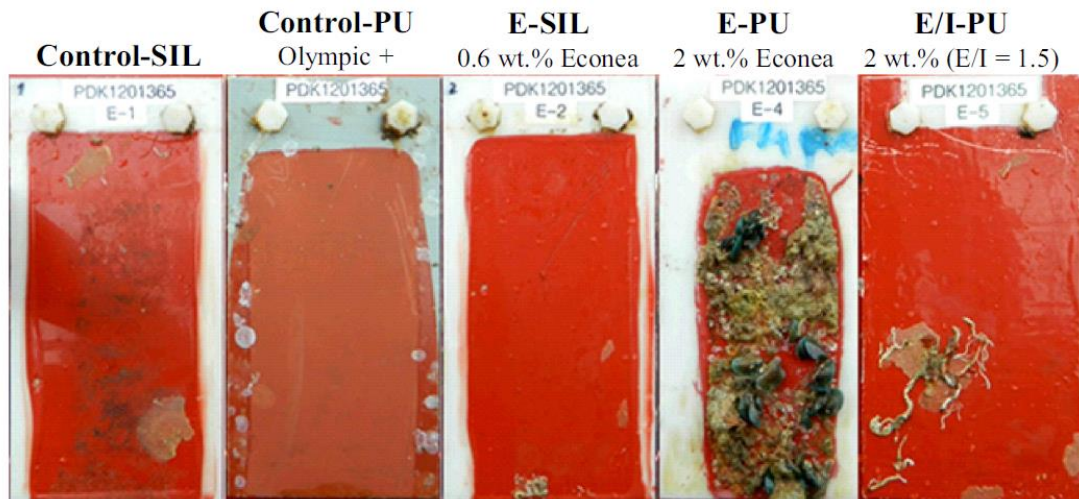


Figure 2-13 Polycarbonate coated panels with foul-release silicone (SIL), polyurethane (PU) and an acrylic commercial (Olympic+) based marine paints exposed on a raft in Singapore (1°23'33 N, 103°58'34E) for 24 weeks, started in June 2014 taken from Silva et al.,(2019)

2.5.1.3 Dynamic Tests

Dynamic tests are typically conducted to test the performance of coatings when the ship is cruising. Dynamic tests aim to investigate the biocide release rate affected by the water flow in biocide based coatings and to determine the required speed for releasing the biofouling organisms for foul-release coatings. Dynamic tests are commonly conducted by means of a rotating drum which has coated panels on the outer side. New AF coatings are tested for one year whereas test times may exceed this duration for the coatings which are close to being released market. According to the foreseen polishing rate, required test duration, and flow speed, the dry film thickness is determined. The inspection period is selected by considering paint features and fouling pressure of the region for two type AF coatings. It is of note that in general the inspections are made in short periods. In theory, dynamics tests are useful for the ships having high operation activity whereas static and dynamic test cycles are useful for the ships having medium activity ships. Figure 2-15 illustrates a picture of a dynamic rotor setup.



Figure 2-14 Front views of the dynamic rotor setup adapted from (Lindholdt 2015)

2.5.1.4 Ship Test

The ship test method is accepted as the most realistic way to predict the efficiency of AF coatings. However, the duration of the test, costs of a large amount of AF coating, uncontrolled environmental conditions limit these tests only for the coatings which are about to be commercialised. Ship tests are performed whether on small hull areas or on the whole hull (full-ship application). Although the full ship application is a better way of testing as it enables to test coating performance on different sections of the hull, due to financial reasons full ship applications are very limited. Ship tests on the small hull areas can be accounted for a step between laboratory/field tests and full ship applications (Atlar et al. 2018). The advantageous of the small area application is that

it enables to test several promising coatings and to compare to the commercial paint which the remaining hull is coated (Sanchez and Yebra 2009).

2.5.2 Laboratory setups

Laboratory setups are essential equipment for the initial stage of antifouling coating production. These setups are commonly used to check if the polishing and biocide releasing rates are sufficient in order to accelerate paint testing. Developed paint formulations can be tested under artificial and well-controlled conditions (high temperature) to test coating performance. Field tests are still the most useful way of evaluating coating performance under real-life conditions, but laboratory setups are beneficial for raw material and new paint formulation testing. Laboratory setups can be listed as follows (Sanchez and Yebra 2009);

- Couette-type laboratory setup: The setup consists of tanks equipped with two concentric cylinders, the inner cylinder rotates with the paint samples attached to the outer surface of the rotating cylinder. This setup enables us to have constant shear stress which is named Couette flow. The advantage of this set up is that it can be operated at various and tightly controlled seawater conditions such as seawater temperature, pH and seawater compositions. Figure 2-15 shows a schematic drawing and a picture of Couette- type rotary set up.

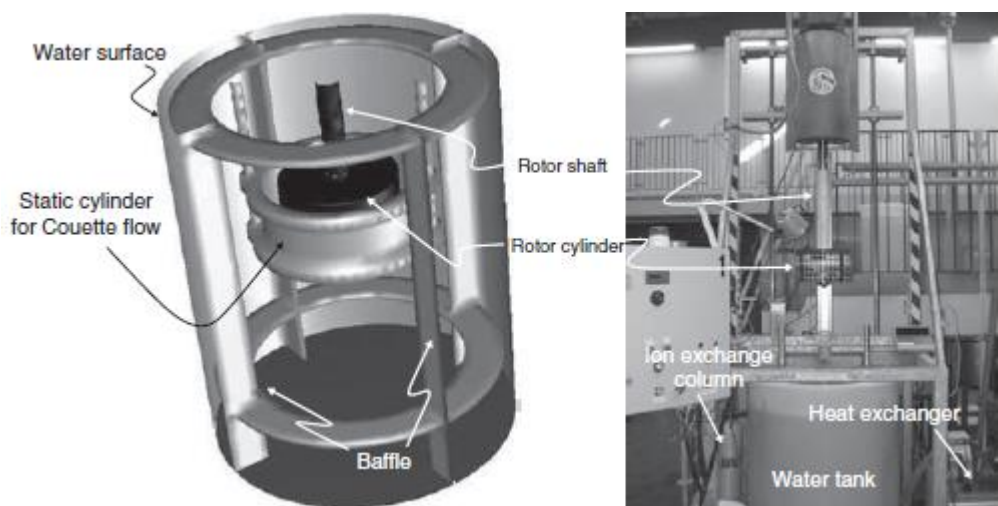


Figure 2-15 Schematic drawing and the picture of Couette-type rotary set-up adapted from Sanchez and Yebra (2009)

- Turbo Eroder type: The rotary setup consists of a tank filled with sixty litres of ASTM artificial seawater. A cylindrical drum is fixed to a motor by means of a central shaft and then arranged within a turbine to have an equal shear stress distribution along the peripheral surface of a rotating cylinder (Sanchez and Yebra, 2009). The decrease in the thickness of the coating can be plotted as a function of rotation time. During the inspections, water properties such as conductivity, salinity and pH are collected, and related adjustments can be made if it is necessary. Figure 2-16 shows a picture of Turbo Eroder setup.

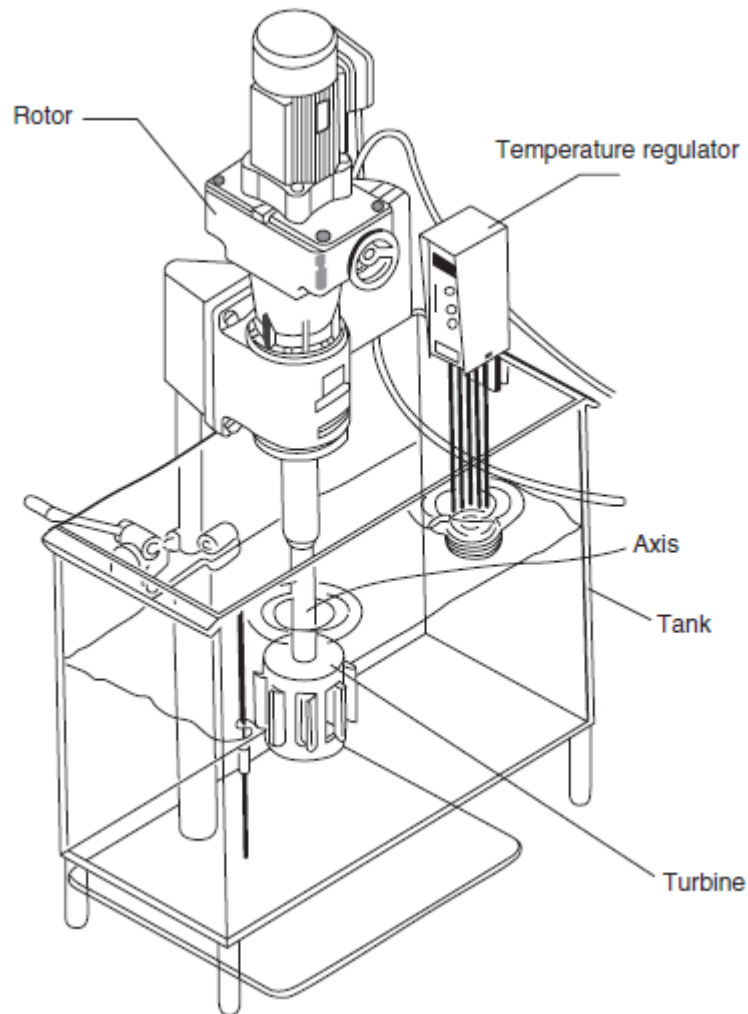


Figure 2-16 Picture of the Turbo Eroder apparatus Sanchez and Yebra (2009)

Table 2-1 Advantages and drawbacks of the Turbo Eroder in comparison with traditional, in situ dynamic drum apparatus

Advantages	Drawbacks
Both artificial and natural seawater can be used	Only four different paints can be tested simultaneously in each setup
Tight control of the seawater composition (pH, salinity, conductivity)	The geometry of the turbine blades is important to prevent deviations in thickness loss results
Temperature range from 25 °C up to 40 °C	The minimal temperature of 40 °C without additional temperature controller
No development of fouling on the coating surface which could diminish the reliability of the thickness loss measurements	Test temperature away from natural seawater conditions
Short-term polishing results	Equivalence to polishing in natural seawater not established yet

As a summary, this setup provides reproducible data for dry film thickness loss and releasing rate from a paint film. The erosion rates of coatings can be compared with each other (Sanchez and Yebra, 2009). Advantages and drawbacks of this setup are outlined in Table 2.1

2.5.3 Other Setups

A patented system which allows to carry out combined static and dynamic ageing tests consists of a cylindrical tank and a motor-driven stirrer within this tank (Swain and Touzot, 2006). Coatings are tested on a rectangular panel which is attached to the panel holder located the inner side of the tank. The advantage of this setup is that it needs comparatively low energy to provide dynamic testing conditions since it rotates the fluid in the tank rather than test panels. The pH, salinity, temperature, and the velocity of the fluid can be monitored. This setup is also suitable for static and dynamic test cycles of thirty days. Figure 2-17 shows the top view of a test tank.

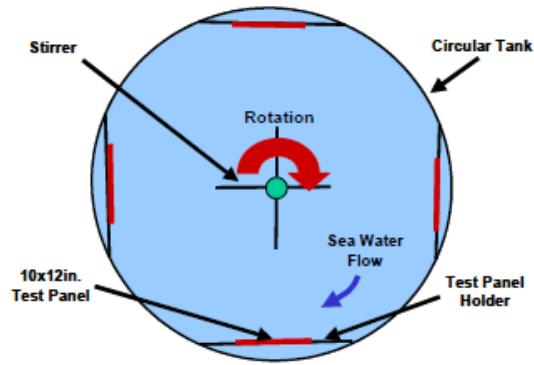


Figure 2-17 Top views of dynamic test tank adapted from Swain et al., (2007)

Slime farm, a laboratory device, which allows growing biofilm on test panels under dynamic condition was designed in the University of Newcastle. A linear jet flow was used to circulate seawater over a number of test panels located in the device. Computational Fluid Dynamics analyses were performed to make sure that the facility has adequate flow and guide vanes were added to the inlet region in order to have homogeneous shear stress distribution over the test panels. This is a state of art tool which is used to understand the effect of biofilm on the drag (Yeginbayeva et al 2019).The general arrangement of the slime farm is given in Figure 2.18.

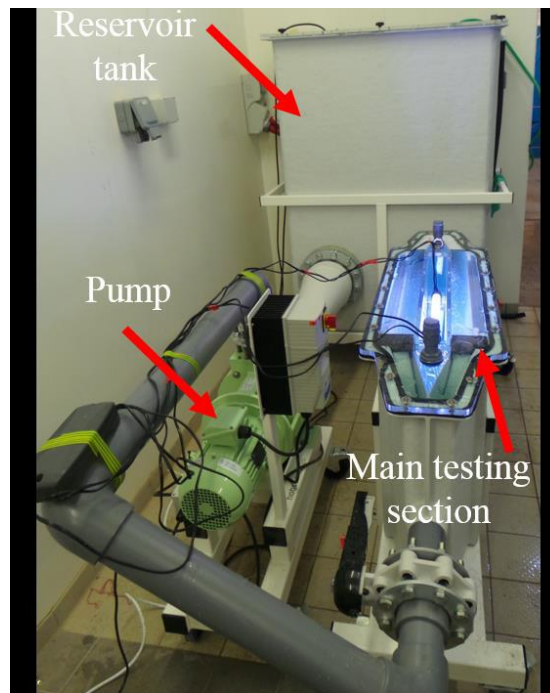


Figure 2-18 General arrangement of a slime growth farm device (view from top) (Atlas et al., 2019)

Multipurpose Flume (MPF) is a testing facility which is designed for testing the long term performance of biocidal and non-biocidal coatings under the real seawater conditions. The advantageous side of this tool is that it can develop fully turbulent flow which can give an idea of the full-scale ship resistance. The two primary purposes of the MPF are to simulate the ageing behaviour of a number of coated flat plates and to measure the pressure drop/drag across the coated panels (Yeginbayeva et al., 2019).
 ASTM D4938 - high-speed water channel

The system is comparatively expensive to build and operate as it needs high power pump to reach high-speed water flow. Only one test panel can be tested for each speed; therefore, it is not suitable for a large number of testing. Naval Research laboratory Key West facility uses a pump which can pump the water with a volumetric cubic rate of 3 m³/s. With the cross-sectional dimensions shown in Figure 2-19, flow speed can reach speeds of 5, 10, 15, 20, 25 and 30 knots. Thickness measurement of the coating can be made at specific time intervals.

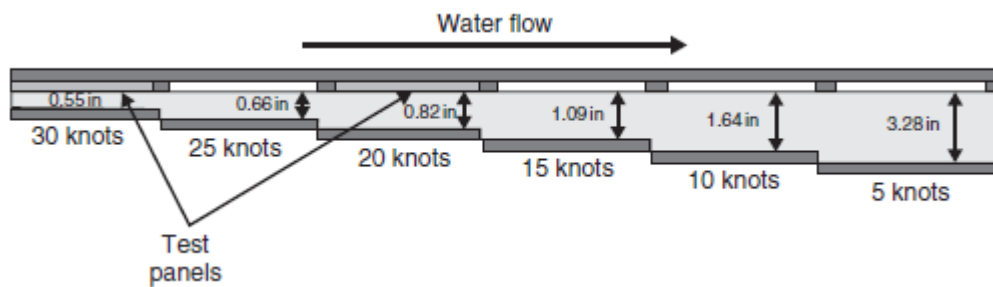


Figure 2-19 Diagram of a high-speed seawater flow channel (top view) adapted from Sanchez and Yebra (2009)

The ideal testing process for assessment of an antifouling coating is given in Figure 2-20. From the base to the top of the pyramid, the number of testable variables and formulations decreases. As shown in the figure short term and medium term tests are used for testing a large number of new raw materials and new formulations whereas long term tests are used for testing formulations which are promising to be commercialised. Since the ship test is expensive and difficult to carry out, it is believed that the development of antifouling coatings will be relying on long term tests in the next years.

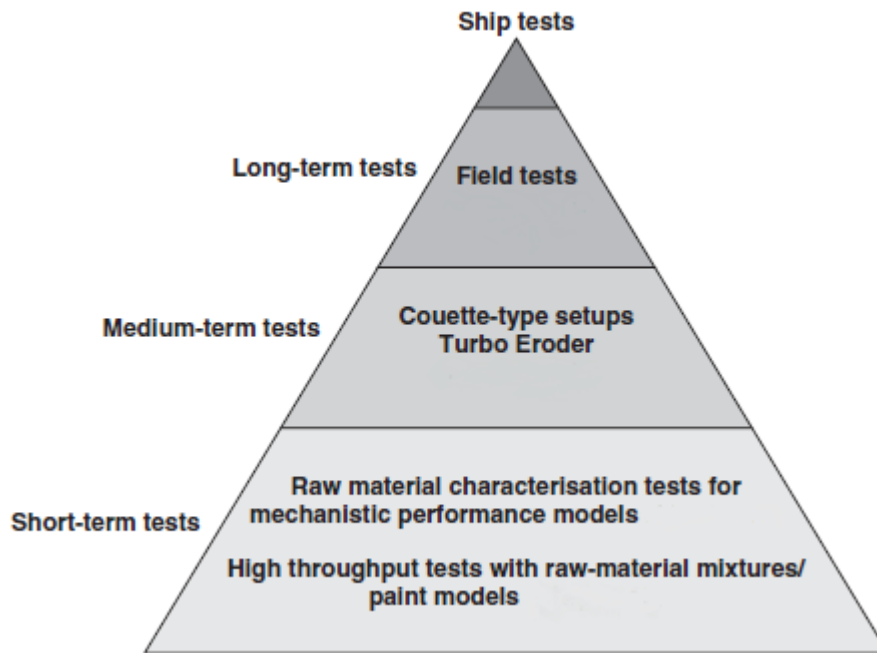


Figure 2-20 Workflow for and efficient antifouling paint design and optimisation adapted from Sanchez and Yebra (2009)

2.6 Effect of Biofouling on Ships

Biofouling on ship hulls increases surface roughness, which in return causes increased ship frictional resistance and power. Therefore, ship operators decide whether to increase power to keep agreed operation speed resulting in increased fuel oil consumption or reduce the speed at fixed engine power by delaying arrival time to the destination which may cause contractual penalties (Townsin 2003; Schultz 2007). Marine fouling-control coatings are prevalently used to smooth hull surfaces to reduce the frictional resistance and fuel consumption of a ship as well as to assist corrosion prevention and protecting against biofouling (Tezdogan and Demirel 2014).

The ship resistance is mainly composed of frictional and wave wave-making resistance. Frictional resistance, especially for low low-speed ships, is the dominant component of ship total resistance. For instance, a tanker cruising at design speed uses the majority of its power for overcoming frictional resistance in calm water.

There is a considerable amount of research in the literature on the effect of biofouling on ship frictional resistance which was conducted by means of various methods including towing flat plates, rotating disks and cylinders, water tunnels and ship trials.

McEntee (1916) conducted the first extensive experimental study on the effects of biofouling on frictional resistance. The flat plates in length of 10 feet were immersed in the Chesapeake Bay for 12 months to determine the change in frictional resistance. Each month a plate was taken for testing at various velocities from 2 to 9 knots for fouled and cleaned conditions at the United States experimental model basin. This study indicated that plates that covered by small barnacles showed four times higher frictional resistance values compared to clean condition after 12 months of seawater exposure. Izubuchi (1934) estimated the increase in frictional resistance coefficient due to biofouling through several ship trials on the destroyer Yudachi during a one-year period one year. Although quantifying the effect of fouling was not precise at a satisfactory level, tests indicated that frictional resistance of the ship doubled after 300 days.

Kempf (1937) developed the roughness coefficients (C_k) by conducting towing tests with an 87.7m pontoon in various surface conditions. Once adding this coefficient into the resistance equation of a real ship to calculate the increase in frictional resistance of a fouled ship, it was observed that frictional resistance of fouled ship is about double that of the un-fouled vessel. Conn et al. (1953) conducted a trial test through a ship hull which was allowed to be fouled for 40 days, over a speed range from 5 to 15 knots and results indicated 5% increase in frictional resistance. Watanabe et al. (1969) investigated the effects of the slime on frictional resistance and the separation of slime by the flow-through experiments on concentric cylinders, a model ship, and a rotating disk. After extrapolating these results to actual ships, the increase in total resistance was estimated to be ~ 10%.

Loeb et al. (1984) conducted an experiment by using rotating discs in order to obtain the effect of biofilm on the frictional drag. The results of the study indicate that frictional resistance increased by ~10-20%. Lewthwaite et al. (1985) obtained 25% and 83% increases in frictional resistance by using small Pitot tube for a 23 m tender vessel after ~240 and ~600 days, respectively. Haslbeck and Bohlander (1992)

conducted a series of laboratory tests and ship trials in order to understand the efficiency of antifouling coatings and to determine the biofilm effect on ship power and fuel consumption. The majority of the tested coatings in the laboratory showed an increase in frictional resistance to range between 10% and 19% at a ship speed of 25 knots. A Knox class frigate Brewton, coated with an ablative antifouling paint, was exposed to seawater for 22 months duration in Pearl Harbor, Hawaii. Then, the frigate was tested in ship trials, and it was observed that clean hull showed 18% decrease in shaft power compare to that of the fouled hull.

Schultz and Swain (2000) and Schultz (2000) conducted experiments on non-coated flat plates by using laser Doppler velocimetry in a recirculating water tunnel. The results indicated that increases in frictional resistance due to slime films and algae formation were in a range from 33% to 187%. Holm et al. (2004) conducted an extensive series of rotating disk tests by using a friction disk machine to examine differences among fouling release coatings. The drag penalties due to micro fouling ranged from 9% to 29%. Schultz (2004) tested the efficiency of 5 different coatings over flat plates after ~287 days seawater exposure and fouling coverages on the surfaces were assessed in accordance with the ASTM D3623 (1994). Following this, experimentally observed roughness functions were used in Granville's similarity law procedure (Granville, 1958) and then the increases in frictional resistance coefficient (C_F) were extrapolated for a 150 m plate representing midsized merchant ships as well as frigates and destroyers. Results indicated that percentage increases in C_F at ship scale in fouled condition ranged from 50% to 217% at 12 knots. Swain et al. (2007) conducted both static and dynamic immersion tests for two different biocide-based and two silicone-based foul release paints. After ~60 days of static immersion, all test surfaces were fouled with various fouling types including slime, barnacle, encrusting bryozoans and tubeworms. Following that, a dynamic test was conducted for 15 days by means of a rotating stirrer which rotates at a rotational speed of 60 rpm. Fouled test surfaces were then towed through a boat cruising at 25 knots, and existing fouling conditions were assessed in terms of frictional resistance.

Following this, Song et al. (2019) used a Computational Fluid Dynamics (CFD) based resistance simulation model to predict the effect of barnacle fouling focussing on the

resistance and wake characteristics of the full-scale KRISO container ship (KCS) hull based on the roughness functions of Demirel et al. (2017). The results of CFD simulations were compared with the results obtained by using Granville similarity law analysis (Granville 1958).

A more recent study provides an extensive and chronological review about the progress of antifouling coatings considering their improvement at reducing frictional resistance as well as their type, working mechanisms, and distribution of applied coatings for various geographical regions (Lindholdt et al., 2015).

Although these experimental studies presented reliable information on a range of fouling types, none of them presents a well-defined parametric study in order to provide detailed insight into the effect of barnacle height, settlement pattern and coverage on the frictional resistance of a ship. A study might be performed to fill this gap by carrying out a systematic experimental and numerical study to assess the effect of barnacle height and coverage on ship resistance and power. A further study could be the investigation of the effect of micro fouling by using 3D technology as similar in this study.

2.7 Theoretical backgrounds – Roughness and Turbulent Boundary Layer

2.7.1 The velocity Profile in The Boundary Layer

As the ship moves through the water, fluid particles right next to the ship hull stick to the ship hull (no-slip condition). Due to the interaction with fluid particles stuck to the hull, fluid particles just above the surface loses their relative velocity. This effect gradually decreases and creates a thin layer (boundary layer) in which water flow velocity changes from zero to free stream velocity at a certain distance from the surface. Biofouling increases the roughness of the hull surface, which causes an increase in boundary layer thickness and frictional resistance of the hull. As the ships are operated at high Reynolds number, on the majority part of the hull length with the exception of the bow section, boundary layer on a ship is a turbulent boundary layer.

The turbulent boundary layers are considered to consist of several regions; viscous sub-layer, the log-law region and the outer region (Schultz and Swain 2000). This subdivision in the turbulent boundary layer is illustrated in Figure 2-21.

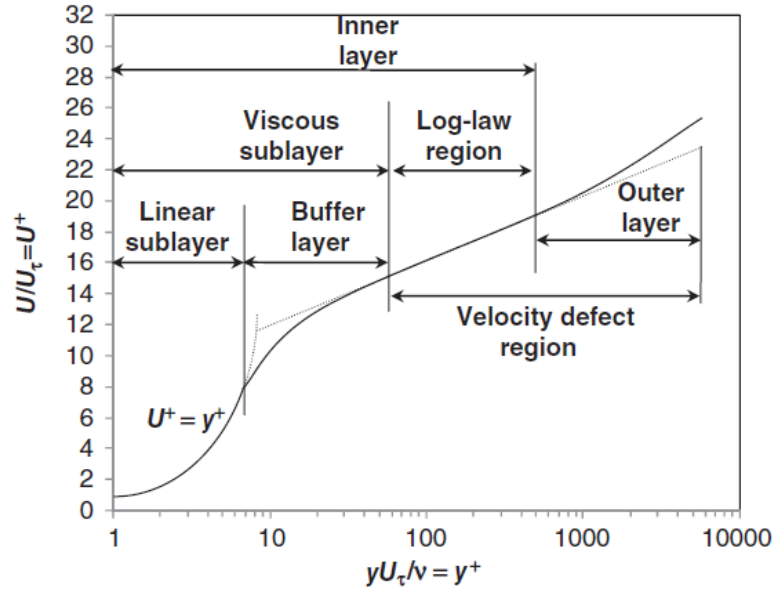


Figure 2-21 Law of the wall plot for a turbulent boundary layer adapted from Schultz and Swain (2000)

As shown in Figure 2-21, the inner region consists of the viscous sublayer and the log-law region. Although inner region composes 10-20% of the total boundary layer (i.e. $y/\delta=0$ to 0.1-0.2) ~70% of variations in velocity occurs in this region. The mean velocity in this region is defined as a function of the wall shear stress, the fluid density, kinematic viscosity, and the distance from the wall. Therefore, the fluid velocity can be demonstrated in the following equation, which is called the law of the wall.

$$\frac{U}{u_{\tau}} = f\left[\frac{yu_{\tau}}{\nu}\right] \rightarrow U^{+} = f[y^{+}] \quad (2.1)$$

The superscript + sign stands for a non-dimensionalized variable in the inner region. The distance from the wall (y^{+}) are non-dimensionalized by the viscous length scale $\left(\frac{\nu}{u_{\tau}}\right)$. The viscous scale is a function of the kinematic viscosity and the friction velocity, as shown in equation (2.2).

$$u_\tau = \sqrt{\frac{\tau_w}{\rho}} \quad (2.2)$$

2.7.1.1 Viscous Sublayer

The linear sub-layer and the buffer layer are the parts of the viscous sublayer, as shown in Figure 2-21. The linear sublayer occurs in a very thin region where $y^+ \leq 7$. In this region, the velocity profile is linear, as shown in equation (2.3).

$$U^+ = y^+ \quad (2.3)$$

In the linear sublayer, the total shear stress is steady and equal to the wall shear stress (τ_0). The wall shear stress can be normalised in order to define the skin friction coefficient as given in Equation 2.4.

$$C_F = \frac{\tau_0}{\frac{1}{2} \rho U_e^2} \quad (2.4)$$

The velocity profile deflects from linear behaviour where y^+ is between 7 and 40. This region is called a buffer layer in which the highest turbulence takes place.

2.7.1.2 Log-Law Region

As shown in Figure 2-21, log-law region ($40 < y^+ < 300$) starts where the viscous sublayer ends, and the flow is also highly turbulent in this region. The total shear stress is constant and exists due to the fluctuating velocity components in the flow. The velocity distribution can be formulated by equation (2.5) (Schultz and Swain, 2000).

$$U^+ = \frac{1}{\kappa} \log(y^+) + C \quad (2.5)$$

Many studies have confirmed the existence of a log-law region of the boundary layer for flows (Klebanoff and Diehl, 1954) (Clauser, 1954). The values assigned for this constants showed variety in different studies, for example, Clauser (1954) used $\kappa=0.41$ and $C=4.9$ whereas Coles (1956) determined the values of κ and C as 0.4 and 5 respectively. Cebeci and Chang (1978) used $\kappa=0.41$ and $C=5.2$.

2.7.1.3 Outer Layer

The remaining part is termed as the outer layer where the velocity profile does not follow the log-law trend at higher y^+ values, as illustrated in Figure 2-21. This deflection is called the wake and is characteristic of the outer layer of the turbulent boundary layer. In this layer, the shear stress changes, as shown in Figure 2-22. The mean velocity profile in the outer layer can be given as a relationship between the velocity defect and non-dimensionalised distance from the boundary (Schlichting, 1979).

$$\frac{U_e - U}{u_\tau} = f\left[\frac{y}{\delta}\right] \quad (2.6)$$

This relation is termed as the velocity defect law. It is discussed in theoretical, the velocity defect at a distance from the wall, y , is because of shear stress at the wall. An important thing about the velocity defect law is that it is valid for both smooth and rough boundaries as the effect of roughness diminishes with respect to the distance from the wall.

In order to describe the velocity profile in the outer region, Coles (1956) defined the law of the wake, which considers the effect of the turbulent wake defect. This can be stated in equation (2.7)

$$U^+ = \frac{1}{\kappa} \ln(y^+) + C + \frac{2\Pi}{\kappa} \sin^2\left(\frac{\pi y}{2\delta}\right) \quad (2.7)$$

As Coles (1956) stated the wake parameter, $\Pi=0.55$ inflows with low freestream turbulence and zero pressure gradient. Schetz (1993) uses 0.51, which was suggested by Clauser.

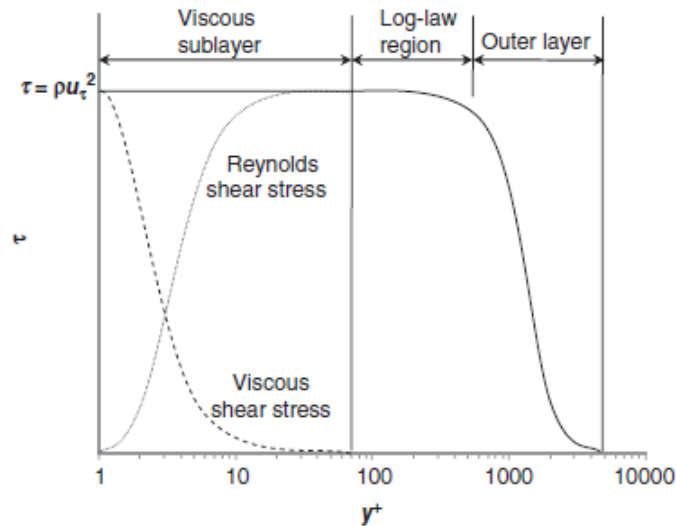


Figure 2-22 Turbulent boundary layer shear stress profile adapted from Ligrani (1989)

2.7.2 The Effect of Surface Roughness on Boundary Layers

Surface roughness increases turbulence in the boundary layer which also increases turbulent and wall shear stress. The roughness can be mainly categorised into two types, such as k-type and d-type. Roughness functions of k-type roughness scale on the roughness height, k whereas roughness function of d-type roughness scale on the pipe diameter, d (Perry et al., 1969). Since the ship roughness have been shown to be k-type, the discussion will focus on this type of roughness.

The previous studies on k-type roughness is sand grain roughness studies which are conducted by Antonia and Luxton (1971, 1972), Ligrani and Moffat (1986), Bandyopadhyay (1987), Krogstad et al.(1992), Shockling et al.(2006) and Schultz and Flack (2007) and Schultz and Flack (2013). The effect of surface roughness on the boundary layer can be analysed in three flow regimes. The first regime is the smooth regime in which roughness elements on the surface are small enough to be covered under the linear sub-layer, and the surface is termed hydrodynamically smooth.

The second flow is termed the intermediate or transitional regime. In this regime, some percentage of roughness elements pass beyond the linear sublayer and causes to form drag and eddy shedding. The last flow condition is the fully rough regime which occurs when most of the roughness elements penetrate through the linear sublayer. Form drag and eddy shedding of the roughness elements made up the surface drag.

2.7.2.1 Roughness Reynolds Number

The surface roughness is defined by means of a parameter which is called the roughness Reynolds number k^+ , which is described as follows:

$$k^+ = \frac{ku_\tau}{\nu} \quad (2.8)$$

Pioneering studies on the effect of roughness were performed through surfaces or pipes which artificially roughened with sand grains; therefore, sand grain height is used to characterise roughness. The equivalent sand grain height, k_s is the height of a sand-grain that would result in the same roughness function of any arbitrary roughness geometry (for instance, artificial barnacle tiles in this study) (Schlichting 1979). The roughness Reynolds number of the flow can be used to identify the flow regime. Schlichting (1979) identified the range of k_s^+ for the flow conditions; the flow regime is identified as smooth where $k_s^+ < 5$, intermediate where k_s^+ between 5 and 70 and fully rough where $k_s^+ > 70$ based on the experimental results.

It is important to note that Schlichting (1979) used uniform sand roughness, and this limits may vary for different type surface roughness as flow regime depends on the nature of the surface roughness. For instance, these limits are comparatively low for a wire mesh roughness and for spanwise grooves, as indicated in Bandyopadhyay (1987). Cebeci and Chang (1978) stated different limits for the flow regimes; $k_s^+ = 2.25$ upper limit for the smooth regime and $k_s^+ = 90$ upper limit for the intermediate regime and k_s^+ above 90 stands for the fully rough regime. It should be noted that ships are typically operated in the intermediate flow regime and sometimes in fully rough regime (Grigson, 1992).

2.7.2.2 Roughness Effect on Mean Velocity

Nikuradse (1933) carried out the first experimental study on the effects of roughness on the boundary layer flows. Pipes are coated with uniform sand grain with maximum density. The surfaces were characterized by the height of the sand roughness elements, k_s . The relation between k_s and the thickness of the linear sublayer δ' affect the roughness on the flow.

If k_s is smaller than $\frac{\delta'}{3}$, the flow is smooth, and the linear sublayer does not penetrate by roughness element. Therefore, the log-law velocity profile is accurate for the law of the wall region. equation (2.9) is the restatement of the log law (Equation (2.3)) with $A = 5.62$ (Kline et al., 1969).

$$U^+ = A \log(y^+) + C \quad (2.9)$$

If k_s is bigger than about seven times the thickness of the linear sublayer, the sublayer is disappeared, and the flow becomes independent of viscous effects. This regime is called fully-rough condition. This relationship is given by equation (2.10).

$$U^+ = A \log\left[\frac{y}{k_s}\right] + B \quad (2.10)$$

where B is equal to 8.5 for fully rough flow, according to Schlichting (1979).

Once the boundary layer is plotted in units of U^+ against $\log y^+$, there will be a downward shift due to roughness function in the velocity profile. Boundary layer profile for all flow regimes can be written as follows (Schultz, 1998).

$$U^+ = A \log(y^+) + B_1 = A \log(y^+) + C - \Delta U^+ \quad (2.11)$$

In the smooth flow regime, $C=B_1$ and roughness function should be equal to zero, $\Delta U^+=0$. For the fully rough regime roughness function can be written as a function of roughness Reynolds number as follows:

$$\Delta U^+ = A \log(k_s^+) + C - B \quad (2.12)$$

2.7.3 Determination of Roughness Functions

Determination of roughness functions is essential as it enables to predict the increase in the frictional resistance of an object covered with a specific roughness by means of a boundary layer method (Granville 1985, 1987). Each roughness type has different

roughness behaviour and roughness functions which need to be determined experimentally.

The roughness functions can be determined through direct or indirect methods. Direct methods measure the velocity profile in the boundary layer whereas indirect methods aim to determine roughness functions by means of measuring pressure drops in pipe flow (Nikuradse 1933), total drag of flat plates (Granville 1978) or torque on rotating disks (Granville 1982). As the towed plate method will be used in this study, further discussion is made on this method.

Determination of roughness functions through overall method was introduced by Granville (1987). The procedure starts with measuring the frictional resistance of a flat plate which is covered with roughness in question. Granville (1987) stated that k^+ and ΔU^+ could be calculated by iteratively solving equation (2.13) and (2.14).

$$k^+ = \left(\frac{k}{L}\right) \left(\frac{Re_L C_F}{2}\right) \left(\sqrt{\frac{2}{C_F}}\right)_R \left[1 - \frac{1}{\kappa} \left(\sqrt{\frac{2}{C_F}}\right)_R + \frac{1}{\kappa} \left(\frac{3}{2\kappa} - \Delta U^{+'}\right) \left(\frac{C_F}{2}\right)_R \right] \quad (2.13)$$

$$\Delta U^+ = \left(\sqrt{\frac{2}{C_F}}\right)_S - \left(\sqrt{\frac{2}{C_F}}\right)_R - 19.7 \left[\left(\sqrt{\frac{C_F}{2}}\right)_S - \left(\sqrt{\frac{C_F}{2}}\right)_R \right] - \frac{1}{\kappa} \Delta U^{+'} \left(\sqrt{\frac{2}{C_F}}\right)_R \quad (2.14)$$

where L is the plate length, Re_L is the plate Reynolds number, $\Delta U^{+'}$ is the slope of the roughness function and subscript of S stands for the smooth condition. Subscript of R stands for the rough condition. The frictional resistance values of smooth and rough conditions should be taken for the same $Re_L C_F$, as explained in Schultz (1998).

2.7.4 Identified Gaps and Conclusions

The literature on the biofouling is reviewed in detail along with factors influencing biofouling, antifouling methods and technologies and the effect of biofouling on a ship. The identified gaps and principal conclusions are given below:

- As presented in Section 2.4, many products exist within the antifouling methods and technologies, but there is no specific selection method for the best antifouling method for the ship in question. Although there are many methods for testing antifouling coating performances against biofouling accumulation, they are limited only for lab-scale tests, and there is no approach to bridge these lab-scale results by taking into account the time factor to ship scale results. For this reason, a decision support tool, which makes tailor-made condition assessment for ships based on the factors affecting coating performance, would be very beneficial. Therefore, this study aims to develop an approach which enables to predict time-dependent increases in ship frictional resistance and powering as well as fuel consumption and to decide about scheduling the appropriate maintenance periods.
- There is no specific technique or way to combine antifouling field test data and ship operational data in combination, which are vital for the coating selection process.
- No systematically study exists to investigate the effect of barnacle fouling on frictional resistance in terms of barnacle height, settlement pattern and coverage area.
- Any surface roughness shows different characteristic behaviours and needs to be determined experimentally.
- There is only a limited number of diagrams and tables exist, which gives increases in the ship frictional resistance and ship effective power for varying length of ships cruising at varying speeds.
- No specific diagrams and tables exist which provide the effect of settlement pattern on ship frictional resistance and powering

3 Methodology

3.1 Introduction

This chapter shows the methodology followed in this thesis.

3.2 Methodology

Relevant methods and approaches are provided in each chapter. However, a general methodology followed in this thesis was provided to show the whole study together with connections between the chapters. Figure 3-1 illustrates the general methodology followed in this thesis.

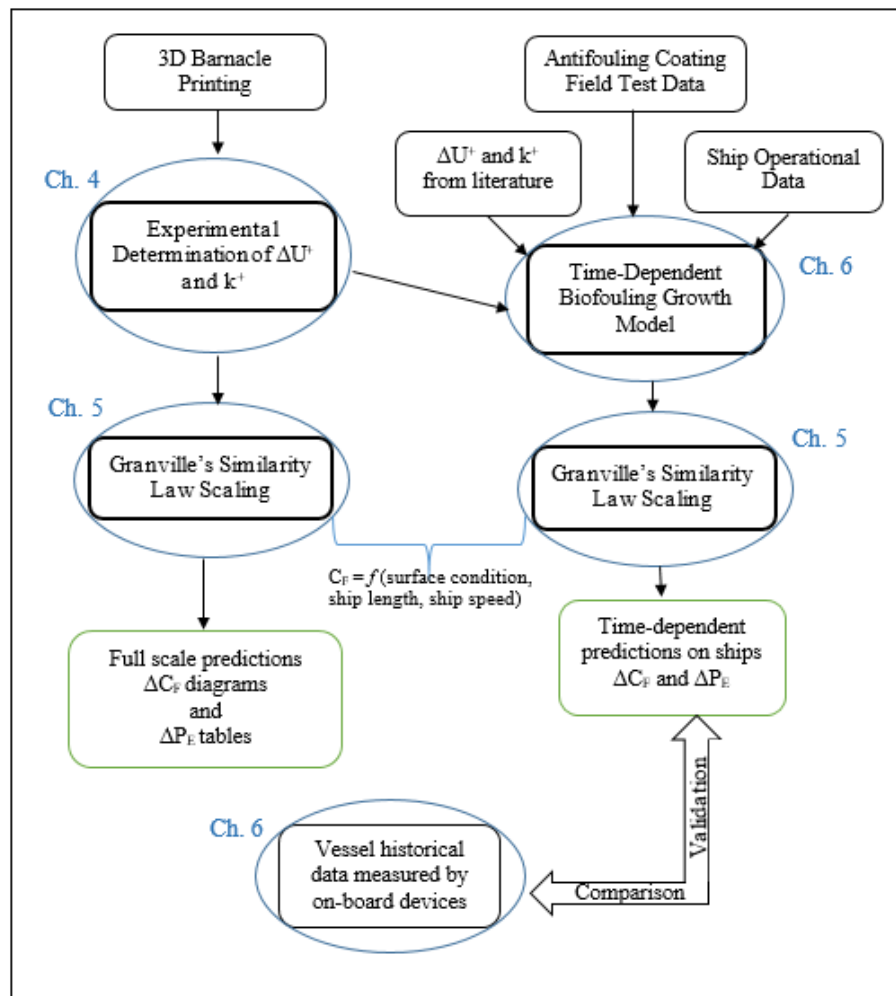


Figure 3-1 The general methodology followed in this thesis

As shown in Figure 3.1, roughness functions both from the literature and the experiments from this study as well as antifouling field test data and ship operational data are used as inputs of the model. Then, the model was developed based on these inputs in order to predict time-dependent biofouling growth in relation to trading route, idle times, ship speed and ship length. Lastly, the model makes time-dependent predictions on the increases in the ship frictional resistance and powering, which then is compared with the vessel historical data and validated.

Drag characterisation and determination of roughness functions require experimental investigation. Therefore, one of the most common barnacles was printed by means of 3D technology. 3D printed barnacle bundles were attached on the flat plates, and the towing test was carried out to determine frictional resistances. Roughness functions, ΔU^+ , and roughness Reynolds number, k^+ , of eighteen different flat plate configurations covered with artificial barnacles were determined by using Granville's (1987) overall method in Chapter 4.

As explained in Chapter 5, Granville's similarity law scaling procedure was performed in order to predict roughness effect of barnacle fouling on the frictional resistances of flat plates of ship length. Experimentally obtained roughness function and roughness Reynolds numbers pairs are employed in an in-house code based on the Granville's (1958) similarity law scaling procedure. This allows predicting the effect of roughness of test surfaces on the full-scale ship resistance. Added frictional resistance diagrams, as well as tables showing increases in the effective power and possible ship speed reductions at fixed effective power were provided for six different case studies.

In Chapter 6, a novel time-dependent biofouling growth model which enables to predict time-dependent biofouling growth and hence increases in the ship frictional resistance was proposed. Antifouling field test data, ship operational data, roughness functions of biofouling conditions from literature and this thesis were employed in this model. First, the model predicts fouling ratings based on the antifouling coating field test data and ship operational data, including ship route and idle time periods. Then, fouling ratings were converted into equivalent sand roughness height in accordance with the roughness functions given in the literature and this thesis.

Predicted equivalent sand roughness heights, roughness function pairs, ship length and ship speed in question are employed in the Granville's (1958) similarity law scaling procedure. This procedure is repeated at each idle time period, and increases in the ship frictional resistances are predicted for the whole ship operation duration in question. Although the model achieved to predict time-dependent increases in the ship frictional resistances, it needed to be validated by means of a case study.

The model was tested using one year of historical ship data measured through onboard devices and time-dependent increases in the ship frictional resistance due to biofouling was predicted over one year of the period. The validation of the model is performed in three stages by conducting delivered power comparisons between the predicted and measured values. In the first stage, the first month of one-year ship operation is taken in which ship was clean (dry-docked). The data is filtered to calm water conditions. Then, power comparisons are made with the expectation of having no difference between compared values. It is important to note that Guldhammer Harvald (1974) power prediction method is used for the validation. The transition from effective power to delivered power was performed by multiplying the related propulsive efficiencies in order to predict delivered power in calm water scenario. The relative percentage errors between measured and predicted delivered power values are reported.

In the second stage, the last one month period of the one year of ship operation is taken in which ship hull is fouled, and power comparisons are repeated in this section. The relative error percentages between the measured and predicted power are caused due to biofouling as the same filtering conditions applied. In the third stage, predicted time-dependent increases in the ship frictional resistance are employed in the Guldhammer Harvald power prediction code, and power comparison is repeated for the last one month period. The decrease in the relative error percentages shows whether the time-dependent biofouling growth model makes sensible predictions.

Figure 3-1 shows the interactions between the main chapters and how they are related to the scope of this thesis as well as the steps that have been followed in order to achieve the objectives of this thesis.

4 Effect of Barnacle Fouling on Ship Resistance and Powering

4.1 Introduction

It is well-known that biofouling has detrimental effects on ship performance. There is no doubt that macro fouling, especially calcareous type fouling such as barnacles, tubeworms and mussels has the worst effect on ships in terms of added frictional resistance and added power requirements. Knowing that truth is not enough; therefore, surface roughness and its' effect on ship resistance should be thoroughly and systematically investigated to have a better understanding and, to have practical answers for ship operators to help them sustain energy-efficient ship operations.

Extensive series of towing tank experiments were carried out by covering flat plates with artificial 3D printed barnacles to understand the effect of surface roughness of macro fouling on ship resistance at Kelvin Hydrodynamics Laboratory in the University of Strathclyde. Having this kind of knowledge will help us to be able to predict the increases in frictional resistance, effective power and subsequently fuel consumption. In light of this study, ship operators will have diagrams showing the additional increase in frictional resistance and ship power under varying fouling conditions. This will help the operators to decide when the ships should be dry-docked.

Eighteen different surface configurations were created and tested in the experiment. Five different configurations, including smallest (S), middle (M) and biggest (B) size barnacles, in uniform mixed and natural settlement mixed configurations were modelled and tested. Surface area coverages for these configurations were selected to be 10%, 20%, 40% and 50% except biggest type configurations (10% and 20% surface coverages). For each test configuration, a flat plate representing the reference plate was also towed to be able to calculate an increase in the drag.

Following sections briefly explain the details of the experiment, including manufacturing of artificial barnacles, experimental facilities, plate preparations, test methodology, repeatability and uncertainty estimates, results of the experiment, determination of roughness functions. The results of the experiment are presented as total resistance coefficients and frictional resistance coefficients. Then roughness functions and roughness Reynolds number of the surfaces are determined.

4.2 Manufacturing of Artificial Barnacles

This study presents the results from resistance tests of flat plates covered with 3D printed artificial barnacles in different types in terms of size and settlement uniformity. *Amphibalanus Improvisus* (Darwin, 1854) (acorn barnacle) as shown in Figure 4-1, a quite common barnacle species, especially in Europe, was selected to represent barnacle fouling in this study.



Figure 4-1: The picture of *Amphibalanus Improvisus*

After the selection of the barnacle type, the shape of barnacle was three-dimensionally scanned and imported to a computer-aided modelling program.

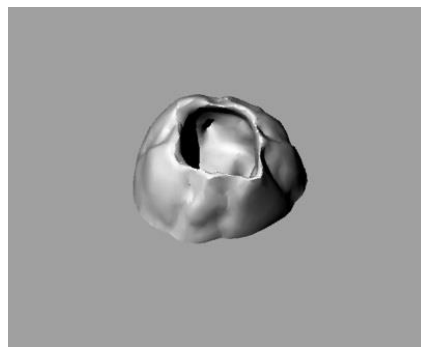


Figure 4-2: The Picture of 3D Scanned Barnacle Model

Figure 4-2 shows the picture of a 3D scanned barnacle model. When a fouled ship surface area is observed, it is usual to see barnacles in varying sizes. This can be attributed to the fact that biofouling is a biological phenomenon and like other livings, these animals born, grow and die. In order to simulate this situation, different sizes of barnacles were designed in a modelling program by scaling original geometry. The derived dimensions of barnacles which represent different stages of barnacle growing have been shown in Table 4-1. For the sake of the experiment and for preventing some uncertainties such as the distance between barnacles and settlement uniformity, models were prepared to be manufactured as bundles in the modelling program. Figure 4-3 shows the CAD version of the Mixed type barnacle bundle.

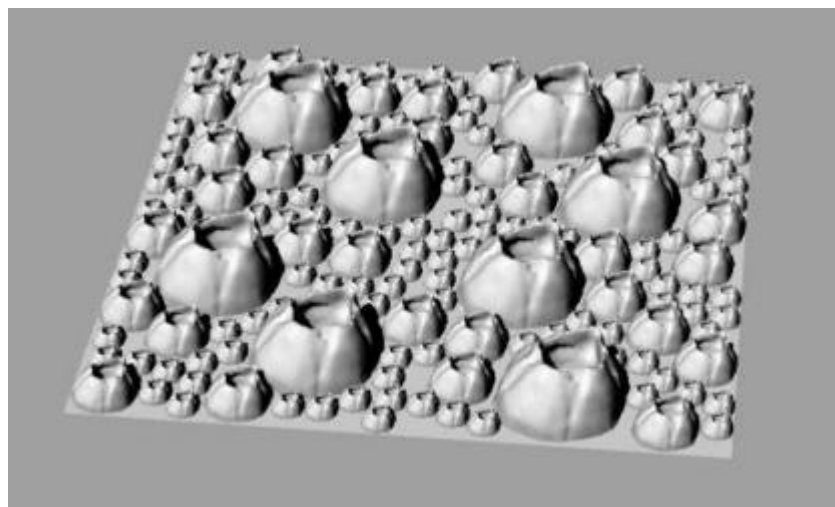


Figure 4-3: Picture of a Mixed type barnacle bundle

Table 4-1 Configuration table

Barnacle Type	Dimensions (diameter & height)	Reference Plate	% 10 Coverage	% 20 Coverage	% 40 Coverage	% 50 Coverage
B type	10 mm & 5 mm	x	x	x		
M type	5 mm & 2.5 mm	x	x	x	x	x
S type	2.5 mm & 1.25 mm	x	x	x	x	x
Mixed	It has three types of barnacle together	x	x	x	x	x
NS	Three types of barnacle with different settlement pattern	x	x	x	x	x
Mixed						

4.3 Experimental Facilities

The experiments, as mentioned before, were carried out at Kelvin Hydrodynamics Laboratory (KHL) in the University of Strathclyde. The KHL test tank has dimensions of 76 m in length, 4.6 m in breadth and 2.5 m in depth. The tank is equipped with a computer-controlled digital drive which can reach speeds up to 5 m/s, four flaps absorbing wave maker and high-quality sloping beach. Its' data acquisition system is a computer-based modular data acquisition/control system, which has 64 input and 20 output channels, and frequency is 60 kHz. The tank holds freshwater, and the temperature of the water was monitored during the experiments. Figure 4-4 shows the photo of the towing tank and carriage.



Figure 4-4: KHL towing tank and carriage

The overall drag measurements were taken by using two linear variable differential transformer (LVDT) type transducers which are electromechanical devices convert mechanical motion into electrical current or voltage that helps us to measure the forces implying on plates.

It should be noted that two transducers were used on plates one for checking the lateral force (lift-force) and the other one for measuring drag force. Plates should be mounted parallel to the flow direction for getting accurate results; therefore, one transducer should measure the lift forces to make sure it is aligned in the right direction during the experiment. Figure 4-5 shows the LVDT transducers used in the experiment.

Before mounting the transducers on the plates, the transducers were calibrated by hanging weights on transducers' gauge and recording the voltage values for each particular weight. Figure 4-6 illustrates the calibration process.

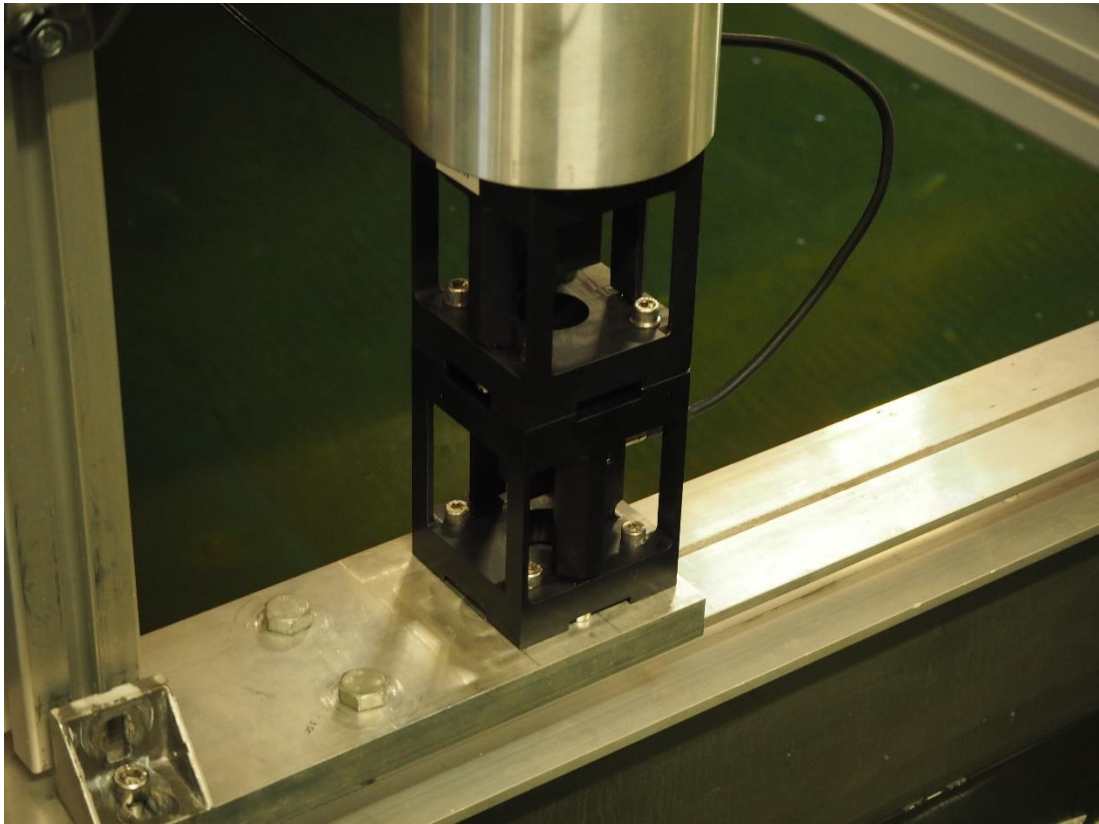


Figure 4-5 LVDT transducers



Figure 4-6: Calibration process

Transducers were calibrated separately in terms of their purpose of use, indicating the expected load range. Drag transducer has a load range up to 140N, whereas lift transducer's load range is from 0 to 50N. Upper range was selected as a high value for preventing any possible measurement mistake. A calibration factor obtained by using the created linear relation between the output voltage and load. Then using this factor, measured voltage values were turned into weight values to compare the loaded weight

and measured weight. Figure 4-7 and Figure 4-8 shows the calibration results for both transducers.

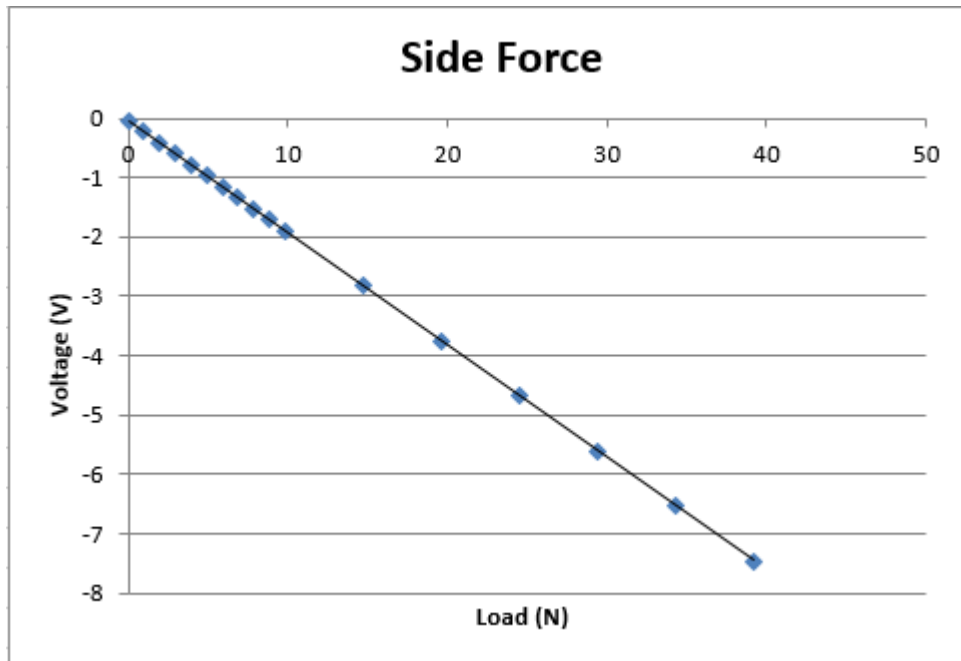


Figure 4-7: Calibration line for Lift Transducer.

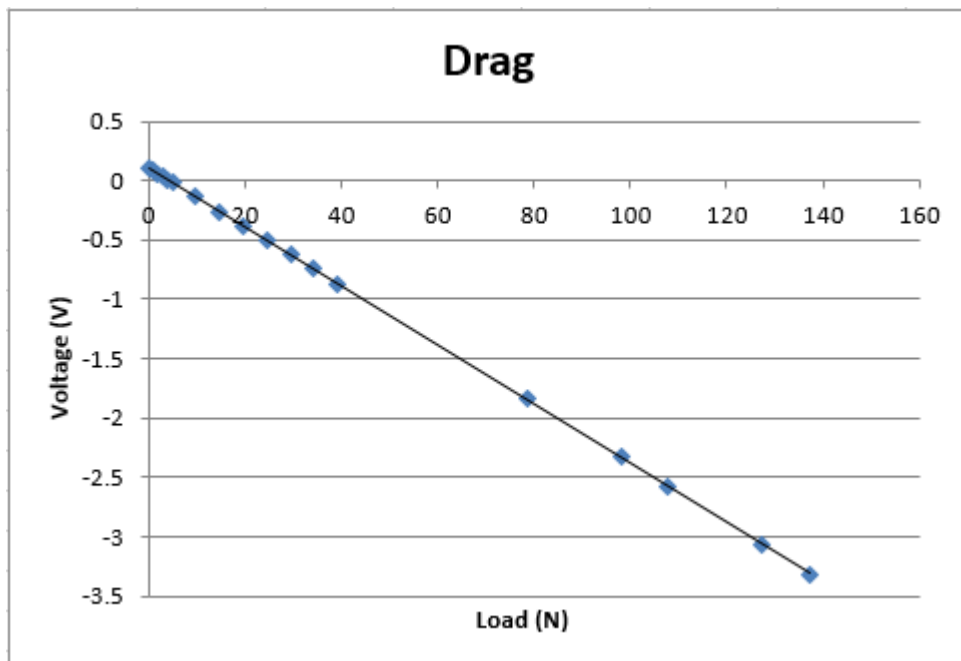


Figure 4-8: Calibration line for Drag Transducer.

4.4 Plate Preparations

Flat plates which used in the experiments were manufactured by KHL technicians using CNC machine. Metal type of flat plates is 304-stainless steel. The leading edge of plates rounded to 2.5 mm radius and sides of plates were smoothed by 80 grit, 120 grit and 320 grit of sandpapers to mitigate extra drag due to the separation and roughness of plates. Figure 4-9 presents a schematic of the flat plate test fixture

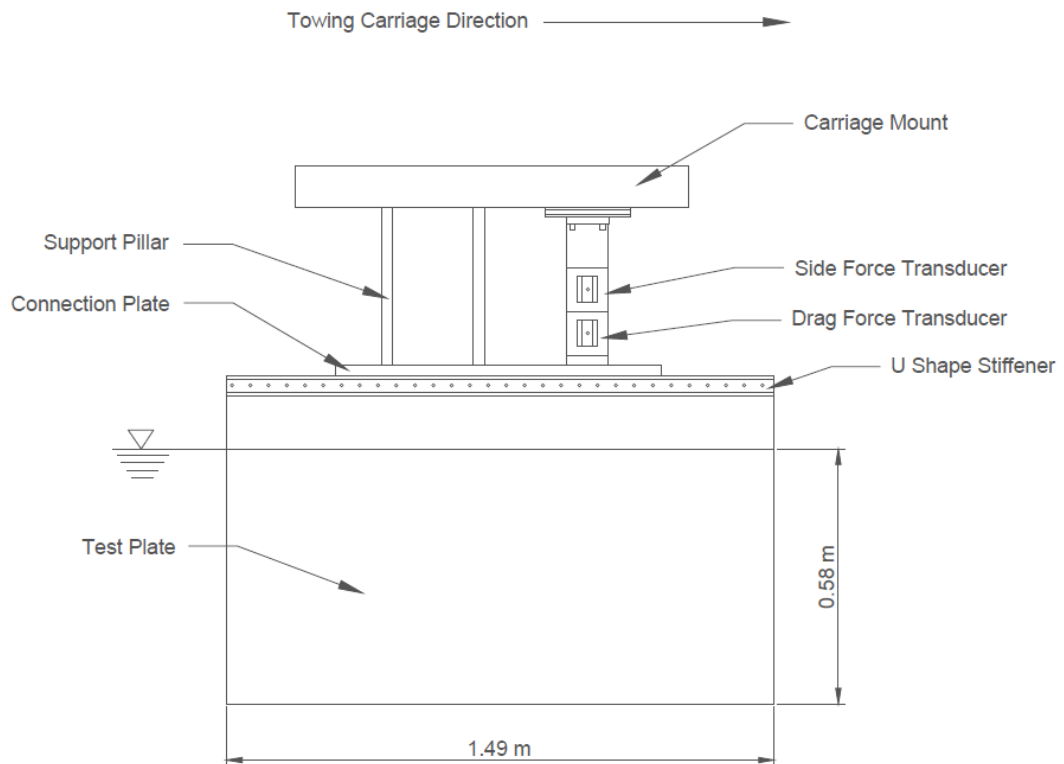


Figure 4-9: Schematic of the flat plate test fixture

The experiment configurations can be seen in Section 4.2 in Table 4-1. The area coverage percentages were adjusted with respect to the ASTM D6990-5 standards (2011). Square bundle areas were calculated as keeping the same bundle area over flat plate area ratio in ASTM standards. The following figures (4-10 to 4-13) show locations of bundles on flat plates for in a range of 10% to 50% percentage coverage. It should be noted that the plates in the pictures are upside down.



Figure 4-10: 10% of barnacle coverage on the flat plate



Figure 4-11: 20% of barnacle coverage on the flat plate

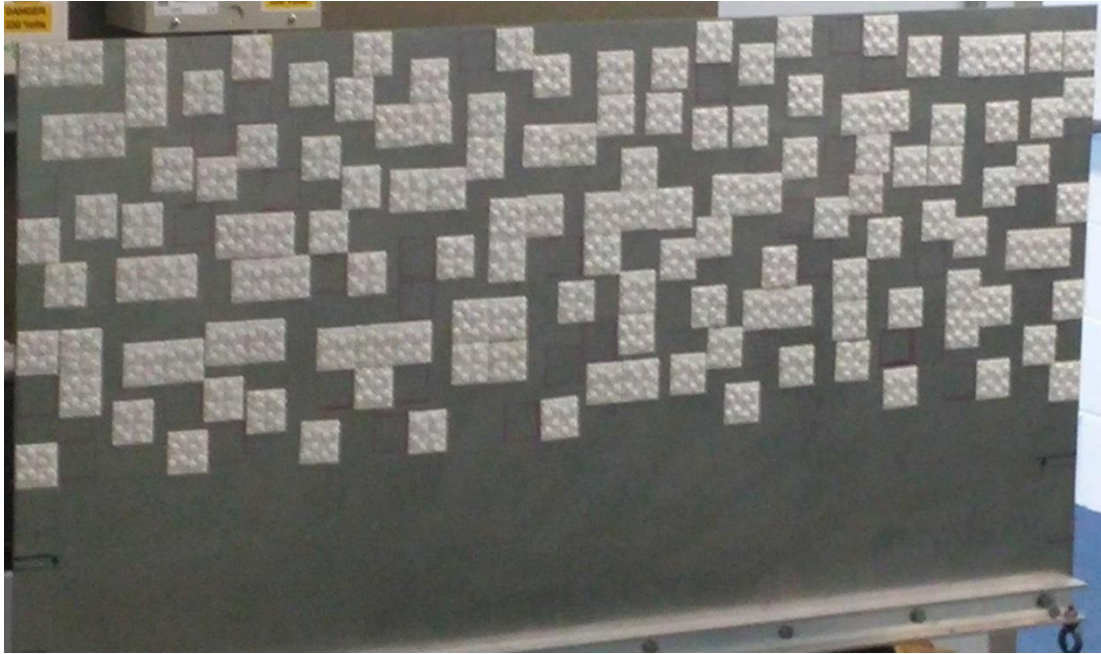


Figure 4-12: 40% of Barnacle coverage on a Flat Plate

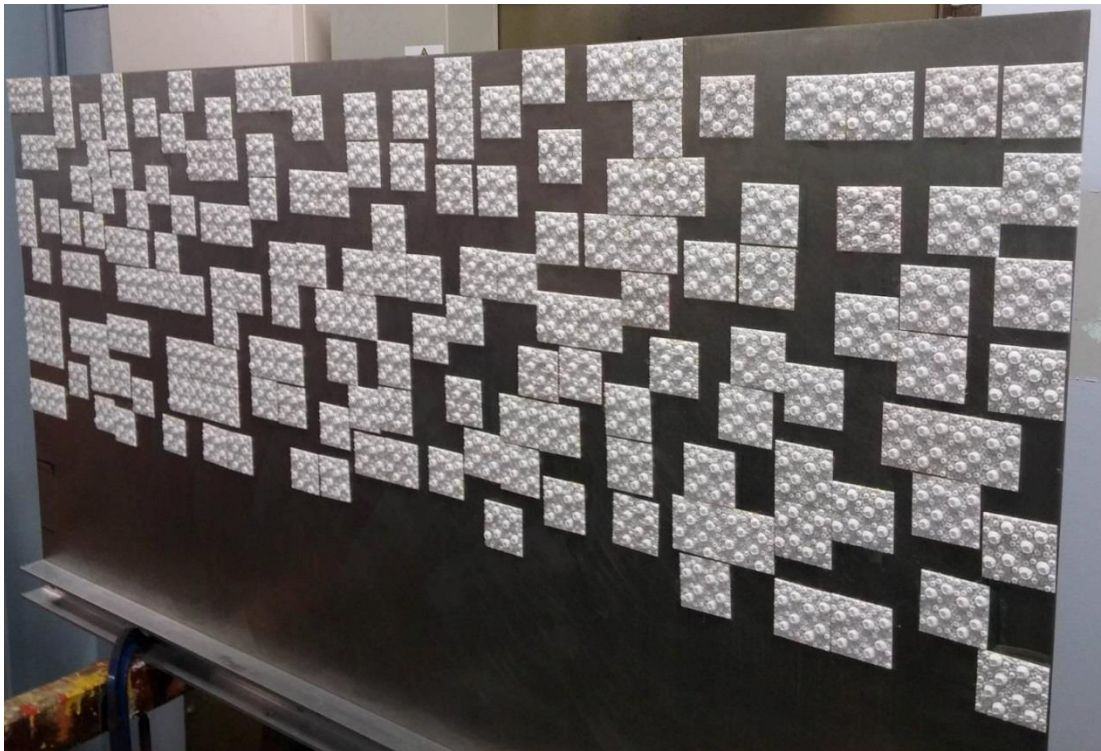


Figure 4-13: 50% Percentage of Barnacle Coverage on a Flat Plate

The pictures presented above belong to the mixed type barnacle configurations but also same coverage standards and identical experiment procedure have been used for the other configurations with the standard settlement.

The barnacle settlement, designed in accordance with ASTM D6990-05, led researchers to investigate the effect of barnacle settlement on frictional resistance if the barnacles are located chaotically aiming to simulate barnacle settlement in nature. To date, numerous studies have been conducted to assess the effect of various fouling presence on ship resistance and powering. Despite this interest, no one, to the best of authors' knowledge, has investigated the settlement effect of barnacle fouling on ship resistance and powering.

To fill this gap, chaotic barnacle settlement, which is called natural settlement (NS) was designed to represent barnacle settlement in nature. NS Mixed type configuration has different settlement pattern, which is shown in the following pictures from Figure 4-14 to Figure 4-17.

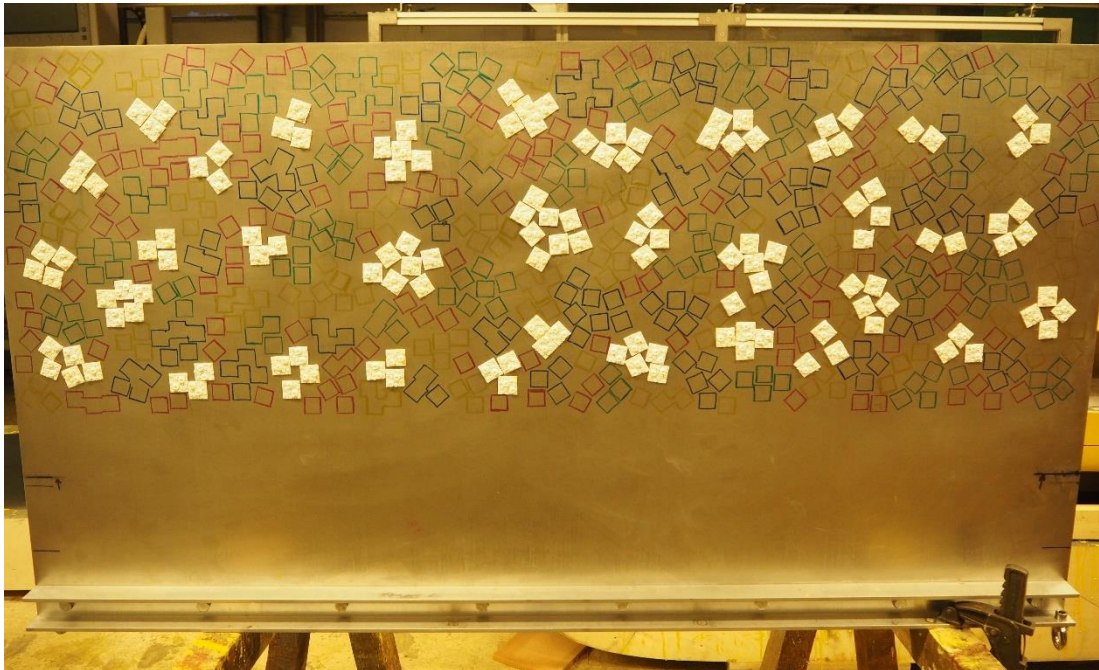


Figure 4-14 NS Mixed 10% barnacle coverage on a flat plate



Figure 4-15 NS Mixed 20% barnacle coverage on the flat plate

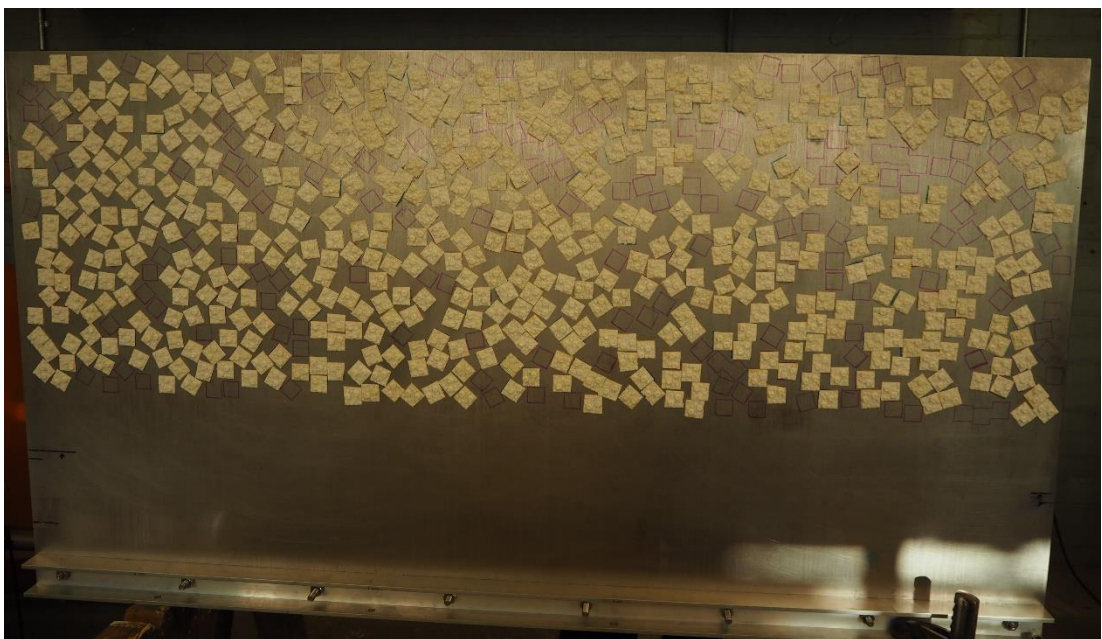


Figure 4-16 NS Mixed 40% barnacle coverage on a flat plate



Figure 4-17 NS Mixed 50% barnacle coverage on a flat plate

4.5 Test Methodology

The test methodology is adapted from the studies of Schultz (2004) and Demirel (2015). The experiment starts with the alignment of the reference plate. The reference plate was towed, and the side force was monitored using the side transducer until the side force was measured as zero. The side force was monitored at each run to make sure that the reference plate was kept aligned.

The overall drag of the flat plate (R_T), consists of the residuary (R_R) and frictional resistance (R_f) according to the ship resistance theory of William Froude as given in equation (4.1).

$$R_T = R_f + R_R \quad (4.1)$$

Frictional resistance is found by integrating tangential stresses of surface which drag the water due to viscous effects whereas residual resistance is a force that happens as a consequence of ship's movement-based phenomena such as waves and Eddy effects

which cause differences on pressure distributions all over the ship surface (Woods Hole Oceanographic Institute 1952).

In this study thin flat plate, 0.5 mm thickness was used; therefore the resistance occurs due to the form of the model can be neglected due to negligibly small thickness to length ratio., and so the attached barnacles' bundles will affect only the frictional resistance of flat plate. In order to calculate the frictional resistance differences between the bare flat surface and the surface which covered with barnacles, the total resistance coefficients were obtained for each configuration within the defined speed range using the equation (4.2).

$$R_T = \frac{1}{2} \rho S C_T V^2 \quad (4.2)$$

where V is speed, C_T is the total resistance coefficient, S is the wetted surface area, and ρ is the density of water. The related water properties such as water density and kinematic viscosity at different temperatures for basic resistance calculation were taken from ITTC Recommended Procedures of Freshwater and Seawater properties, report code 7.5-02-01-03 (2011). With the assumptions mentioned above, Froude's hypothesis can be expressed by equation (4.3) at below, as indicated in Schultz (2007).

$$C_T = C_F(Re) + C_R(Fr) \quad (4.3)$$

The total resistance coefficient is equal to the sum of the frictional resistance coefficient, C_F , which is a function of Reynolds number, and residual resistance coefficient, C_R , which is a function of Froude number.

The ITTC 1957 formula is commonly used to calculate frictional resistance coefficients for both models and full-scale ships. However, as this formula is developed for ship and model correlation, it is not appropriate to use this formula for predicting frictional resistance of flat plates. Schoenherr (1932) re-assessed Froude's

original data by using Prandtl-von Karman theory and found an equation for C_F as a function of Reynolds number and the formulation of a skin friction line which can be used for smooth surfaces as shown in the equation (4.4).

$$\frac{0.242}{\sqrt{C_f}} = \log_{10}(Rn C_F) \quad (4.4)$$

Once the test results were obtained, as a first step, total drag coefficient (C_T) was calculated through general total drag equation as the density of water (ρ), wetted surface area (S) and speed (V) are defined. Then, the Karman - Schoenherr equation (4.4) was employed to calculate the frictional resistance coefficient (C_{FS}) of the reference plate (smooth plate). As C_{TS} is composed of C_{FS} and the residuary resistance coefficient (C_R), C_{RS} can be obtained by subtracting C_{FS} value from the C_{TS} value of the reference plate. The calculated C_{RS} value was taken as the C_{RR} value of all test surfaces since the roughness has a negligible effect on the residuary resistance. Therefore, the C_{FS} values calculated by Karman – Schoenherr equation represent frictional resistance coefficient in smooth condition whereas the C_F values, which were calculated by subtracting the C_R values from the C_{TR} values for the rough conditions represent the C_{FR} . The mathematical expression for this is presented in equations (4.5), (4.5) and (4.7).

$$C_{R_s} = C_{T_s} - C_{F_s} \quad (4.5)$$

$$C_{R_s} = C_{R_r} \quad (4.6)$$

$$C_{F_r} = C_{T_r} - C_{R_r} \quad (4.7)$$

where subscript S indicates smooth condition, whereas subscript R indicates the rough condition.

4.6 Repeatability and Uncertainty Estimates

The uncertainty estimates were made by using ITTC Recommended Procedures for Resistance, Uncertainty Analysis, and Example for Resistance test, report code 7.5-02-02-02 (2002b). Uncertainty is given in the form of general formula as the root of total squares of the uncertainties of total bias and precision limits.

$$(U_x)^2 = (B_x)^2 + (P_x)^2 \quad (4.8)$$

where U_x is the total uncertainty, B_x is the total bias limit, and P_x is the total precision limit. B_x occurs due to mismeasurement of devices used in an experiment such as thermometer and LVDT. It can be calculated by total squares of multiplication of partial derivative of considered quantity concerning variables and the bias which belong to this variable.

$$(B_x)^2 = \left(\frac{\partial x}{\partial t} B_t\right)^2 + \left(\frac{\partial x}{\partial y} B_y\right)^2 + \left(\frac{\partial x}{\partial z} B_z\right)^2 \dots \quad (4.9)$$

where x is a function of variables t , y and z as seen at below:

$$x = f(t, y, z) \quad (4.10)$$

The total precision limit P_x is caused by differences which can occur because of misalignment between the repeated tests. It can be calculated at the following equations.

$$P(x_M) = \frac{KSDev}{\sqrt{M}} \quad (4.11)$$

$$P(x_S) = KSDev \quad (4.12)$$

where M is the number of runs for which the precision limit is to be established, $SDev$ is the standard deviation established by multiple runs and K is equal to 2 according to the methodology of ITTC (2002b). Formulation of $SDev$ as below:

$$SDev = \left[\frac{\sum_{k=1}^M (x_k - x_{average})^2}{M - 1} \right]^{1/2} \quad (4.13)$$

The steps of uncertainty analysis can be found in ITTC (2002b). In this experiment, the uncertainty analysis has been done for two different speeds which represent low speed (1.857 m/s) and high speed (3.591 m/s) whose equal to Reynolds number of $\sim 2.6 \times 10^6$ and $\sim 5 \times 10^6$, respectively. The uncertainty limits for the three essential quantities C_T , C_F and ΔU^+ were presented as values of bias, precision, total uncertainty, and the change in percentage of whose quantities for all barnacle coverages configurations in two speeds. The analysis of uncertainty was tabulated Table 4-2, Table 4-3, and Table 4-4, respectively.

As shown in Table 4-2, the bias uncertainty in C_T ranged from $\pm 5.8\%$ at the lower Reynolds number to $\pm 1.66\%$ at the higher Reynolds number, whereas precision uncertainty in C_T ranged from $\pm 1.7\%$ at lower Reynolds number to $\pm 0.84\%$ at higher Reynolds number. The total uncertainty percentages in C_T are $\pm 6\%$ at low speed and $\pm 1.71\%$ at high speed.

The bias uncertainty in C_F ranged from $\pm 5\%$ at the lower Reynolds number to $\pm 1.46\%$ at the higher Reynolds number, whereas precision uncertainty in C_F ranged from $\pm 1.93\%$ at lower Reynolds number to $\pm 1.04\%$ at higher Reynolds number. The total uncertainty percentages in C_F are $\pm 5\%$ at low speed and $\pm 1.8\%$ at high speed.

When the total uncertainty limits for drag coefficients compared with the previous study of Schultz (2004), uncertainty limits at both studies are considered the same for low and high Reynolds number.

The bias uncertainty in ΔU^+ ranged from $\pm 14.6\%$ at lower Reynolds number to $\pm 3.6\%$ at higher Reynolds number while the precision uncertainty in ΔU^+ ranged from $\pm 0.35\%$ at lower Reynolds number to $\pm 0.85\%$ at higher Reynolds number. The total uncertainty for ΔU^+ is $\pm 14.64\%$ at low speed whereas $\pm 3.6\%$ at high speed. Moreover, results again can be compared with Schultz (2004). Comparatively having high error limits in ΔU^+ might be the consequence of the use of the indirect method, i.e. an overall

method that includes the regression equations (Demirel 2015). B, M and S symbols in Table 4.2 refer to the biggest, middle and smallest type configurations, whereas NS and Mix stand for natural settlement and mixed.

Table 4-2: Uncertainty limits in C_T

	Term	1.857 m/s		3.591 m/s	
		Value	% of C_T	Value	% of C_T
Reference plate	B _{CT}	6.484E-05	1.625	1.99068E-05	0.568
	P _{CT}	2.963E-05	0.743	2.96349E-05	0.846
	U _{CT}	7.129E-05	1.787	3.57003E-05	1.019
10% B-type	B _{CT}	6.644E-05	1.043	2.50056E-05	0.404
	P _{CT}	8.591E-06	0.135	9.45423E-06	0.153
	U _{CT}	6.699E-05	1.052	2.67332E-05	0.431
20% B-type	B _{CT}	6.793E-05	0.853	2.85551E-05	0.368
	P _{CT}	1.902E-05	0.239	1.71097E-05	0.221
	U _{CT}	7.055E-05	0.885	3.32887E-05	0.430
10% M-type	B _{CT}	9.94E-05	1.785	2.98396E-05	0.569
	P _{CT}	3.071E-06	0.055	2.50113E-05	0.475
	U _{CT}	9.945E-05	1.785	3.89355E-05	0.739
20% M-type	B _{CT}	9.891E-05	1.527	3.13246E-05	0.499
	P _{CT}	1.559E-05	0.241	1.64571E-05	0.262
	U _{CT}	0.0001001	1.545	3.53845E-05	0.563
40% M-type	B _{CT}	0.0001002	1.3013	3.34594E-05	0.442
	P _{CT}	2.539E-05	0.33	1.35432E-05	0.179
	U _{CT}	0.0001034	1.343	3.60964E-05	0.476
50% M-type	B _{CT}	9.995E-05	1.261	3.4026E-05	0.433
	P _{CT}	3.736E-05	0.472	1.03584E-05	0.132
	U _{CT}	0.0001067	1.347	3.55677E-05	0.452

	Term	Value	% of C _T	Value	% of C _T
10% S-type	B _{CT}	0.0002895	5.872	7.8191E-05	1.668
	P _{CT}	8.508E-05	1.711	1.75344E-05	0.374
	U _{CT}	0.0003017	6.069	8.01329E-05	1.711
20% S-type	B _{CT}	0.0002895	3.633	7.85686E-05	1.014
	P _{CT}	1.952E-05	0.346	2.67232E-05	0.496
	U _{CT}	0.0002901	5.148	8.29889E-05	1.540
40% S-type	B _{CT}	0.0002898	4.416	7.91002E-05	1.247
	P _{CT}	1.952E-05	0.346	2.67232E-05	0.496
	U _{CT}	0.0002904	5.153	8.34923E-05	1.549
50% S-type	B _{CT}	0.0002897	4.274	7.92682E-05	1.200
	P _{CT}	1.952E-05	0.346	2.67232E-05	0.496
	U _{CT}	0.0002904	5.153	8.36516E-05	1.552
10% Mix-type	B _{CT}	0.0002896	4.620	7.88928E-05	1.320
	P _{CT}	1.991E-05	0.318	8.51797E-06	0.143
	U _{CT}	0.0002903	4.638	7.93513E-05	1.329
20% Mix-type	B _{CT}	0.0002899	3.786	7.9943E-05	1.052
	P _{CT}	0.0002457	3.158	3.21388E-05	0.424
	U _{CT}	0.00038	4.885	8.61614E-05	1.137
40% Mix-type	B _{CT}	0.0002904	2.998	8.15177E-05	0.855
	P _{CT}	0.0001634	1.701	2.96646E-05	0.312
	U _{CT}	0.0003332	3.468	8.67475E-05	0.912
50% Mix-type	B _{CT}	0.0002906	2.846	8.20899E-05	0.817
	P _{CT}	3.314E-05	0.324	5.2486E-05	0.520
	U _{CT}	0.0002925	2.859	9.74347E-05	0.966

	Term	Value	% of C _T	Value	% of C _T
10% NS Mix-type	B _{CT}	0.00028932	4.503	7.89237E-05	1.266
	P _{CT}	7.49726E-05	1.153	3.99497E-06	0.064
	U _{CT}	0.000298876	4.597	7.90247E-05	1.267
20% NS Mix-type	B _{CT}	0.000289675	3.633	8.00001E-05	1.030
	P _{CT}	7.47917E-05	0.932	1.509E-05	0.194
	U _{CT}	0.000299175	3.726	8.14109E-05	1.046
40% NS Mix-type	B _{CT}	0.000290236	2.895	8.17405E-05	0.834
	P _{CT}	8.75999E-05	0.873	5.51292E-05	0.561
	U _{CT}	0.000303168	3.020	9.85938E-05	1.003
50% NS Mix-type	B _{CT}	0.000290259	2.767	8.22409E-05	0.794
	P _{CT}	4.26417E-05	0.408	4.46273E-05	0.432
	U _{CT}	0.000293375	2.804	9.3569E-05	0.905

Table 4-3 Uncertainty limits in C_F

	Term	1.857 m/s		3.591 m/s	
		Value	% of C_F	Value	% of C_F
Reference plate	B _{CF}	6.74846E-05	1.812	2.29162E-05	0.691
	P _{CF}	3.12003E-05	0.838	9.41914E-06	0.191
	U _{CF}	7.43481E-05	1.997	2.47765E-05	0.747
10% B-type	B _{CF}	9.27166E-05	1.519	3.17279E-05	0.528
	P _{CF}	8.59081E-06	0.141	9.45423E-06	0.153
	U _{CF}	9.31137E-05	1.526	3.17279E-05	0.528
20% B-type	B _{CF}	9.33501E-05	1.212	3.36156E-05	0.445
	P _{CF}	1.90198E-05	0.247	1.71097E-05	0.221
	U _{CF}	9.5268E-05	1.237	3.77194E-05	0.499
10% M-type	B _{CF}	0.000139914	3.013	4.11464E-05	0.888
	P _{CF}	3.07141E-06	0.066	2.50113E-05	0.540
	U _{CF}	0.000139948	3.014	4.81518E-05	1.040
20% M-type	B _{CF}	0.000139564	2.514	4.22356E-05	0.746
	P _{CF}	2.68406E-05	0.484	1.64571E-05	0.291
	U _{CF}	0.000142122	2.560	4.53286E-05	0.801
40% M-type	B _{CF}	0.000140509	2.073	4.38423E-05	0.631
	P _{CF}	2.53867E-05	0.375	1.35432E-05	0.195
	U _{CF}	0.000142784	2.107	4.58865E-05	0.661
50% M-type	B _{CF}	0.000140303	2.004	4.42762E-05	0.612
	P _{CF}	3.73589E-05	0.534	1.03584E-05	0.143
	U _{CF}	0.000145192	2.074	4.54718E-05	0.628

	Term	Value	% of C _F	Value	% of C _F
10% S-type	B _{CF}	0.000139224	3.159	4.05752E-05	0.988
	P _{CF}	8.50798E-05	1.931	1.75344E-05	0.427
	U _{CF}	0.000163162	3.702	4.42019E-05	1.076
20% S-type	B _{CF}	0.000139412	2.828	4.12643E-05	0.880
	P _{CF}	8.50798E-05	1.726	1.75344E-05	0.374
	U _{CF}	0.000163323	3.313	4.48352E-05	0.956
40% S-type	B _{CF}	0.000305984	5.067	8.39957E-05	1.458
	P _{CF}	9.80601E-06	0.162	5.97051E-05	1.036
	U _{CF}	0.000306141	5.069	0.000103053	1.788
50% S-type	B _{CF}	0.000305971	4.890	8.4154E-05	1.396
	P _{CF}	1.16787E-06	0.019	6.26081E-05	1.039
	U _{CF}	0.000305973	4.890	0.000104889	1.740
10% Mix-type	B _{CF}	0.000409403	7.061	0.000110873	2.012
	P _{CF}	1.99124E-05	0.343	8.51797E-06	0.155
	U _{CF}	0.000409887	7.069	0.0001112	2.018
20% Mix-type	B _{CF}	0.000409625	5.699	0.000111623	1.565
	P _{CF}	0.000245664	3.418	3.21388E-05	0.450
	U _{CF}	0.000477644	6.645	0.000116158	1.628
40% Mix-type	B _{CF}	0.000409946	4.448	0.000112756	1.243
	P _{CF}	0.000163387	1.773	2.96646E-05	0.327
	U _{CF}	0.000441306	4.789	0.000116593	1.286
50% Mix-type	B _{CF}	0.000410073	4.210	0.00011317	1.182
	P _{CF}	3.31381E-05	0.340	5.2486E-05	0.548
	U _{CF}	0.00041141	4.223	0.000124749	1.303

	Term	Value	% of C _F	Value	% of C _F
10% NS Mix-type	B _{CF}	0.000409184	6.954	0.000110895	1.952
	P _{CF}	7.49726E-05	1.274	3.99497E-06	0.070
	U _{CF}	0.000415996	7.070	0.000110967	1.953
20% NS Mix-type	B _{CF}	0.000409625	5.511	0.000111623	1.547
	P _{CF}	7.56601E-05	1.018	1.509E-05	0.209
	U _{CF}	0.000416554	5.605	0.000112638	1.561
40% NS Mix-type	B _{CF}	0.000409833	4.296	0.000112917	1.210
	P _{CF}	4.99856E-05	0.524	2.96646E-05	0.318
	U _{CF}	0.00041287	4.328	0.000116749	1.251
50% NS Mix-type	B _{CF}	0.000409849	3.873	0.00011328	1.093
	P _{CF}	3.31381E-05	0.313	5.2486E-05	0.506
	U _{CF}	0.000411187	3.886	0.000124848	1.205

Table 4-4: Uncertainty limits in ΔU^+

	Term	1.857 m/s		3.591 m/s	
		Value	% of ΔU^+	Value	% of ΔU^+
10% B-type	$B_{\Delta U^+}$	0.145944283	2.320	0.051591138	0.65885
	$P_{\Delta U^+}$	8.59081E-06	0.00014	9.45423E-06	0.15260
	$U_{\Delta U^+}$	0.145944283	2.3203	0.051591138	0.65885
20% B-type	$B_{\Delta U^+}$	0.105338353	1.1765	0.039677198	0.37876
	$P_{\Delta U^+}$	1.90198E-05	0.00021	1.71097E-05	0.22079
	$U_{\Delta U^+}$	0.105338355	1.1765	0.039677202	0.37876
10% M-type	$B_{\Delta U^+}$	0.326974031	5.3403	0.096736359	1.29610
	$P_{\Delta U^+}$	3.07141E-06	0.00005	2.50113E-05	0.00034
	$U_{\Delta U^+}$	0.326974031	5.3403	0.096736362	1.29610
20% M-type	$B_{\Delta U^+}$	0.478034699	5.6755	0.14156582	1.49046
	$P_{\Delta U^+}$	2.68406E-05	0.00032	1.64571E-05	0.00017
	$U_{\Delta U^+}$	0.4780347	5.6755	0.141565821	1.49046
40% M-type	$B_{\Delta U^+}$	0.190085646	1.84217	0.057581628	0.49578
	$P_{\Delta U^+}$	2.53867E-05	0.32962	3.02836E-05	0.39936
	$U_{\Delta U^+}$	0.190085648	1.8422	0.057581636	0.49578
50% M-type	$B_{\Delta U^+}$	0.181117633	1.70411	0.054887148	0.45688
	$P_{\Delta U^+}$	2.68406E-05	0.00025	1.64571E-05	0.00014
	$U_{\Delta U^+}$	0.181117635	1.70411	0.054887151	0.45688

	Term	Value	% of ΔU^+	Value	% of ΔU^+
10% S-type	$B_{\Delta U^+}$	0.351145224	14.643	0.113575683	3.60712
	$P_{\Delta U^+}$	8.50798E-05	0.00355	1.75344E-05	0.00056
	$U_{\Delta U^+}$	0.351145235	14.643	0.113575684	3.60712
20% S-type	$B_{\Delta U^+}$	0.282527247	6.64	0.091507802	1.76107
	$P_{\Delta U^+}$	8.50798E-05	0.002	1.75344E-05	0.00034
	$U_{\Delta U^+}$	0.28252726	6.64	0.091507803	1.76107
40% S-type	$B_{\Delta U^+}$	0.488490663	7.862	0.143635172	1.94920
	$P_{\Delta U^+}$	1.95192E-05	0.3464	4.6286E-05	0.85866
	$U_{\Delta U^+}$	0.488490664	7.86174	0.14363518	1.94920
50% S-type	$B_{\Delta U^+}$	0.464119966	6.968	0.134885678	1.67289
	$P_{\Delta U^+}$	1.95192E-05	0.3464	4.6286E-05	0.85866
	$U_{\Delta U^+}$	0.464119967	6.968	0.134885685	1.67289
10% Mix-type	$B_{\Delta U^+}$	0.693186912	11.98062	0.202163064	2.93753
	$P_{\Delta U^+}$	8.50798E-05	0.00147	1.75344E-05	0.00025
	$U_{\Delta U^+}$	0.693186917	11.98062	0.202163065	2.93753
20% Mix-type	$B_{\Delta U^+}$	0.509025214	6.19776	0.140332541	1.42388
	$P_{\Delta U^+}$	8.50798E-05	0.00104	1.75344E-05	0.00018
	$U_{\Delta U^+}$	0.509025221	6.19776	0.140332542	1.42388
40% Mix-type	$B_{\Delta U^+}$	0.357441043	3.27421	0.100768398	0.80785
	$P_{\Delta U^+}$	1.95192E-05	0.34635	4.6286E-05	0.85866
	$U_{\Delta U^+}$	0.357441044	3.27421	0.100768409	0.80785
50% Mix-type	$B_{\Delta U^+}$	0.330602136	2.87764	0.093655344	0.71825
	$P_{\Delta U^+}$	1.95192E-05	0.34635	4.6286E-05	0.85866
	$U_{\Delta U^+}$	0.330602137	2.87764	0.093655355	0.71825

	Term	Value	% of ΔU^+	Value	% of ΔU^+
10% NS Mix-type	$B_{\Delta U^+}$	0.678272839	11.42881	0.193458002	2.67453
	$P_{\Delta U^+}$	8.50798E-05	0.00143	1.75344E-05	0.00024
	$U_{\Delta U^+}$	0.678272844	11.42881	0.193458003	2.67453
20% NS Mix-type	$B_{\Delta U^+}$	0.485183984	5.61478	0.138105567	1.37670
	$P_{\Delta U^+}$	8.50798E-05	0.00098	1.75344E-05	0.00017
	$U_{\Delta U^+}$	0.485183991	5.61478	0.138105568	1.37670
40% NS Mix-type	$B_{\Delta U^+}$	0.340378476	3.01254	0.096801374	0.75665
	$P_{\Delta U^+}$	1.95192E-05	0.34635	4.6286E-05	0.85866
	$U_{\Delta U^+}$	0.340378477	3.01254	0.096801385	0.75665
50% NS Mix-type	$B_{\Delta U^+}$	0.294228334	2.38406	0.08361639	0.60260
	$P_{\Delta U^+}$	1.95192E-05	0.34635	4.6286E-05	0.85866
	$U_{\Delta U^+}$	0.294228335	2.38406	0.083616403	0.60260

4.7 Results

The results of the resistance experiments been presented in this section. The resistance coefficients C_T , C_F and the change in C_T and C_F coefficients with respect to the reference plate (plain surfaces of each configuration) were illustrated in the graphs. The C_T and C_F were calculated more extensively, as explained in Section 4.5, and the results are discussed in details through corresponding figures.

4.7.1 Total Resistance Coefficients

C_T values of all surfaces were calculated for ten different speeds by using equation (4.2) in Section 4.5. The increases in the C_T values respect to the reference plates (plain surfaces) were tabulated in Table 4-5 and Table 4-6. The comparisons of C_T values were illustrated in Figure 4-18. The figure showed that barnacle sizes and coverage areas have a significant effect on total resistance coefficients (C_T). As expected, the configurations which have higher barnacle heights and coverage rates caused a greater change in the C_T values with respect to reference plates. In addition, Figure 4-18 indicated that the natural settlement (NS) mixed configurations showed higher increases in C_T compared to standard settlement mixed configurations. The configurations were listed in order from the one that caused the highest change to the lowest change.

As given in Table 4-5, Table 4-6 and as shown in Figure 4-18, NS Mixed 50% caused the highest percentage change in the C_T values in a range from 163.23% to 191.76% with an average increase of 180.07% compared to reference plate of NS Mixed. This followed by Mixed 50% which caused an increase in the C_T values with an increase of 145.25% at the lowest speed, 177.13% at the highest speed and an average increase of 154.76% with respect to the reference plate of the NS Mixed. From Figure 4-18 it is evident that NS Mixed 40% caused the third-highest change in the C_T values from 139.7% at the lowest speed and 164.44% at the highest speed, with an average increase of 154.76% compared to reference plate. The following configuration is Mixed 40%, which changes C_T , ranging from 122.45% to 155.68% at the lowest and highest speeds, respectively. The average increase in C_T due to Mixed 40% configuration is 144.25% compared to the reference plate.

The increases in C_T due to the Biggest 20% were calculated to be in a range from 100.27% to 115.32% at the lowest and highest speeds, respectively. Whereas it was calculated that Biggest 20% caused an average increase of 110.3% in C_T compared to the reference plate. The results indicated that the following configurations are Middle 50% and NS Mixed 20%. The increases in C_T due to Middle 50% range from 90.37% to 115.25% with an average increase of 105.06% whereas these numbers altered to 92.61%, 109.65% and 103.04% for NS Mixed 20%.

As can be seen from Figure 4-18, following configurations are Middle 40% and Mixed 20% with increases of 84.35% and 77.93% at lowest speeds, 104.38% and 101.94% at highest speeds, respectively. In addition, Middle 40% caused an average increase of 97.52% whereas this number altered to 94.09% for Mixed 20%. It is seen from the comparison in Figure 4-18. Smallest 50% and Biggest 10% are the following configurations causing increases to range from 65.54% to 81.11% and from 61.11% to 72.31% respectively. Besides, Smallest 50% and Biggest 10% caused average increases of 74.48% and 68.70% with respect to the reference plate.

Table 4-5, Table 4-6 and Figure 4-18 jointly show that the increases in C_T caused by Middle 20% and NS Mixed 10% are very close to each other with average increases of 64.93% and 64.37%, respectively. The increases in C_T due to Middle 20% and NS Mixed 10% were calculated to be 57.03% and 57.36% at the lowest speed and 69.96% and 68.78% at the highest speeds, respectively. Smallest 40% and Mixed 10% caused changes in C_T values, with increases ranging from 53.89% to 67.18% and from 45.83% to 60.07% respectively. The average increases in C_T for these configurations are 61.96% and 55.26%.

As can be seen from Figure 4-18 the configurations which have comparatively less effect can be listed as Smallest 20%, Middle 10% and Smallest 10% with increases of 41.44%, 36.15% and 23.70 at the lowest speed whereas these numbers altered to 43.74%, 41.82% and 24.73% at the highest speed respectively. Moreover, the average increases in the C_T for these configurations are 42.52%, 39.60% and 24.62% respectively.

Table 4-5 Percentage increase in the C_T values of test surfaces with respect to reference plate (Smallest, Middle and Biggest)

Speed m/s	Percentage increase in C_T (%) with respect to Plain Surfaces of each test configuration									
	Smallest 10%	Smallest 20%	Smallest 40%	Smallest 50%	Middle 10%	Middle 20%	Middle 40%	Middle 50%	Biggest 10%	Biggest 20%
1.5	23.70	41.44	53.89	69.53	36.15	57.23	84.35	91.95	61.11	100.27
1.857	20.37	37.83	56.21	65.54	35.31	57.03	87.12	90.37	63.17	104.16
3.287	25.99	45.57	65.74	78.26	42.17	69.04	103.54	113.18	72.13	113.66
2.131	24.79	41.90	59.41	72.15	36.20	61.64	92.59	98.06	65.54	105.97
3.591	24.73	43.74	64.53	75.79	41.82	69.30	104.38	112.15	72.15	115.32
3.013	26.97	45.23	67.18	81.11	43.00	69.96	103.72	110.98	70.83	113.42
2.435	23.76	40.30	58.78	72.39	38.79	62.95	95.66	101.83	69.04	108.61
3.45	25.75	43.91	65.66	78.36	42.33	69.17	105.11	115.25	72.31	115.94
3.14	25.52	44.82	66.86	78.77	41.27	68.73	102.47	112.26	71.23	114.50
2.739	24.59	40.51	61.35	72.90	39.00	64.24	96.26	104.58	69.46	111.15
Average	24.62	42.52	61.96	74.48	39.60	64.93	97.52	105.06	68.70	110.30

Table 4-6 Percentage increase in the C_T values of test surfaces with respect to reference plate (Mixed and Ns Mixed)

Percentage increase in C_T (%) with respect to Plain Surfaces of each test configuration								
Speed m/s	Mixed 10%	Mixed 20%	Mixed 40%	Mixed 50%	NS Mixed 10%	NS Mixed 20%	NS Mixed 40%	NS Mixed 50%
1.5	45.83	77.93	122.45	145.25	57.36	92.61	139.70	163.23
1.857	50.24	86.42	132.22	154.49	60.26	96.17	144.73	169.14
3.287	59.46	99.85	152.55	178.67	67.29	106.90	160.50	187.02
2.131	55.64	92.52	144.34	166.05	62.37	98.63	148.30	172.19
3.591	57.94	99.38	151.72	177.13	68.78	109.65	164.44	191.76
3.013	57.88	99.35	151.43	176.13	65.00	106.68	158.67	183.74
2.435	55.26	93.67	142.08	165.95	62.91	101.20	153.28	176.70
3.45	60.07	101.94	155.68	180.05	67.87	108.51	163.11	189.18
3.14	58.27	99.49	151.50	176.16	67.00	106.42	159.31	184.96
2.739	51.98	90.39	138.53	164.51	64.83	103.66	155.52	182.77
Average	55.26	94.09	144.25	168.44	64.37	103.04	154.76	180.07

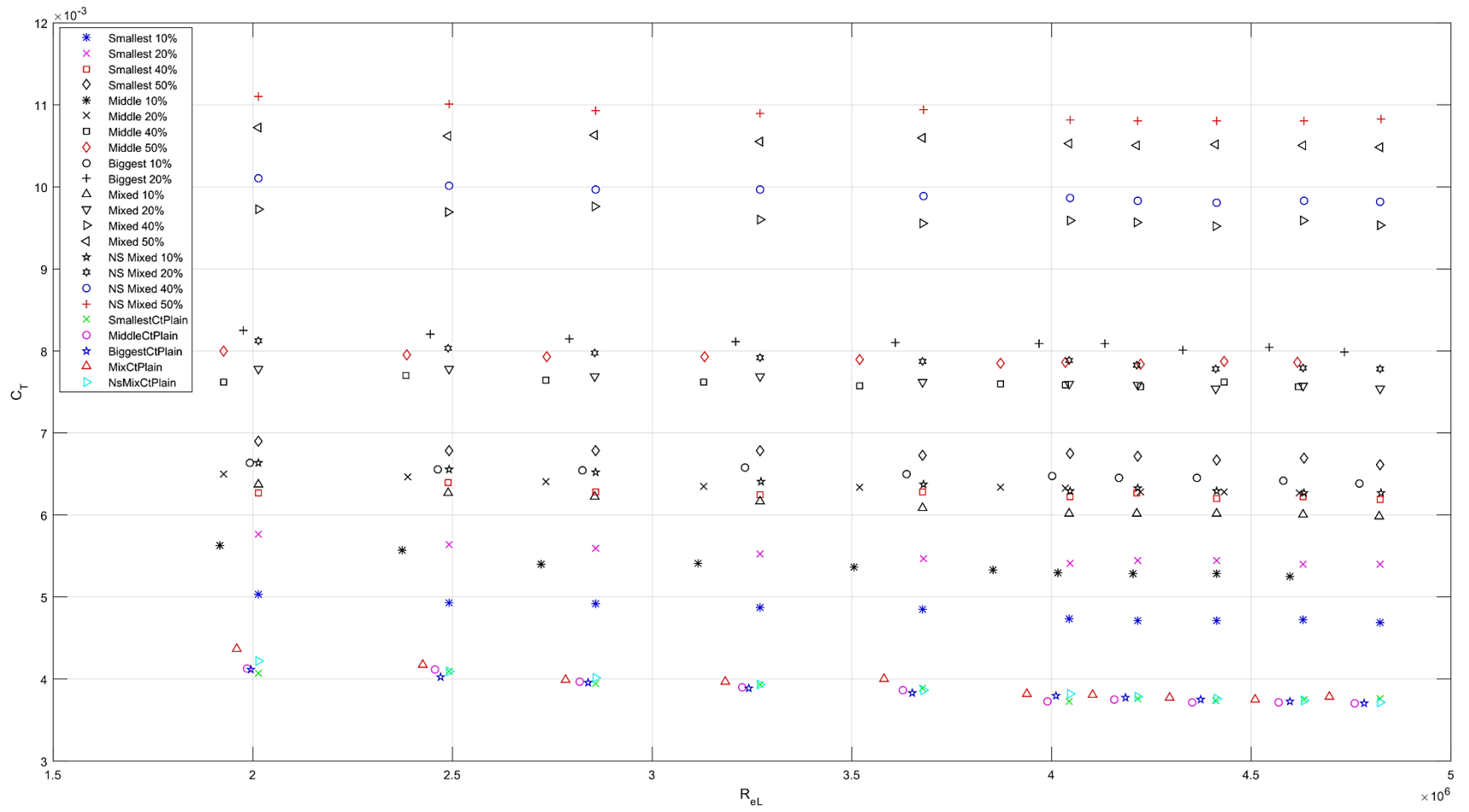


Figure 4-18 C_T values of test surfaces

4.7.2 Frictional Resistance Coefficients

Frictional resistance coefficient (C_F) values of all test surfaces were calculated, as stated in Section 4.5. The C_F values were illustrated in Figure 4.19, together with Schoenherr (1932), representing the reference plate. The changes in percentages of C_F values of test configurations respect to the reference were tabulated in Table 4-7 and Table 4-8.

As expected, the order for C_T values of configurations from highest to lowest increase compared to reference plate did not change for C_F values. It can be seen that NS Mixed 50% caused the most significant effect on the C_F , with an average increase of 199.29% with respect to the reference plate. Mixed 50% followed this with an average increase of 190.15%. NS Mixed 40% caused the third largest change in C_F with an average increase of 171.17% and this followed by Mixed 40% with an average increase of 162.18%.

The results presented in Table 4-7, Table 4-8 and the Figure 4-19 indicates that following configurations are in descending order of effect: Biggest 20% (on average 119.31%), Middle 50% (on average 115.97%), NS Mixed 20% (on average 113.81%), Middle 40% (on average 107.81), Mixed 20% (on average 105.76%), Smallest 50% (on average 78.25%), Biggest 10% (on average 75.13%), Middle 20% (on average 72.32), NS Mixed 10% (on average 69.92%), Smallest 40% (on average 69.03%), Mixed 10% (on average 62.07%), Middle 10% (on average 43.97), Smallest 20% (on average 42.95) and Smallest 10% (on average 22.95).

As the main aim of this thesis to investigate the effect of barnacle on the frictional resistance, in this section C_F values are analysed thoroughly under three sections such as the effect of barnacle height, effect of coverage area and effect of settlement pattern.

Table 4-7 Percentage increase in the C_F values of test surfaces with respect to reference plate (Smallest, Middle and Biggest)

Speed m/s	Percentage change in C_F (%) with respect to Plain Surfaces of each test configuration									
	Smallest 10%	Smallest 20%	Smallest 40%	Smallest 50%	Middle 10%	Middle 20%	Middle 40%	Middle 50	Biggest 10%	Biggest 20%
1.5	18.91	39.82	57.08	69.40	38.86	61.71	90.34	97.43	62.41	102.74
1.857	18.42	37.64	62.28	68.13	40.07	65.17	97.20	104.40	65.87	106.96
3.287	24.85	46.61	73.75	82.94	46.82	76.86	114.59	122.86	80.67	125.43
2.131	22.97	41.54	64.98	74.38	39.79	67.93	101.39	109.55	69.24	113.16
3.591	23.91	45.50	73.87	81.85	47.37	78.70	117.88	126.59	82.85	128.17
3.013	25.46	45.37	73.98	84.50	47.17	76.97	113.45	121.14	78.97	124.68
2.435	22.35	40.70	65.73	76.31	42.86	69.77	105.36	114.58	75.58	117.58
3.45	24.89	45.32	74.55	84.07	47.35	77.61	117.24	124.94	80.93	128.17
3.14	24.25	45.63	74.80	83.26	45.82	76.53	113.41	121.96	78.95	125.22
2.739	23.50	41.33	69.33	77.63	43.58	71.98	107.20	116.20	75.81	120.95
Average	22.95	42.95	69.03	78.25	43.97	72.32	107.81	115.97	75.13	119.31

Table 4-8 Percentage increase in the C_F values of test surfaces with respect to reference plate (Mixed and Ns Mixed)

Speed m/s	Percentage change in C_F (%) with respect to Plain Surfaces of each test configuration							
	Mixed 10%	Mixed 20%	Mixed 40%	Mixed 50%	NS Mixed 10%	NS Mixed 20%	NS Mixed 40%	NS Mixed 50%
1.5	51.81	88.11	138.45	165.64	59.01	98.29	149.61	174.52
1.857	56.34	96.91	148.27	173.75	63.72	104.09	157.50	183.78
3.287	66.64	111.92	170.99	200.72	74.50	119.73	179.67	209.39
2.131	61.22	101.80	158.82	182.17	68.00	108.97	163.87	192.42
3.591	66.16	113.48	173.26	202.98	74.61	121.32	182.69	211.91
3.013	64.61	110.90	169.04	197.01	72.03	119.47	177.50	206.11
2.435	61.85	104.83	159.02	186.64	68.93	112.33	168.94	196.12
3.450	67.55	114.62	175.05	202.72	74.77	121.19	182.31	210.58
3.140	65.32	111.53	169.83	198.52	74.59	119.55	178.64	208.74
2.739	59.25	103.55	159.06	191.38	69.03	113.18	170.94	199.37
Average	62.07	105.76%	162.18%	190.15%	69.92%	113.81%	171.17%	199.29%

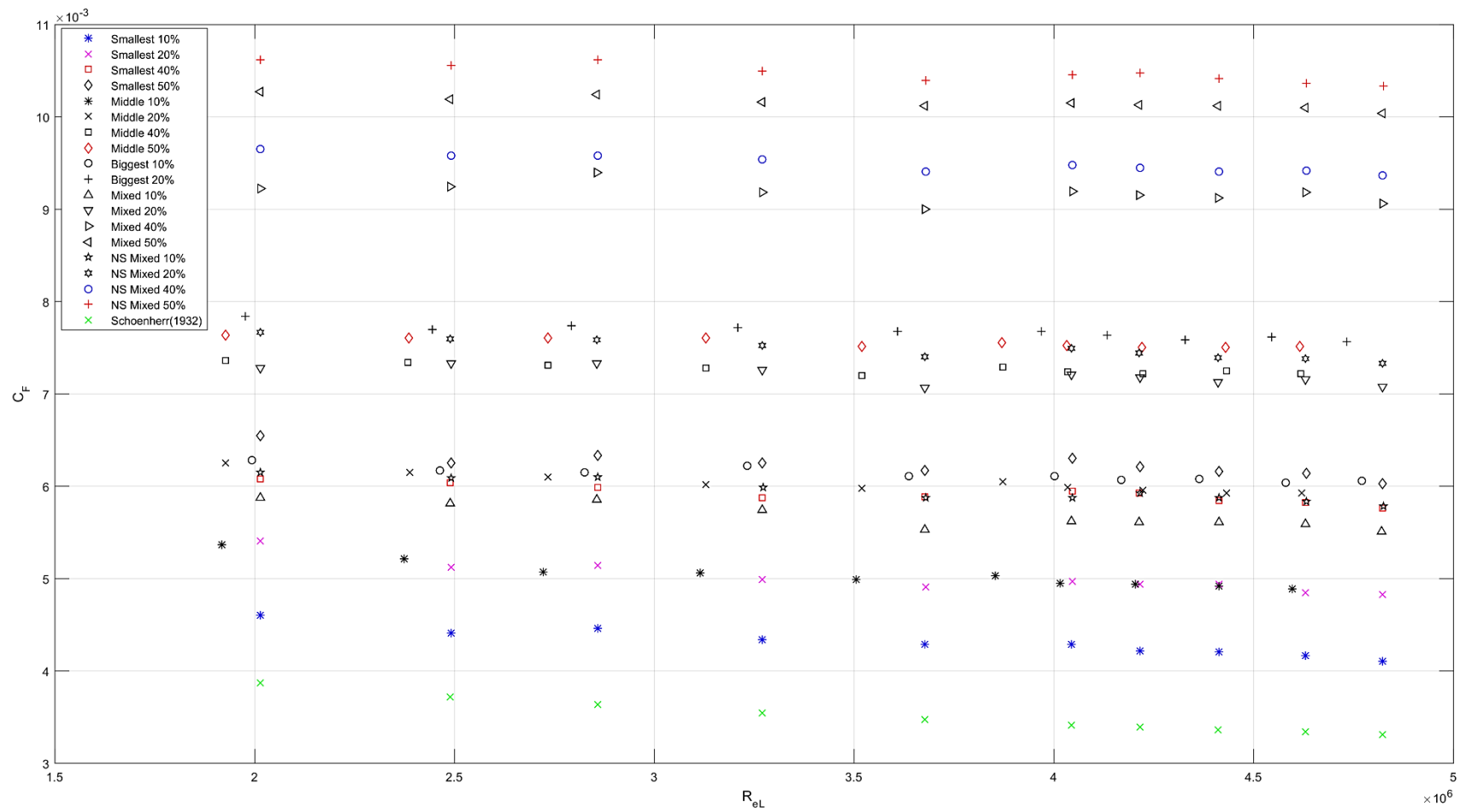


Figure 4-19 C_F values of all test surfaces

4.7.2.1 Effect of Barnacle Height on Frictional Resistance Coefficient

The effect of barnacle height on the C_F is shown by Figure 4-20, Figure 4-21, Figure 4-22 and Figure 4-23 which demonstrate C_F values for 10%, 20%, 40% and 50% configurations together with Schoenherr (1932) values. NS Mixed configurations were not included in this analysis since it does not have the same settlement with other configurations. The percentage changes in the C_F values with respect to the reference plate are given in Table 4-7 and Table 4-8.

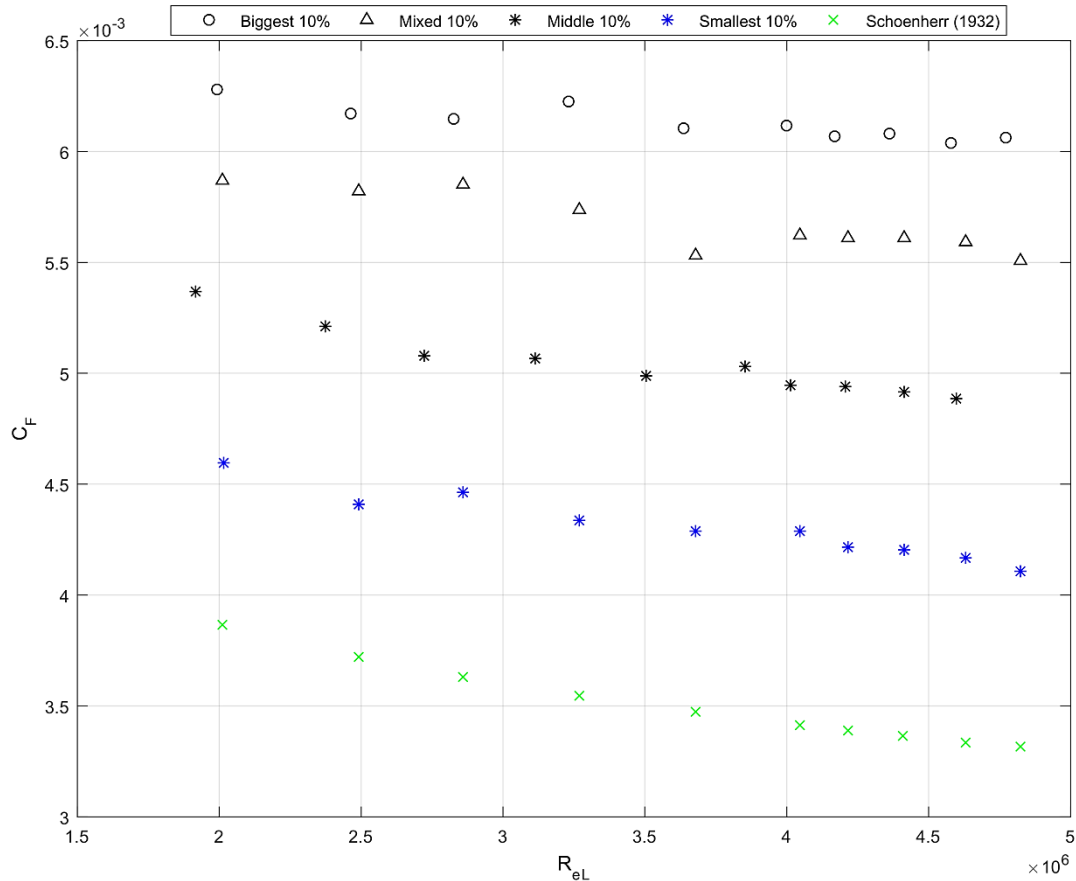


Figure 4-20: C_F comparison for 10% coverage area

Table 4-7, Table 4-8 and Figure 4-20 jointly indicate that the Biggest 10% caused the greatest change between the configurations of 10% coverage with an increase of 62.41% at the lowest speed and an increase of 82.85% at the highest speed (on average 75.13%). This was followed by Mixed 10% with increases ranging from 51.81% to 67.55% (on average 62.07%). The range of percentage changes in the C_F due to Middle 10% and Smallest 10% are from 38.86% to 47.37% (on average 43.97%) and from

18.42% to 25.46% (on average 22.95%) with respect to the reference plate, respectively.

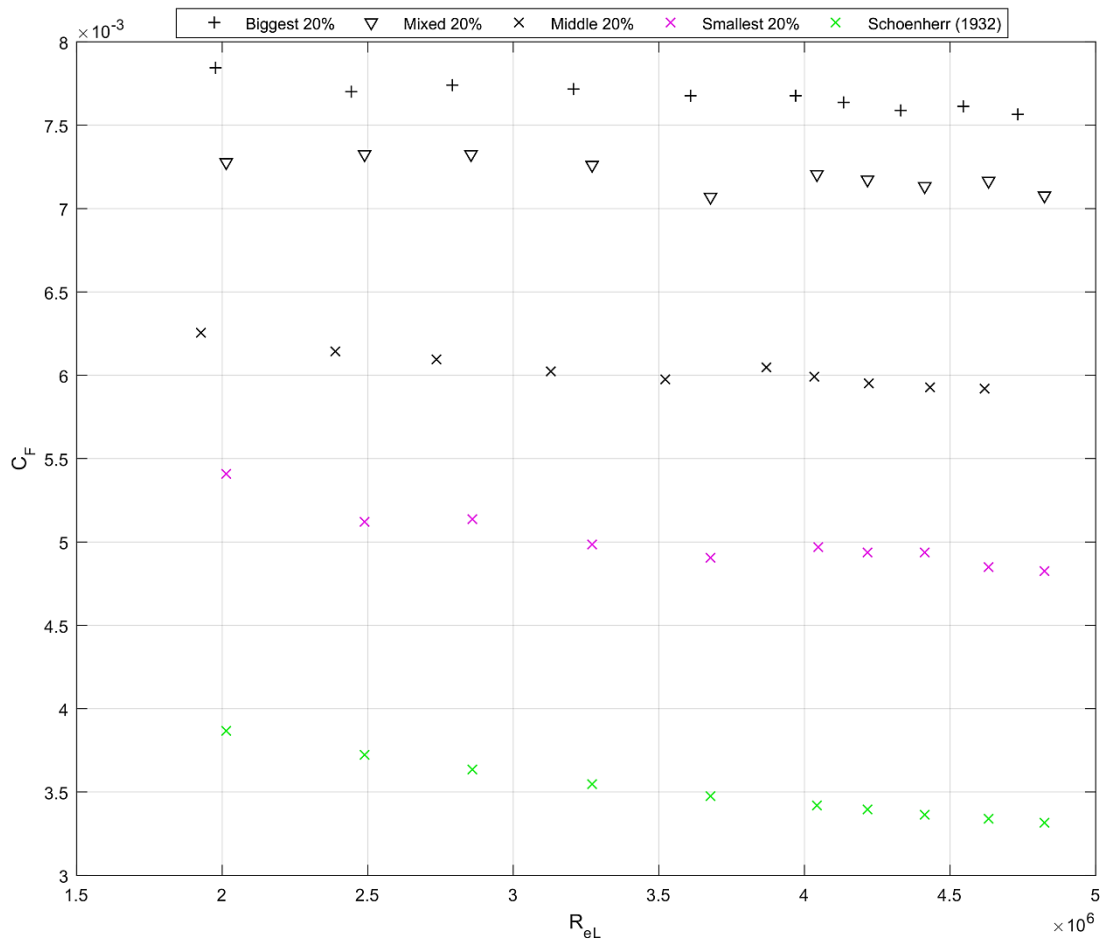


Figure 4-21 C_F comparison for 20% coverage area.

As it can be seen in Figure 4-21, Table 4-7 and Table 4-8, Biggest 20% caused the greatest change in the C_F values with an average increase of 119.31% between the configurations of 20% coverage. This was followed by Mixed 20%, which increased C_F values 105.76% on average with respect to the reference plate. These values altered to 72.32% and 42.95% for the configurations of Middle 20% and Smallest 20%, respectively.

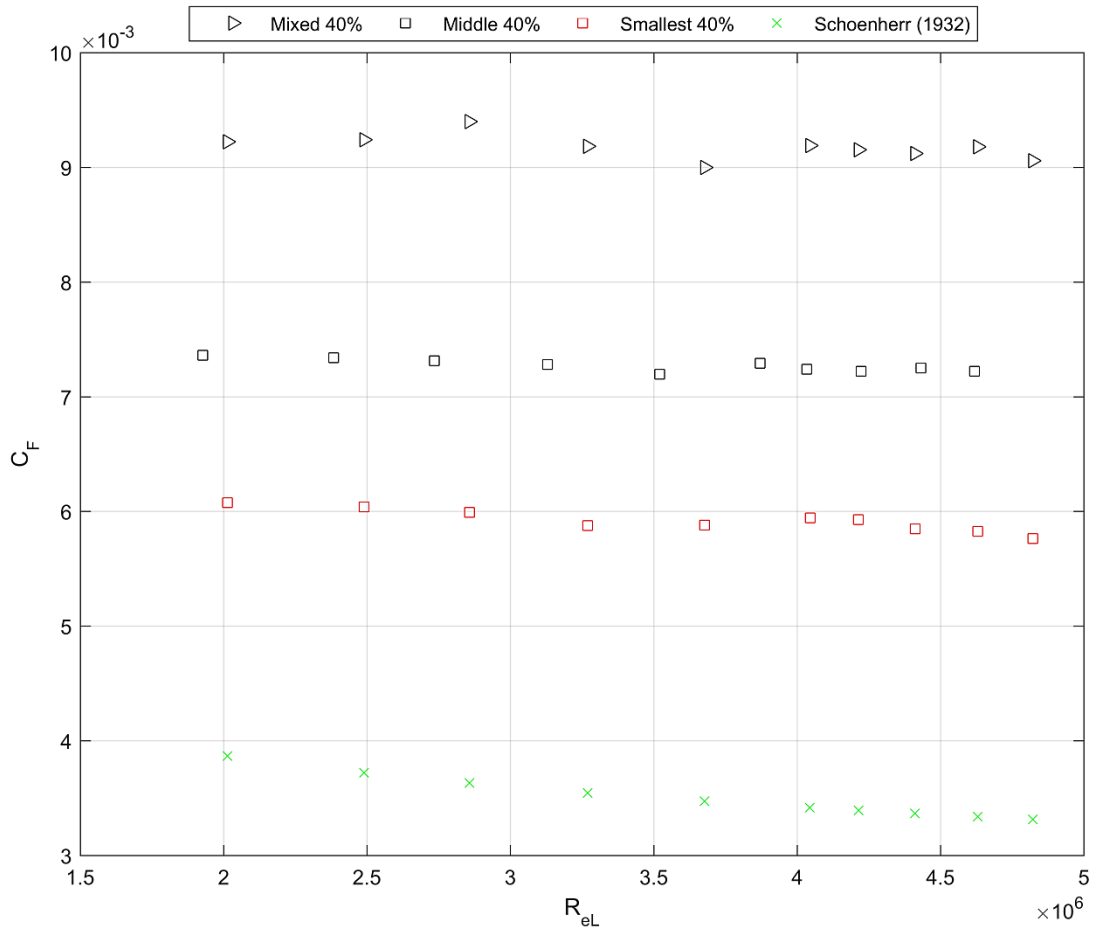


Figure 4-22 C_F comparison for 40% coverage area.

As shown in Figure 4-22, Table 4-7 and Table 4-8 the highest change in the C_F between 40% configurations caused by Mixed 40% with an increase of 138.45% at Reynolds number of $\sim 2 \times 10^{-6}$ and increase of 173.26% at Reynolds number of $\sim 4.8 \times 10^{-6}$. These values altered to 90.34% and 57.08% at the lowest Reynolds number and 117.88% and 73.87% at highest Reynolds number for Middle 40% and Smallest 40%, respectively.

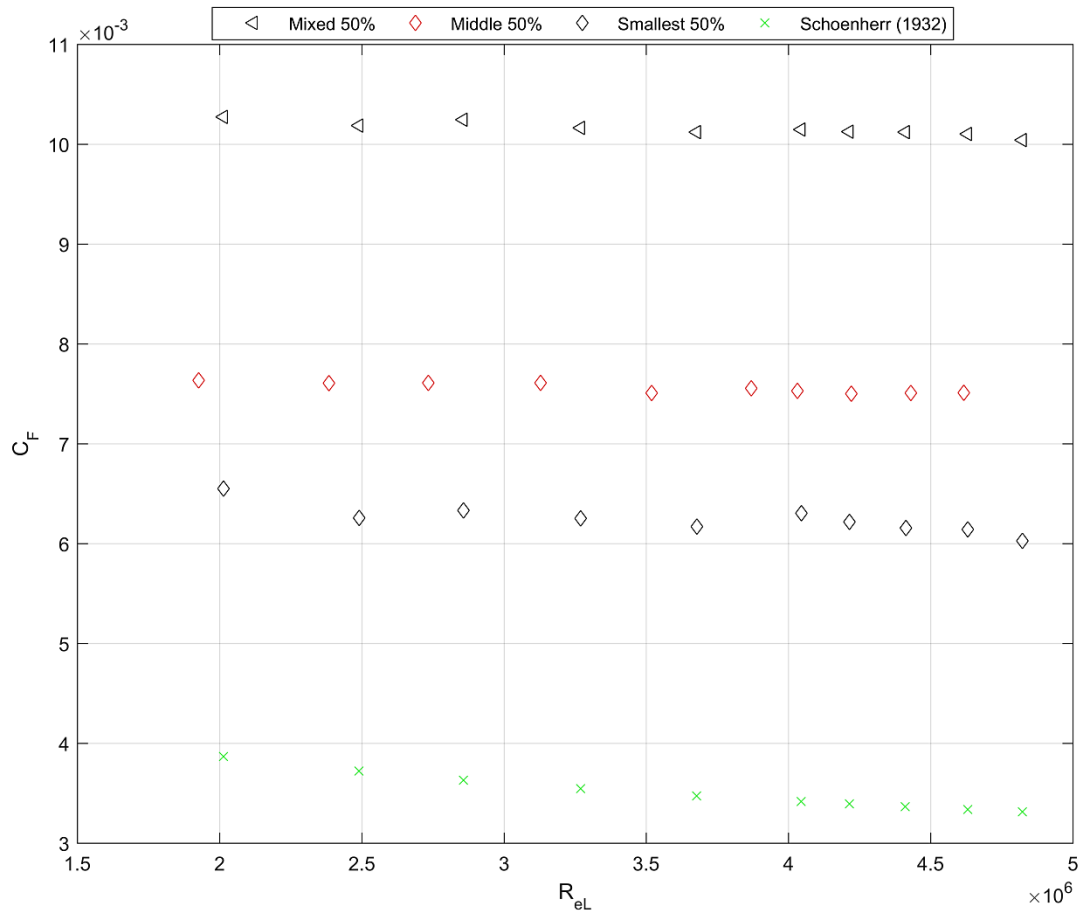


Figure 4-23 C_F comparison for 50% coverage area

Table 4-7, Table 4-8 and Figure 4-23 jointly show that Mixed 50% increased the C_F values with a 165.64% at the lowest Reynolds number and 202.98% at the highest Reynolds number compared to reference plate. This was followed by Middle 50% and Smallest 50% with an increase of 97.43% and 69.4% at the lowest Reynolds number whereas these numbers changed to 126.59% and 84.5% at the highest Reynolds number, respectively.

The results of the analysis indicate that barnacle size significantly affects the C_F values. The biggest changes in the frictional resistance are caused by the Biggest configurations. Mixed configurations are ranked as the second configurations, which caused the highest increase in the C_F values. It is interesting to note that the effect of increasing barnacle height outweighs the effect of increasing coverage area. For instance, 50% Smallest configuration caused an average of 78.25% increase in the frictional resistance, while Biggest type configuration caused an average of 75.13% with an only 10% surface coverages. It is important to note that although the mixed

configuration includes evenly distributed three different sized barnacles together, the effect of big sized barnacles on the frictional resistance overweighs the others. Figure 4-20 and Figure 4-21 jointly demonstrate that C_F values of mixed configurations are comparatively close to the values of the biggest configurations. It is important to note that results show consistency with Schultz's hypothesis on selecting the largest roughness height for developing the scaling parameter for the surfaces covered with barnacles (Schultz 2004).

4.7.2.2 Effect of Barnacle Coverage Area on Frictional Resistance

As seen and expected from Figure 4-19, the coverage area has a substantial effect on the frictional resistance and change in the frictional resistance rises with the increase in the coverage area.

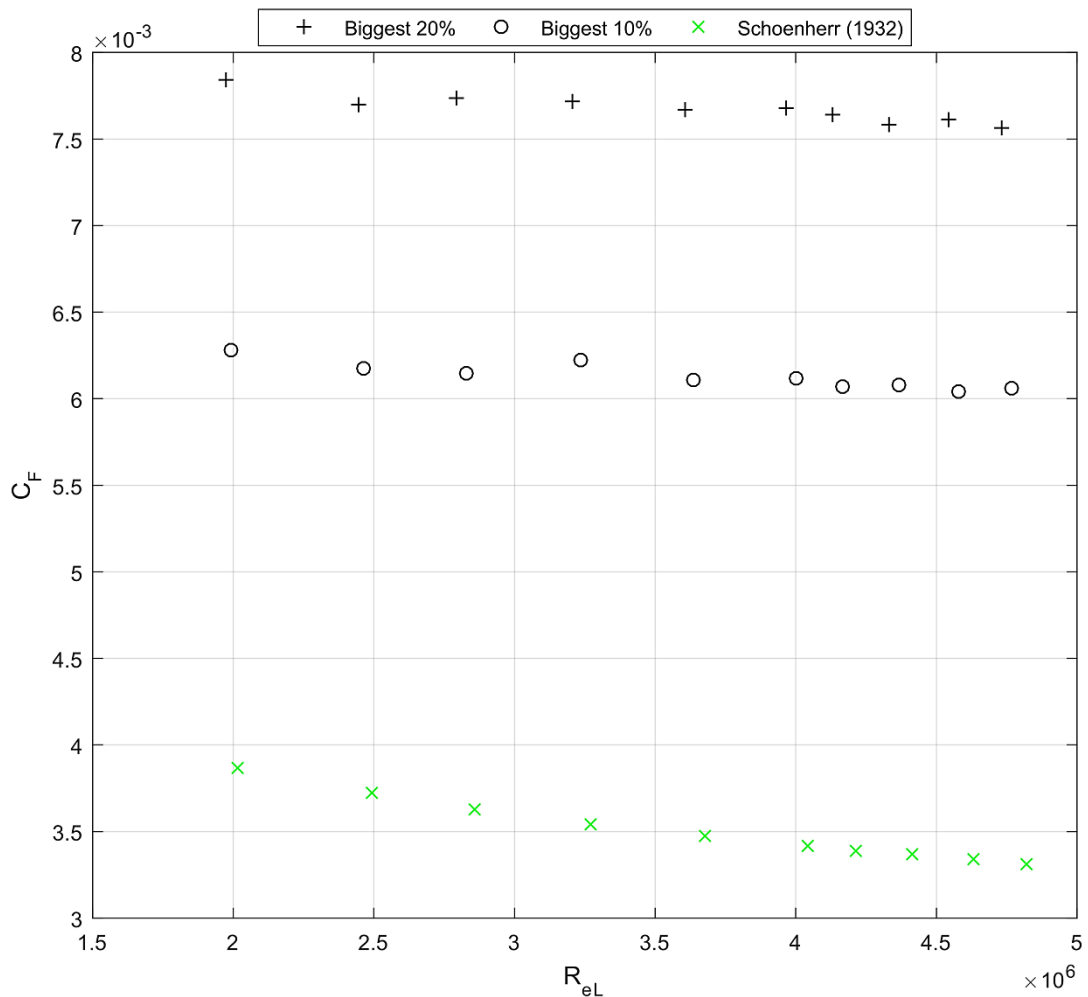


Figure 4-24 C_F comparison for the biggest type configurations

As seen in Figure 4-24 and Table 4-8, Biggest 10% changed the C_F values with an average increase of 75.13% compared to reference plate, whereas this number altered to 119.31% for Biggest 20%. The results indicated that although the change in the coverage area is same, the increase between the Biggest 10% and reference plate (the difference is 75.13%) is higher than the increase in C_F between the Biggest 10% and Biggest 20% (the difference is 44.18%).

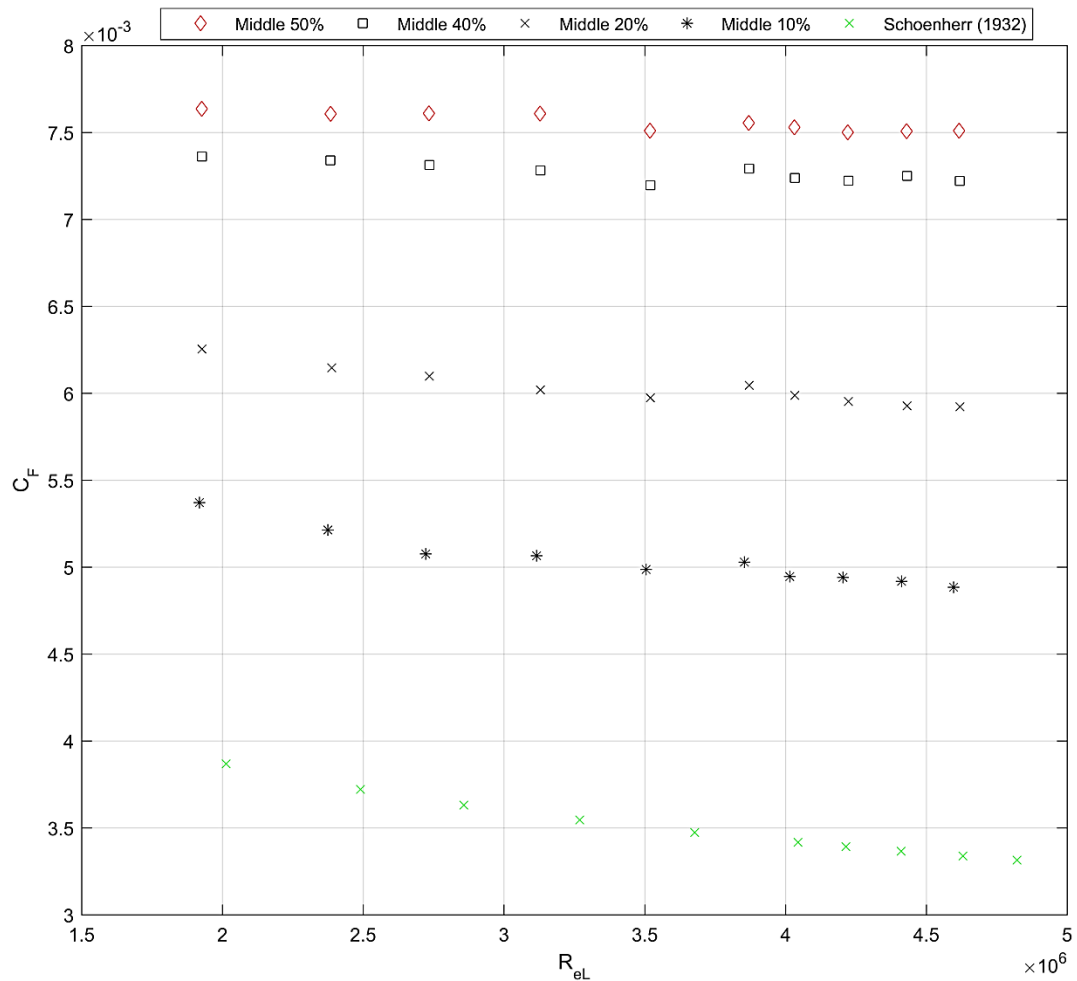


Figure 4-25 C_F comparison for the middle type configurations

As can be seen from Figure 4-25 and Table 4-7, Middle 50% increased the C_F with an average increase of 115.97% whereas this value altered to 107.81%, 72.32% and 43.97% for Middle 40%, Middle 20% and Middle 10%, respectively.

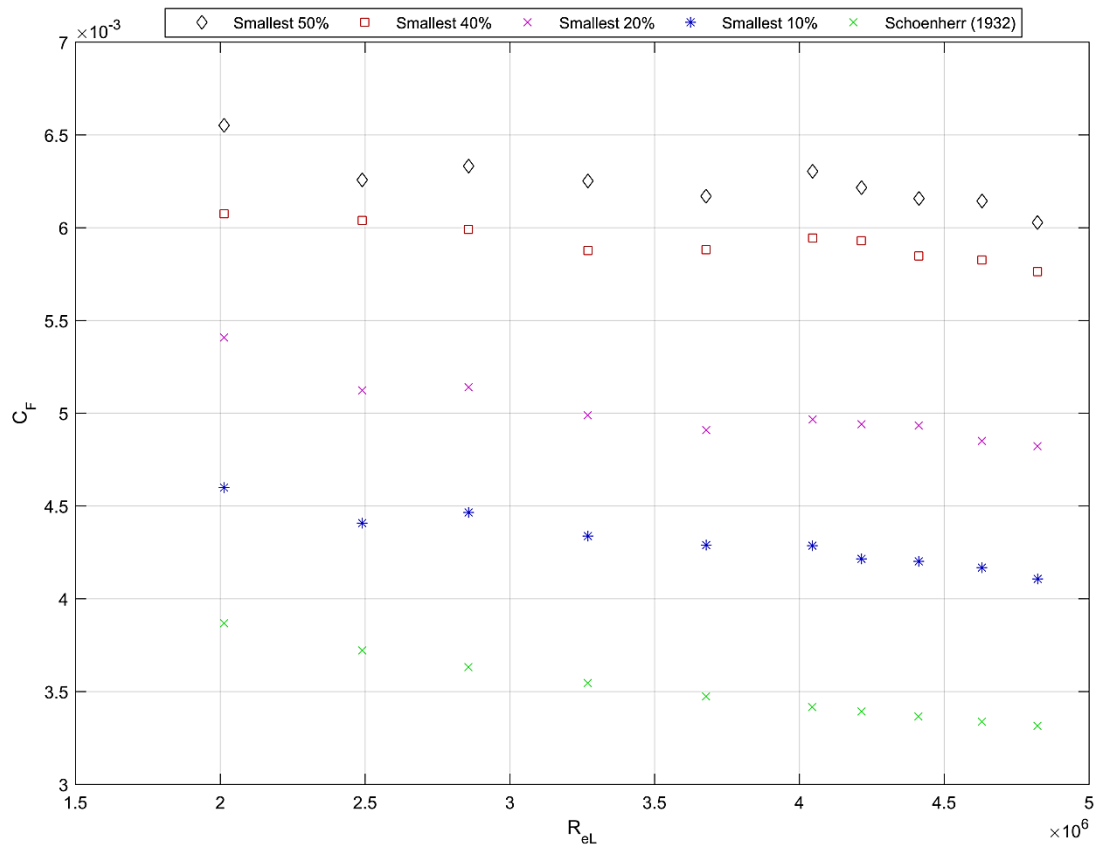


Figure 4-26 C_F comparison for the smallest type configurations.

The results given in Figure 4-26 and Table 4-9 indicate that the Smallest 50% caused the highest change in the C_F , with an average increase of 78.25% among the Smallest type configurations. It was followed by the Smallest 40%, Smallest 20% and Smallest 10% with average increases of 107.81%, 42.95% and 22.95% as expected.

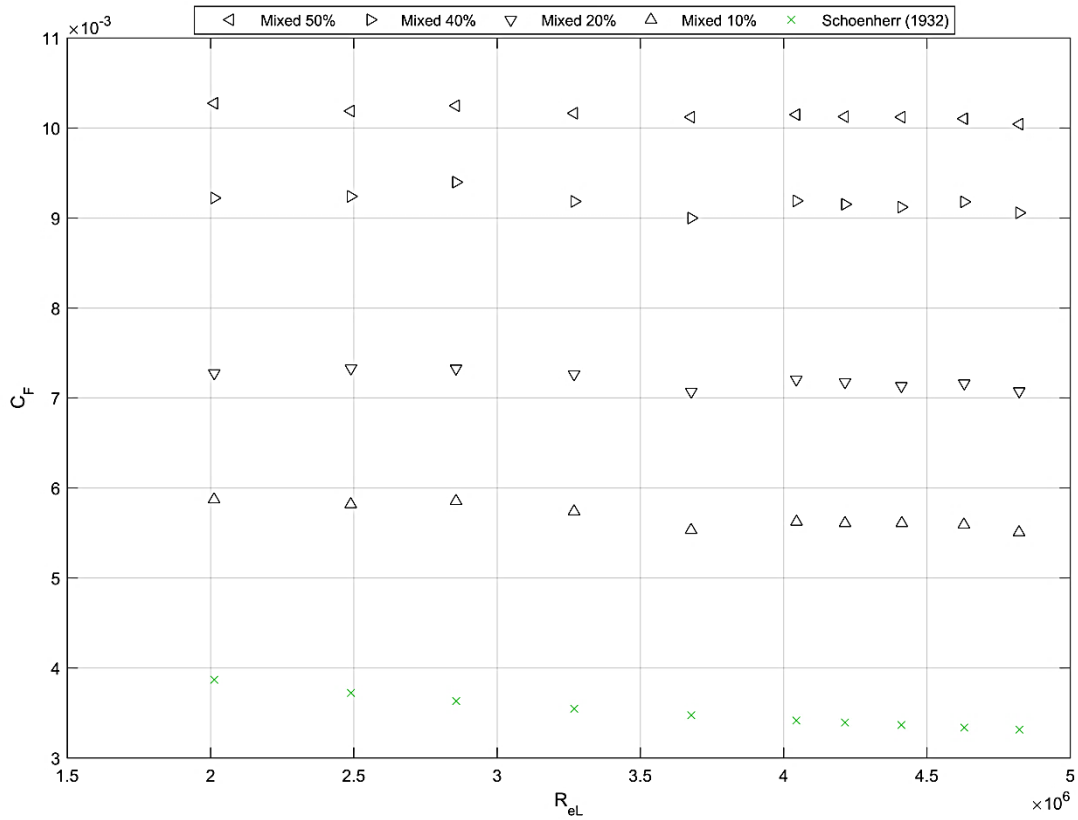


Figure 4-27 C_F comparison for the Mixed type configurations.

Figure 4-27 and Table 4-10 jointly showed that Mixed 50% and Mixed 40% caused a change in the C_F with average increases of 190.15% and 162.18% whereas these values altered to 105.76 and 62.07% for Mixed 20% and Mixed 10% configurations, respectively.

Table 4-9 Change in the C_F values of the test plates with respect to the reference plate

Configuration	The average change in C_F (%)	Configuration	The average change in C_F (%)	Configuration	The average change in C_F (%)
Smallest 10%	22.95	Middle 10%	43.97	Biggest 10%	75.13
Smallest 20%	42.95	Middle 20%	72.32	Biggest 20%	119.31
Smallest 40%	69.03	Middle 40%	107.81	-	-
Smallest 50%	78.25	Middle 50%	115.97	-	-

Table 4-10 Change in C_F values of the test plates with respect to the reference plate

Configuration	Average change in C_F (%)	Configuration	Average change in C_F (%)
Mixed 10%	62.07	NS Mixed 10%	69.92
Mixed 20%	105.76	NS Mixed 20%	113.81
Mixed 40%	162.18	NS Mixed 40%	171.17
Mixed 50%	190.15	NS Mixed 50%	199.29

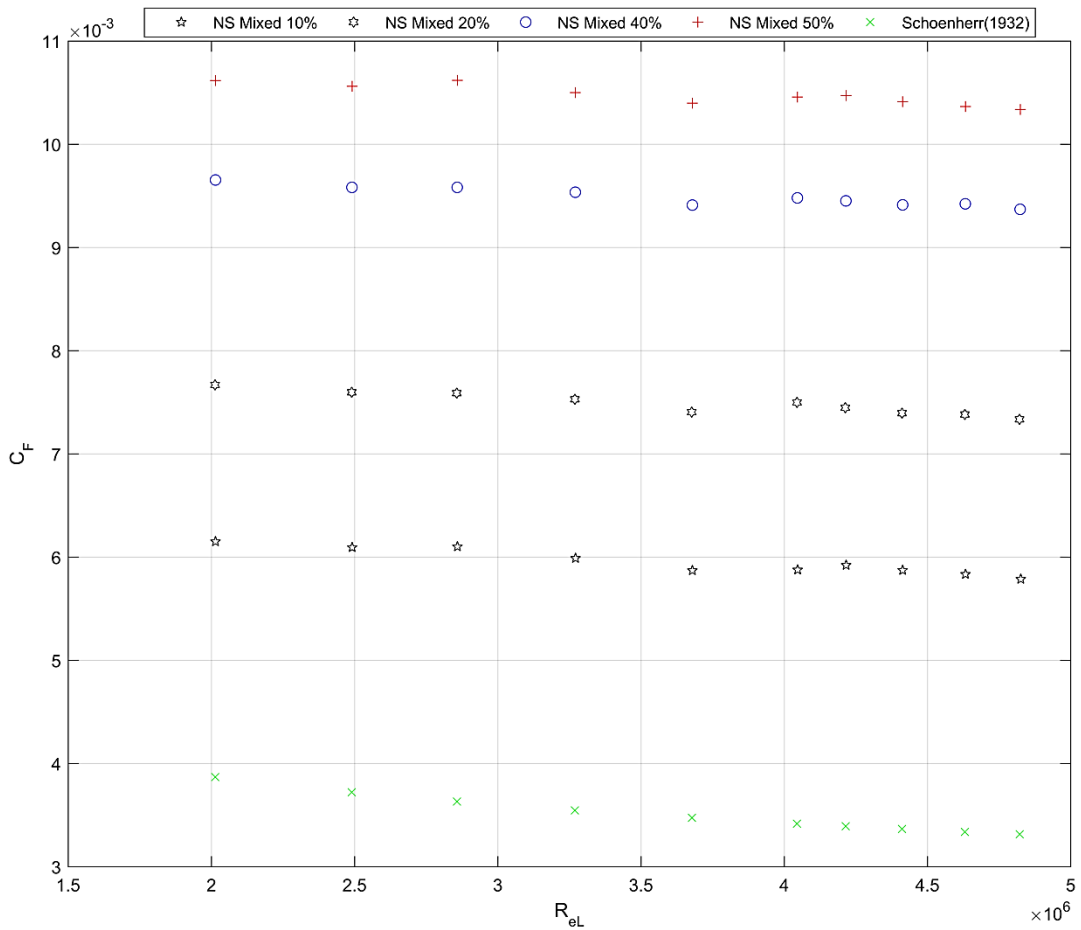


Figure 4-28 C_F comparison for the NS Mixed type configurations.

The change in the C_F due to NS Mixed 50% is the highest increase with an average increase of 199.29% while NS Mixed 40% increased the C_F with an average increase of 171.17% compared to the reference plate as shown in Figure 4-28 and Table 4-10. Following this, NS Mixed 20% and NS Mixed, 10% increased the C_F with an average increase of 113.81% and 69.92% compared to the reference plate, respectively.

As expected and seen from the results, the configurations which have higher coverage rates caused the higher increases in the C_F . For all configurations, the rate of increase in C_F between coverage areas of 10% and 20% are comparatively higher than that of 40% and 50% as shown in Table 4-9 and Table 4-10. These results confirm that until a certain level, increase in coverage area has a dominant effect on frictional resistance, however, once coverage area reaches this level the increase in the coverage area has less impact on frictional resistance.

For example, the average $\Delta C_F\%$ between Smallest 10% and Smallest 20% was calculated to be 20% whereas the average $\Delta C_F\%$ between Smallest 40% and Smallest 50% was predicted to be 9.22%. For the Mixed configurations, the average $\Delta C_F\%$ between the lower coverage rates (10% to 20%) was 52.13% while this value altered to 27.97% between the higher coverage rates (40% to 50%).

It is fundamental to note that the results are consistent with Schultz's assumption stating that "*the effect of increased per cent coverage of barnacle in drag is largest for small coverage and smaller for large coverage*" (Schultz 2004). These findings are also in accordance with the findings of Kempf (1937) and Macdonald (2000).

4.7.2.3 Effect of Barnacle Settlement Pattern on Frictional Resistance

The effect of the settlement pattern on the frictional resistance is jointly shown in Table 4-8 and Table 4-10 and Figure 4-29. Table 4-8 shows the percentage change in the C_F values with respect to the reference plate at all test speeds. Table 4-10 tabulates the average percentage changes in C_F values with respect to the reference plate, whereas Figure 4-29 shows the C_F values of the Mixed and NS Mixed configurations.

The results presented in Table 4-8 indicate that the $\Delta\%$ in C_F were calculated in a range from ~51.81% to ~67.55% for Mixed 10% and from ~59% to ~74.77% for NS Mixed 10% configurations. These values altered to ~88.1% at the lowest Reynolds number and to ~113.5% at the highest Reynolds number for Mixed 20% configurations. The relative differences for NS Mixed, 20% configuration, were calculated to be from ~98.3% to ~121.3%. The relative differences in the C_F values for Mixed 40% and NS Mixed 40% configurations were predicted to be in a range from ~138.5% to ~175% and from ~149.6 to ~182.7%, respectively. These ranges altered to from ~165.6% to ~202.9% for Mixed 50% configuration and from 174.5% to 211.9% for NS Mixed 50% configuration.

The results tabulated in Table 4-8 showed that average $\Delta\%$ in C_F due to settlement pattern was calculated to be 7.84% for 10% coverage, 8.05% for 20% coverage, 8.99% for 40% coverage and 9.14% for 50% coverage rates. It is interesting to note that the increase in the $\Delta\%$ in C_F between 10% and 20% coverage rates was comparatively

higher than the increase in the $\Delta\%$ in C_F between the 40% and 50% coverage rates. Therefore, the author believes that although the effect of settlement pattern increases with the increasing surface coverage rates, the rate of increase decreases.

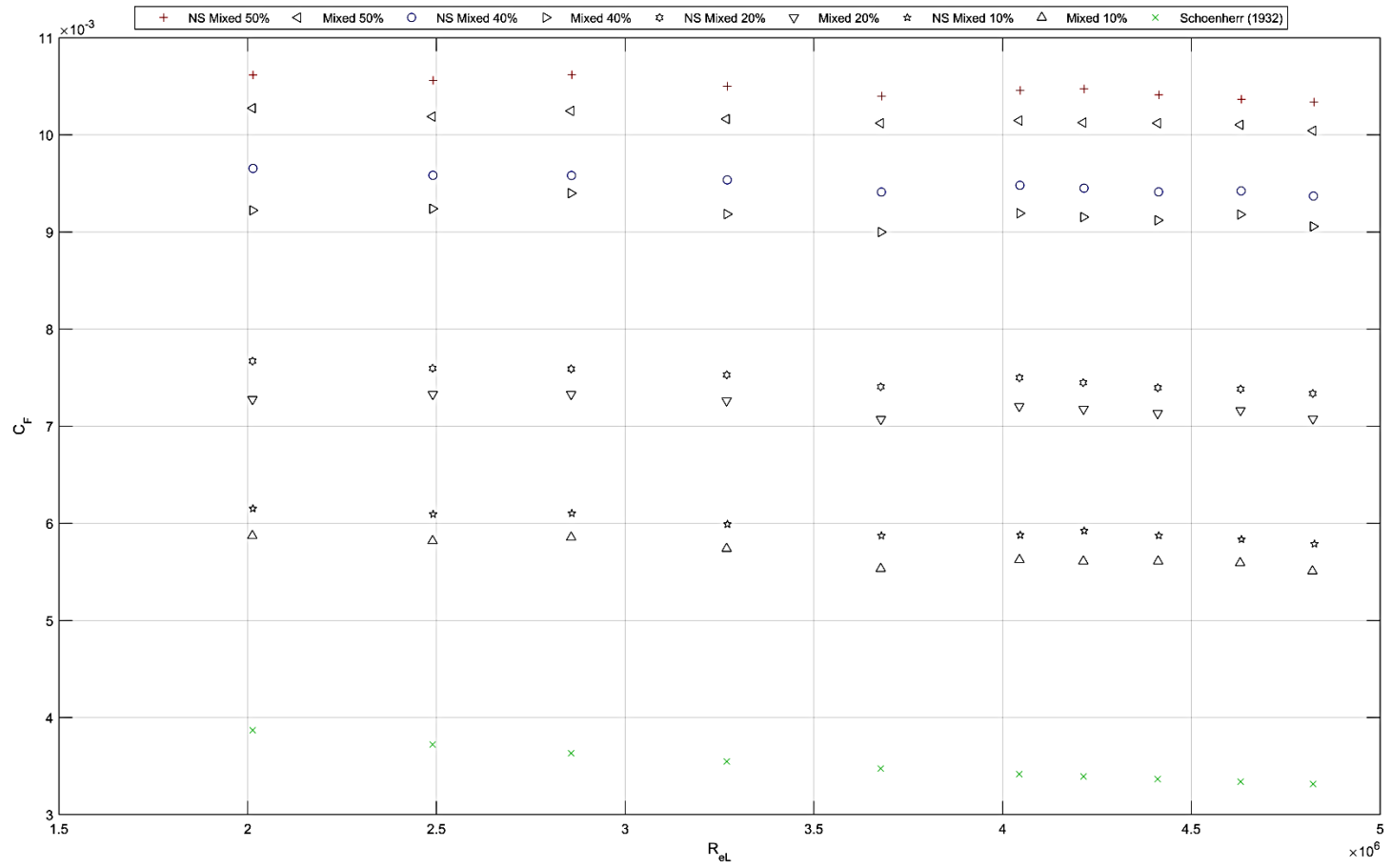


Figure 4-29 C_F comparison of mixed and natural settlement mixed configurations.

4.8 Determination of Roughness Functions

Roughness function values (ΔU^+) and roughness Reynolds numbers (k^+) for all test surfaces were calculated by using equation (2.13) and (2.14) based on the overall drag method of Granville (1987). The details of this method are provided in Chapter 2, Section 2.7.3.

First, only the roughness functions of test surfaces were illustrated in Figure 4-30 and then the roughness functions of test surfaces along with the Colebrook type roughness function of Grigson (1992), were illustrated in Figure 4-31. The roughness length scale k for the surfaces covered with barnacles was calculated through $k = 0.059h$ (%coverage)^{0.5}, as suggested in Schultz (2004). It is important to note that h was taken as the highest roughness height, which is 5mm in this study based on the assumption that the largest roughness height has a dominant influence on frictional resistance.

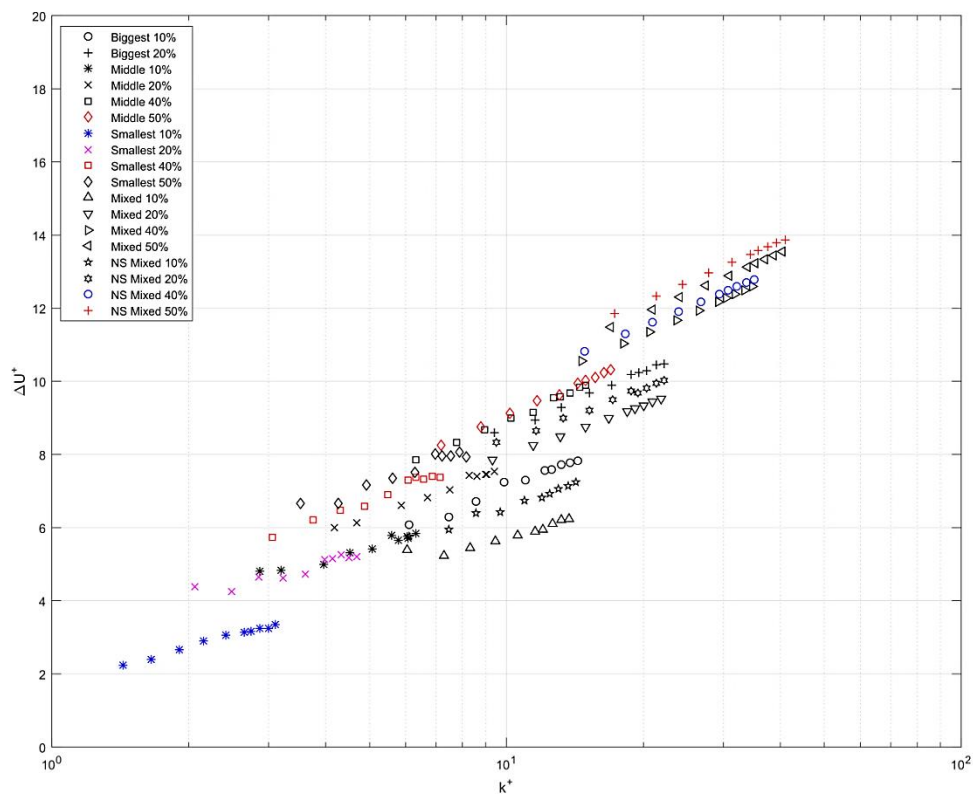


Figure 4-30: The roughness functions for all of the test surfaces.

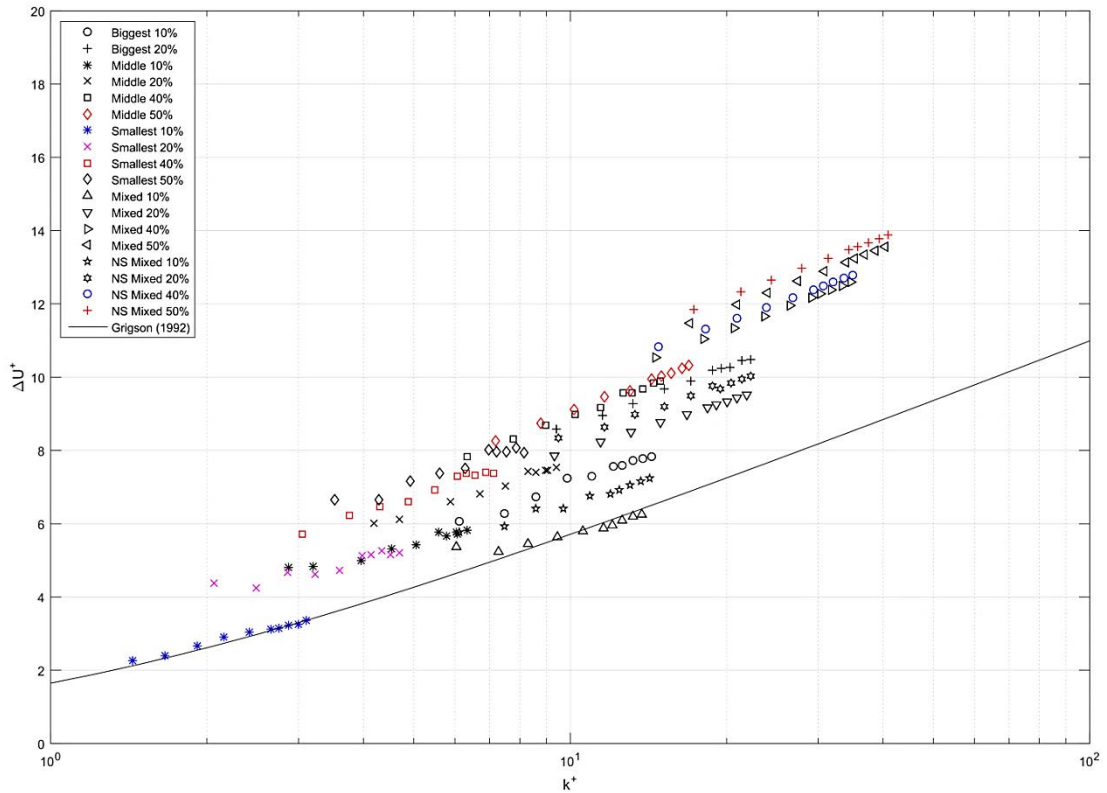


Figure 4-31: The roughness functions for all of the test surfaces together with the roughness function model of Grigson (1992).

Figure 4-31 shows that roughness functions of the surfaces follow an upward trend with the increasing roughness Reynolds number as expected. No collapse was observed between the test results and Colebrook-type roughness functions of Grigson (1992) by using the same roughness length scale formula given by Schultz (2004). As shown in Figure 4-31 the flow over the majority of the test surfaces is fully rough, and the roughness functions showed a logarithmic dependence on k^+ which confirms that the roughness functions of presented test surfaces agree well with the roughness functions of Grigson (1992).

Since the only parameter that changes in roughness length scale formula is the coverage rate, the roughness function values of test surfaces which have the same coverage rates, are positioned on the same range on the logarithmic k^+ axis. As expected, NS mixed 50% and mixed 50% showed the highest roughness function values and these followed by the test surfaces of NS mixed 40%, mixed 40%, B 20%, NS mixed 20%, mixed 20 %, B 10%, NS mixed 10% and B 10%.

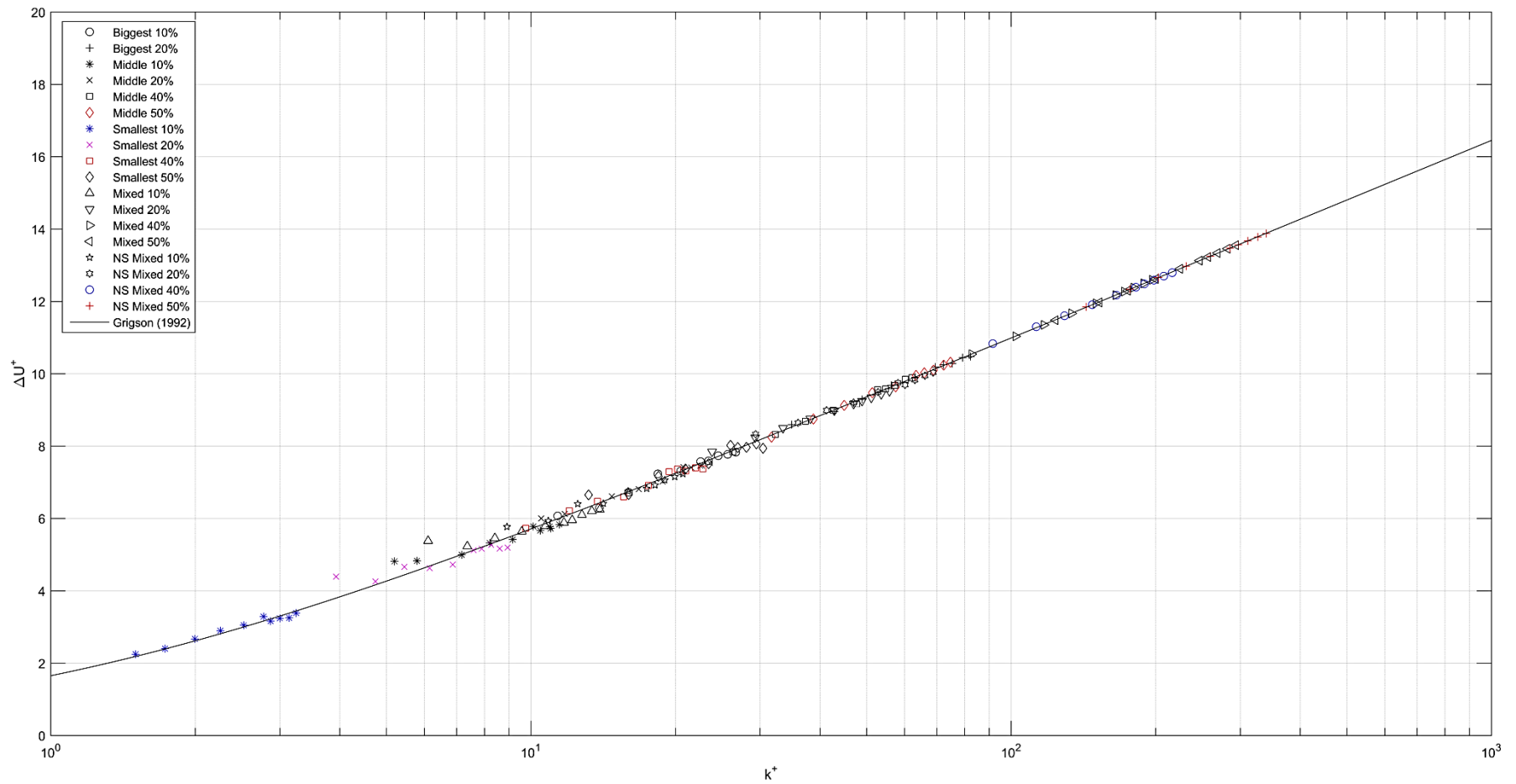


Figure 4-32: The roughness functions for all test surface, using corresponding k_G values together with the roughness function of Grigson (1992).

Although no collapse was observed between test surfaces and given roughness function model by using roughness length scale of Schultz (2004), this can be achieved by using different scaling for each test surface as suggested by Demirel et al., (2017).

Therefore, roughness function values (ΔU^+) were employed in the roughness function formula of Grigson, and corresponding roughness Reynolds numbers (k^+) were calculated as explained in Demirel et al., (2017) by using the equation (2.13). Following this, roughness lengths named as k_G by Demirel et al., (2017) were calculated in order to have excellent agreement with a roughness function of Grigson (1992).

The results presented in Figure 4-32 show that excellent agreement was obtained between test surfaces and Colebrook-type roughness function as so-called hydrodynamic roughness length scales, k_G values are used as roughness lengths. These results confirm that the roughness functions of surfaces are still required to be obtained experimentally. The developed roughness length scales or analytic fits are not applicable for every kind of surfaces

Roughness functions of the test surfaces (k^+ , ΔU^+) for both roughness length scale of Schulz and hydrodynamic roughness length scale, k_G were given in Table 4-11, Table 4-12, Table 4-13, Table 4-14, Table 4-15 and Table 4-16.

Table 4-11 ΔU^+ and k^+ values of test surfaces for $k=0.059$ h (coverage %) ^{0.5} (Biggest and Smallest).

k⁺ Biggest 10%	ΔU^+ Biggest 10%	k⁺ Biggest 20%	ΔU^+ Biggest 20%	k⁺ Smallest 10%	ΔU^+ Smallest 10%	k⁺ Smallest 20%	ΔU^+ Smallest 20%	k⁺ Smallest 40%	ΔU^+ Smallest 40%	k⁺ Smallest 50%	ΔU^+ Smallest 50%
6.107976	6.066528	9.42298	8.59434	1.43785	2.25012	2.06045	4.39041	3.04812	5.72793	3.52692	6.65009
7.463117	6.29001	11.56805	8.95355	1.65611	2.39806	2.48770	4.25544	3.76020	6.21352	4.27537	6.66082
13.19586	7.731871	20.35732	10.27911	2.87081	3.23640	4.33369	5.26622	6.56893	7.31738	7.52229	7.96381
8.583637	6.721083	13.21143	9.28603	1.91181	2.65696	2.85837	4.65949	4.29957	6.47641	4.93124	7.16338
14.35402	7.830495	22.22452	10.47565	3.10503	3.34950	4.68752	5.19614	7.13329	7.36893	8.14371	7.93732
12.12788	7.571702	18.75515	10.18210	2.65570	3.12628	3.98480	5.12378	6.06640	7.29007	6.96722	8.01818
9.877869	7.231911	15.19557	9.68312	2.15866	2.89469	3.22708	4.62519	4.87834	6.59379	5.61117	7.36316
13.80422	7.773791	21.40010	10.44238	3.00151	3.25028	4.51297	5.16623	6.88259	7.39759	7.88643	8.06304
12.5933	7.590844	19.50850	10.24934	2.74586	3.15926	4.14172	5.16179	6.31243	7.36705	7.21447	7.95874

Table 4-12 ΔU^+ and k^+ values of test surfaces for $k=0.059$ h (coverage %) ^{0.5} (Middle and Mixed)

k⁺ Middle 10%	ΔU^+ Middle 10%	k⁺ Middle 20%	ΔU^+ Middle 20%	k⁺ Middle 40%	ΔU^+ Middle 40%	k⁺ Middle 50%	ΔU^+ Middle 50%	k⁺ Mixed 10%	ΔU^+ Mixed 10%	k⁺ Mixed 20%	ΔU^+ Mixed 20%
2.87076	4.81410	4.18860	5.99948	6.33425	7.84124	7.18905	8.24718	6.03540	5.37797	9.32699	7.84523
3.19819	4.82574	4.69061	6.12281	7.76092	8.32060	8.78676	8.74950	7.27965	5.22997	11.46601	8.23922
6.04240	5.77047	8.98154	7.45602	13.76701	9.67706	15.63360	10.09922	12.61630	6.09816	20.01067	9.34018
3.96423	4.99186	5.87839	6.61295	8.96328	8.68331	10.18660	9.12492	8.31229	5.45436	13.10542	8.49839
6.06931	5.72155	9.04896	7.46363	14.92861	9.89099	16.95657	10.31836	13.74407	6.24407	21.82878	9.51696
5.58538	5.77536	8.28928	7.41821	12.67160	9.55933	14.37453	9.95300	11.57004	5.88173	18.38674	9.16936
4.53216	5.31764	6.68912	6.80883	10.23860	8.98677	11.65736	9.47664	9.45414	5.63816	14.94215	8.75590
6.32686	5.83388	9.40857	7.53170	14.47213	9.84742	16.41326	10.23563	13.22892	6.20674	20.98108	9.43629
5.77392	5.66451	8.60053	7.40843	13.16173	9.58358	14.95581	10.02219	12.03769	5.95371	19.13731	9.24996

Table 4-13 ΔU^+ and k^+ values of test surfaces for $k = 0.059 h$ (coverage %) ^{0.5} (Mixed and NS Mixed)

k⁺ Mixed 40%	ΔU^+ Mixed 40%	k⁺ Mixed 50%	ΔU^+ Mixed 50%	k⁺ NS Mixed 10%	k⁺ NS Mixed 10%	k⁺ NS Mixed 20%	k⁺ NS Mixed 20%	k⁺ NS Mixed 40%	k⁺ NS Mixed 40%	k⁺ NS Mixed 50%	k⁺ NS Mixed 50%
14.62899	10.54332	16.98728	11.47789	6.11348	5.76945	9.49693	8.32792	14.81670	10.83135	17.26706	11.84580
18.04514	11.03165	20.95563	11.97326	7.45712	5.93477	11.63884	8.64119	18.25785	11.29873	21.30330	12.34150
31.78219	12.38068	36.93675	13.33876	13.03487	7.06072	20.37718	9.82598	32.08332	12.58899	37.48705	13.66985
20.66952	11.35112	24.01049	12.29748	8.58793	6.40030	13.34644	8.98574	20.90380	11.60459	24.40440	12.66162
34.71905	12.59524	40.35320	13.55531	14.22117	7.23334	22.25090	10.03162	35.02790	12.79344	40.93206	13.87585
29.16765	12.17325	33.88645	13.12863	11.94730	6.82374	18.78854	9.74581	29.44553	12.39012	34.40109	13.46840
23.61907	11.66759	27.43965	12.61782	9.70735	6.41216	15.19385	9.20398	23.87374	11.90727	27.87820	12.97467
33.34493	12.49709	38.74984	13.45596	13.66330	7.15157	21.38248	9.94854	33.65394	12.70024	39.32233	13.78187
30.37230	12.27092	35.29404	13.22775	12.44131	6.91841	19.45162	9.68973	30.66490	12.48396	35.82545	13.56356

Table 4-14 ΔU^+ and k^+ values of test surfaces for k_g (Biggest and Smallest)

k⁺ Biggest 10%	ΔU^+ Biggest 10%	k⁺ Biggest 20%	ΔU^+ Biggest 20%	k⁺ Smallest 10%	ΔU^+ Smallest 10%	k⁺ Smallest 20%	ΔU^+ Smallest 20%	k⁺ Smallest 40%	ΔU^+ Smallest 40%	k⁺ Smallest 50%	ΔU^+ Smallest 50%
11.36623	6.06653	34.91845	8.59434	1.502632	2.247047	3.93034	4.39041	9.75192	5.72793	13.18416	6.65009
13.88799	6.29001	42.86735	8.95355	1.730724	2.398056	4.74533	4.25544	12.03009	6.21352	15.98196	6.66082
24.55594	7.73187	75.43745	10.27911	3.00015	3.236395	8.26660	5.26622	21.01612	7.31738	28.11943	7.96381
15.97314	6.72108	48.95715	9.28603	1.997948	2.667576	5.45239	4.65949	13.75570	6.47641	18.43372	7.16338
26.71115	7.83049	82.35669	10.47565	3.244924	3.383415	8.94155	5.19614	22.82169	7.36893	30.44240	7.93732
22.56857	7.57170	69.50036	10.18210	2.775352	3.285177	7.60109	5.12378	19.40838	7.29007	26.04451	8.01818
18.38156	7.23191	56.30975	9.68312	2.255921	2.894693	6.15573	4.62519	15.60737	6.59379	20.97538	7.36316
25.68803	7.77379	79.30165	10.44238	3.136748	3.250283	8.60858	5.16623	22.01963	7.39759	29.48063	8.06304
23.43465	7.59084	72.29203	10.24934	2.869571	3.159257	7.90041	5.16179	20.19549	7.36705	26.96874	7.95874

Table 4-15 ΔU^+ and k^+ values of test surfaces for k_G (Middle and Mixed)

k^+ Middle 10%	ΔU^+ Middle 10%	k^+ Middle 20%	ΔU^+ Middle 20%	k^+ Middle 40%	ΔU^+ Middle 40%	k^+ Middle 50%	ΔU^+ Middle 50%	k^+ Mixed 10%	ΔU^+ Mixed 10%	k^+ Mixed 20%	ΔU^+ Mixed 20%
5.19903	4.81410	10.50346	5.99948	26.36107	7.841242	31.69675	8.247179	6.11109	5.37797	23.84065	7.84523
5.79202	4.82574	11.76231	6.12281	32.29839	8.320589	38.74111	8.749496	7.37094	5.22997	29.30819	8.23922
10.94295	5.77047	22.52237	7.45602	57.29376	9.677057	68.92901	10.09922	12.77452	6.09816	51.14915	9.34018
7.17932	4.99186	14.74081	6.61295	37.30222	8.683312	44.91304	9.124917	8.41654	5.45436	33.49867	8.49839
10.99168	5.72155	22.69143	7.46363	62.12795	9.890979	74.76204	10.31836	13.91643	6.24407	55.79639	9.51696
10.11527	5.77536	20.78643	7.41821	52.73503	9.559327	63.37774	9.953004	11.71514	5.88173	46.99823	9.16936
8.20787	5.31764	16.77384	6.80883	42.60967	8.986768	51.39764	9.476639	9.57271	5.63816	38.19353	8.75590
11.45813	5.83388	23.59320	7.53170	60.22825	9.847418	72.36658	10.23563	13.39482	6.20674	53.62959	9.43629
10.45672	5.66451	21.56694	7.40843	54.7748	9.583576	65.94062	10.02219	12.18866	5.95371	48.91676	9.24996

Table 4-16 ΔU^+ and k^+ values of test surfaces for k_G (Mixed and NS Mixed)

k^+ Mixed 40%	ΔU^+ Mixed 40%	k^+ Mixed 50%	ΔU^+ Mixed 50%	k^+ NS Mixed 10%	k^+ NS Mixed 10%	k^+ NS Mixed 20%	k^+ NS Mixed 20%	k^+ NS Mixed 40%	k^+ NS Mixed 40%	k^+ NS Mixed 50%	k^+ NS Mixed 50%
82.80555	10.54332	123.71597	11.47789	8.91506	5.76945	29.37132	8.32792	91.54346	10.83135	143.28618	11.84580
102.14220	11.03165	152.61685	11.97326	10.87444	5.93477	35.99563	8.64119	112.80428	11.29873	176.77991	12.34150
179.89906	12.38068	269.00507	13.33876	19.00827	7.06072	63.02084	9.82598	198.22355	12.58899	311.07656	13.66985
116.99717	11.35112	174.86496	12.29748	12.52347	6.40030	41.27675	8.98574	129.15201	11.60459	202.51353	12.66162
196.52279	12.59524	293.88660	13.55531	20.73822	7.23334	68.81571	10.03162	216.41634	12.79344	339.66407	13.87585
165.09978	12.17325	246.79019	13.12863	17.42231	6.82374	58.10762	9.74581	181.92624	12.39012	285.46851	13.46840
133.69274	11.66759	199.83906	12.61782	14.15587	6.41216	46.99027	9.20398	147.50150	11.90727	231.33999	12.97467
188.74471	12.49709	282.20956	13.45596	19.92469	7.15157	66.12993	9.94854	207.92744	12.70024	326.30610	13.78187
171.91852	12.27092	257.04144	13.22775	18.14271	6.91841	60.15834	9.68973	189.46002	12.48396	297.28816	13.56356

4.9 Chapter Summary and Conclusions

Effect of barnacle fouling on frictional resistance is systematically experimented at KHL towing tank by means of flat plates covered with 3D printed barnacles. Eighteen different configurations, varying in terms of barnacle sizes, coverage areas and settlement pattern, were designed in order to assess the effect of barnacle fouling in detail.

Following the required surface preparation process, varying barnacle bundles mainly designed for each configuration were attached on the flat plates. Then, the plates were towed at a specific range of speeds, and the total resistance values were measured. The measured drag values were then non-dimensionalised, and total frictional coefficients were calculated. This is based on the assumptions proposing the frictional resistance coefficients of the smooth plates overlap with Karman-Schoenherr friction line (Schoenherr, 1932), and the effect of roughness on the residual resistance coefficient is negligible. Uncertainty of the experiment results was estimated through repeatability tests, and the uncertainty estimations were found sufficient compared to the previous study of Schultz (2004).

Results of the experiments were compared by means of figures and tables in Section 4.7. The analysis of the results showed that the barnacle height and coverage area have a significant effect on frictional resistance. As expected, the configurations which have higher barnacle height and coverage rates caused higher increases in the frictional resistance. Average increases in the C_T were calculated to be in a range from 24.62% to 180.07% whereas average increases in the C_F were calculated to be in a range from 22.95% to 199.29% considering all test surfaces.

The results indicated that the effect of barnacle height on the frictional resistance is more dominant compared to the effect of the coverage area. It can be seen from Table 7, only 20% coverage for Biggest type configurations caused a higher increase compared to the 50% Middle coverage. This can be attributed to the fact that higher roughness elements create more perturbations on the flow compared to the smaller roughness elements covered more extensive areas.

The effect of the settlement pattern was analysed by comparing the Mixed and NS Mixed configurations. It is found that the effect of settlement pattern on frictional resistance was in a range from 7.84% to 9.14%. It can be stated that the barnacle experiments conducted according to the standards may show differences up to 10% with the real situation, which tends to be settled more chaotically. This difference may occur due to the fact that as the natural settlement is chaotic, more roughness elements, which encounter with flow cause disruption, whereas, in the standard settlement, roughness elements are located behind the others, and hence they interact less with the water flow.

Roughness function values of the test surfaces were calculated following Granville's overall method (Granville 1987). Roughness length scales were calculated through $k = 0.059h (\%coverage)^{0.5}$, which is suggested by Schultz (2004) for the surfaces with barnacle fouling. Roughness functions of the surfaces follow an upward trend with the increasing roughness Reynolds number as expected. It was found that no collapse was observed between the test results and Colebrook-type roughness functions of Grigson (1992) using the same roughness length scale.

However, once the roughness functions (ΔU^+) were employed in the roughness function formula of Grigson's, by using so-called hydrodynamic roughness length scales, k_G excellent agreement with the roughness function of Grigson (1992) is obtained. The behaviours of roughness functions are in agreement with the findings of Schultz (2004).

The effect of barnacle fouling on ship resistance and powering will be predicted for six different ships operating at varying speeds in Chapter 5, employing the experimentally obtained roughness functions in Granville's similarity law scaling procedure.

5 Granville's Similarity Law Scaling Procedure

5.1 Introduction

Having conducted an extensive series of experiments with a flat plate covered with barnacle fouling it would be incomplete if the effect of barnacle fouling had not been analysed for full-scale ships. As it is practically impossible to investigate the effect of roughness on ships at full-scale by means of towing tests, Granville's similarity law scaling procedure was used in order to predict the effect of roughness at full-scale (Granville 1958).

Once the roughness functions (ΔU^+) of test surfaces are known, Granville's similarity law scaling can be used to predict the effect of roughness on the frictional resistance of flat plates of ship lengths. In the literature there are several examples of the use of this method such as Schultz (2002), Schultz(2004), Shapiro (2004), Schultz (2007), Flack and Schultz (2010), Demirel et al.,(2017), Uzun et al.,(2017) and Uzun et al.,(2019).

A method for predicting the effect of coating roughness and fouling on the frictional resistance and powering at the full-scale ship was provided by Schultz (2007). Later, Demirel (2015) using the experimental data of his PhD and the experimental data of Schultz (2004) generated useful added resistance diagrams to be used by less experienced end-users.

This chapter aims to predict the effect of barnacle fouling on ship resistance at the full-scale ship. Therefore, experimentally obtained roughness functions (ΔU^+) were employed in an in-house code carrying out Granville's similarity law scaling procedure in order to determine C_{FR} at full-scale ships. Afterwards, increases in the frictional resistance and effective power of ships and decreases in the ship speeds due to roughness were presented for different type ships operating at varying ship speeds.

This chapter is organised as follows: In Section 5.2, Granville’s similarity law scaling procedure is explained step by step. Increases in the frictional resistance and ship effective power along with the decreases in the ship speed at fixed effective power were presented in Section 5.3. Last, the chapter summary and conclusion are given in Section 5.4.

5.2 Methodology

An in-house code conducting the similarity law scaling procedure of Granville (1958) was developed and used to predict the effect of roughness on frictional resistance of ships at full-scale. The procedure is explained step by step as following, which is also can be found in detail in Schultz (1998), Shapiro (2004), Schultz (2007) and Demirel (2015).

- As a first step, the C_{FS} of a smooth plate is calculated by using equation (4.4) and then is plotted against $\log(Re_L)$ as shown in Figure 5-1.
- The second step is to shift the plotted C_{FS} curve by a distance of $\Delta U^+ / (\ln(10) / \kappa)$ to the right side in the $\log(Re_L)$ direction as shown in Figure 5-1.

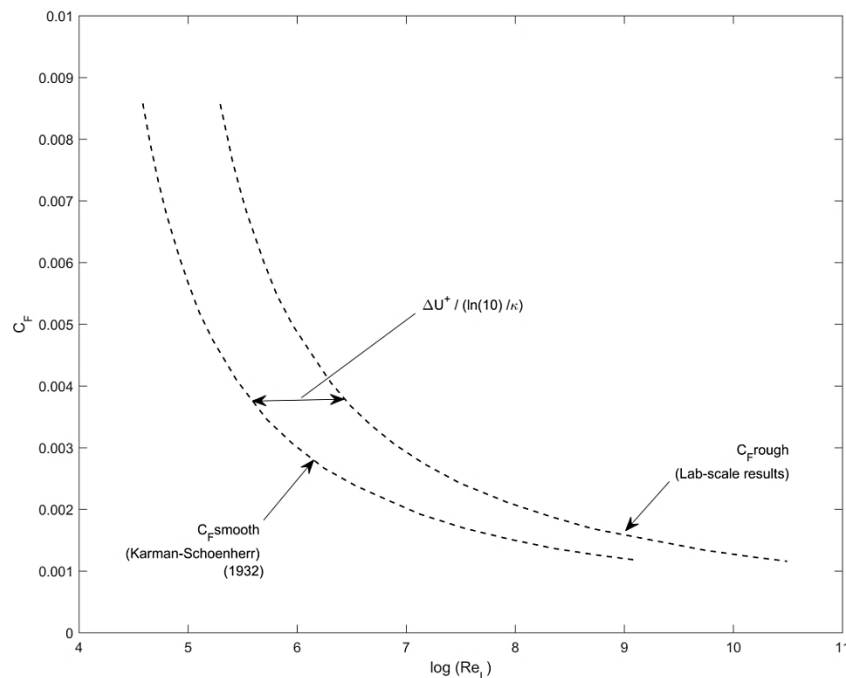


Figure 5-1: C_{FS} and shifted the frictional line for C_{FR} .

- The next step is to plot the line of constant L_{plate}^+ , which satisfies equation (5.1).

$$Re_L = \frac{L_{plate}^+}{\sqrt{\frac{C_F}{2} \left(1 - \frac{1}{\kappa} \sqrt{\frac{C_F}{2}}\right)}} \quad (5.1)$$

where L_{plate}^+ is

$$L_{plate}^+ = \frac{L_{plate}}{\text{viscous length scale}} \quad (5.2)$$

The viscous length scale (ν/U_τ) can be calculated by

$$\frac{\nu}{U_\tau} = \frac{k}{k^+} \quad (5.3)$$

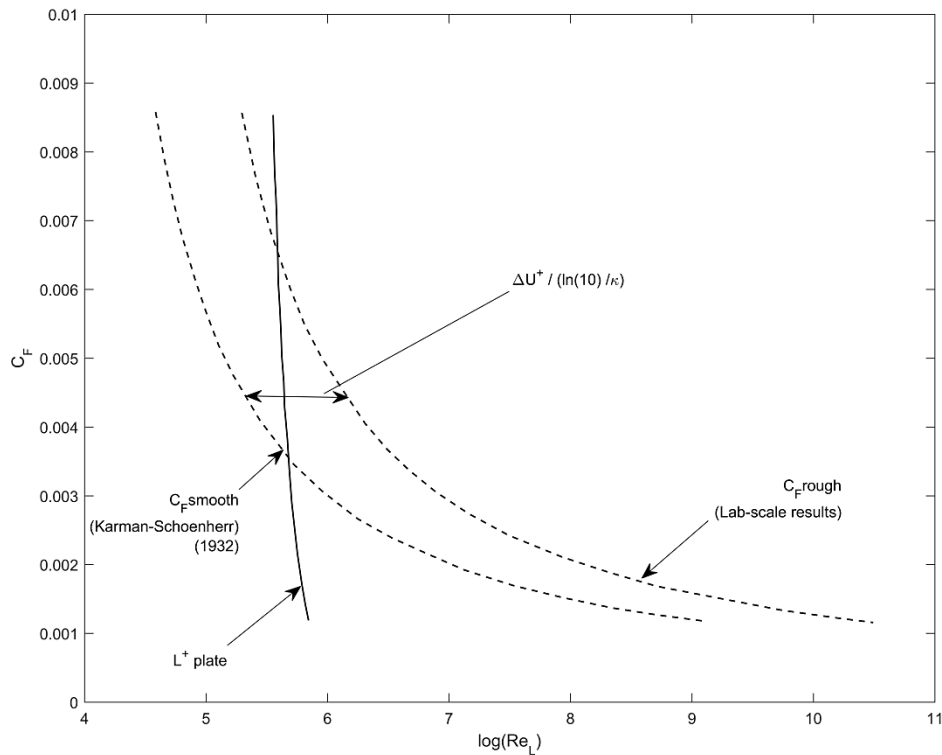


Figure 5-2: The third step of the Granville scale up.

L_{plate}^+ can be calculated by using equation (5.1) if laboratory-scale C_F values obtained by experiments or it can be calculated by equation (5.2) if the viscous length scale, which can be calculated through equation (5.3), is known.

- The fourth step is to shift the line of constant L_{plate}^+ by a distance of $\log(L_{ship}/L_{plate})$ in the positive $\log(Re)$ direction. The intersection point of this line with the C_{FR} curve gives the C_{FR} value for the ship, as shown in Figure 5-3.

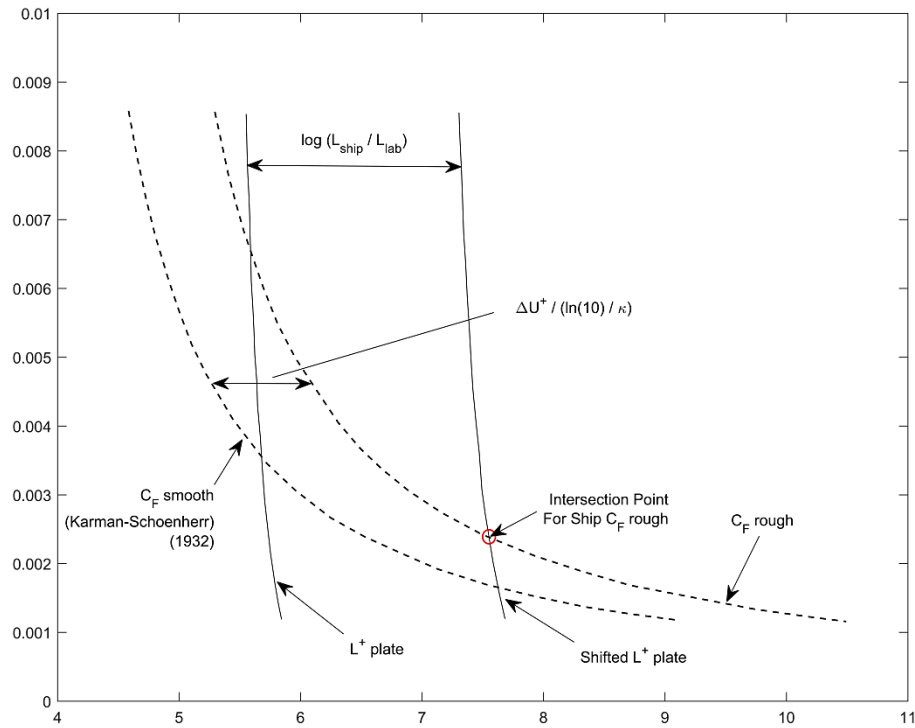


Figure 5-3: Granville scale-up procedure.

The increase in the frictional resistance of the ship (ΔC_F) due to roughness can be found by calculating the difference between C_{FR} of the ship (which is the intersection point shown in Figure 5-3) and the C_{FS} of the ship (which is the smooth value given by equation (5.5) for a plate of ship length).

The inputs of the code can be listed as roughness height (k), roughness functions (ΔU^+), corresponding roughness Reynolds numbers (k^+), length of the plate and the length of the ship in question.

5.3 Prediction of the Roughness Effects of Biofouling on Ship Resistance and Powering

Experimentally obtained roughness functions and roughness Reynolds numbers were employed in Granville's similarity law scaling code and predictions were made for the test conditions. The diagrams showing the increases in the frictional resistance and increases in the effective power were provided along with the decreases in ship speed due to given roughness.

5.3.1 Added Resistance and Effective Power of Ships

The roughness due to biofouling accumulation causes increases in the frictional resistance, which leads to an increase in the effective power, P_E , which is the necessary power to move ship through water. P_E is a function of total resistance, R_T , and ship speed, which is given in equation (5.4).

$$P_E = R_T V \quad (5.4)$$

Where R_T is defined by equation (4.2), equation (5.4) can be rewritten as below:

$$P_E = \frac{1}{2} \rho S C_T V^3 \quad (5.5)$$

The percentage increase in P_E due to roughness can be expressed by

$$\Delta P_E \% = \frac{C_{TR} - C_{TS}}{C_{TS}} \times 100 = \frac{\Delta C_F}{C_{TS}} \times 100 \quad (5.6)$$

which is similar to that used by Demirel et al. (2017). ΔC_F is the increase in the frictional resistance, which can be obtained from the diagrams or the tables given in the following sections. C_{TS} is the total resistance coefficient of the ship, which is composed of other types of resistances; however, the evaluation of this does not lie in the interest of this study. So, C_{TS} values of the ships used in the case studies were taken from the report of the experiments that were performed earlier at the Kelvin Hydrodynamics Laboratory at the University of Strathclyde (Demirel 2015).

Moreover, if the intention is to provide fixed effective power, the design ship speed decreases due to barnacle fouling. The percentage reductions in design speed at a fixed effective power can be calculated by the following equations (5.7), (5.8) and (5.9).

$$C_{TR} = C_{TS} + \Delta C_F \quad (5.7)$$

where ΔC_F stands for the increase in the frictional resistance due to fouling.

$$V_{reduced} = \sqrt[3]{\frac{P_E}{0.5\rho S C_{TR}}} \quad (5.8)$$

where $V_{reduced}$ is the reduced ship speed due to increased C_{TR} value because of the fouling conditions. The percentage difference between the ship design speed (V) and the reduced speed ($V_{reduced}$) can be found by using equation (5.9).

$$\% \Delta V = \left(\frac{V - V_{reduced}}{V} \right) \times 100 \quad (5.9)$$

The full-scale predictions in this study were made for flat plates representing the length of 230 m container ship, length of 270 m LNG ship, length of 180 m bulk carrier, length of 120 m special purpose vessel, length of 60 m special purpose vessel and length of 250 m tanker ship. Then, calculated ΔC_F values were plotted for an appropriate range of ship speed for the case studies, similar to those presented by Demirel et al., (2017). The added resistance diagrams for these ships were illustrated in the following figures (Figure 5-4 to Figure 5-15), which can also be used in the increased effective power calculation.

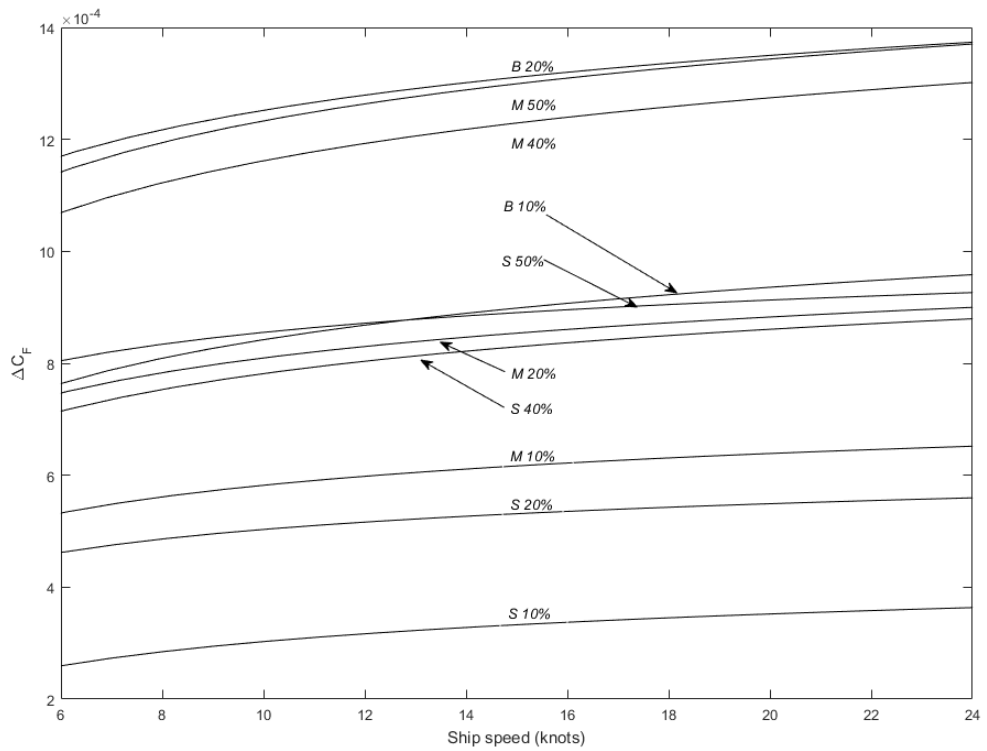


Figure 5-4 Added frictional resistance diagram for a 230 m container ship with different barnacle fouling conditions

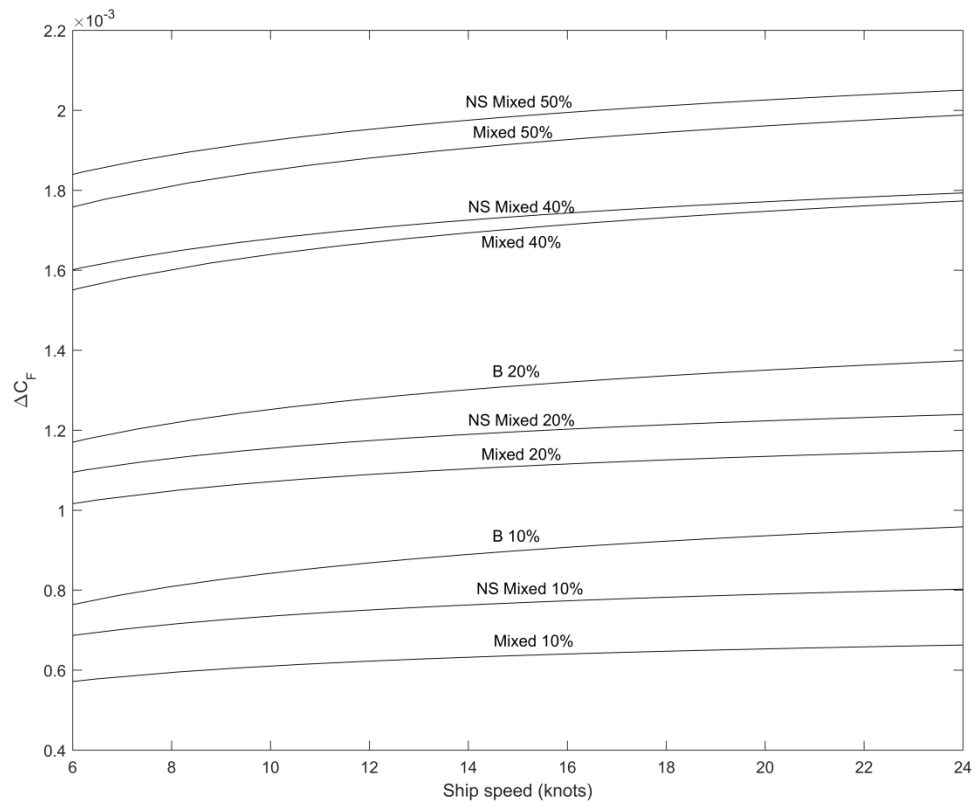


Figure 5-5 Added frictional resistance diagram for a 230 m container ship with different barnacle fouling conditions

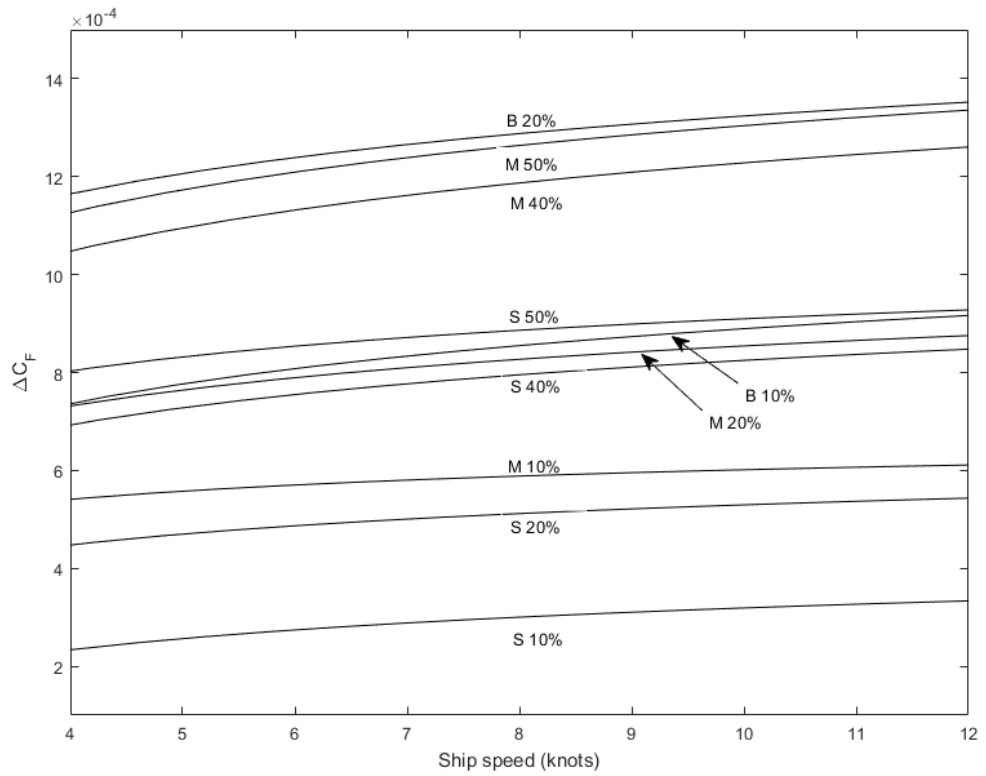


Figure 5-6 Added frictional resistance diagram for a 180 m bulk-carrier with different barnacle fouling conditions

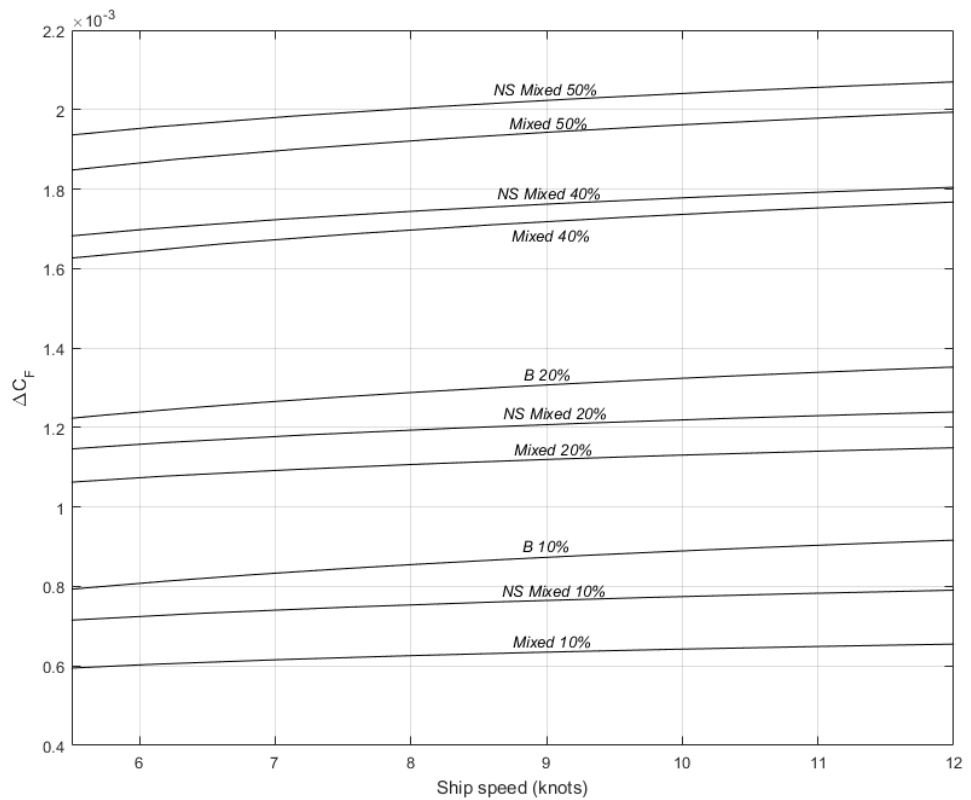


Figure 5-7 Added frictional resistance diagram for a 180 m bulk-carrier with different barnacle fouling conditions

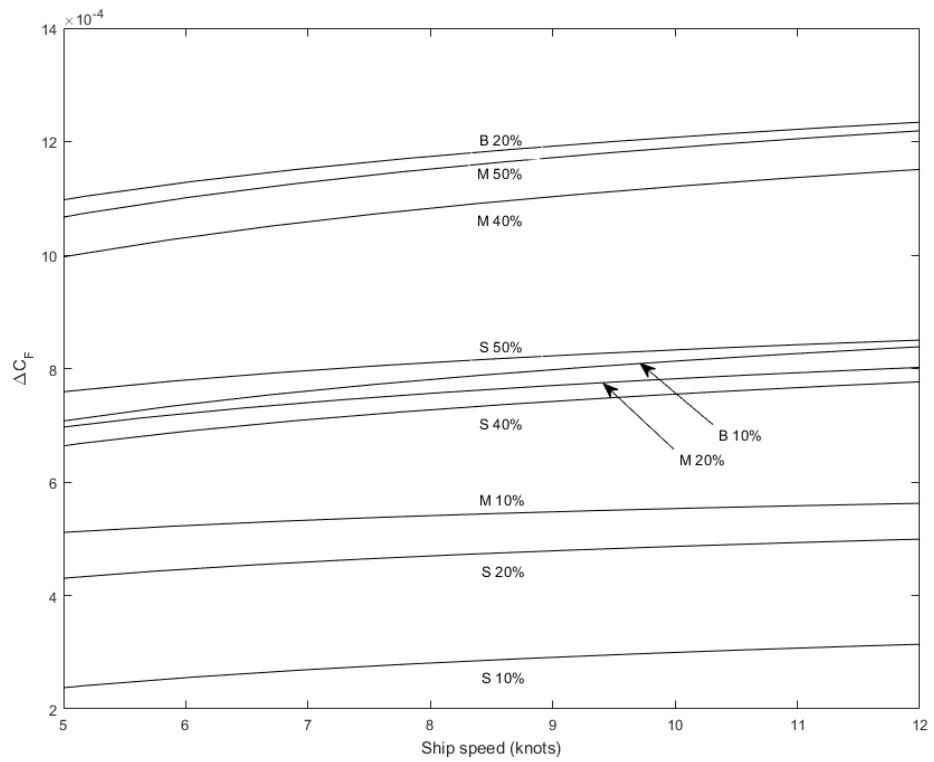


Figure 5-8 Added frictional resistance diagram for a 270 m LNG carrier with different barnacle fouling conditions

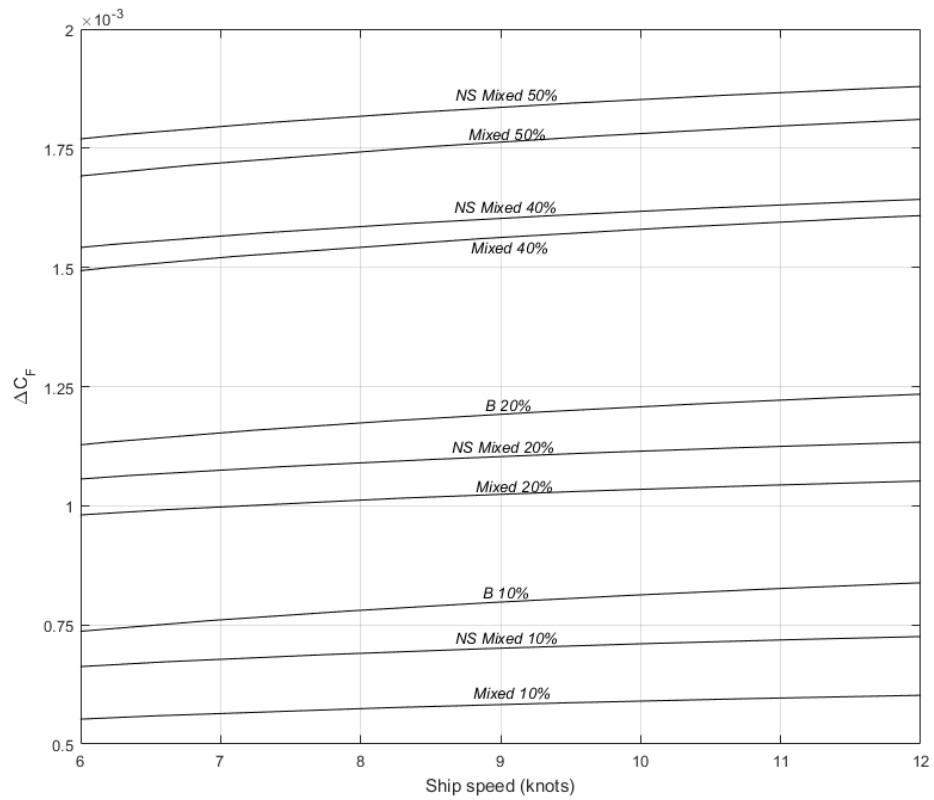


Figure 5-9 Added frictional resistance diagram for a 270 m LNG carrier with different barnacle fouling conditions

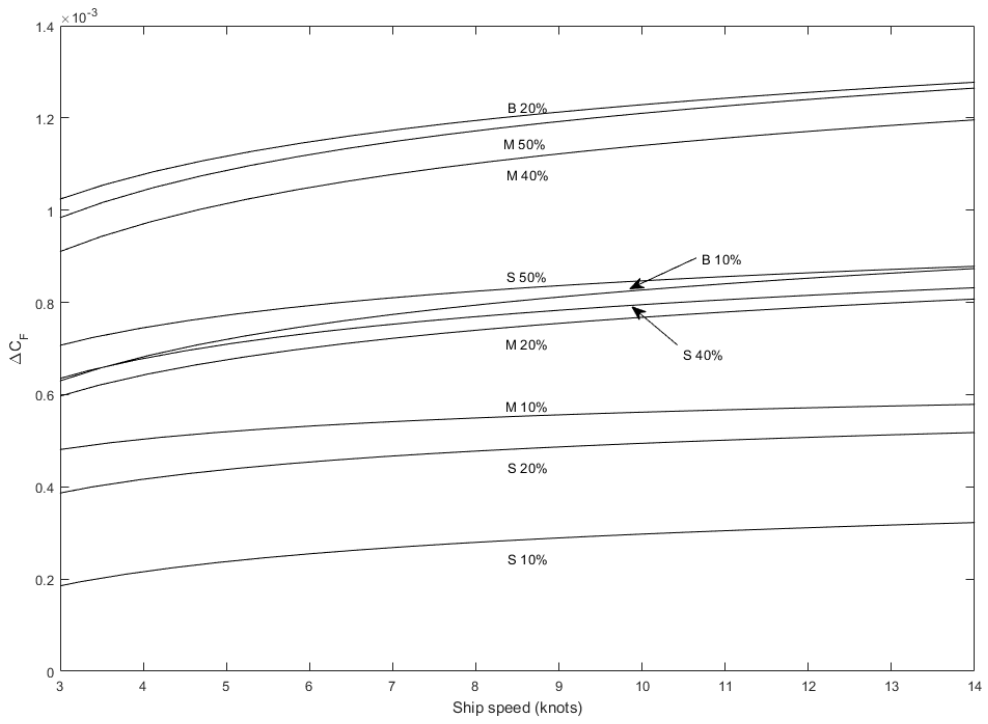


Figure 5-10 Added frictional resistance diagram for a 250 m tanker with different barnacle fouling conditions

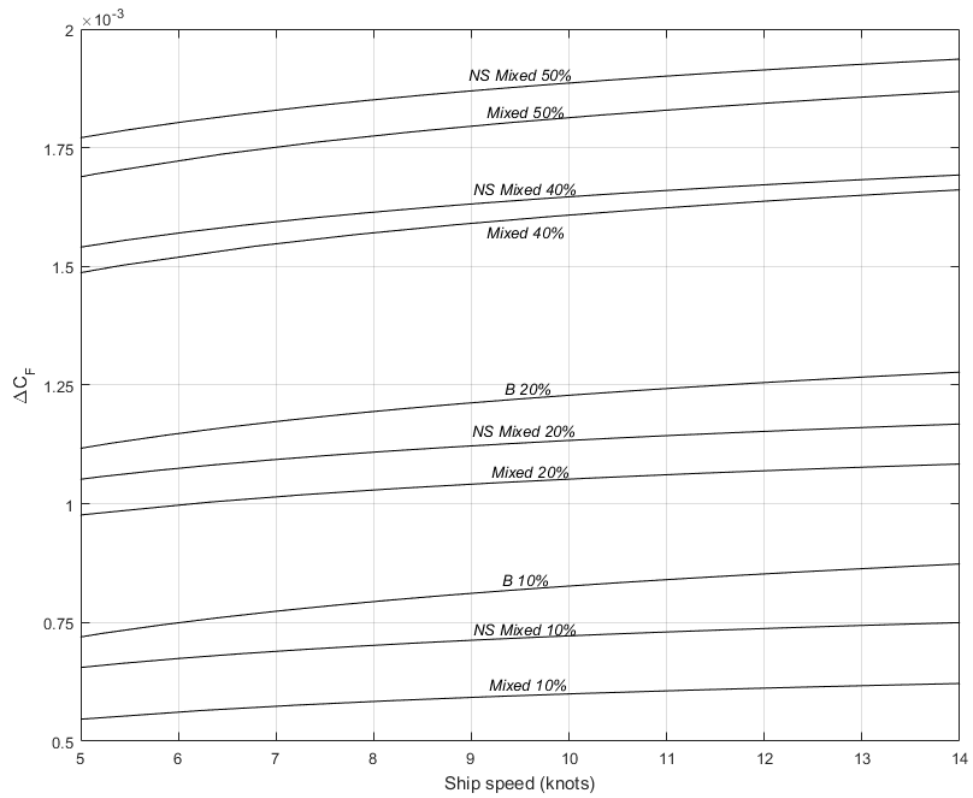


Figure 5-11 Added frictional resistance diagram for a 250 m tanker with different barnacle fouling conditions

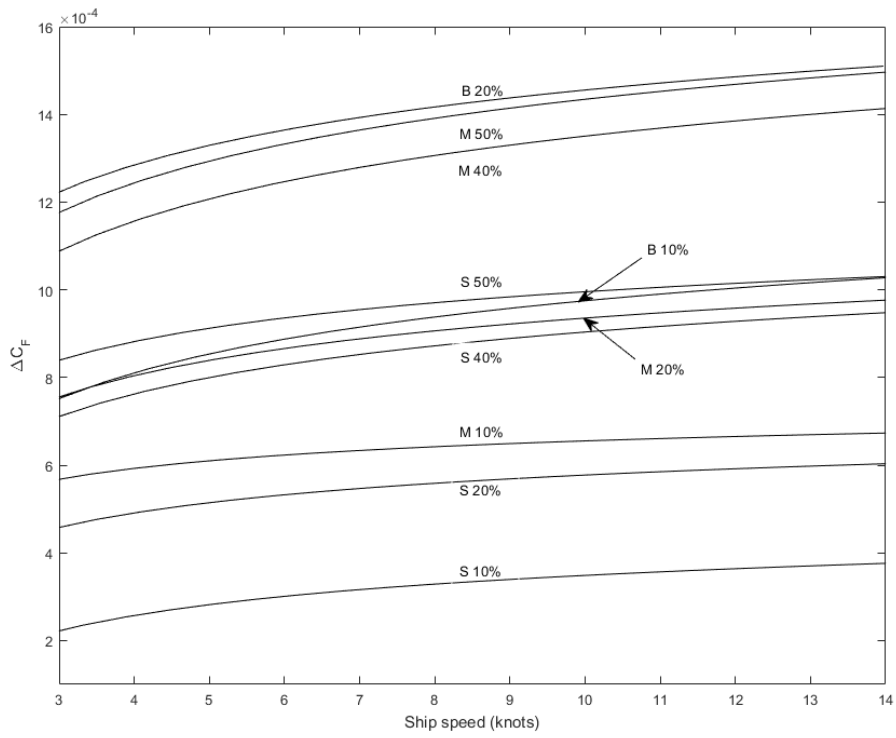


Figure 5-12 Added frictional resistance diagram for a 120 m special purpose vessel with different barnacle fouling conditions

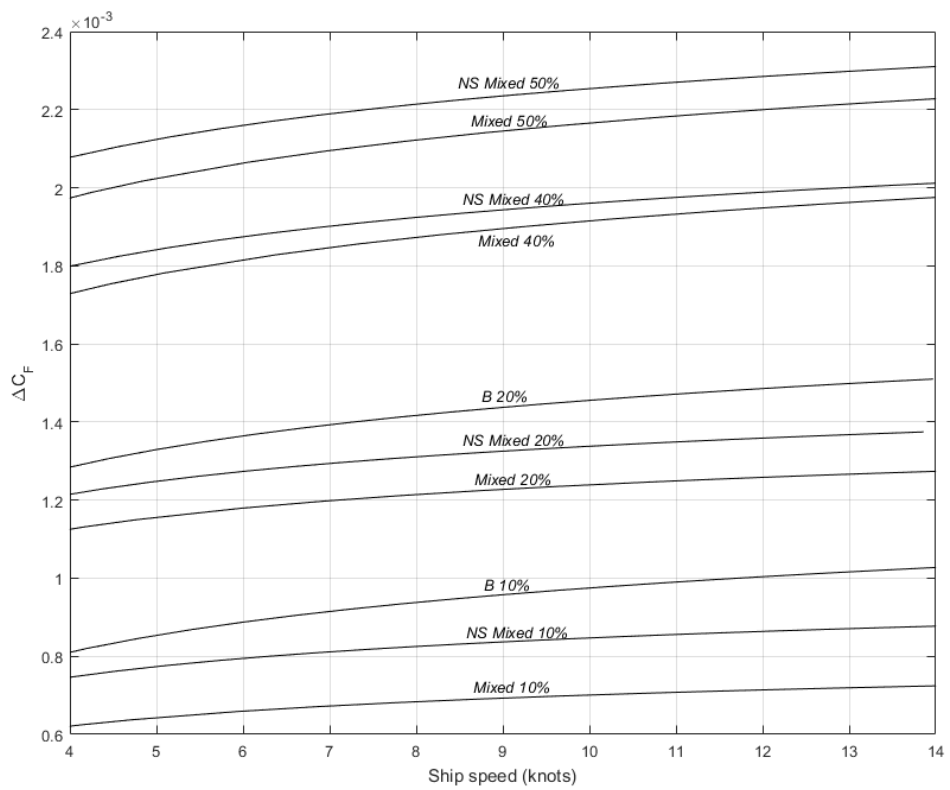


Figure 5-13 Added frictional resistance diagram for a 120 m special purpose vessel with different barnacle fouling conditions

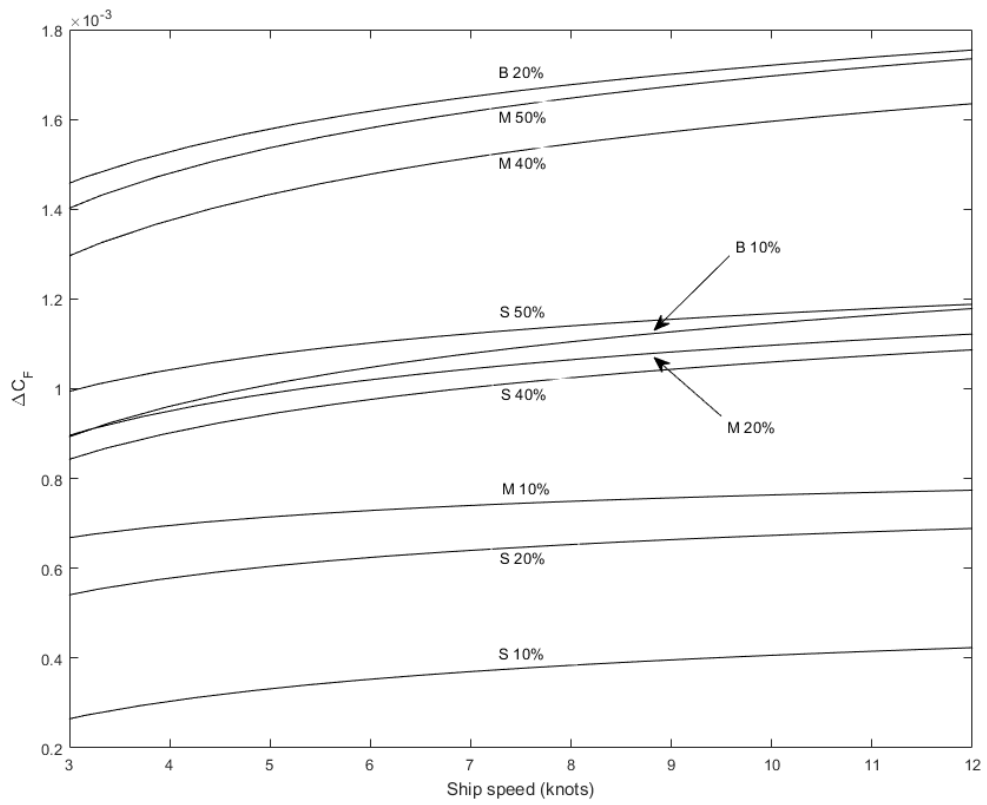


Figure 5-14 Added frictional resistance diagram for a 60 m special purpose vessel with different barnacle fouling conditions

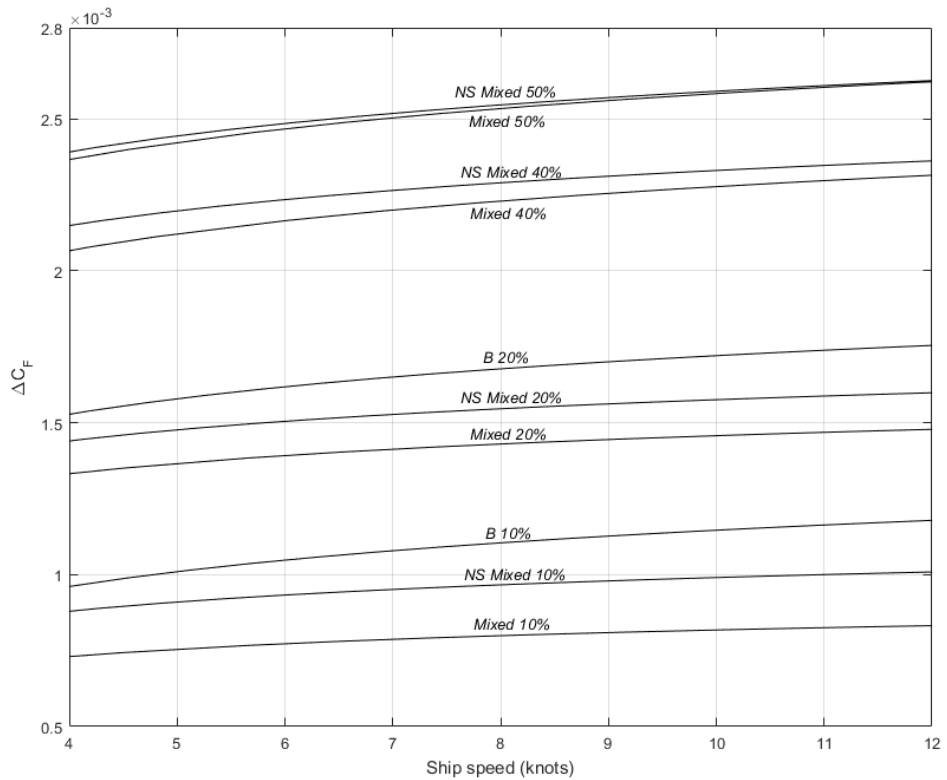


Figure 5-15 Added frictional resistance diagram for a 60 m special purpose vessel with different barnacle fouling conditions

Table 5-1 Increases in frictional resistance and powering compared to smooth conditions

Ship Type	230 m Container ship @ 24 knots		270 m LNG ship @ 12 knots		180 m Bulk-carrier @ 12 knots		120 m Special purpose vessel @ 14 knots		60 m Special purpose vessel @ 12 knots		250 m Tanker ship @ 14 knots	
	% ΔP_E &% ΔC_F		% ΔP_E &% ΔC_F		% ΔP_E &% ΔC_F		% ΔP_E &% ΔC_F		% ΔP_E &% ΔC_F		% ΔP_E &% ΔC_F	
10% Smallest	17.48	27.17	13.79	21.90	15.52	22.23	15.27	24.35	9.82	24.78	12.73	22.92
20% Smallest	26.95	41.92	22.42	35.65	25.48	36.68	24.52	39.12	15.96	40.24	20.44	36.82
40% Smallest	42.35	65.90	34.57	55.12	39.48	56.50	38.49	61.38	25.17	63.42	31.88	57.44
50% Smallest	44.65	69.57	35.98	57.41	43.42	62.40	41.98	67.18	27.61	69.83	34.63	62.28
10% Middle	31.40	48.87	25.77	41.11	28.58	41.78	27.43	43.92	17.97	45.48	22.88	41.30
20% Middle	43.33	67.40	35.74	57.07	41.06	59.13	39.82	63.78	25.98	65.42	32.89	59.34
40% Middle	62.61	97.29	51.00	81.01	58.96	84.67	57.53	91.94	37.95	95.85	47.20	84.99
50% Middle	65.98	102.65	54.23	86.47	62.53	89.87	60.95	97.48	40.30	101.83	49.96	90.05
10% Biggest	46.15	71.82	37.11	58.91	42.72	61.20	41.76	66.67	27.32	68.90	34.49	62.13
20% Biggest	66.22	103.16	54.91	87.59	63.26	90.89	61.45	98.15	40.71	102.77	50.50	91.09
10% Mixed	31.92	49.66	26.70	42.43	30.68	44.15	29.44	46.96	19.27	48.53	24.51	44.07
20% Mixed	55.33	86.08	46.65	74.19	53.81	77.47	51.77	82.57	34.23	86.19	42.75	76.91
40% Mixed	85.51	133.32	71.79	115.02	82.43	117.98	80.34	128.26	53.60	134.96	65.61	118.24
50% Mixed	95.74	149.01	80.40	128.06	93.02	133.17	90.57	144.47	60.71	152.78	73.76	132.88
10% NS Mixed	38.62	60.05	32.24	51.36	36.92	52.95	35.68	56.98	23.40	59.06	29.61	53.35
20% NS Mixed	59.78	93.27	50.14	79.48	58.10	83.76	55.94	89.27	37.06	93.47	46.12	83.09
40% NS Mixed	86.33	134.24	73.07	116.71	84.41	121.31	81.77	130.39	54.70	137.72	66.81	120.33
50% NS Mixed	98.74	153.67	83.65	133.77	96.87	139.34	93.90	149.71	60.92	153.84	76.44	137.68

Table 5-2 Speed reductions in fouled conditions for ships compared to smooth conditions

Ship Type	230 m Container ship @ 24 knots			270 m LNG ship @ 12 knots			180 m Bulk-carrier @ 12 knots		
	Ship Speed in smooth condition	Reduced Speed for fixed EHP	% reduction in speed for fixed EHP	Ship Speed in smooth condition	Reduced Speed for fixed EHP	% reduction in speed for fixed EHP	Ship Speed in smooth condition	Reduced Speed for fixed EHP	% reduction in speed for fixed EHP
10% Smallest	23.75	22.51	5.23	11.98	11.47	4.21	11.80	11.24	4.70
20% Smallest	23.92	22.09	7.64	12.10	11.31	6.52	12.31	11.42	7.29
40% Smallest	23.96	21.30	11.11	12.37	11.20	9.42	11.73	10.50	10.50
50% Smallest	24.24	21.43	11.58	12.44	11.23	9.74	12.16	10.78	11.33
10% Middle	24.03	21.94	8.70	12.42	11.50	7.36	12.12	11.15	8.04
20% Middle	23.91	21.21	11.31	12.51	11.30	9.68	12.35	11.01	10.83
40% Middle	23.70	20.16	14.96	11.98	10.44	12.83	12.08	10.35	14.31
50% Middle	23.92	20.21	15.54	12.36	10.70	13.45	12.15	10.34	14.95
10% Biggest	23.98	21.13	11.88	11.91	10.72	9.99	11.82	10.50	11.18
20% Biggest	24.22	20.45	15.58	12.41	10.73	13.57	12.12	10.29	15.07
10% Mixed	23.96	21.84	8.82	12.02	11.11	7.58	12.29	11.24	8.53
20% Mixed	23.93	20.67	13.65	12.10	10.65	11.98	12.32	10.67	13.37
40% Mixed	24.38	19.84	18.62	12.88	10.75	16.50	11.75	9.62	18.16
50% Mixed	24.00	19.19	20.06	12.26	10.07	17.85	11.77	9.46	19.68
10% NS Mixed	23.80	21.35	10.31	12.28	11.19	8.89	11.94	10.75	9.95
20% NS Mixed	24.52	20.98	14.46	11.76	10.27	12.67	12.47	10.71	14.16
40% NS Mixed	23.83	19.36	18.73	12.54	10.45	16.71	12.15	9.91	18.45
50% NS Mixed	24.00	19.09	20.46	12.67	10.35	18.34	12.24	9.76	20.21

Table 5-3 Speed reductions in fouled conditions for ships compared to smooth conditions

Ship Type	120 m Special purpose vessel @ 14 knots			60 m Special purpose vessel @ 12 knots			250 m Tanker ship @ 14 knots		
	Ship Speed in smooth condition	Reduced Speed for fixed EHP	% reduction in speed for fixed EHP	Ship Speed in smooth condition	Reduced Speed for fixed EHP	% reduction in speed for fixed EHP	Ship Speed in smooth condition	Reduced Speed for fixed EHP	% reduction in speed for fixed EHP
10% Smallest	13.83	13.19	4.63	12.06	11.69	3.07	14.01	13.46	3.92
20% Smallest	13.85	12.87	7.05	12.00	11.42	4.82	14.05	13.20	6.01
40% Smallest	13.79	12.37	10.29	11.95	11.09	7.21	14.08	12.84	8.81
50% Smallest	14.19	12.63	11.03	12.32	11.36	7.80	13.88	12.57	9.44
10% Middle	14.23	13.13	7.76	12.35	11.68	5.36	14.29	13.35	6.64
20% Middle	14.27	12.76	10.57	11.91	11.03	7.41	14.23	12.94	9.04
40% Middle	14.02	12.05	14.06	12.16	10.92	10.17	14.01	12.32	12.09
50% Middle	14.11	12.04	14.67	12.22	10.92	10.67	14.11	12.33	12.63
10% Biggest	13.89	12.37	10.98	12.03	11.10	7.74	14.06	12.73	9.41
20% Biggest	13.97	11.91	14.76	12.14	10.83	10.76	14.22	12.41	12.74
10% Mixed	13.81	12.67	8.24	11.92	11.24	5.70	13.85	12.87	7.05
20% Mixed	13.79	12.00	12.98	11.88	10.77	9.35	13.90	12.35	11.19
40% Mixed	13.91	11.42	17.84	11.89	10.31	13.33	14.10	11.92	15.48
50% Mixed	13.82	11.14	19.34	11.84	10.11	14.63	14.06	11.69	16.82
10% NS Mixed	13.94	12.59	9.67	12.12	11.30	6.77	14.08	12.92	8.28
20% NS Mixed	13.86	11.95	13.77	12.05	10.85	9.98	14.07	12.40	11.88
40% NS Mixed	13.78	11.29	18.06	11.89	10.28	13.54	14.03	11.83	15.68
50% NS Mixed	13.75	11.03	19.81	12.16	10.38	14.66	14.03	11.61	17.24

The frictional resistances in fouled conditions were compared with the calculated C_F values through Karman–Schoenherr (1932), which represents the smooth conditions. Then, all percentage increases in ΔC_F and hence ΔP_E for the case ships at cruise speed were summarized in Table 5-1.

The percentage increases for 270 m LNG ship sailing at 12 knots were given in Table 5-1. Increases in ΔC_F vary in a range from 21.9% to 58.91% and change in ΔP_E vary from 13.79% to 37.11% for the configurations of the 10% coverage rate. While 20% coverage rate caused an increase in these values from 35.65% to 87.59 for ΔC_F and from 22.42% to 54.91 for ΔP_E , the configurations of 40% coverage changed these ranges from 55.12% to 116.71% and from 34.57% to 73.07% for ΔC_F and ΔP_E respectively. Finally, the predictions for 50% mixed are 128.06% for ΔC_F and 80.04% ΔP_E , whereas these values are 133.77% for ΔC_F and 83.65% for ΔP_E for 50% NS mixed for the percentage increases in ΔC_F and ΔP_E , respectively.

The full-scale predictions for the 180 m bulk-carrier at 12 knots were made as to be in a range from 22.23% to 61.20 for ΔC_F and from 15.52% to 42.72% for ΔP_E for the configurations of 10% coverage. Whereas these numbers altered to the values from 36.68% to 90.89% in ΔC_F and from 25.48% to 63.26% in ΔP_E for 20% coverage rate, respectively. The 40% and 50% configurations caused an increase in a range from 56.50% to 121.31% and from 62.40% to 139.34 in ΔC_F whereas this ranges changes to from 39.48% to 84.41% and 43.42% to 96.87% in ΔP_E , respectively.

On the other hand, the 60 m special purpose vessel sailing at 12 knots, under the fouled conditions that tested in the study, showed increases in a range from 24.78% to 59.06% and from 40.24% to 93.47% in ΔC_F , whereas values of the range altered to from 9.82% to 23.40% and from 15.96% to 37.06% in ΔP_E for 10% and 20% configurations respectively. The configurations of 40% coverage lead to increases in the C_F within a range of 63.42% to 137.72% and a range of 25.17% to 54.7% in ΔP_E , whereas these values altered to 69.83% and 153.84% in ΔC_F and 27.61% and 60.92% in ΔP_E respectively for 50% configurations.

The results for 120 m special purpose vessel sailing at 14 knots showed increases in ΔC_F , range from 24.35% to 66.67% whereas increases in ΔP_E were predicted to be in a range of 15.27% to 41.76% for 10% configurations. The 20% coverage rate in the same sequence showed increases in ΔC_F range from 39.12% to 89.27% whereas this range altered to from 24.52% to 55.94% in ΔP_E . The increases for the configurations of 40% and 50% were predicted to be in a range from 61.38% to 130.39% and from 67.18% to 149.71% in ΔC_F whereas these values altered to 38.49%, 81.77%, 41.98% and 93.9% in ΔP_E respectively.

The predictions for 250 m tanker ship sailing at 14 knots showed a possible increases range from 22.92% to 53.35 in ΔC_F while ΔP_E exposed to increases ranges from 12.73% to 34.49% for 10% configurations type respectively. The configurations of 20% coverage caused an average increase in a range from 36.82% to 91.09% in ΔC_F and from 20.44% to 50.5% in ΔP_E , respectively. The 40% and 50% configurations increased C_F in a range from 57.44% to 120.33% and from 62.28% to 137.68% whereas there number altered to from 31.88% to 66.81 from 34.63% to 76.44%.

Finally, the percentage increases in ΔC_F and ΔP_E for 230 m container ship which sails at 24 knots are predicted to be 49.66% and 31.92% for 10% mixed 60.05% and 38.62% for 10% NS mixed and 71.82% and 46.15% for 10% B type configuration, respectively. These values have changed to 86.08% and 55.3% for 20% mixed 93.3% and 59.78% for 20% NS mixed and 103.16% and 66.22 for 20% B type configuration. As expected, the highest values were observed for the 50% mixed and 50% NS mixed configurations with increases of 149.01% and 153.67% in ΔC_F and 95.74% and 98.74% in ΔP_E respectively. The configurations of 40% mixed and 40% NS mixed showed close increases to the 50% configurations with the increases of 133.32% and 134.24% in ΔC_F and 85.51% and 86.33% in ΔP_E , respectively. The percentage increases in ΔC_F and ΔP_E due to Smallest and Middle configurations range from 27.17% to 69.57% and ranges from 48.87% to 102.65% in ΔC_F whereas these values changed to from 17.48% to 44.65% and from 31.40% to 65.98% in ΔP_E .

Overall, the percentage differences in P_E between the configurations that settled according to the ASTM standards and according to the proposed natural settlement showed interestingly close values to each other. The highest difference in P_E with 6.7% belonged to the 10% coverage configurations of container ship case whereas this value was 10.39% for the C_F . The results showed that the differences in C_F and P_E between natural settlement and standard settlement configurations for those which have the same coverage rate decreased as the coverage rate increased from 10% to 50%. Interestingly, configurations of 40% coverage showed almost identical increases so that the lowest differences between C_F and P_E were observed between 40% NS mixed and 40% mixed configurations. These values are slightly lower than the values that the author estimated, and there is a room for researching the reason for this difference. The differences between C_F and P_E can be seen in Table 5-1.

The percentage speed reductions at fixed effective power in cruise speeds due to fouling conditions were calculated through equation (5.8) and shown in Table 5-2 and Table 5-3. The results showed that the percentage reduction in speed ranges between 5.23% and 20.46%, which corresponds to a speed loss of 1.24 - 4.91 knots for 230 m container ship sailing at 24 knots. The percentage speed reduction for 270 m LNG ship sailing at 12 knots was predicted to be in a range between 4.21% and 18.34% which converts to a speed loss of 0.52-2.32 knots.

The predictions for 180 m bulk-carrier and 60 m special purpose vessel sailing at 12 knots were carried out, and results showed that the percentage reduction in ship speed changes between 4.7% and 20.21% and between 3.07% and 14.66% which correspond to speed losses of 0.56-2.48 knots and 0.37-1.78 knots respectively.

The fouling conditions in the study reduced the ship speed in a range between 4.63% and 19.81% and between 3.92% and 17.24% respectively for the ships of 120 m special purpose vessel and 250 m tanker ship sailing at 14 knots. The speed losses for these ships ranged between 0.64 and 2.72 knots, and between 0.55 and 2.42 knots respectively for 120m special purpose vessel and 250m tanker ship.

5.4 Discussion of the Results and Conclusions

An experimental study investigating the effect of barnacle on ship resistance and powering has been presented. The 3D printed artificial surfaces were used for modelling barnacle fouling. The flat plates covered with barnacles were towed, and total resistances of plates were measured over a specific range of speed. The frictional resistance values were then calculated.

Finally, the overall drag method of Granville (1987) was employed to calculate the roughness functions of the test surfaces and then the changes in frictional resistance at ship scale were predicted by using Granville's similarity law scaling for the case studies. The increases in frictional resistance and effective power over a different range of ship speeds were illustrated in diagrams. Moreover, based on the assumption of fixed effective power, possible speed reductions due to fouled conditions were calculated for various ship design speeds.

This study revealed that barnacle fouling has a severe effect on ship resistance and powering. An interesting outcome from the results is that the settlement pattern does not affect the frictional resistance and power as much as expected, especially at the ship scale. Also, it is demonstrated that increased coverage rate minimises the effect of settlement pattern, which means rates of differences in C_F and P_E between the natural settlements and standard settlements decrease with the increase in coverage rate.

The range of percentage increases varies from 27.17% to 153.67% in C_F , 17.748% to 98.7% in P_E for a 230 m Container ship cruising at the design speed of 24 knots. These values altered to 221.90% and 133.7% in C_F , 13.79% and 83.6% in P_E for a 270 m LNG ship at a design speed of 12 knots. These increases were predicted to be 22.23% to 139.34% in C_F , 15.52% and 96.87% in P_E for 180 m of Bulk-carrier at 12 knots whereas these values changed to 24.35% and 149.7 in C_F , 15.27% and 93.9% in P_E for 120 m special purpose vessel at design speed of 14 knots. Finally, the percentage increases in C_F and P_E ranged from 24.78% to 153.8% and 9.82% to 60.9% for a 60 m

special purpose vessel at design speed of 12 knots whereas these values altered to from 22.92% to 137.68 in C_F and from 12.73% to 76.44% in P_E for a 250 m tanker.

The average difference in ΔC_F between standard and natural settlement configurations were predicted to be up to a maximum of 10.53% at model scale results. The percentage differences ranged from 0.92% to 10.53% in ΔC_F and from 0.21% to 6.7% in ΔP_E due to settlement pattern at full-scale results.

Due to fouling conditions, the percentage speed reductions at fixed effective power were predicted to be in a range from 5.23% to 20.46% at a ship speed of 24 knots for 230 m of Container ship, from 4.21% to 18.34% at a ship speed of 12 knots for 270 m LNG carrier and from 4.7% to 20.2% at a ship speed of 12 knots for a 180 m of Bulk-carrier. These values changed to from 4.6% to 19.8% at a ship speed of 12 knots for 120 m of special purpose vessel, from 3.07% to 14.66% at a ship speed of 12 knots for 60 m of special-purpose vessel and from 3.92% to 17.24% at a ship speed of 14 knots for 250 m tanker.

It can be seen from the above figures that added resistance values shows an increasing trend with increasing ship speed. However, the slope of this increase is higher at especially low speeds compared to the slope at high speeds which means the increase in the added resistance is higher at slow speed than the increase at high speeds. The effect of roughness on the frictional resistance is mainly related to length and towing speed of the object in question.

As tabulated in Table 17, for a given ship speed and surface condition, the increase in the frictional resistance due to roughness is more significant for the small length of the plate. For example, at 12 knots NS Mixed barnacle configuration caused increases of 153.84%, 139.34% and 133.77% in the frictional resistance for 60 m length of the flat plate, 180 m length of flat plate and 270 m length of the flat plate, respectively.

This can be attributed to the fact that the viscous length scale decreases with the decreasing Reynolds number. For constant speed, the viscous length scale is increasing with the increasing values of the Reynolds number, and the effect of roughness on the frictional resistance should, therefore, decrease with increasing ship length. This outcome is consistent with the outcome given in Demirel (2015).

As seen from Table 17, for constant speed and roughness condition, an increase in the frictional resistance and the increase in the effective power show differences, as expected. This difference depends on the total resistance coefficients of the ships used in the case studies since, in this study, the effective power is calculated as a function of total resistance coefficient. Since the total resistance coefficient of a ship is a unique value for speed, the effect of roughness should be assessed, particularly for each ship. This means even for a similar roughness condition, speed and length, the increase in the effective power show differences and therefore, it needs to be calculated separately for each case.

For example, although 230 m Container ship and 60 m Special purpose vessel have nearly same changes in frictional resistance with 153.67% and 153.84% increases, corresponding changes in the effective power are 98.74% for Container ship and only 60.92 for 60 m Special purpose vessel. This can be attributed to the fact that the C_T values of the 60 m of Special purpose vessel are comparatively larger than the C_T values of 230 m Container ship.

The proposed diagrams are suitable for predicting the increases in frictional resistance, effective power and hence fuel consumption due to fouling conditions. In addition to that, the presented possible speed reductions due to given fouling conditions can be used as a reference source for ship operators. Therefore, the author hopes that this research may support decision-makers by helping them to decide on the most effective ship hull cleaning and maintenance schedule for barnacle fouling

6 Time-Dependent Biofouling

Growth Model

6.1 Introduction

The International Maritime Organization (IMO) identified marine biofouling as one of the primary problems from both economic and ecologic points of view. It threatens the ecological balance of world seas by transferring invasive aquatic species and causes a reduction in hydrodynamic performance of ships, which in turn increases fuel costs and greenhouse gases (GHG) emissions.

To minimise these effects, IMO introduced a biofouling management plan/guideline and strongly suggested that its application should come into force for ships. The biofouling management plan shows that choosing the appropriate antifouling system is a critical decision, and this process needs to be supported by technical advisors. The factors that need to be considered while choosing an antifouling system are defined as follows: expected dry-docking periods, ship speed, ship operation profile, ship type and legal requirements (IMO, 2012).

As presented in Chambers et al. (2006) several methods are currently being used to mitigate biofouling, however, for now, the best known and useful approach is the fouling control coatings in protecting ships against biofouling accumulation (Tezdogan and Demirel, 2014). The main types of coating technologies are Self-Polishing Copolymer (SPC), Controlled Depletion Polymer (CDP), conventional paints and Foul-Release coatings. Although these coatings have different working mechanisms, they can be categorised as biocidal and non-biocidal coatings. Products of biocidal technologies which are SPC, CDP and conventional type of coatings release copper ions and booster biocides to prevent biofouling on the ship hull. SPC, CDP, and conventional type coatings are effective against invertebrate organisms, but SPC type paints have longer maintenance spans (~5 years) compared to CDP (~3

years) and conventional paints (~12–18 months). The SPC technique uses a chemical reaction through hydrolysis of heavy metals by also smoothing itself, whereas CDP technique has a soluble matrix physically dissolving in water by releasing biocide. However, it underperforms during stationary times of ships, and its self-smoothing feature is not as useful as SPC type paints (Chambers et al., 2006). The foul-release coatings, with an environmentally friendly approach, do not release toxic substances but reduce attachment strength of fouling organisms and release attached organisms when the ship is underway. Foul-release coatings have a very different surface texture which in general leads to lower added resistance for a newly applied coating than is the case for CDP and SPC coatings (Anderson et al., 2003). However, this type of coatings can clean itself at high speeds (>15 knots) and is sufficient for ships which have high activity operating profile. Otherwise, they need to be cleaned frequently. Besides, these paints are prone to abrasion damage because of their surface features (Dafforn et al., 2011).

In general, an antifouling coating's performance is tested through various ageing tests for more than ten years before being available in the market (Kiil and Yebra, 2009). These ageing tests can be separated into two groups: laboratory tests and field tests. The standard testing process starts with short-term laboratory tests to evaluate the formulation/material used in the paint and follows with medium-term (months) tests to measure the polishing and leaching performance of the coating. The products which show satisfactory performance are transferred to field tests which are comparatively long-term tests, including static tests, dynamic tests, and ship tests. Paint manufacturers have to rely on these long-term tests for checking paint performance on a regular period since a potential mistake in paint design would cause high-cost penalties. The static tests conducted by immersing the coated test panels into natural seawater simulate the conditions that coating would be exposed to during the ship's idle times. Test sites are usually selected from the regions as diverse as possible, such as relatively cold, temperate and warm environments to test coating performance. Dynamic tests, additionally aim to provide shear stress on coating plates immersed in natural seawater usually via a rotating mechanism (i.e., rotating drum) for evaluating the performance of the coating in dynamic conditions. These tests are useful to determine the polishing rates of self-polishing coatings and releasing ability of foul-

release coatings (Sanchez and Yebra, 2009). An approach of combined static and dynamic tests, and also ship tests were proposed as a more realistic way to simulate antifouling coating performance under real conditions (Lindholdt et al., 2015; Swain et al., 2007). Despite the fact that the ship tests bring potential higher accuracy, implementation of these techniques poses various problems associated with the preparation of a large amount of paint, coordination with the ship-owner and regular monitoring of paint performance on the ship hull. Even though dynamic testing is reasonably cheap compared to ship tests, it is still more expensive compared to static tests as the test rig needs motion, which means continuous power usage.

A tailor-made condition assessment should be made by considering the factors mentioned above, and this assessment requires a time-dependent biofouling growth model to estimate and mitigate the losses due to biofouling. This model can be used as a decision support-tool, regarding the effect of biofouling roughness on ship frictional resistance and hence the increase in power requirement as well as for deciding the appropriate maintenance schedule. In this study, a simplified time-dependent biofouling growth model was proposed based on the long-term antifouling field test data for estimating the increase in frictional resistance and powering due to marine fouling on the ship hull. First, fouling ratings (FR) and surface coverages (SC) for calcareous type fouling were converted into the equivalent sand roughness heights in accordance with the data provided by Schultz (2007) and Uzun et al. (2017). Then, the equivalent sand roughness heights were employed in Granville's similarity law scaling process (Granville, 1958; Granville, 1987) with the provided roughness functions of corresponding fouling conditions to calculate the increases in frictional resistance. Finally, the increases in the effective power of the ship due to the increase in frictional resistance were calculated for calm water conditions.

First, the developed model was tested and validated using a one-year-long operation data of a 176-m handy-max oil tanker. The fouling ratings, surface coverages for calcareous type fouling, increase in frictional resistance and powering were predicted during this time. Then, the results were validated through comparisons on real-world operation data, acquired via on-board data acquisition system and that were filtered to only retain those data recorded in calm water conditions.

Besides, a case study was performed using a three-year-long operation data of 258 m crude oil carrier. The same analyses were conducted for this case, and increases in effective power were predicted and then compared to the ship performance report provided by a ship performance analysis company.

6.2 Modelling Approach

6.2.1 General Perspective

The main aim of this study is to predict the increases in ship frictional resistance and powering due to the accumulation of biofouling on a ship hull during a selected ship operation period. To achieve these goals, two complementary models, namely, the time-dependent biofouling growth model and the added frictional resistance prediction model, were developed. The first model, predicts biofouling growth by taking idle times into account during a ship operation period based on the acquired field test data for a specific antifouling coating which the ship is painted with. The second model then estimates increases in ship frictional resistance and powering based on the predicted biofouling condition for the ship under consideration. The developed models are explained in detail in the following sections.

6.2.2 Ideal Biofouling Growth Model

The relation between environmental conditions and biofouling growth is investigated through laboratory or field experiments. Marine biofouling growth on a specified surface, with unlimited experimental data, would have been formulated as in relation to the parameters listed in Eq. (6.1) (Woods Hole Oceanographic Institute, 1952) (Lehaitre et al., 2008).

$$BG = f_1(SST, psu, pH, v, I, S, t, m_t, \sigma, \theta_c, R_t, \eta_c) \quad (6.1)$$

where BG is biofouling growth, SST is seawater surface temperature, PSU is salinity (dissolved salt content of the water), pH is acidity, v is speed of the water flow, I is light intensity, S is concentration of nutrients, t is time of the exposure to water, m_t is

micro-texture of surface, σ is surface potential, θ_c is the contact angle which is a measure of wettability, R_t is a roughness parameter which is the total height of the roughness profile and η_c is an antifouling coating performance parameter (efficiency of the antifouling coating including performance of chemical contents and leaching rate). Although it is not well established, surface colour and contour have various effects on biofouling growth as well (Gregory and Bhushan, 2012).

Despite the fact that there are a substantial amount of experimental and modelling studies on biofouling growth, these studies rather have been focused on a single type of biofouling growth or the effect of few parameters (Darvehei et al., 2018). Therefore, a comprehensive biofouling growth model that predicts biofouling growth rate under varying environmental conditions does not exist. There are significant barriers in the path to a thriving comprehensive biofouling growth model. This sort of comprehensive growth model considers the effects of various parameters shown in equation (6.1) and validation of the model becomes more complicated as the number of parameters increase. It is important to note that validation of the model with many parameters needs large data collection which requires extensive time and resources.

Moreover, the environmental conditions, even on the same day, show differences for the outdoor experimental studies and these regularly fluctuating parameters make prediction difficult for short term models. However, if the model is designed for the long term, these issues can be simplified. For instance, the effect of seasonal changes on biofouling growth in a particular location can be averaged through 2–3 years long field tests.

Biofouling growth models with this amount of parameters are not useful for the end-users such as naval architects, ship operators and ship owners. A simplified long term model with a limited number of parameters would be applicable and more comfortable to validate. This model may be helpful for end-users as a preliminary attempt of a decision support-tool by providing a prediction on biofouling growth as well as the increase in power requirements due to this growth.

6.2.2.1 Simplification of the Ideal Model

The author proposed the following simplifications over the ideal formulation to develop a simplified biofouling growth model for ships. A list of simplifications and the development of the simplified equation were presented together with the explanations supported by the researches in the literature.

The conducted simplifications are;

- Surface properties (m_t , σ , θ_c , R_t)

The surfaces properties such as m_t , σ , θ_c and R_t affect biofouling on the surface. Hydroids, bryozoans and ascidians search the surface for grooves, pits, cracks, and crevices in the micro-texture (m_t) to settle in for protection against steady water flow (Fingerman et al., 1999; Railkin, 2004). Microfouling organisms are in search of a hollow that they can settle in for maximum protection and attachment points which enable them to have higher adhesion strength (Scardino et al., 2008).

The extracellular polymeric substance (EPS) flows into the crevices formed by surface roughness (R_t). This enables organisms to have strong bio-adhesion on the rough surfaces whereas adhesive contacts only on surface asperity peaks on the smooth surfaces cause low bio-adhesion strength (Gregory and Bhushan, 2012). The maximum peak-to-through roughness height, in general, varies between 30 and 150 μm for newbuilding applications depending on the quality of the application and the type of coating. For example, the maximum peak-to-through roughness height is expected to be in a range between 30 and 129 for SPC type coatings whereas this range changes to 7 and 85 for FR coatings (Howell and Behrends, 2006; Candries, 2001).

Surface potential (surface charge) (σ) also influences the attachment of micro-organisms. Kerr et al. (1998) showed that applied negative surface potential (between 65.4 and 230.4 mV) reduces bacterial fouling whereas positive surface potential (34.5–234.9 mV) increased the percentage of settlement compared to the uncharged reference surface. However, this amount of change

in surface potential cannot occur unless it is applied from outside, which is not practical for antifouling coatings on the ship hulls.

The wettability of a surface is assessed by the contact angle (θ_c); where the contact angles are less than 10° , the surface behaves superhydrophilic, which shows high wettability and high surface energy. On the other hand, contact angles over 150° are classed as superhydrophobic surface and exhibit low wettability and low surface energy. Despite the fact that microorganisms prefer to attach on hydrophilic surfaces, this may change according to the type of species, i.e., hydrophobic surfaces are more suitable for *Ulva linza* (Gregory and Bhushan, 2012). Polyurethane-based antifouling coating formulations, which include biocides exhibit stable behaviour in terms of wettability, whereas silicone-based coatings may go hydrophilic in time (Silva et al., 2019).

As the intention of the model is to predict biofouling growth on a particular specific coating that applied on a ship, the author believes that long term lab and field test data would capture the effects of surface properties on biofouling growth. It is assumed that the applied coating type will not change during the ship operations for the foreseen duration. The effects of environmental factors (temperature, salinity, etc.) on coating surface properties such as roughness and texture were ignored. However, the author believes that the effect of changing surface properties can be measured by the field tests. Therefore, these effects were also taken into account and represented by the antifouling coating parameters. The only surface parameter that substantially changes with the environmental conditions is the η_c , (antifouling coating performance parameter), and it will be one of the main parameters that the model stands on.

- Light intensity (I)

Light intensity and light spectrum are parameters that strongly affect plant type biofouling community from microalgae to weeds. It is associated with the water depth in the models presented in the literature (Darvehei et al., 2018). Photosynthetic macrofouling types, mostly algae, are generally common in the

0–40 m range where is rich in nutrients and with high light level. However, other types of organisms (mussels, barnacles, tubeworms, etc.) which get their energy from the sources in the sea, can grow at deeper waters without having affected by light intensity (Lehaitre et al., 2008). It should be noted that as the ship draft ranges between 5 m and 20 m for large merchant vessels, it can be assumed that light intensity will not be varying by a large extent. Therefore light intensity and light spectrum of the locations are accepted as the same with the places where the biofouling field test is conducted.

- Concentration of nutrients and water flow velocity (S , v)

Nutrient abundance is critical for marine fouling from biofilm formation to macro fouling as all living organisms need food to sustain their lives. At this point nutrient abundance is also connected with seawater flow rate and closeness of location to shore. Coastal waters are generally richer than oceanic waters in terms of nutrient abundance due to human-based discharges (Lehaitre et al., 2008). Therefore, as ship gets closer to shores, biofouling growth accelerates. With the available data, biofouling growth is modelled when the ship stays at ports at stable water velocity, and the concentration of nutrients is accepted as same for every port.

- pH

Due to the lack of data about the effect of pH on total biofouling growth rather than on a particular species, it is not possible to model responses of pH changes. However, as stated in Cullimore (1999), Kroeker et al. (2013) and Darvehei et al. (2018) pH levels between 6.5 and 10 are suitable for an extensive range of biofouling organisms. Furthermore, as shown in Takahashi et al. (2014), pH values of seawater range from 7.74 to 8.4 on a global scale. Considering this limited change in pH values on world seas, the effects of pH on biofouling growth were simplified for this model.

- Salinity (PSU)

Salinity is a decisive parameter for the growth of biofouling organisms and different types of biofouling have varying reactions to salinity changes (Thiyagarajan et al., 2003) (de Castro et al., 2018). Despite the importance of salinity, to the author's knowledge and as stated in (Darvehei et al., 2018), no mathematical model is covering this effect. The reasons for this might be that the salinity studies in the literature (Qiu and Qian, 1998) aim to observe salinity tolerances of biofouling organisms instead of modelling the effect of salinity on biofouling growth rate. In addition, world seas' salinity value ranges between 30 and 36 PSU and biofouling organisms' salinity tolerance covers this range. Based on the simplifications explained, the most dominant parameters were based on the antifouling coating performance parameter and exposure time to seawater.

Based on the given assumptions, equation. (6.1) was simplified and turned into equation (6.2) to model the biofouling growth on ships for the idle time periods at each port during a ship operation period. Therefore, without an intention of following the physiologically detailed mechanistic approach for formulating effects of each parameter at cell scale, a simplified growth model was developed depending on the exposure time and antifouling coating performance parameter as shown by Eq. (2)

$$BG = f_2(t, \eta_c) \quad (6.2)$$

$$\eta_c = g(\Delta SST) \quad (6.3)$$

where t is the exposure time and η_c is the antifouling coating performance parameter, and ΔSST is the change in sea surface temperature. It is important to note that coating performance exhibits differences according to the geographical region. This can be attributed to the fact that temperature has the dominant effect on the biofouling growth

as stated in Thiyagarajan et al. (2003), Qiu and Qian (1998), Villanueva et al. (2011), Farhat et al. (2016) and Lord (2017). Therefore, the change in sea surface temperature (Δ SST) was used as a parameter to predict the changes in coating performance, as shown in equation (6.3).

6.2.3 Development of a Time-Dependent Model for an SPC type antifouling coating

6.2.3.1 Field Test data

Extensive static field tests data were provided by a paint company for an SPC type antifouling coating paint product. The tests were conducted from one to three years in two regions, including Mediterranean and Equatorial regions, which are environmentally diverse in terms of geographical features. In these field tests, biofouling growth on coated and immersed plates was assessed according to ASTM D6990-05 (2011), and ASTM D3623-78a (2012) performance standards and evaluations were recorded for mainly three types of biofouling accumulations through monthly observations. These analyses were then supported with image processing, which enables obtaining colour contrast and having a more accurate quantification of the fouled area, number, and size of the attached fouling organisms.

Based on the image analyses, the fouling coverages on the panels were rated by coverage rating based on coverage areas similar to Braun-Blanquet (1932) scale method. The coverage ratings with equivalent covered surface areas were presented in Table 6-1.

Table 6-1 The coverage ratings with an equivalent covered surface adapted from (Silva et al., 2019)

Coverage Rating	Covered Area (%)
0	0
1	0-2
2	3-5
3	6-25
4	26-50
5	51-100

Antifouling field tests results were analysed by a paint company, and biofouling accumulations on the test panels were categorised into three main groups: slime, non-shell organisms and calcareous type fouling. The maximum rating of each biofouling group varies considering their hydrodynamics effect on frictional drag. These types along with their maximum ratings (a) include;

- Slime: including absorbed inorganic and organic matter, trapped silt and detritus and other unidentified slimes (Rating 0–20).
- Non-shell organisms (shorter than 5 mm): Plants, soft-bodied organisms, weed, very isolated (limited) barnacle accumulation (Rating 0–50).
- Calcareous type fouling (higher than 5 mm): Barnacles, mussels, tubeworms, etc.(Rating 0–100)

A fouling rating parameter, named antifouling performance index (API) was developed independently to measure the antifouling performance of coated ship hulls by the paint company. The developed index aims to measure the effects of major foulants on the antifouling performance in dynamic conditions (Silva et al., 2019). The API formula given in Silva et al. (2019) was adapted to express the fouling rating (FR) in this study, as shown in equation (6.4). The slight difference between the FR and API is that the clean surface is represented by 0 for FR, whereas it is represented by 100 for API.

$$\begin{aligned}
FR = & (0.2 \times \text{Area covered by slime} \\
& + 0.5 \times \text{Area covered by non-shell organisms shorter than 5 mm} \\
& + 15 \times \text{area covered by calcareous fouling higher than 5 mm})
\end{aligned}
\tag{6.4}$$

where the area covered by fouling organisms is taken from the upper limit for the equivalent coverage rating.

The model aims to design a simplified long term model by averaging short term seasonal effects using 2–3 years long field data. The approach behind the model was to design it in three steps, including delay, growth, and saturation at maximum rating point. Considering this approach and in the light of previous biologic models, it was envisaged that the biologic growth model tends to follow a sigmoid function. In this study, however, it was observed that a Gaussian type fit is effective to represent the correlation between fouling rating and time. The Gaussian function is similar to the sigmoid function in nature, but it provides better accuracy with fewer parameters. Although the Gaussian function graph is a symmetric bell-shaped curve, in this study, the half-bell curve was used to satisfy the saturation phase at the maximum point. Therefore, once the rating reaches a maximum point, the fit is fixed on this point to account for the fact that growth and its hydrodynamic effects are limited. It is accepted based on the assumption that the hydrodynamic performance of the surface will gradually deteriorate in time.

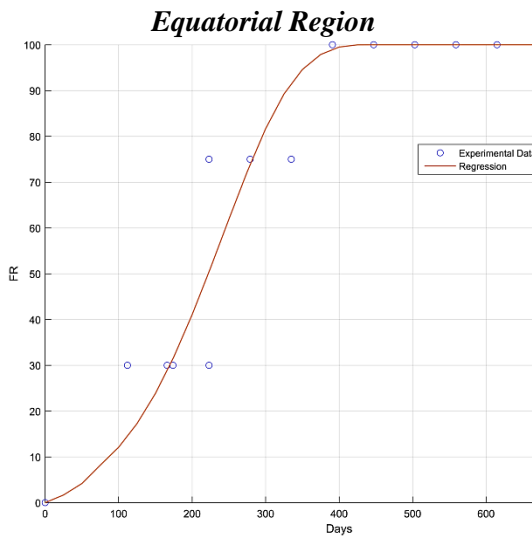


Figure 5a. Type A fouling growth according to immersed time in the Equatorial region

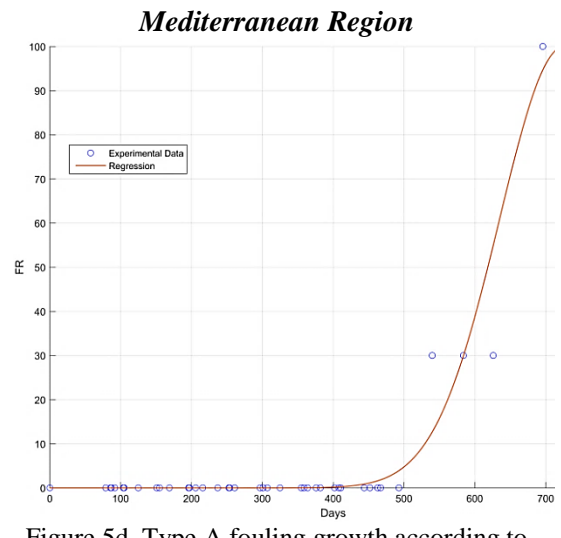


Figure 5d. Type A fouling growth according to immersed time in Mediterranean region

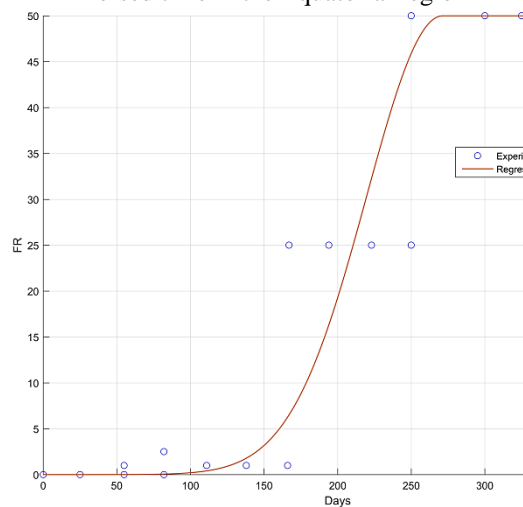


Figure 5b. Type B fouling growth according to immersed time in the Equatorial region

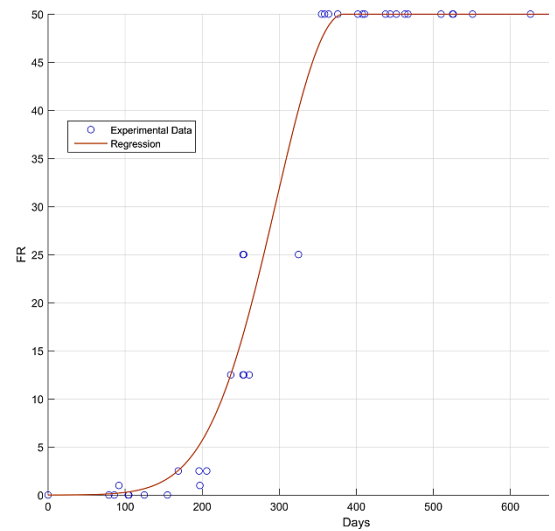


Figure 5e. Type B fouling growth according to immersed time in Mediterranean region

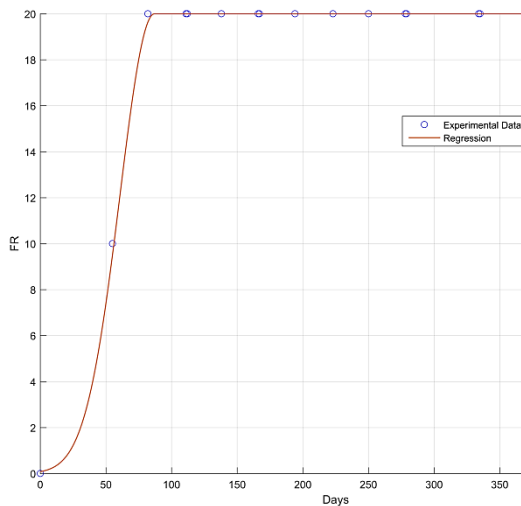


Figure 5c. Type C fouling growth according to immersed time in the Equatorial region

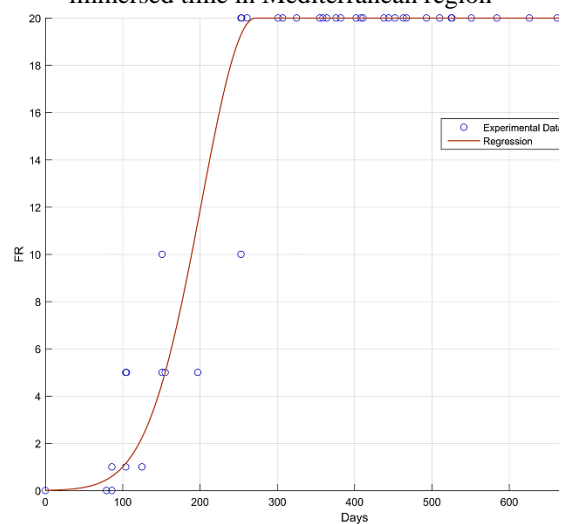


Figure 5f. Type C fouling growth according to immersed time in Mediterranean region

Figure 5a, 5b, 5c and Figure 5d, 5e, 5f illustrate the rating data for three types of fouling obtained from the field tests conducted over varying periods of time at Equatorial and Mediterranean regions, respectively. The Gaussian function shown in equation (6.5) was fitted on the data, as illustrated in the figures above. However, during the growth phase, it was observed that there are deviations between the Gaussian fit and the data points as similarly reported in Breur (2001). This deviation can be attributed to the fact that seasonal changes occur during the year since field tests are conducted via several replica test panels which are immersed at varying seasons of the year. Therefore, the replica panels immersed in the warm seasons show rapid biofouling growth compared to those, which were immersed in the cold seasons.

$$FR = ae^{-\left(\frac{t-t_0}{\tau}\right)^2} \quad (6.5)$$

where FR is the rated biofouling growth, a is the maximum rating, t is the sum of idle time, t₀ is the time that rating reaches to the maximum point and τ is the half-width of the bell curve. t₀ and τ are taken as coating performance parameters (η_c) since they define the time in which fouling rate reaches the maximum point and the time span of growth after the delay time. When the ship spent idle time in an arbitrary region on the route, t₀ and τ are calculated through equation (6.5) separately.

Although there are deviations between the trend and data points due to seasonal changes, the model is able to predict the general trend in the data. As the main aim of the model is to average short term effects including seasonal changes on biofouling growth by using long term field test data, the Gaussian fit is successfully employed in order to average seasonal changes on the biofouling growth. The coating performance parameters (t₀, τ) were determined via equation (6.5) fitted on the data, as shown in Table 6-2 for each type of fouling in both regions.

Table 6-2 Antifouling coating performance parameters for each type of fouling

Type of fouling	Location	t_0	τ	SPC type Antifouling Coating
Calcareous fouling (Type A)	Equatorial	379.4	187.2	
	Mediterranean	726.4	129.7	
Non-shell organisms (Type B)	Equatorial	271.4	73.11	
	Mediterranean	383.5	124.4	
Slime (Type C)	Equatorial	87	37.08	
	Mediterranean	271.9	99.31	

In order to predict biofouling growth for each individual idle time period, a specific growth rate for each period needs to be calculated and multiplied with the idle time. “A specific growth rate (μ) can be calculated by taking a partial derivative of equation (6.5) with respect to t .” The specific growth rate is the speed of the growth, and it varies according to the temperature in conjunction with geographic location. Multiplying the specific growth rate with the idle time gives the fouling growth, which specifically belongs to this individual idle time period. Therefore, if this process is repeated for each region where the ship spends idle time, the accumulative fouling rating over a period of operation can be written as given in equation (6.6).

$$FR_{tot} = \sum_{i=0}^n \left(\frac{\partial FR}{\partial t} \right)_i t_i + \left(\frac{\partial FR}{\partial t} \right)_{i+1} t_{i+1} \cdots \left(\frac{\partial FR}{\partial t} \right)_n t_n \quad (6.6)$$

It is important to note that the coverage area of calcareous type fouling is not explicitly expressed in the provided FR equation, as shown in equation (6.4). The effect of different SCs, i.e. 25% and 50%, were neglected. Without a doubt, this condition does not represent reality. Since there is no meaningful rating for calcareous type fouling, it needs to be analysed separately to predict its effect on ship resistance, appropriately. For this reason, a logistic growth model was developed based on the provided coverage area data from the field test to predict calcareous type fouling surface coverage as a function of time. The logistic function curves were fitted on the field test data for calcareous type fouling in both Equatorial and Mediterranean regions, as explained in Sarkar (2005).

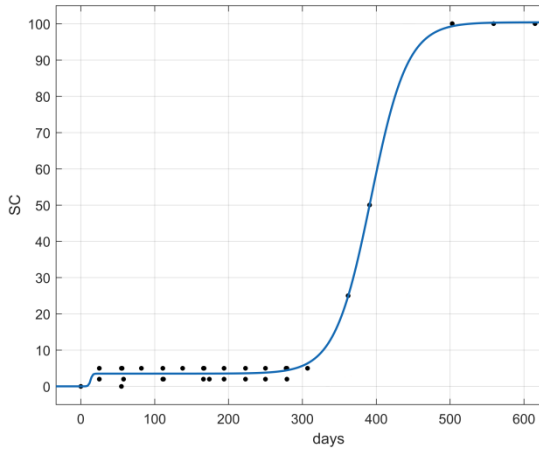


Figure 5g Calcareous type fouling surface coverage respect to time in Equatorial region

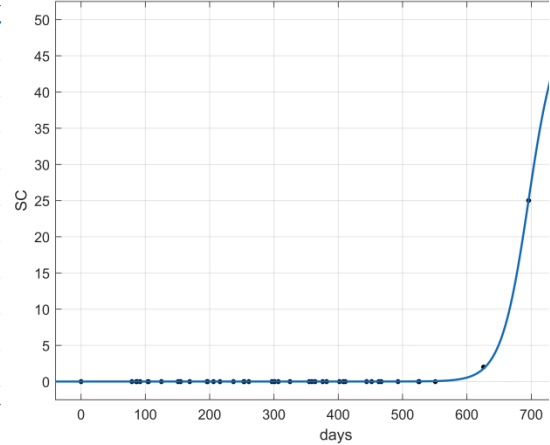


Figure 5h Calcareous type fouling surface coverage respect to time in the Mediterranean region

Figure 5g and 5h show logistic curves for SC of calcareous type fouling fitted by using equation (6.7). Table 6-3 gives constant values of the curves for both Equatorial and Mediterranean regions.

$$SC = \frac{P - p}{1 + (\exp^{b-ct})} + \frac{d}{1 + (\exp^{f-gt})} \quad (6.7)$$

where SC is the percentage of surface coverage, P, p, b, c, d, f, and g are logistic curve constants indicated in Table 6-3, t is the sum of idle times.

Table 6-3 Constants of logistic curves

Equatorial	Mediterranean
P=100	P=0.00517
b=16	b=10
c=0.0407	c=40
d=3.5	d=50
f=10.32	f=32.81
g=0.7759	g=0.04715
p=3.101	p=0

The trend between the SC and the time changes regarding the value of growth parameters which are b for Equatorial region and f for the Mediterranean region. This parameter for an arbitrary region can be predicted similarly by using temperature in equation ((6.9), as will be explained in Section 6.2.3.2 below.

By taking the partial derivative of equation (6.7) with respect to t, the expansion rate can be calculated. Then, multiplying the rate at which SC expands with the idle time gives the calcareous type fouling SC, which specifically belongs to this individual idle time period. In order to predict accumulative SC during the total operation, this process is repeated for each idle time. This can be expressed by equation (6.8)

$$SC_{tot} = \sum_{i=0}^n \left(\frac{\partial SC}{\partial t} \right)_i t_i + \left(\frac{\partial SC}{\partial t} \right)_{i+1} t_{i+1} \dots \left(\frac{\partial SC}{\partial t} \right)_n t_n \quad (6.8)$$

6.2.3.2 Effect of Temperature on Biofouling

The type and SC of biofouling accumulation on an antifouling coating indicate the performance of the coating. Since biofouling growth is strongly dependent to sea surface temperature as indicated in several studies (Crisp and Bourget, 1985; Epelbaum et al., 2009; Farhat et al., 2016; Qiu and Qian, 1998; Thiyagarajan et al., 2003), sea surface temperature is accepted as the dominant parameter for antifouling coating performance as shown in equation (6.3). Due to the limited availability of field test data, the antifouling coating performance parameters and logistic curve growth parameters (b or f) for an arbitrary region were interpolated or extrapolated by using equation (6.9), which is based on the performance parameters obtained from the field tests. Equation (6.9) shows the linear extrapolation or interpolation process for antifouling coating performance parameter.

$$\eta_{ca}(\Delta SST) = \frac{\eta_{cy}(SST_a - SST_x) + \eta_{cx}(SST_y - SST_a)}{SST_y - SST_x} \quad (6.9)$$

where η_{ca} is the antifouling coating performance parameter at an arbitrary location, η_{cy} is the performance parameter of the coating at the field test location y, η_{cx} is performance parameter of the coating at the field test location x, SST_a is the sea surface temperature at an arbitrary location, SST_y is the sea surface temperature at the location y, SST_x is the sea surface temperature at the location x.

It should be noted that as the ship moves from one port to another port, the model calculates new parameters to be employed in equation (6.5) and equation (6.7) to predict FR and SC for calcareous type fouling in an arbitrary region on the ship route.

The seawater temperature at any arbitrary location SST_a was predicted via a function based on the latitude degree of the location. This regression was fitted on the data collected from NOAA (National Oceanic and Atmospheric Administration) for average sea surface temperature (Pielke, 2012). The regression for SST_a is presented in equation (6.10). It is important to note that differences in SSTs due to longitude changes were neglected as these differences are relatively small compared to those in latitude as given in Bijl et al. (2009).

$$SST_a = 12.5 + 15 \left(\cos \left(\frac{\textit{latitude degree}}{28.64} \right) \right) \quad (6.10)$$

The author is aware that reproducing coating performance parameters for the locations in question by using a single parameter (temperature) over the field test data sets at two different locations would not precisely simulate real conditions. Nevertheless, the author proposes a pilot study for attempting to develop a simplified biofouling growth model to be utilised for the prediction of ship energy efficiency. Furthermore, it is essential to take into account that the model is flexible to utilise further field data set at extensive locations, and improving the capacity of field test data as it will lead to the more accurate growth model.

6.2.4 Added Resistance and Powering Prediction Tool

The prediction of the ship frictional resistance and powering due to the change in roughness profile of the ship hull caused by biofouling accumulation has been calculated according to the following procedure. The required effective power for a ship can be calculated by equation (5.4). Total resistance can be represented as recommended by the ITTC (1978), as shown in equation (6.11):

$$R_T = R_F + R_R + \Delta R_F + R_{AA} \quad (6.11)$$

where R_F is the frictional resistance, the R_R is the residual resistance, the ΔR_F is the increase in the frictional resistance due to biofouling, and the R_{AA} is the air drag resistance. In terms of total resistance coefficient, C_T , as per equation (6.12):

$$C_T = (C_F)(1 + k_0) + C_R + \Delta C_F + C_{AA} \quad (6.12)$$

where $(1 + k_0)$ is the form factor, C_F is the base frictional resistance coefficient, C_R is the residual resistance coefficient, C_{AA} is the air drag coefficient, and ΔC_F is the

increase in frictional resistance due to biofouling. Therefore it is possible to calculate the effective power (equation (5.4) according to equation (5.5)):

The percentage increase in the frictional resistance and effective power is expressed by equation (6.13) and equation (5.6), similar to the one used by Tezdogan et al. (2015) and Demirel et al. (2017b).

$$\Delta R_T\% = 100 \frac{\Delta R_F}{R_T} \quad (6.13)$$

where C_{TR} is the total resistance coefficient in rough condition, C_{TS} is the total resistance coefficient in a smooth condition which needs to be known in order to calculate ΔP_E for the ship in question. However, the calculation of C_{TR} is not an easy task to perform, and it requires determination of the drag characteristics of the hull roughness.

Drag characterisation, in other words, determination of roughness functions, of any specified arbitrarily rough surface which is the test surfaces covered with biofouling accumulation in this study, can be revealed thanks to similarity laws of turbulent shear flows. The roughness functions of a rough surface can be determined through direct and indirect methods.

The direct method can be used to measure the velocity profile of the boundary layer close to surfaces in a flow facility (Granville, 1987). On the other hand, roughness functions can be obtained via indirect methods, i.e. by measuring pressure drop in pipe flow (Nikuradse, 1933) or the total drag of flat plates (Granville, 1978) and the torque on rotating disk (Granville, 1982). Even though the methods may show variations in the application, there is a similarity in these procedures, which is plotting the appropriate drag coefficient against the relevant Reynolds number.

Roughness causes a downward shift in the velocity profile, which is commonly shown as ΔU^+ . It is a function of the roughness Reynolds number k^+ defined as the ratio of the roughness length scale k to the viscous length scale, as explained in Schultz (2004). The roughness effect on a log-law velocity profile can be seen in Figure 6-1 (Schultz and Swain, 2000).

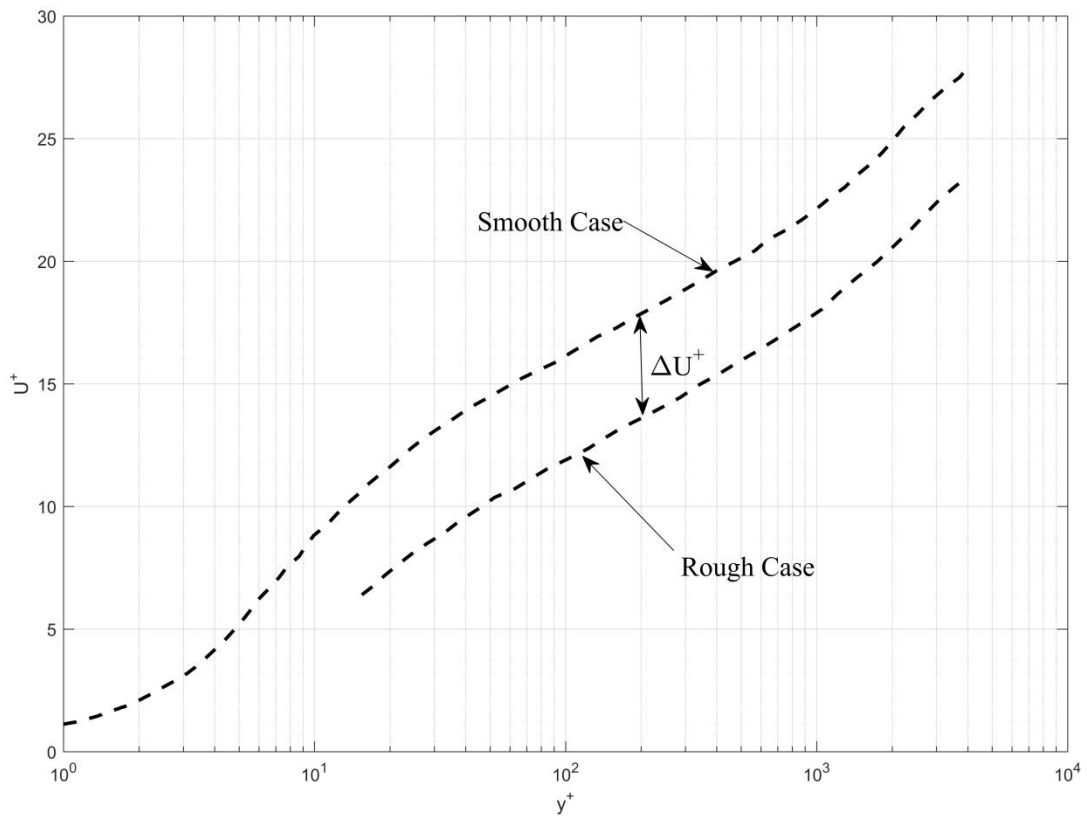


Figure 6-1 Illustration of a downward shift in log-law velocity profile due to the roughness effect (adapted Schultz and Swain 2000)

where U^+ is the non-dimensional velocity in the boundary layer and y^+ is the non-dimensional normal distance from the wall. Details can be found in Schultz and Swain (2000) and (Hama, 1954). Once the roughness functions are determined, i.e. $\Delta U^+ = f(k^+)$ for any test surfaces covered with specific roughness due to biofouling accumulation, the frictional drag of a ship or any object covered with this specified roughness can be found through similarity law analysis (Granville, 1958, 1987). When ΔC_F is calculated, it is employed in the equation 6, and the percentage increases in the effective power are calculated.

6.2.4.1 Fouling ratings and roughness functions correlations

The roughness functions of any surfaces covered with the biofouling accumulation are required to calculate the increase in frictional resistance of the ship and need to be determined experimentally. However, conducting an experimental study with living organisms faces several challenges, for instance, protecting the surface with organisms while transferring it to a test facility as well as controlling differences in environmental

conditions. In addition, any biologic substance leakage into the test facility may cause significant financial penalties.

As an alternative approach to experiments, the author partially uses the roughness functions data with the corresponding equivalent sand roughness heights provided by Schultz (2007). According to the data presented in Table 6-4, predicted fouling ratings were assessed in terms of condition descriptions and converted into equivalent sand roughness heights for slime, non-shell and heavy calcareous type fouling as shown in Table 6-5.

Table 6-4 A ranges of representative coating and fouling conditions. The values of equivalent sand roughness heights and average coating roughness are based on the measurements of Schultz (2004) adapted from Schultz (2007)

Description of condition	NSTM Rating	$k_s(\mu m)$	$Rt_{50}(\mu m)$
Hydraulically smooth surface	0	0	0
Typical as applied AF coating	0	30	150
Deteriorated coating or light slime	10-20	100	300
Heavy slime	30	300	600
Small calcareous fouling or weed	40-60	1000	1000
Medium calcareous fouling	70-80	3000	3000
Heavy calcareous fouling	90-100	10000	10000

However, the roughness functions provided in Schultz (2007) are not suitable to represent the fouling conditions of 25% and 50% barnacle coverage. As indicated in Schultz (2004) and Schultz (2007) coverage areas of fouled plates for calcareous type fouling description were ~60% for medium calcareous fouling and 75% for heavy calcareous fouling. For this reason, the author used their own roughness functions for barnacle fouling proposed in Uzun et al. (2017).

The roughness functions of 20% Mix configuration in Uzun et al. (2017) were used to represent 25% coverage area whereas 50% Mix configuration in Uzun et al. (2017) were used to represent 50% coverage for calcareous type fouling in this study. The

fouling condition of which has more than 50% barnacle coverage area was represented by the roughness functions of heavy calcareous fouling provided by Schultz (2007). It is of note that, in our study, the fouling rating of 70 was taken in the k_s range of 30–1000 if there is only an initial calcareous fouling accumulation up to 5% coverage as similarly shown in Schultz (2007). Cases which have higher barnacle coverage, independently from FR, will be assessed as calcareous type fouling with coverage rating of 3, 4, and 5 according to the predicted SC area. Table 6-5 gives the surface descriptions and the corresponding characteristics used in this study.

Table 6-5 Fouling descriptions in relation with coverage ratings, percentage of coverage and equivalent sand roughness heights in conformity with roughness functions provided in Schultz (2007) and Uzun et al. (2017)

	Coverage Rating	Coverage Area	Fouling Rating	$k_s(\mu m)$	Roughness functions
Hydraulically smooth surface	0	0	0	0	
SPC type coating	0	0	0	30	Schultz (2007)
Slime	0-5	0-100%	0-20	30-300	Schultz (2007)
Non-shell organisms and very isolated barnacles (up to 5% coverage)	0-5	0-100%	0-70	30-1000	Schultz (2007)
Calcareous type fouling	3	25%	-	2000	Uzun et al.(2017)
Calcareous type fouling	4	50%	-	6000	Uzun et al.(2017)
Calcareous type fouling	5	100%	-	10000	Schultz(2007)

Then, the roughness functions were employed in the model to be used in the Granville’s (Granville, 1958, 1987) similarity law scaling procedure, similar to those performed in Demirel (2015), Demirel et al., (2019) and Schultz (2007) for the length and the speed of the ship in question for each predicted equivalent sand roughness

height. The predictions on ΔC_F were made under the assumptions that the listed fouling conditions can be simulated by the provided roughness functions and roughness length scales. The author believes that it is a well-founded assumption as Schultz (2007) approved these assumptions and applicability of this method by comparing results of his predictions with the full-scale studies of Hundley and Tate Sr (1980) and Haslbeck and Bohlander (1992). The time-dependent equivalent sand roughness height, $k_s(t)$ can be calculated by equation (6.14) and equation (6.15). These equations are based on the parameters of FR_{tot} and SC_{tot} referring to total fouling rating in equation (6.6) and the total percentage of SC area in equation (6.8), respectively.

$$k_s(t) = \begin{cases} 0.007143FR_{tot}^2 + 13.36FR_{tot} + 30, & 0 < FR_{tot} \leq 70 \\ 30, & FR_{tot} = 0 \end{cases} \quad (6.14)$$

$$k_s(t) = \begin{cases} 2.4669SC_{tot}^2 - 24.84SC_{tot} + 1065.7, & 5 < SC_{tot} \leq 50 \\ 80SC_{tot} + 2000, & 50 < SC_{tot} \leq 100 \end{cases} \quad (6.15)$$

A regression, as shown in equation (6.14) was fitted to calculate the equivalent sand roughness heights for the predicted fouling ratings. The regression given in the equation (6.15) was used to predict the equivalent sand roughness heights when the model predicts the calcareous type fouling coverage is higher than 5%. It is important to note that if the SC_{tot} is higher than 5% SC $k_s(t)$ is calculated using equation (6.15). These regressions were developed based on the equivalent sand roughness heights provided in Table 6-5.

6.3 Validation

6.3.1 A real ship application

Predictions of fouling ratings for the SC of calcareous type fouling and increases in frictional resistance were made for a 176-m tanker coated with the same SPC type antifouling coating for the duration of the one-year operation. The time-dependent fouling ratings, the SC areas of calcareous type fouling and the increases in frictional resistance of the ship were predicted over the whole duration of the operation. The results were compared against the power data acquired by on-board measurement devices.

6.3.1.1 Ship description and operation data

The ship used in this case was a handy-max oil tanker. Table 6-6 shows the main features of the ship, which is mainly operated under short term contracts, as reported in Coraddu et al. (2017). For this reason, the route of the ship is flexible and spread on the broad range of geographic locations all over the world. Therefore, it is an excellent case to validate the proposed model as the ship sails in the broader regions and spends considerable idle times at ports. The real-world dataset includes operational modes of manoeuvring, loading, unloading, sailing, and port stays. However, as the aim of this study is modelling biofouling growth during idle times during the one-year period, operational modes were divided into two groups as sailing (if the operation involves speed) and idle times (if there is no speed).

Table 6-6 Ship profile

Ship type	Oil tanker
Design Length (L)	176 m
Design Draught (T)	11 m
Design Displacement (Δ)	50800 t
Design speed (V)	14 knots

Figure 6-2 shows the relative frequency of idle times according to the latitude degrees. It should be noted that the effect of longitude change on SST values was neglected as

justified in Section 6.2.3.2. Idle time occurrence frequency was calculated through dividing the idle times at each latitude degree by the total idle times in the operation. It can be stated that the ship operation profile carries high fouling risk as the majority of idle times took place in the tropics and subtropics regions where latitude degrees remained between 0° and 30°. Overall, the ship was idle approximately 30% of the entire operation in this region where SSTs are comparatively high.

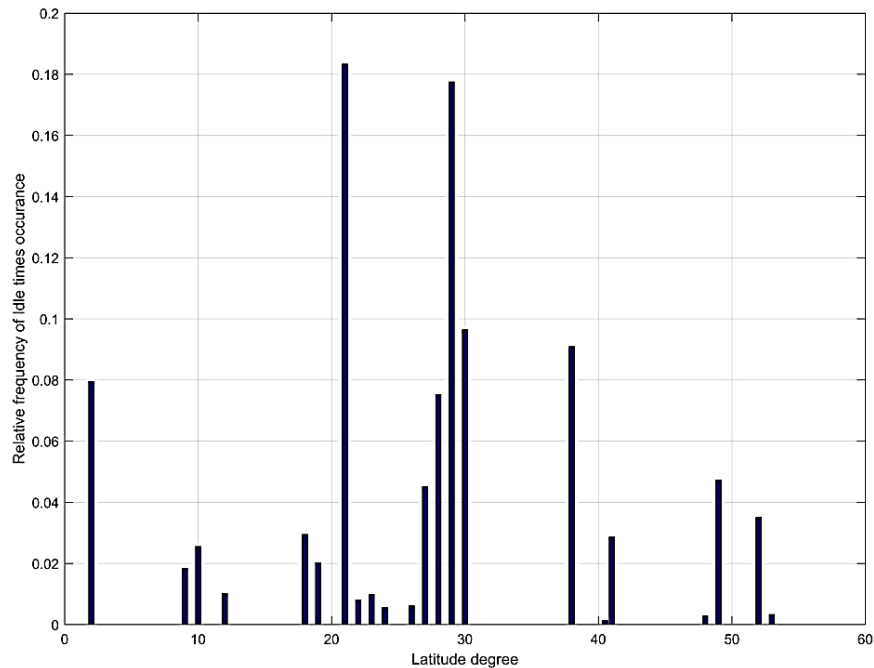


Figure 6-2 Relative frequency of idle time occurrence according to latitude.

The ship is equipped with a data logging system for on-board monitoring and land-based performance control system. Although the data measuring frequency is 15 s, it has been processed into 15 min averages in order to make it easier in terms of data handling. It is important to highlight that the company providing the data conducts the data processing, so the data were not influenced or modified by the author. The list of available measurements and can be found in Table 6-7, while in Figure 6-3, the propulsive layout is depicted together with the propulsive measurements utilised for the validation part (Chapter 6.3.2).

As the on-board devices make measurements in real-time as listed in Table 6.7, it is not easy to be sure of their reliability and accuracy during the monitoring. It is widely

known that speed through water (LOG speed) measurement is partly reliable because the flow going through to the device can be affected by the hull or the other environmental conditions. Although the speed over ground (GPS speed) measurements are more consistent compared to LOG speed, it does not take into account current effects which can reach up to 2 to 3 knots and causes increases in ship power. A mass flowmeter was used to measure fuel consumptions since it is more accurate compared to volume flowmeters. Although the fuel-specific energy content (LHV) was not measured uncertainty on LHV is around ± 2 MJ/kg, which can cause a $\pm 5\%$ variation in measurements. The shipyard informed that uncertainties of propeller speed, torque measurement and fuel mass flow are $\pm 0.1\%$, $\pm 1\%$ and $\pm 3\%$ respectively. One year ship operation from 03/2012 to 03/2013 was taken as time domain for the time-dependent biofouling growth model.

Table 6-7 Measured values available from the continuous monitoring system (Coraddu et al., 2017).

#	Variable name	Unit	#	Variable name	Unit
x_1	Time stamp	[YY-MM-DD, hh:mm]	x_{20}	CPP Setpoint	[%]
x_2	Latitude	[°, ', "]	x_{21}	CPP Feedback	[%]
x_3	Longitude	[°, ', "]	x_{22}	Fuel Density	[kg/m ³]
x_4	Fuel consumption	[kg/15 mins]	x_{23}	Fuel Temperature	[°C]
x_5	Auxiliary engines power	[kW]	x_{24}	Ambient Pressure	[mbar]
x_6	Shaft generator power	[kW]	x_{25}	Humidity	[%]
x_7	Propeller shaft power	[kW]	x_{26}	Dew Point Temperature	[°C]
x_8	Propeller speed	[rpm]	x_{27}	Shaft Torque	[kN m]
x_9	Ship draft (forward)	[m]	x_{28}	Rudder Angle	[°]
x_{10}	Ship draft (aft)	[m]	x_{29}	Acceleration X direction	[m/s ²]
x_{11}	Draft Port	[m]	x_{30}	Acceleration Y direction	[m/s ²]
x_{12}	Draft Starboard	[m]	x_{31}	Acceleration Z direction	[m/s ²]

x_{13}	Relative wind speed	[m/s]	x_{32}	GyroX	[rpm]
x_{14}	Relative wind direction	[°]	x_{33}	GyroY	[rpm]
x_{15}	GPS heading	[°]	x_{34}	GyroZ	[rpm]
x_{16}	Speed over ground (GPS)	[kn]	x_{35}	Roll	[rad]
x_{17}	Speed through water (LOG)	[kn]	x_{36}	Pitch	[rad]
x_{18}	Sea depth	[m]	x_{37}	Yaw	[rad]
x_{19}	Seawater Temperature	[°C]			

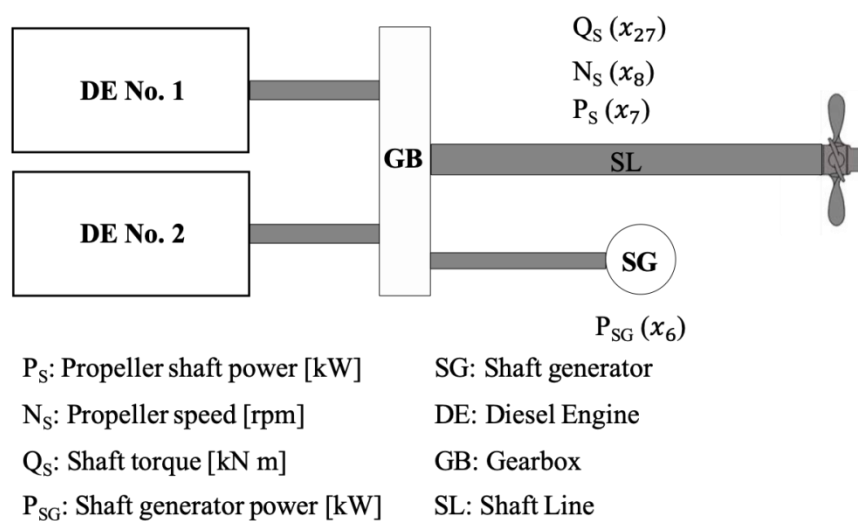


Figure 6-3 Propulsion plan layout

6.3.1.2 Time-dependent predictions

Figure 6-4 shows the estimated FR, percentage of calcareous type fouling surface coverage (SC%), and percentage increases in frictional resistance (ΔC_F %) of the ship with respect to the time and absolute values of latitude degrees of the regions where the ship sailed or spent idle time. It can be seen from the figure that the fouling ratings were predicted to be ~0.4 for non-shell type fouling whereas this number altered to ~6.3 for slime type fouling and ~6.7 for total fouling rating at the end of one year of operation. The percentage of the SC area for calcareous type fouling was predicted to be $\sim 4 \times 10^{-6}$ which means that the model predicted no calcareous type fouling. At the

end of the one year of ship operation, the percentage increase in the frictional resistance due to biofouling was calculated to be ~32% as shown in Figure 6-4. It is important to note that a significant percentage of increase in ΔC_F was observed in the month of Jan-13 from ~5% to ~30%. This can be attributed to the fact that the ship spent ~15 days of idle time in a region of $\sim 0-1.5^\circ$ in latitude and ~6 days of idle time in a region of $\sim 10^\circ$ in latitude. These regions are equatorial, which receives the most solar irradiance; therefore, these regions tend to have the highest SSTs as it can be predicted through equation (6.10).

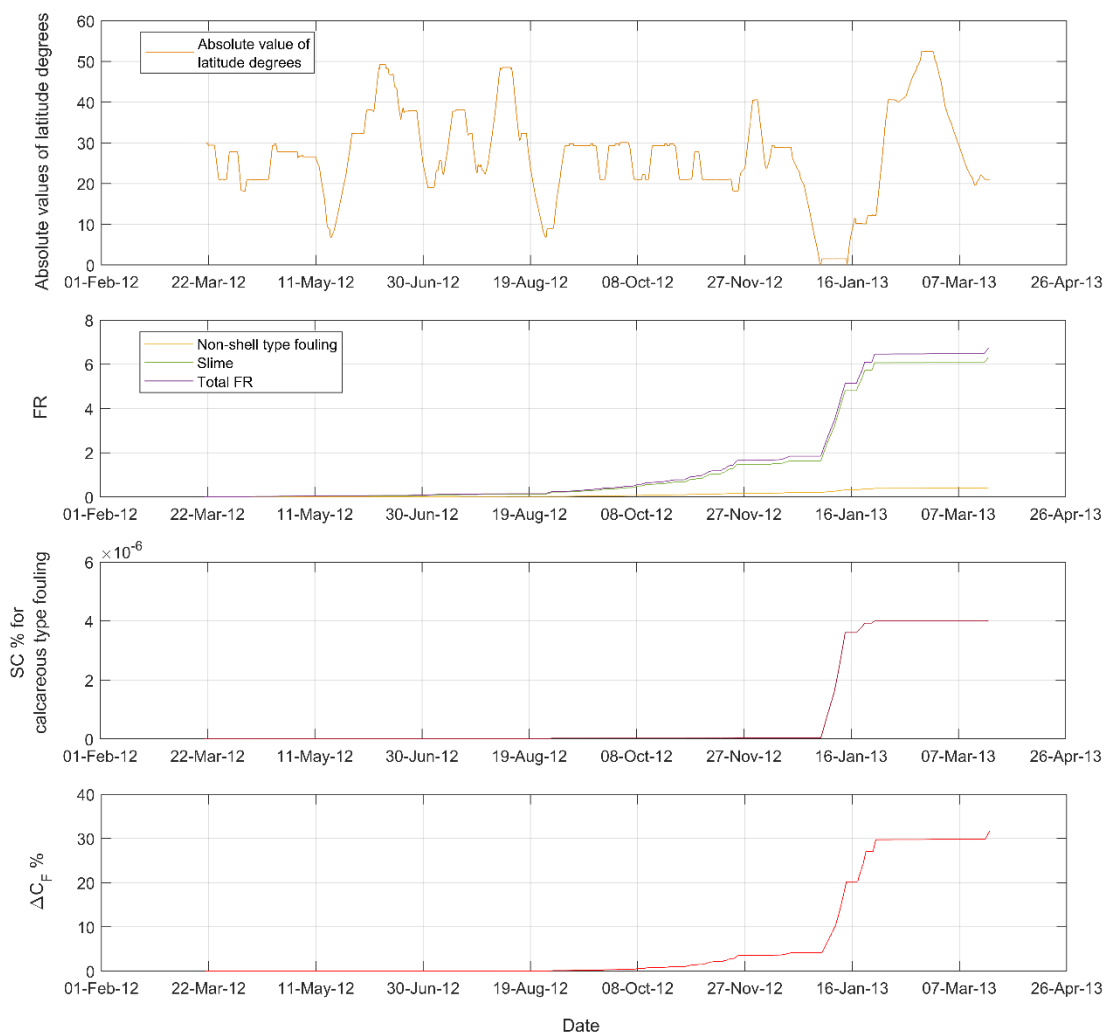


Figure 6-4 Estimation of the fouling ratings, percentage of surface coverage for calcareous type fouling, percentage of increases in the frictional resistance in respect to time.

6.3.2 Comparison of the results with power measurements

The validation of the time-dependent biofouling model has been carried out by comparing the estimated delivered powers (P_{DE}) to the delivered power ($P_{DM} - x_{17}$) data acquired from real ship operation via on-board measuring devices.

In particular, a numerical model has been developed to evaluate the ship estimated delivered powers, for different ship speed V (x_{17}), forward T_f (x_{10}), and aft T_a (x_9), drafts in calm water scenario. In this respect, the effects of manoeuvring, acceleration, and deceleration on ship power were eliminated along with the environmental effects such as waves, current and wind, by filtering. Table 6-8 summarises the filtered measurements and filtering conditions which are assumed the same for all ship types in this study.

Table 6-8 Data filtering

Filtered Measurement	Filtering Condition
Wind speed	< 3 knots
Sea State	< 2 Beaufort scales
Rudder position	-1° to 1°
Speed through water rate of change	≤ 0.25 knots/min
Mean Shaft speed rate of change	≤ 0.5 rpm

The model is based on the knowledge of the ship's hull geometry, mass distribution and the propeller characteristics. The system input taken into account, as reported in Figure 6-5, are the main propeller speed N (x_8), the ship speed V (x_{17}), and the forward T_f (x_{10}), and aft T_a (x_9), drafts. The estimated delivered powers, P_{DE} is used as model output. The detailed description of the numerical model can be found in (Coraddu et al., 2017); nevertheless, for the sake of completeness, a summary is hereby reported.

The core of the procedure is the engine-propeller matching code utilised to evaluate the total delivered powers (Coraddu et al., 2011a). The prediction of ship resistance in calm water, and the evaluation of total hull resistance coefficient C_T in equation (6.12) have been carried out utilising the Guldhammer Harvald (GH) method. For each forward and aft drafts (Figure 6-5) from the vessel historical dataset described in

Section 6.3.1.1, the equilibrium displacement is calculated, together with the necessary input variables required by the GH method by means of the method proposed by in Coraddu et al. (2011b) It is worth noting that the propulsion coefficients t and w have been corrected in magnitude as reported in Lützen and Kristensen (2012):

$$\mathbf{w_c = w_h - 0.45 + 0.08 M} \quad (6.16)$$

$$\mathbf{t_c = t_h - 0.45 + 0.08 M} \quad (6.17)$$

where w_h and t_h are propulsion coefficients obtained with the GH method, and M is the length–displacement ratio.

The propeller thrust and torque have been computed for different pitch settings based on the knowledge of the geometrical features of the propeller, by means of a viscous method presented in Gaggero et al. (2010). The values were implemented in the numerical model through the non-dimensional thrust K_T and torque K_Q coefficients. Once the displacement, shaft rate of revolutions and vessel speed are selected, the equilibrium advance coefficient J_{eq} is defined according to the equation (6.18), together with the non-dimensional thrust and torque coefficient, according to equations (6.19) and (6.20):

$$J_{eq} = \frac{V(1 - w_c)}{nD} \quad (6.18)$$

$$K_Q = \frac{Q}{\rho n^2 D^5} \quad (6.19)$$

$$K_T = \frac{T}{\rho n^2 D^5} \quad (6.20)$$

where w_c is the wake factor corrected in magnitude, n is the propeller rate of revolution, D is the propeller diameter, and T is the required thrust of the propeller. Finally, the open water propeller efficiency η_o can be estimated utilising equation (6.21).

$$\eta_o = \frac{J_{eq} K_T}{2\pi K_Q} \quad (6.21)$$

The propeller open water torque, P_o can be evaluated according to equation (6.22).

$$P_o = 2\pi n Q_o = 2\pi n K_Q \rho n^2 D^5 \quad (6.22)$$

Starting from the propeller torque, the estimated delivered power, P_{DE} is computed by the taking into account the different components of the total propulsion efficiencies as given in equation (6.23).

$$P_{DE} = \frac{P_E}{\eta_T} = \frac{P_E}{\eta_o \eta_h \eta_r \eta_s} \quad (6.23)$$

Here η_t is the overall efficiency, while η_h is the hull efficiency, η_o , is the propeller efficiency in open water, η_r is the relative rotative efficiency, and η_s is the shaft line efficiency. The hull efficiency η_h is a function of the modified wake fraction, w_c , and the modified thrust deduction fraction, t_c .

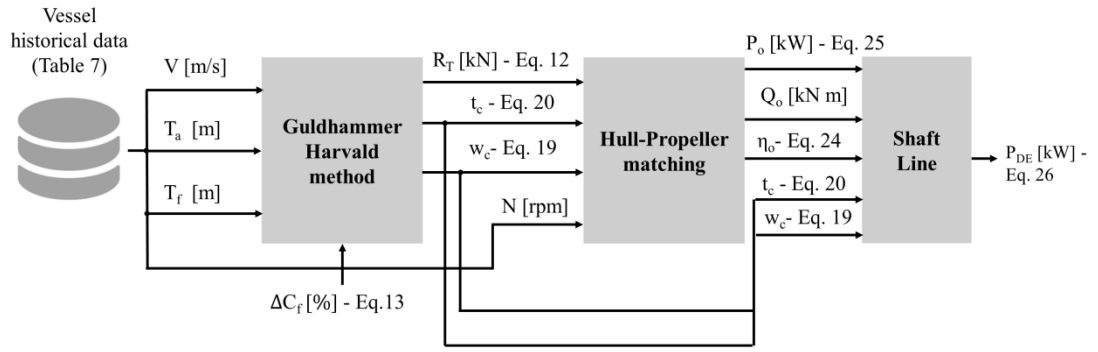


Figure 6-5 Estimated delivered-power-modelling flowchart

The validation of the time-dependent biofouling was carried out through three case analyses, namely Case A, Case B and Case C on delivered power comparisons in two separate time periods, as shown in Figure 6-6 and Table 6.9. Figure 6-7 and Figure 6-8 shows P_{DM} values at varying ship speeds in the first and second period.

It is of note that the Case A was carried out in the first time period in which the ship was considered fouling-free whereas Case B and Case C were conducted in the second time period in which the ship has fouling. The analyses were performed for the ship in the calm water scenario in which ship speed range from 10 knots to 15 knots whereas ship displacements range from 50000 to 52000 ton.

Independently of the adopted scenario, the author defines the error that the proposed approach commits to approximating the real data with reference to the Relative Error Percentage (REP) indexes of performance. The REP is computed by taking the mean square loss but a normalization term composed of the sum of the squared true values. Then the result is square rooted and reported in percentage:

$$REP = 100 \sqrt{\frac{\sum_{i=1}^n (P_{DEi} - P_{DM})^2}{\sum_{i=1}^n P_{DM}^2}} \quad (6.24)$$

Table 6-9 Time periods for delivered power comparison

Case	Periods	Dates	Samples	Fouling Status	Speed Range [kn]	Displacement Range [t]
A	1st	t ₀₁ : 17/05/12 t _{E1} : 24/05/12	76	0	12-13.5	50000-52000
B	2nd	t ₀₂ : 22/02/13 t _{E2} : 18/03/13	98	0	10.5-13.5	
C				1		

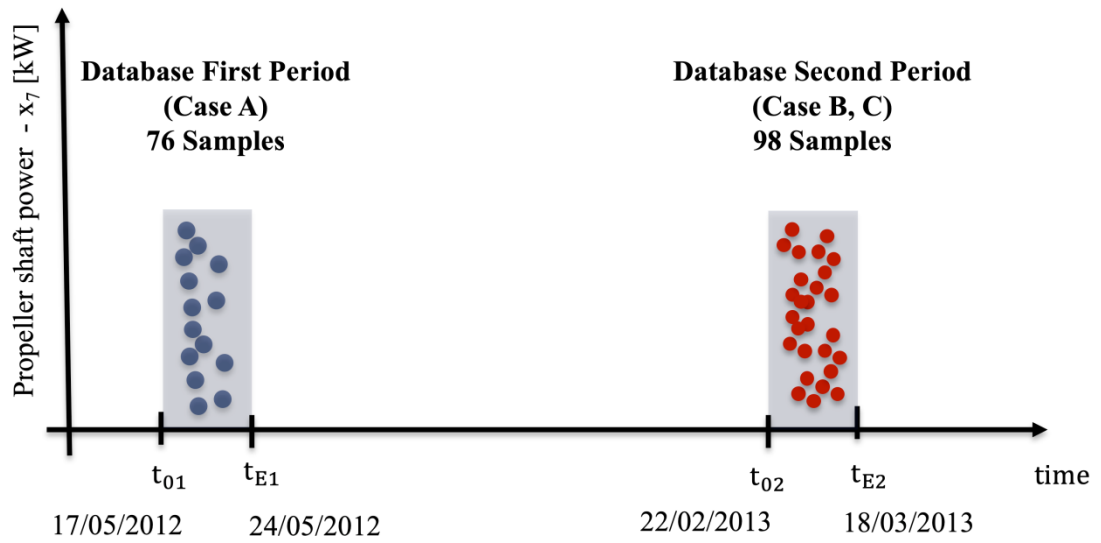


Figure 6-6 Time periods for delivered power comparison

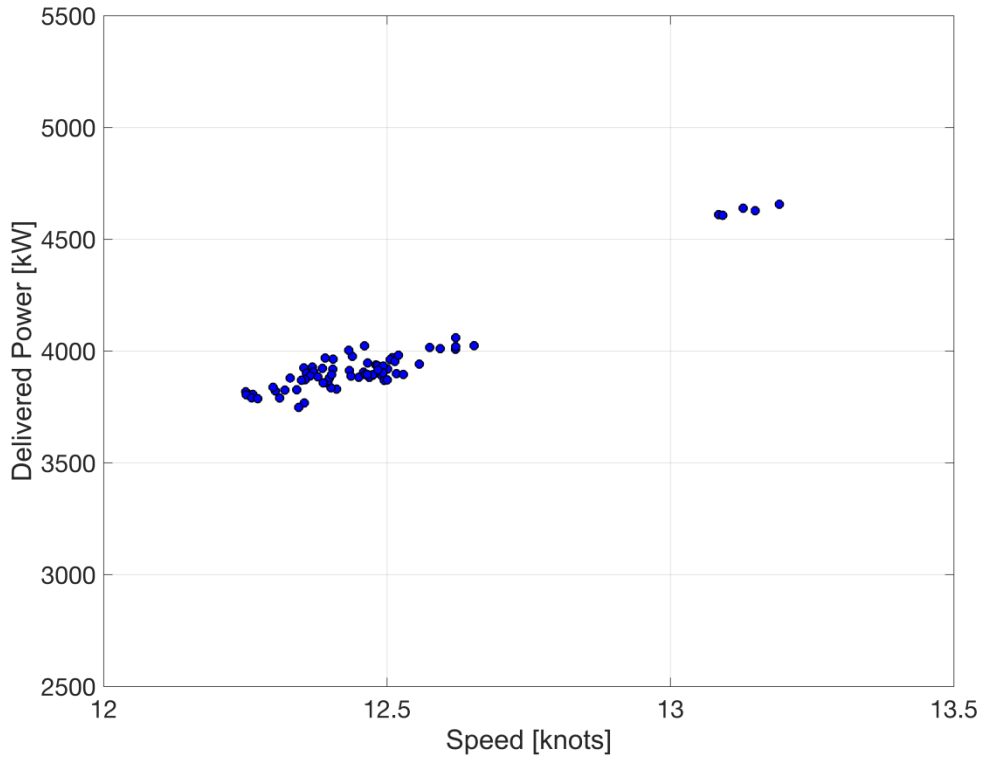


Figure 6-7 First Period - 17/05/12-24/05/12

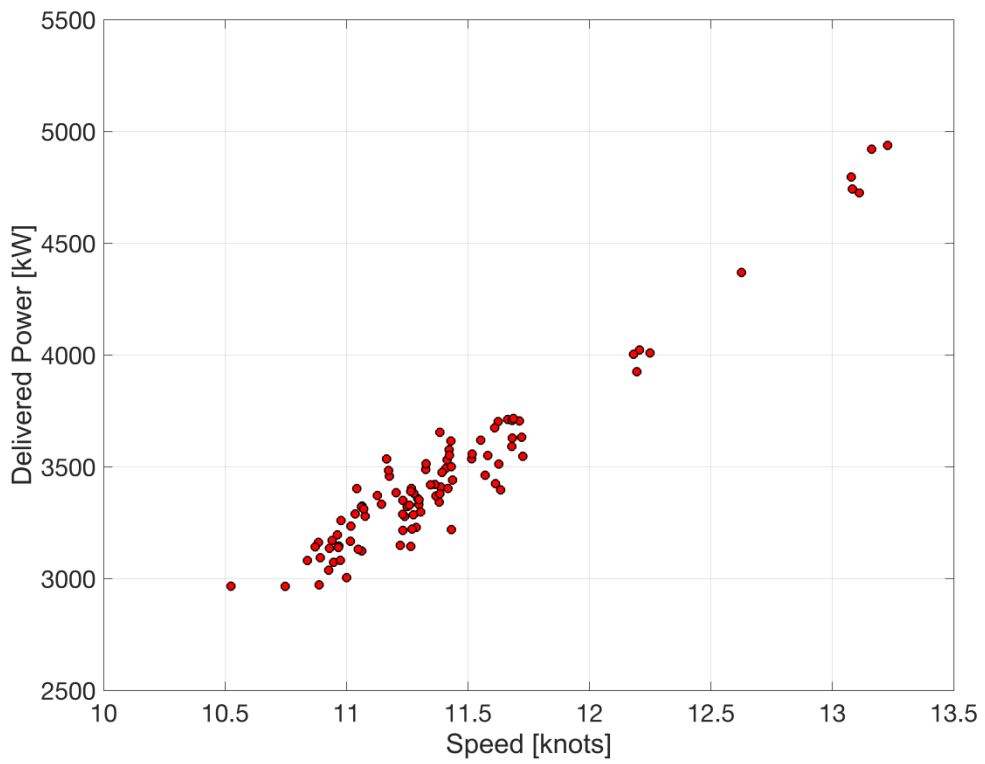


Figure 6-8 Second period – 22/02/13-26/03/13

a) CASE A

Figure 6-9 shows the P_{DM} and P_{DE} values at varying ship speeds, while Figure 6-10 shows the scatterplots between predicted and real values of the output values.

Figure 6-11 reports the relative frequencies of the REP distribution between the P_{DM} and P_{DE} values. The comparisons, in this case, were made to ensure that the in-house GH code accurately predicts delivered power values where the ship hull is considered as smooth after approximately two months from the beginning in the first time period (without any fouling). The analysis shown in Figure 6-9–Figure 6-11 revealed that the P_{DE} values matched reasonably well with P_{DM} such that the average REP value was only 1.8%. These results have further strengthened the confidence in the hypothesis that the GH power prediction method is a credible way to make these analyses for the fouled condition.

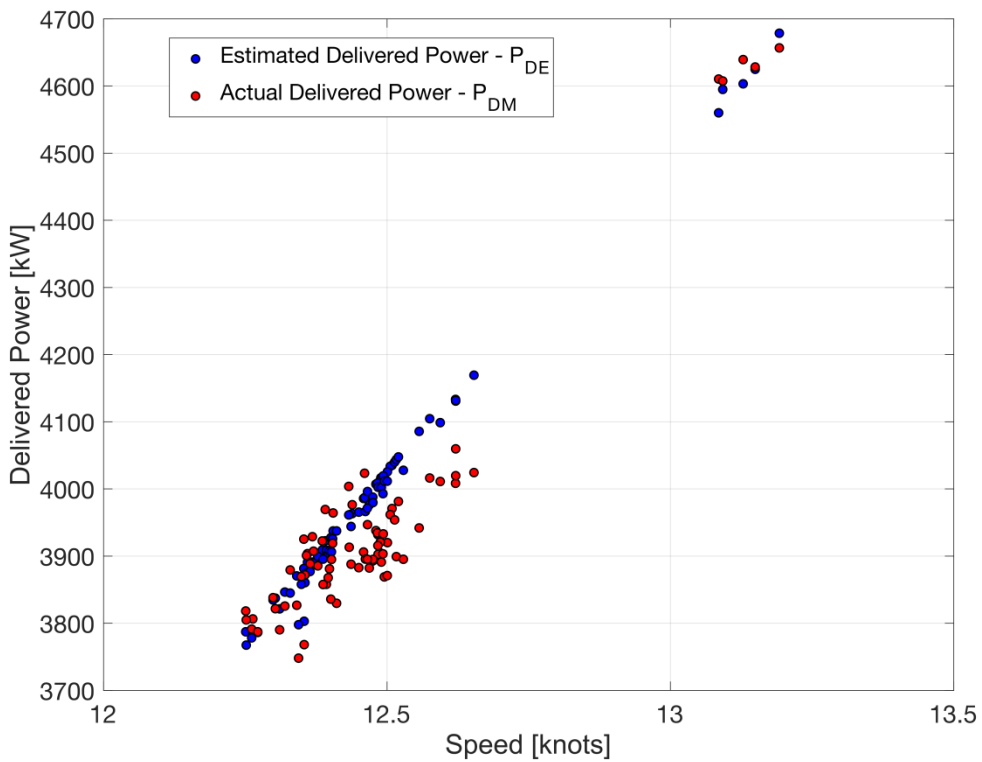


Figure 6-9 P_{DM} and P_{DE} comparisons at various ship speeds – CASE A

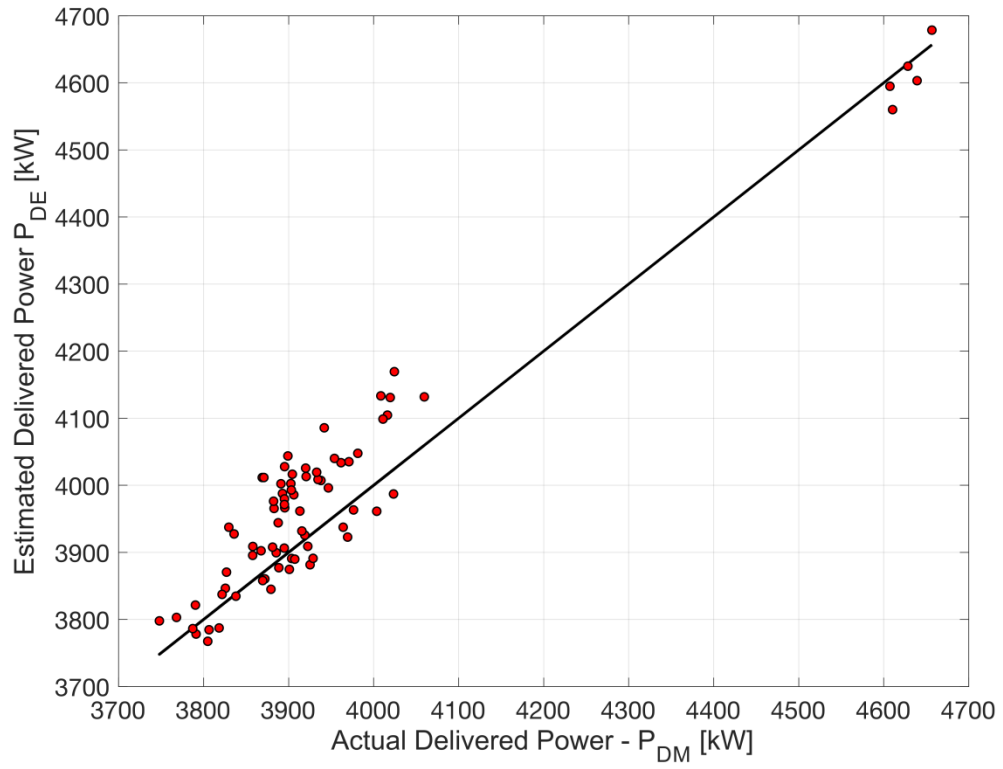


Figure 6-10 GH model scatterplot – CASE A

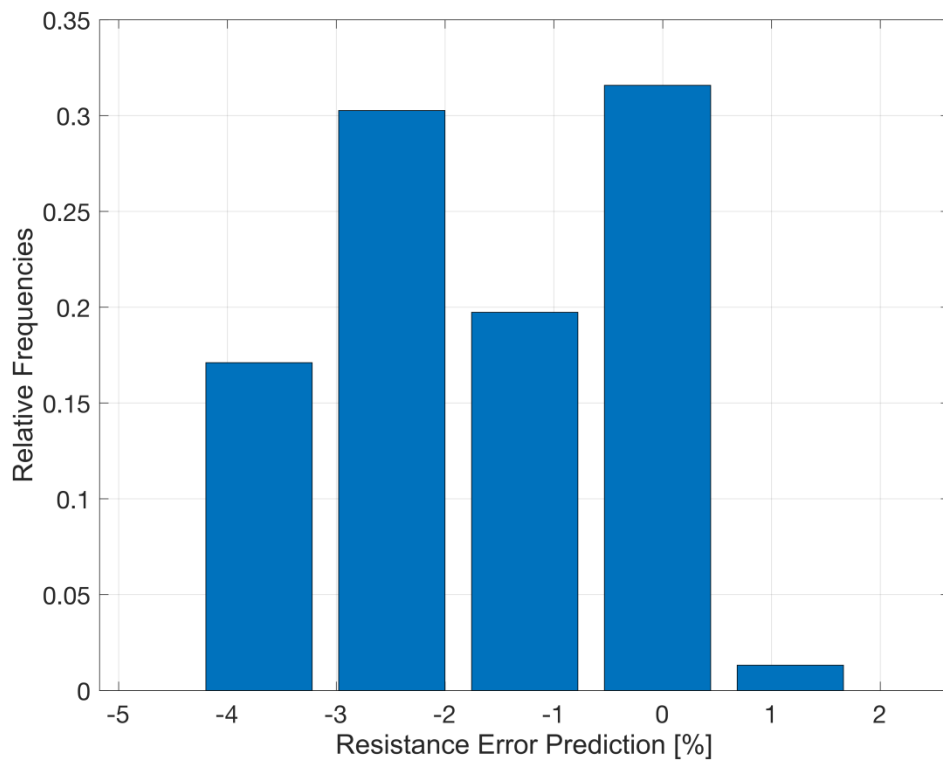


Figure 6-11 Relative frequencies of relative error percentage distribution – CASE A

b) Case B (No Fouling Correction)

Figure 6-12 shows the P_{DM} and P_{DE} values at varying ship speeds, while Figure 6-13 shows the scatterplots between predicted and real values of the output values. Figure 6-14 reports the relative frequencies of the REP distribution between the P_{DM} and P_{DE} . The effective power estimation was made using the GH power prediction method similar to that used for CASE A, i.e. without taking into account any fouling effect. The analysis, in this case, was performed to show the effect of biofouling on ship resistance and powering after a one-year operation in the second time period. Due to fouling accumulation, it is expected to observe a significant difference between the P_{DE} and P_{DM} values. This difference was reflected in REPs between P_{DE} and P_{DM} . The results presented in Figure 6-12 and Figure 6-13 indicate that there is a significant discrepancy between P_{DE} and P_{DM} values due to biofouling accumulation on the ship hull. Figure 6-14 presents relative frequencies of REP values distribution between P_{DE} and P_{DM} . The average REP value was calculated to be ~14.7%.

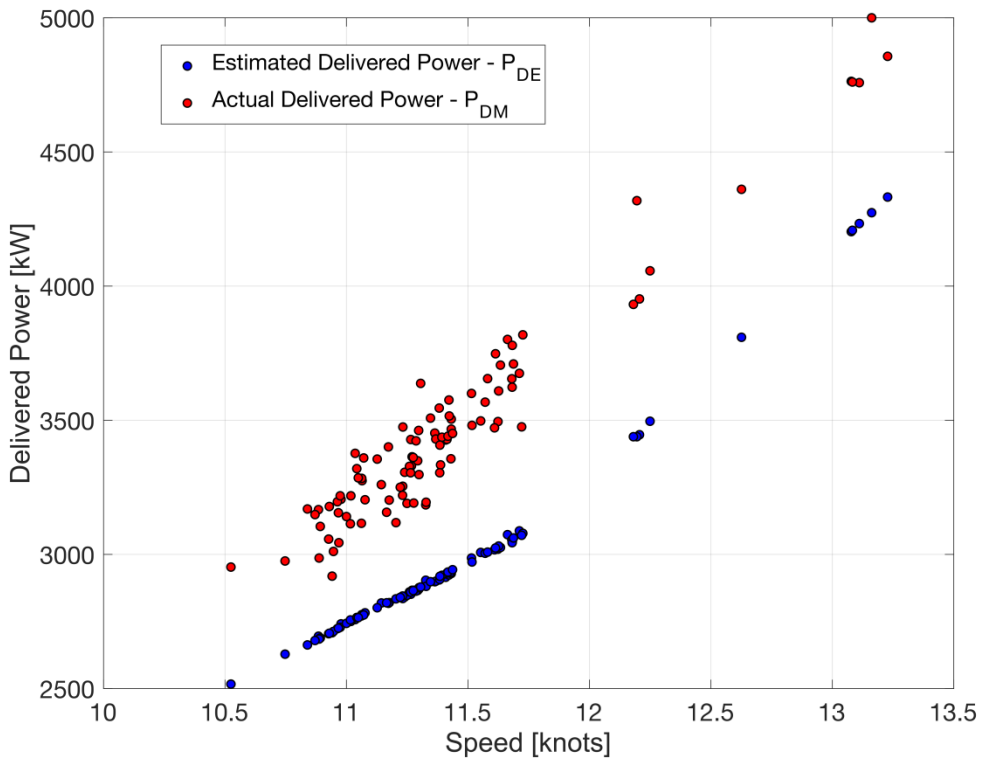


Figure 6-12 P_{DM} and P_{DE} comparisons at various ship speeds – CASE B

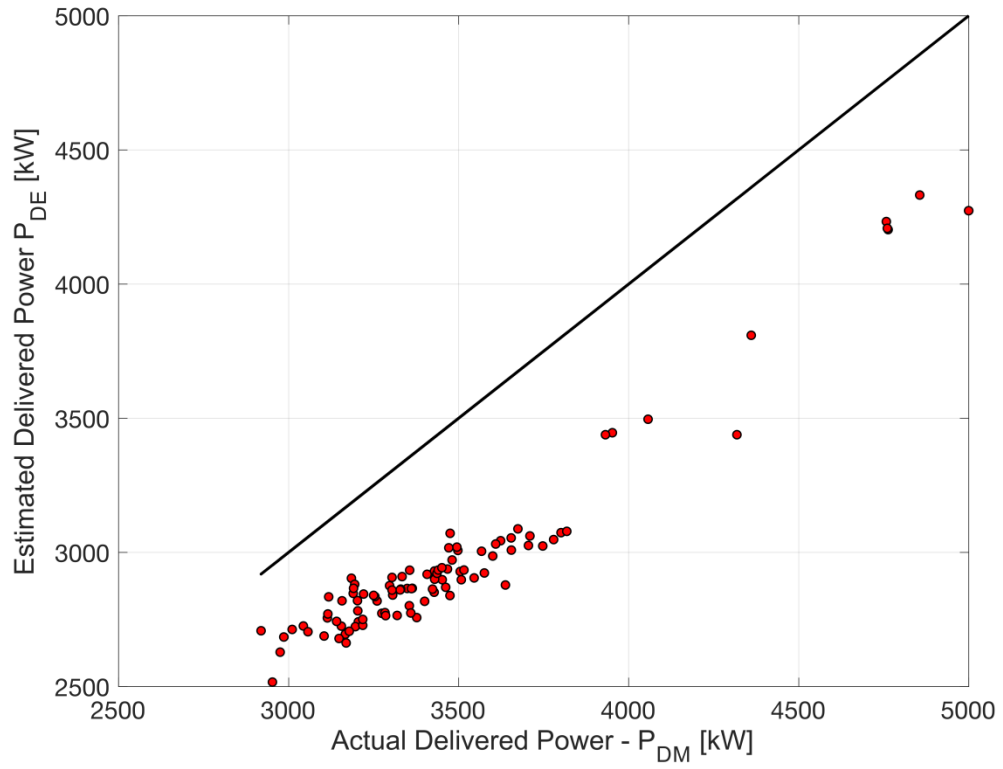


Figure 6-13 GH model scatterplot – CASE B

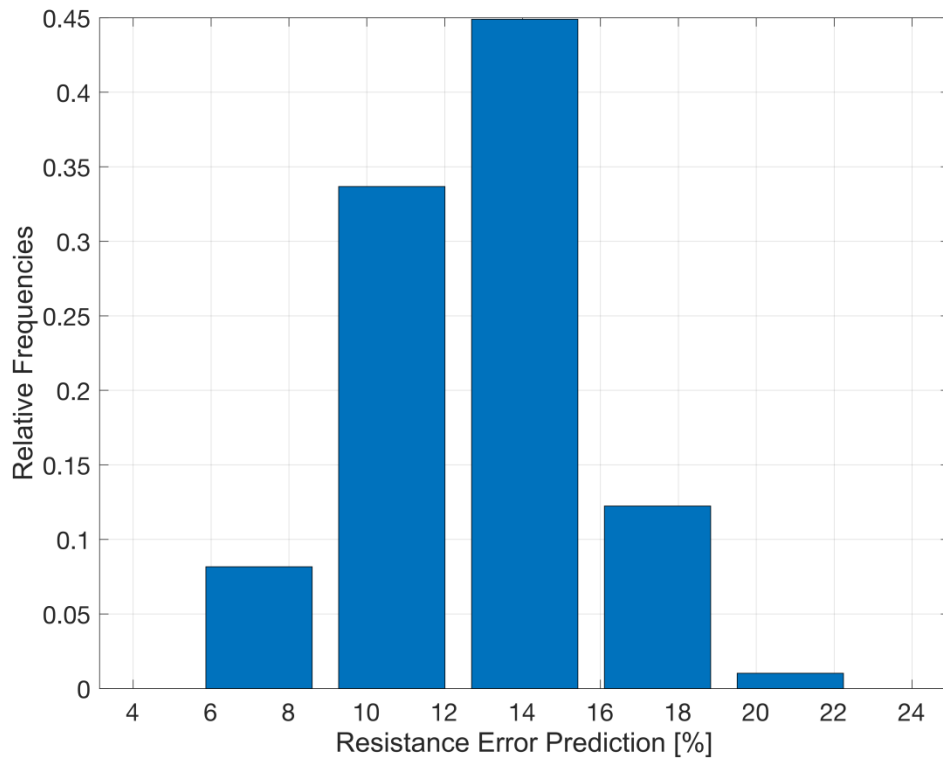


Figure 6-14 Relative frequencies of relative error percentage distribution – CASE B

c) Case C (fouling correction)

The ΔC_F predictions were employed into the equation of C_T , as shown in the equation (6.12), and Figure 6-5, in the GH power prediction code. Following this, the analysis was repeated to test the time-dependent model's predictions in the second time period.

Shown for the comparisons in Figure 6-15 is the actual delivered power measured by on-board devices together with the estimated delivered power (P_{DE}) predicted by GH code employed with ΔC_F predictions. From Figure 6-16, it is evident that once the ΔC_F predictions were employed into GH code, P_{DE} values showed a good correlation with P_{DM} values with an only 2.7% REP value. In addition, Figure 6-17 illustrates the relative frequencies of relative error percentage distribution.

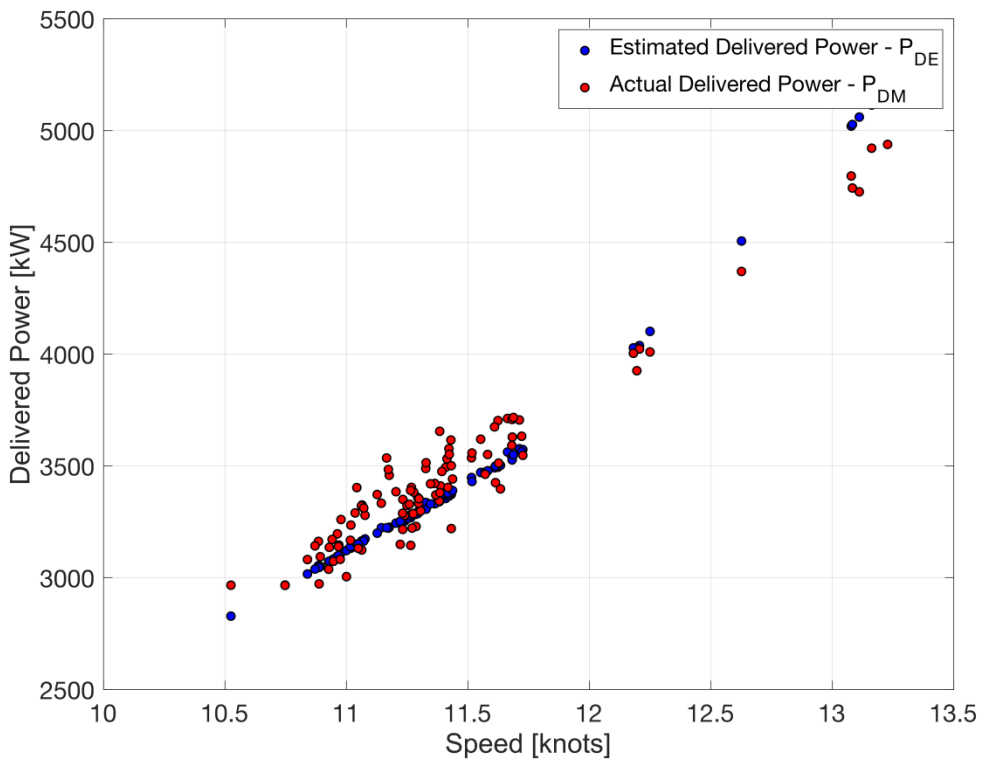


Figure 6-15 P_{DM} and P_{DE} comparisons at various ship speeds – CASE C

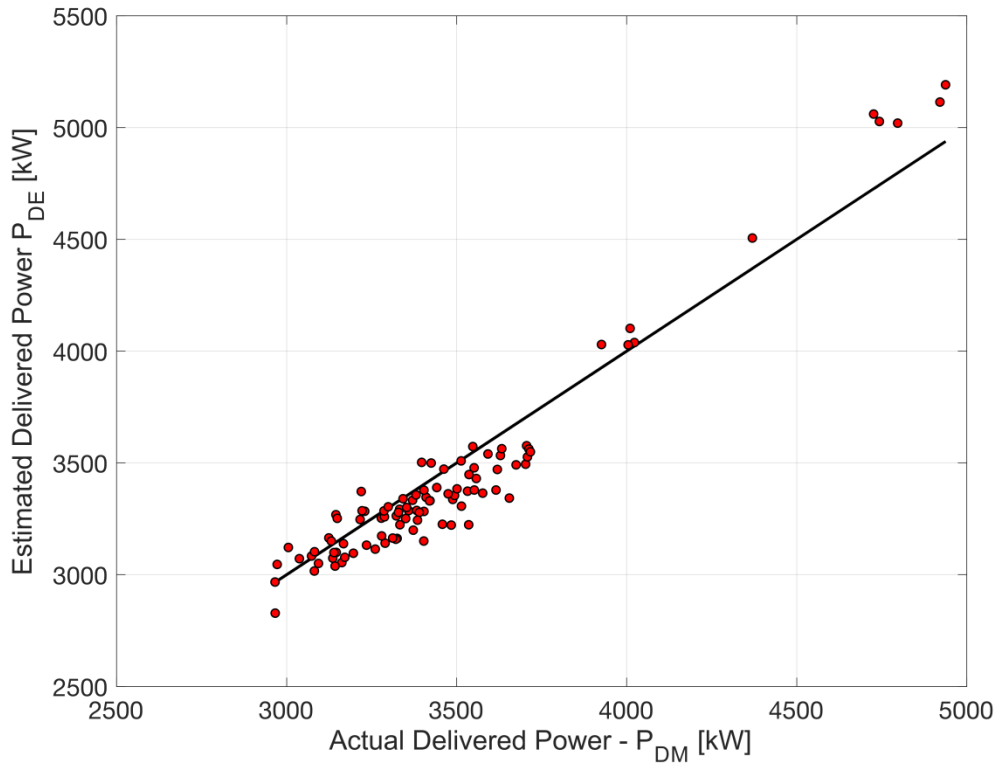


Figure 6-16 GH model scatterplot – CASE C

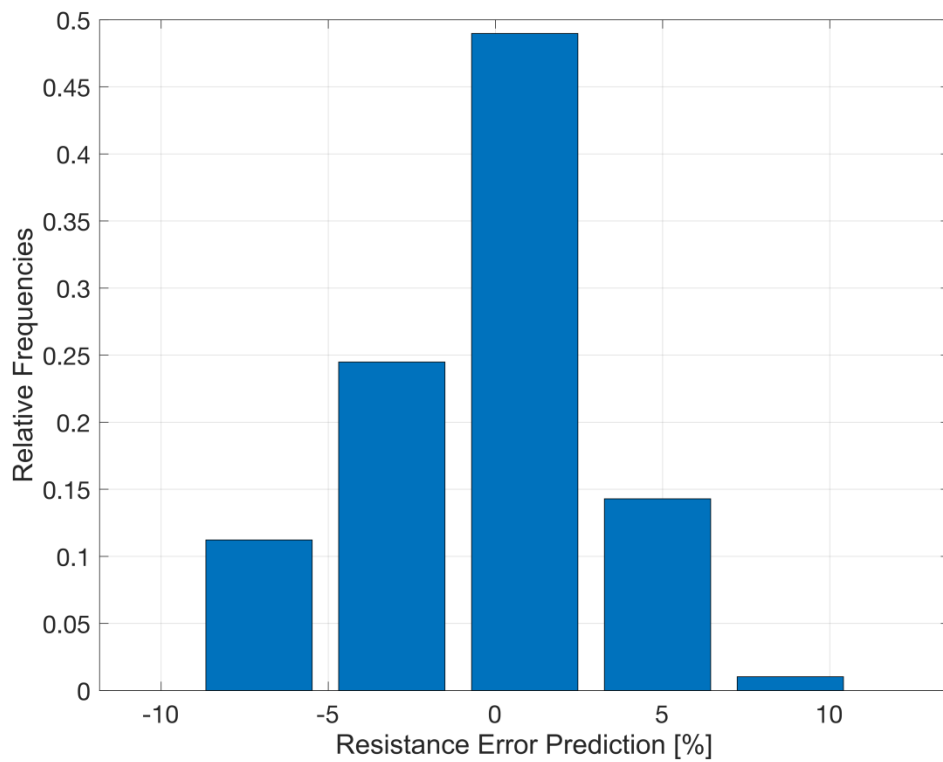


Figure 6-17 Relative frequencies of relative error percentage distribution – CASE C

Table 6-10 Summary of case results

CASE	No of Sample	REP [%]
A	76	1.8
B	98	14.7
C	98	2.7

Table 6-10 shows the results of the analysis conducted in each case through REP values of a given number of samples. From Table 6-10, it is evident that average REP values between P_{DM} and P_{DE} were calculated to be ~1.8 over a 76 of sample for Case A whereas this value changed to ~14.7 and ~2.7 over 98 of sample for Case B and Case C, respectively.

The results presented in Table 6-10 summarise that the GH power prediction code predicted the delivered power accurately with an only ~1.8% REP in Case A in which ship had no fouling on the hull surface. However, after one year it was observed that comparison between the P_{DM} and P_{DE} in Case B average REP value increased to ~14.7% due to the effect of biofouling on the ship hull. Finally, the time-dependent biofouling model's predictions were tested through employing the predicted ΔC_F into GH power prediction code. The results show that average REP values decreased from ~14.7 to ~2.7% in Case C once the predictions of time-dependent biofouling model are taken into account.

The result of the analyses showed that there is a very good agreement between the model's prediction and the real data. This can be accepted as a strong indication for the validation of the model for this case. The author believes that further validation is needed for longer ship operation periods and different ships. For this reason, a case study was carried out to test the model for a different ship type operating for a longer period.

6.4 Case Study

A case study was conducted for a 258 m crude oil carrier coated with the same SPC type antifouling coating for the duration of a ~3-year operation. The model predicted fouling ratings, calcareous type fouling coverage area, percentage increases in frictional resistance of ship and percentage increase of the effective power over the 3 years of ship operation. The predicted percentage increases in effective power were compared with the results provided by a company which gives performance monitoring service for ships based on the data recorded by the crew or auto log systems in ships at periodic intervals. The recorded data then are corrected for wind, waves, sea current, fuel oil quality, and water temperature in order to calculate the effect of biofouling on ship resistance and powering at calm water scenario. The report provided by the shipping company indicated that the percentage increase in effective power due to biofouling for the ship in the selected time period was calculated to be ~21% at the design speed of 15 knots.

6.4.1 Ship description and operation data

The ship profile was presented in Table 6-11. The ship route representing the regions where the ship sailed during the selected time period was illustrated in Figure 6-18. It is evident from Figure 6-18 and Figure 6-19 the ship was mostly operated in the Atlantic Ocean and had a substantial percentage of idle times in a region between the latitude degrees of 0°–10° (loading operation) and 30°–50° (unloading operation). The total idle time for the ~3 years of ship operation was reported to be ~322 days.

Table 6-11 Ship profile

Ship type	Crude oil carrier
Design Length	258 m
Design Breadth (B)	45.5 m
Design Draught (T)	16 m
Design Displacement (Δ)	160000 t
Design speed (V)	15 knots



Figure 6-18 Illustration of the ship route

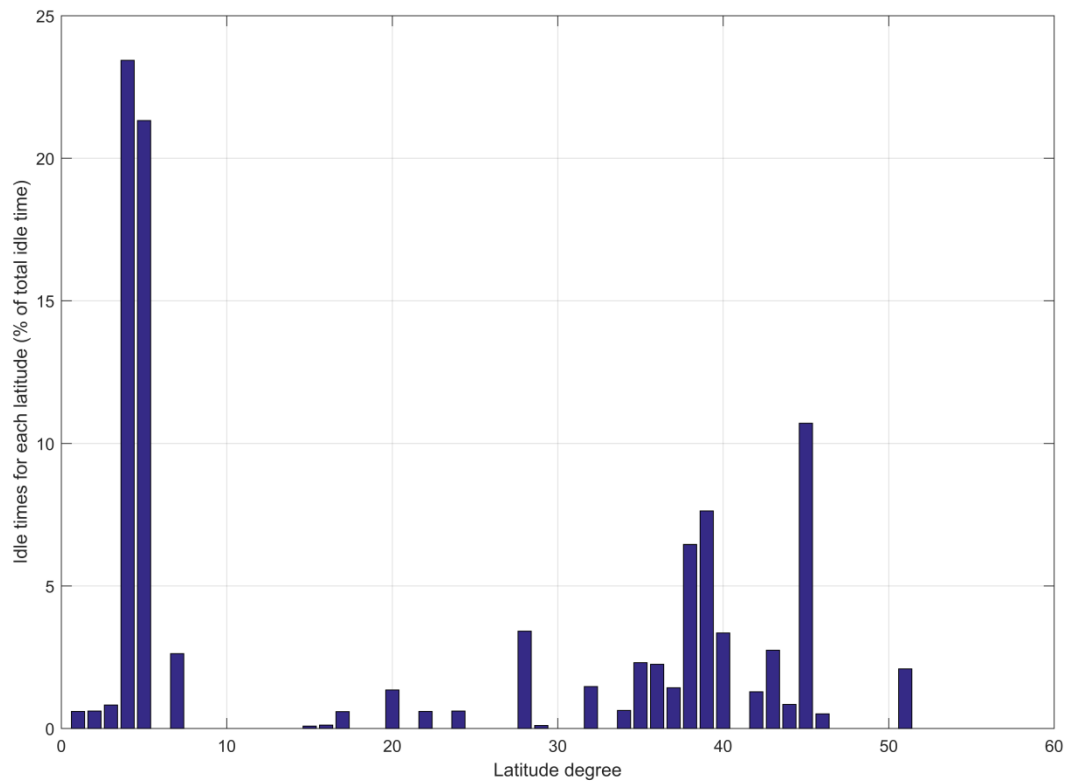


Figure 6-19 Idle times for each latitude degree (% of total idle time)

6.4.2 Results

Figure 6-20 demonstrates the estimated fouling ratings (FR), calcareous type fouling surface coverage (SC%) and percentage increases in frictional resistance ($\Delta C_F\%$) and effective power ($\Delta P_E\%$) of the ship with respect to the time.

The results presented in Figure 6-20 show that fouling ratings for the case study were predicted to be ~ 30 and ~ 20 for non-shell and slime type fouling respectively, whereas total fouling rating was predicted to be ~ 50 . Percentage of SC for calcareous type fouling was predicted to be $\sim 2 \times 10^{-3}$, which means no calcareous type fouling was estimated for this case.

The change in the frictional resistance of the ship during the 3 years of operation was illustrated depending on the predicted fouling ratings and SC areas for calcareous type fouling, as shown in Figure 6-20. As seen from the figure, the percentage increase in the frictional resistance was predicted to be $\sim 43\%$ which in return caused $\sim 25\%$ increases in the effective power of the ship at the design speed of 15 knots at the end of 3 years operation.

It is evident from Figure 6-20 that the $\Delta P_E\%$ predicted by the time-dependent model, illustrated with a blue line, and the $\Delta P_E\%$ provided by ship performance analysis company, illustrated by the orange line, showed different trends. This can be attributed to the fact that the values provided by the company are average values for a selected time of period; therefore, the increase follows a linear trend, as shown in Figure 6-20. However, it is expected that the accumulation of biofouling on ship hull takes time dependency on the efficiency of fouling control coatings in real conditions.

The $\Delta P_E\%$ predicted by the time-dependent model was also averaged over the operation time to present a better comparison with the $\Delta P_E\%$ given by the company. It was observed that there is only $\sim 4\%$ difference between the results.

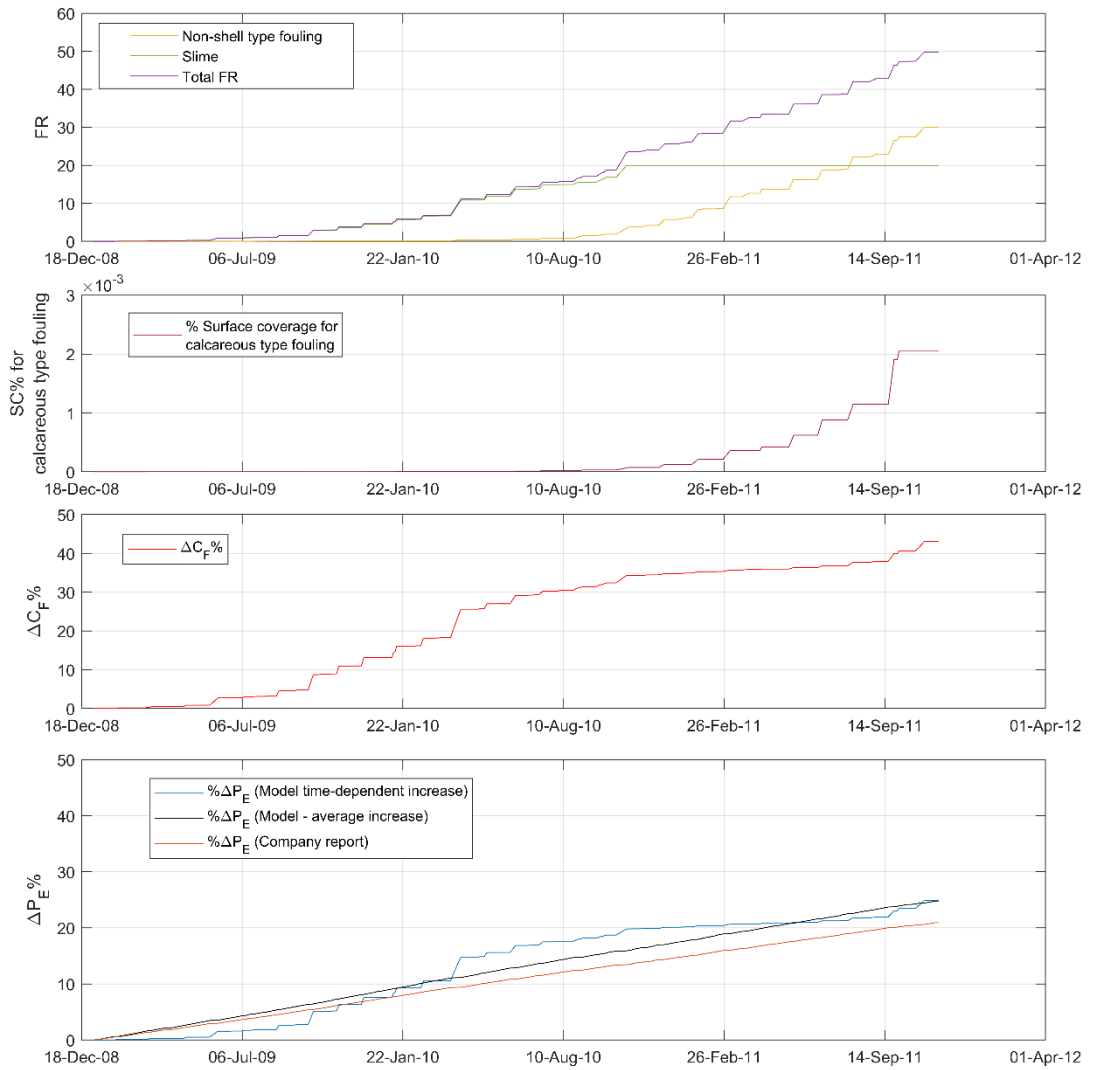


Figure 6-20 Estimation of the fouling ratings, percentage of surface coverage for calcareous type fouling, increase in the frictional resistance and percentage increase in effective power with respect to time

6.5 Discussion and Conclusion

A novel model which correlates the antifouling coating field tests and ship operations were developed to predict time-dependent biofouling growth for the ship operation in question. The effects of time-dependent biofouling growth on ship frictional resistance and powering were predicted using the developed model.

The antifouling field tests data, which were provided by a paint company for an SPC type coating was used to create a time and fouling growth correlation at two separate locations where the coating was tested for around three years. It was observed that a Gaussian type fit sufficiently represented the time and fouling growth correlation. First, the coating performance coefficients, which show the trend of biofouling growth against time, were determined by using Gaussian fit at the test locations and then these coefficients were derived for any region in question using the sea surface temperature as an extrapolation/interpolation parameter. However, the fouling rating function, which was provided by the paint company, was not suitable to predict the effect of the SC area of calcareous type fouling. Therefore, a sub-logistic growth model was also developed for estimating the SC area of calcareous type fouling. It is important to note that idle times during the ship operation was employed as the time parameter in the developed model, which means the model predicts biofouling growth over the periods when the ship is stationary.

Predicted fouling ratings and the SCs for calcareous type fouling were then, turned into k_s values based on the data provided in the literature (Schultz, 2007) (Uzun et al., 2017). The k_s values and corresponding roughness functions for the predicted fouling condition were employed in Granville's similarity law procedure (Granville, 1958) to predict the effect of biofouling on the ship frictional resistance and powering at ship scale.

Firstly, the predictions were made using one-year long ship operation data, which is acquired by on-board measuring devices. The fouling ratings, calcareous type fouling coverages along with the percentage increase in ship frictional resistance and effective power were predicted for calm water conditions. The model was validated by comparing the data obtained by on-board devices and filtered by only retaining those data recorded in calm water conditions and the predicted power values via the GH method in two periods, in the beginning, and at the end of one year of operation. The GH power prediction method (Guldhammer and Harvald, 1974) was used to predict delivered power at calm water scenarios. It was shown that the P_{DE} values showed a good agreement with the P_{DM} values, with an average error of $\sim 1.79\%$ in REP in the first period when the ship was clean. On the other hand, it was observed that

comparisons between P_{DE} and P_{DM} in the second period showed a considerable change in REP values with a ~14.73% difference. This can be attributed to the fact that during a one-year of ship operation biofouling occurred on the ship hull and caused an increase in ship resistance and powering. Following that, the ΔC_F values predicted using time-dependent biofouling growth model was included in the GH power prediction code. Then, it was observed that REP values significantly reduced to ~2.68%.

Later, a case study was performed on a 3-year of ship operation. The time-dependent biofouling growth prediction was made, and increases in $\Delta C_F\%$ and $\Delta P_E\%$ were calculated for calm water conditions. The predicted $\Delta P_E\%$ was then, compared to an operational report showing the actual increases in effective power. The report was provided by a ship performance analysis company (Propulsion Dynamics) which performs computerised hydrodynamic performance analysis based on the actual vessel performance data acquired by the crew or monitoring systems. It was observed that $\Delta P_E\%$ prediction of model and $\Delta P_E\%$ calculation of company did not show a good agreement. This is due to the fact that the company report illustrates the average increase of P_E over a certain selected time period rather than showing individual time-dependent P_E increases due to biofouling accumulation at each part of the operation. Therefore, a valid comparison was made between the averaged predicted $\Delta P_E\%$ and $\Delta P_E\%$ calculated by the company and results showed that the difference between those two was ~4%.

The predicted total fouling ratings were found to be ~6.7 for the operation used in the validation step and ~50 for the case study. The predictions made on SC of calcareous type fouling indicated that no calcareous type fouling occurred for both operations. The percentage increases in frictional resistance of the 176 m vessel were predicted to be ~32% at a ship speed of 14 knots at the end of one-year long ship operation. These values changed to ~43% in ΔC_F and ~25% in ΔP_E for 258 m vessel at a design speed of 15 knots, respectively.

It is important to note that the model uses the roughness functions for specific fouling conditions which were provided in the literature. Without a doubt, these roughness conditions do not exactly represent all fouling conditions during time-dependent

biofouling growth. However, each fouling condition was represented by an appropriate roughness function with a predicted equivalent sand roughness height. As future work, it should be emphasised that roughness functions of real-fouled surfaces should still be required to extend the existing roughness function data in the literature.

The main advantage of the developed model is that as the developed model predicts time-dependent increases in P_E of the ship, it is effective to decide the best maintenance (dry-docking) and/or hull cleaning intervals in order to operate ships in the most profitable and environmentally friendly way.

The author is aware that the model has some assumptions and limitations that originated from a lack of data and impracticability of modelling some certain effects on biofouling. These can be summarised as follows.

- First, the author believes that the ideal biofouling prediction model should have both static and dynamic immersion test data. The static field tests data can be used to model biofouling growth while a ship is stationary, whereas dynamic field tests data can be used to model biofouling growth when the ship is cruising. Since there are no accessible dynamic test data, the model was developed based on the static field immersion tests to predict biofouling accumulation over the idle times during the ship operations. It is well-known that biofouling growth decreases with increased water speed after a certain limit. Therefore, it is reasonable to assume that biofouling growth during idle times outweighs the biofouling growth during cruising times. However, in case of having dynamic test data, biofouling growth prediction for the ship voyages could be estimated by inserting this data into the model.
- Moreover, the author believes that the detachment process of fouling organisms due to environmental factors such as temperature, salinity and other species etc. have been captured via long term field test data. However, the main key parameter regarding cleaning phenomenon is the ship speed. The adhesion strengths of fouling organisms and shear stress on the ship hull due to ship speed should also be considered. The cleaning phenomenon was neglected as it is not realistic to reach to required shear stresses in order to overcome the

adhesion strengths of biofouling organisms on biocidal antifouling coatings (Oliveira and Granhag, 2016).

Future work will concentrate on turning the developed model into a life-cycle assessment model, as proposed by Wang et al. (2018). Once the antifouling field test data are included in the model for different SPC type coatings, the model will be capable of comparing different SPC type coatings in terms of fuel consumptions costs, incurred costs from paint application, ship maintenance costs, and more importantly GHG emissions. Then, it would be used as a decision-support tool in SPC type antifouling coating selection process for any ship, operating profile, and route in question.

7 Discussion

7.1 Introduction

The research carried out in this thesis have been discussed. First, achieved research aims and objectives was demonstrated in Section 7.2 by explaining each specific objectives given in Section 1.4. Following that, novelties and contributions to the literature in this PhD are provided in Section 7.3. Finally, a general discussion and essential outcomes will be given in Section 7.4.

7.2 Achievement of Research Aims and Objectives

The objectives listed in Chapter 1 were described as follows:

- *To review the existing literature on biofouling, essential factors of biofouling growth, antifouling coatings and testing methodologies, modelling the roughness effects of different fouling conditions on ship resistance and powering.*
- *To investigate and show the usability of antifouling field tests in correlation with real ship operations for antifouling coating selection for the ship in question.*

The ‘Critical Review’ in Chapter 2 achieved this aim by providing an extensive literature review on the pointed research topics and questions in this thesis. Reviewed topics are listed as; types of marine fouling, the factors influencing biofouling, antifouling methods and technologies, antifouling performance tests and investigations on the effect of fouling on ship resistance and powering. The gaps in the literature focussing on the roughness database for predicting the effect of biofouling both at the laboratory and full-scale ships were investigated.

The following objectives were achieved in Chapter 4:

- *To manufacture the selected barnacle species by using 3D printing technology in order to conduct a systematic study and to create an extensive biofouling roughness database by making variations on coverage rates, dimensions and settlement pattern.*
- *To determine the roughness functions of an extensive range of barnacle fouling configurations by using Granville's (1987) overall method.*
- *To investigate the effect of barnacle dimensions and settlement patterns on frictional resistance.*
- *To verify the settlement pattern proposed by ASTM standards by proposing a new chaotic settlement pattern in order to investigate differences in frictional resistance between two different settlement patterns.*

Flat plates with eighteen different surface configurations were towed, and the resistance coefficients were calculated. These configurations were tabulated in Table 1 in Chapter 4. Later, roughness functions of the test surfaces were calculated through an indirect method. An extensive comparison of test surfaces was presented. The effect of barnacle size, coverage areas and settlement pattern were demonstrated.

The following objectives were achieved in Chapter 5:

- *To extrapolate the experimental roughness data on full-scale ships through similarity law scaling to show increases in frictional resistance and required ship power or to show reductions in ship design speed.*
- *To generate added resistance diagrams to predict the increases in the frictional resistance coefficients and effective powers of ships due to barnacle fouling.*

First, an in-house code for Granville's similarity law scaling was developed in order to extrapolate lab-scale results to ship-scale. Then, roughness functions of test surfaces

were employed in the code, and full-scale predictions were made. The severe effects of barnacle fouling on ship resistance and powering as well as ship speed reductions were presented through six different ships operating at varying speeds. Additional friction resistance diagrams and tables showing increased effective power and reduced ship speeds due to barnacle fouling configurations were provided to end-users. This may help end-users to predict the effect of barnacles fouling on ship resistance, considering the barnacle sizes and coverage areas in the real situation.

The next objectives were achieved in Chapter 6:

- *To develop a time-based model that predicts the effect of biofouling on ship resistance combining antifouling coating field tests with ship operation data including ship speed, idle time-frequency, and ship route.*
- *To generate figures showing time-dependent increases in frictional resistance with related dependent parameters of ship route and operational profile.*
- *To test and validate time-based fouling model by performing simulations for one year of a real ship operation data and then comparing the results with data analysis tool (Uzun et al., 2019) for ship operation data collected via on-board measurement devices.*

Extensive research on the factors influencing biofouling growth was presented in order to determine a dominant parameter that can be a pillar for a simplified time-dependent biofouling prediction model. The results of parameter assessment showed that sea surface temperature could be addressed as the dominant factor affecting ship frictional resistance and powering. As the dominant parameter is determined, the time-dependent biofouling prediction model was developed based on the ship operational data, antifouling coating field tests, biofouling roughness database in literature and this thesis. First, the model was tested against one-year-long operation data of a 176 m long tanker measured by on-board measurement devices. The model was validated by comparing the data obtained by on-board devices and filtered by only retaining those data recorded in calm water conditions and the predicted power values via the GH method in two periods, in the beginning, and at the end of one year of operation. The

results showed that the developed time-dependent growth model made a significant improvement in the relative error percentages between the predicted and measured power data as a result of data comparison. Secondly, a case study was performed using noon-report data for 3-years operation of a 258 m long crude-oil carrier. Finally, the predictions were compared to ship performance reports that were provided by the ship operator, and the comparison showed that there is a good agreement between the results.

7.3 Novelties and Contributions to the Field

The main novelties achieved within this PhD study are given as follows:

- **Time-dependent Biofouling Model:** To the best of this author's knowledge, this work is novel as the literature contains little, if any, work that is similar. This is likely because previous investigators viewed the modelling of time-dependent fouling build-up as a problem that was too complex and intractable. However, the present work takes a rather simplistic approach and illustrates satisfactory predictions of resistance and powering penalties for operational ships.

This was achieved by developing a time-dependent biofouling growth model which predicts the increases in ship frictional resistance by using coating field tests, ship operation data, roughness data and similarity law scaling procedure. This model will provide end-users to assess ship route in terms of energy-efficient ship operation and enable them to schedule their maintenance operations in advance. Such a model may also help the owners to select the most appropriate paint for their operation profile.

- **Systematic Investigation of the Effect of Barnacle Fouling on Ship Resistance:** To the best of this author's knowledge, this is the first study systematically investigating and quantifying the effect of barnacle fouling in terms of varying surface coverages, barnacle sizes and settlement pattern. Eighteen different surface configurations on barnacle fouling were tested. Then, added resistance diagrams, increased effective power values and reduced ship speed values were presented for six different ships operating at varying ship speeds. This may

help end-users to estimate the effect of a particular barnacle fouling on ship resistance so that the appropriate hull maintenance regime can be developed

Other main contributions to the field within this PhD study are listed below:

- A significant contribution was made to the existing roughness database by providing the roughness functions of eighteen different barnacle fouling surface.

7.4 General Discussion

This thesis can be separated into two main sections; experimental investigation of the effect of barnacle fouling and developing a time-dependent biofouling growth model based on coating test data, ship operation data and roughness database including produced roughness data in the experiments within this PhD.

As explained in detail in Chapter 4, the overall method through flat plates can be used to measure total frictional resistance of surfaces. The difficulties in conducting these experiments can be summarised as follows. The barnacle arrangement on the flat plate is designed according to the ASTM standards. In order to diminish the side forces barnacle tiles needed to be attached symmetrically on both sides of the flat plates. This was the first difficulty appeared before starting the experiments. This procedure starts with drawing ASTM settlement standards in a Computer Aided Drawing (CAD) software by addressing different colours for varying coverage rates. Then, these drawings were printed out on a paper, which is the same size as the flat plate, and then square holes which are drawn in different colours were made. Then, these square marks which address where barnacle tiles should be attached on the flat plates were drawn on the plate using pens with permanent ink in different colours according to colours of squares. The paper showing the barnacle squares were rotated to the appropriate direction in order to symmetrically arrange barnacles on both two surfaces of the flat plate. This process needed to be conducted carefully; therefore, it was time-consuming.

Later, the alignment process of the flat plate was performed in order to be sure that no side forces are affecting the flat plate. As suggested in Demirel (2015), an extra transducer which measures the side forces was used and side forces were measured at both low and high speeds until the side forces are effectively zero. Nothing changed in the set up once the correct alignment was achieved.

The speed range of towing test can be accounted for as a limitation for the experiments conducted in this thesis. Due to the speed restriction in the tank, only the available roughness functions could have been obtained for the Reynolds number. This may be enhanced by increasing the speed range of the towing tank test, which was not feasible for this experiment as the experiments were towed up to the highest allowed speed. An alternative way can be using longer plates which provides higher Reynolds number and higher roughness functions pairs.

In Chapter 5, Granville's similarity law scaling was used to predict the effect of roughness for full-scale ships. Granville's similarity law scaling was developed based on the assumption that the flow is insensitive to the wall boundary condition where the roughness height is a very small fraction of the boundary layer thickness (Granville, 1987). Later, it is found that the mean flow is similar in the outer layer, even in the flow where k is a significant fraction of the boundary layer thickness (Flack and Schultz 2004). It should be mentioned that although friction velocity varies along the length of the flat plate, a surface condition at a given speed was represented by a single roughness Reynolds number and roughness function. It should also be noted that this method can only predict the change in the frictional drag and it is assumed that the pressure drag of the hull is not expected to change significantly by the effect of roughness. However, it is beneficial for the preliminary investigation of the effect of the surface roughness on the total resistance as the roughness functions are known.

In Chapter 6, it was shown that a simplified time-dependent biofouling growth model could be developed in order to predict the effect of biofouling roughness on ship resistance and power in time. This means that once the related antifouling coating test data, ship characteristics and ship operational data are given as input, the model can predict a time-dependent increase in the frictional resistance of the ship in question due to biofouling growth. The main difficulties for the developed model can be

attributed to the validation phase of the model. First, a ship coated with the same or at least equivalent kind of antifouling coating is required to be used as a case study of the model. Second, the validation phase of the model required a detailed ship operation data which should be ideally measured by onboard devices in very short time intervals like every 15 seconds (averaged to 15 mins). Finally, the predicted increases in the frictional resistance and powering should be checked with the real measured power data in different periods within the total ship operation duration. The first period should be the start period of the model, which indicates the initial ship hull condition. Then, other comparison periods should be referenced according to the initial period, and increases should be compared considering the initial period.

It should be noted that the model was developed assuming that the biofouling growth during the static conditions (idle times) overweigh the biofouling growth in dynamic conditions. Although this is a reasonable assumption once the dynamic field test data is obtained for the related coating, it should be inserted into the model in order to predict biofouling growth during cruising times.

The roughness functions values of barnacle fouling were taken from the experiments conducted within this study along with the other type fouling's roughness functions which are provided in the literature. There is no doubt; the used roughness functions do not exactly simulate all conditions of naturally growing biofouling accumulation. However, each fouling condition was represented by an appropriate roughness function with a predicted equivalent sand roughness height.

7.5 Chapter Summary

This chapter summarises the achieved research aims and objectives, providing a general discussion on the limitations, assumptions and difficulties faced with during the PhD study. Novelties and contributions were also clearly presented.

8 Conclusions and Recommendations

8.1 Introduction

This chapter outlines the conclusions of the studies performed within this PhD and recommendations will be presented for future research as a further study of the work presented in the main chapters of this thesis.

8.2 Conclusions

Our knowledge of the effect of biofouling roughness is primarily based on the lab-scale data, which focuses on turbulence structure, especially for coatings and soft fouling such as bacteria, diatomaceous slime and algae. To the best of the author's knowledge, there is very limited roughness function data for the barnacle fouling. An aim of the study was therefore not only produce roughness data for barnacle fouling but also to scale up these lab data to full-scale size in order to investigate the effect of barnacle fouling on full-scale ship resistance.

A series of experiment with artificial barnacles was systematically conducted to determine the effect of barnacle fouling on the ship frictional resistance. Eighteen different surface configurations in varying coverage rates, barnacle sizes and settlement pattern were tested. It should be noted that the study did not aim to investigate the relation between the surface morphology and roughness functions, instead of this, with an engineering perspective, the effects of designed barnacle configurations on full-scale ship frictional resistance were investigated. Drag characteristics of each configuration were provided, and full-scale predictions were made for ship frictional resistances.

It was shown in Chapter 4, barnacle fouling even the smallest barnacle size configuration with the lowest surface coverage significantly affects frictional resistance of flat plates. The outcome of the study confirmed that increasing barnacle size and surface coverage areas increased the frictional resistance of flat plates.

As consistent with this outcome, B type barnacle configuration, which consists of the only the largest size of barnacles caused the maximum increase in frictional resistance compared to other barnacle configurations with the same coverage rates. Mixed type barnacle configuration, which consists of three different barnacle geometry in size (S, M and B), showed similar behaviour to the B type barnacle configuration. This can be attributed to the fact that the effect of the presence of the B type barnacle overweighs the effect of other barnacles. It is observed from the comparisons between S type, and B type barnacle configurations, the effect of barnacle size is more dominant compared to the effect of coverage area on the frictional resistance. The settlement pattern given by ASTM standards were questioned through a comparison with a new chaotic barnacle settlement pattern which represents barnacle settlement in nature.

After the drag characteristics of flat plates covered with barnacles were obtained and the roughness functions are determined, lab-scale results were extrapolated to full-scale flat plates of ship sizes. This extrapolation was made through Granville's similarity law scaling procedure for six different ship length. It is shown that the barnacle fouling vitally affected the ship frictional resistance in Chapter 5.

As an outcome of this extrapolation, added frictional resistance diagrams were provided as well as tables showing increased effective powers or reduced ship speeds at a fixed effective power. The results indicate that the increase in the ship frictional resistance changes in a range from 21.9% up to 153.85% whereas these values altered to 9.82% and 98.74% for the increase in the effective power. The effect of settlement pattern on ship frictional resistance was calculated to be up to ~10.5. This diagrams and tables can help ship operators to predict the percentage of ship speed reductions, added frictional resistances and increases in the effective power for their ships cruising at particular speeds under the varying barnacle fouling conditions.

In Chapter 6, a time-dependent biofouling growth prediction model was proposed to predict the time-dependent effects of biofouling on ship resistance and powering. The model was validated through one year of ship operation. Predictions of power increases in time were compared to power data measured by onboard devices. The model successfully predicted the increases in the ship frictional resistance and powering due to biofouling accumulation on the ship hull after one year of ship operation. Then, a case study for a ship operation of three years was performed, and the predictions were compared to a report provided by a ship analyst company. The comparison showed that the predicted power values agree well with the power values provided in the report.

The significant advantage of the model is that it enables the use of antifouling coating field test data combining with ship operation data in order to predict biofouling growth in time. Roughness function data in the literature was combined with the roughness data produced in the experiment within this PhD and used for specific fouling conditions in order to simulate the roughness condition of the ship.

The analysis indicates that the model can be used as a decision support tool for performance assessment of antifouling coating for the ship which cruising on the route in question.

8.3 Summary of Conclusions

- The effect of barnacle fouling on both lab-scale and full-scale frictional resistance is significant. There are significant power penalties in the ship effective power due to this increase in the ship frictional resistance.
- Barnacle height and surface coverage are essential parameters and substantially affect the frictional resistance.
- Change in the barnacle height is more effective on the frictional resistance than the change in the coverage area.

- Drag characteristics of Mixed type barnacle configurations are similar to the drag characteristics of B type barnacle configurations. This means the existence of B type barnacle overweighs the existence of other type barnacles.
- NS pattern increased the frictional resistance more than the standard settlement pattern.
- The effect of barnacle fouling on ship frictional resistance shows differences at even under same roughness condition according to the ship length, ship speed and ship form. This means the effect of barnacle fouling should be assessed, particularly for each ship.
- Time-dependent biofouling growth model predicted the time-dependent increases in the ship frictional resistances accurately based on the comparisons between predictions and real-world ship data.
- This model can be used as a decision support tool to select the most effective antifouling coating for the ship in question. Also, it can be used to decide the best maintenance schedules for the ships in order to prevent extra fuel consumptions and emissions due to biofouling.

8.4 Recommendations for Future Research

- In Chapter 4, an extensive experimental study was carried out to get insight into the effects of barnacle fouling by means of artificial 3D printed barnacles. A piece of future work might be the investigation of other type fouling organisms by using 3D technology, especially for slime, algae, weed and soft fouling organisms.
- Drag characterisation of flat plates covered with barnacles was made through the overall method. Although the main aim of the study, the effect of barnacle

fouling on frictional resistance, is achieved, it would be interesting to measure velocity profile in the boundary layer using laser Doppler velocimetry (LDV). Future work can be the testing surfaces covered with barnacles in the fully-turbulent channel to reach higher speeds and fully turbulent regimes for each configuration.

- In addition, the surface texture of the artificially produced barnacle surfaces can be captured by means of optical surface profilometer in order to relate surface characteristics to roughness functions and drag.
- In Chapter 5, increases in the ship frictional resistances and powering as well as possible ship speed reductions at fixed effective power were provided for six different ships through diagrams and tables. Similar data can be produced for ships varying in lengths and ship speeds.
- In Chapter 6, a novel time-dependent biofouling growth model was developed based on the antifouling coating field tests, roughness functions and ship operational data. The model was developed based on the assumption that the static fouling growth (idle conditions) overweighs the dynamic fouling growth. However, dynamic fouling test data should be included in the model in order to simulate biofouling growth under the dynamic conditions (cruising).
- The roughness database in the literature is not extensive and have lack of experimental study, especially for soft biofouling type. Rating standards for the surfaces with biofouling shows conflicts and cannot be reversible to each other. There is a certain lack for the biofouling rating systems and their hydrodynamic assessment for the ship frictional resistance. A detailed biofouling rating system evaluating the condition of the surface should be developed together with the roughness functions and corresponding universal roughness unit such as equivalent sand roughness heights (k_s) to be able to make better predictions for ship frictional resistances.

- Once more than one antifouling coating test data is updated into the model, it can be used to compare the performance of antifouling coatings amongst the available coatings for a ship for the route in question. A further study is to develop a life cycle assessment tool based on the time-dependent biofouling growth model in order to analyse the performance of antifouling coating during 30 years of the life cycle. The life cycle assessment should cover environmental and monetary effects born from paint production to application, hull maintenance and added fuel consumption due to biofouling on the ship hull.

References

- ANTARES Collaboration (2002). Nucl. Inst. Meth., A 484, 369.
- Abarzua, S., & Jakubowski, S. (1995). Biotechnological investigation for the prevention of biofouling. I. Biological and biochemical principles for the prevention of biofouling. Marine Ecology Progress Series, 123, 301-312.
- Almeida, E., Diamantino, T. C., & de Sousa, O. (2007). Marine paints: the particular case of antifouling paints. Progress in Organic Coatings, 59(1), 2-20.
- Anderson, C. (2000). Coatings, antifouling. Kirk-Othmer Encyclopedia of Chemical Technology, 1-28.
- Anderson, C., Atlar, M., Callow, M., Candries, M., Milne, A., & Townsin, R. (2003). Proceeding of the Institute of Marine Engineering. Science and Technology (IMarEST) Part B: Journal of Marine Design and Operations, 4, 11-23.
- Anderson, D. E. (1971). Method and apparatus for coating articles utilizing rotating crucible coating apparatus including a centrifugal-type crucible. In: Google Patents.
- Anderson, M. (1995). Variations in biofilms colonizing artificial surfaces: seasonal effects and effects of grazers. Journal of the Marine Biological Association of the United Kingdom, 75(3), 705-714.
- Antonia, R., & Luxton, R. (1972). The response of a turbulent boundary layer to a step change in surface roughness. Part 2. Rough-to-smooth. Journal of Fluid Mechanics, 53(4), 737-757.
- Armstrong, V. N. (2013). Vessel optimisation for low carbon shipping. Ocean Engineering, 73, 195-207.
- ASTM D3623-78a (1998), Standard Method for Testing Antifouling Panels in Shallow Submergence, ASTM International, West Conshohocken, PA, 1998,
- ASTM D6990-05(2011), Standard Practice for Evaluating Biofouling Resistance and Physical Performance of Marine Coating Systems, ASTM International, West Conshohocken, PA, 2011.
- Atlar, M., Yeginbayeva, I.A, Turkmen, S., Demirel, Y.K., Carhen, A., Marino, A. & Willams, D. (2019) A Rational Approach to Predicting the Effect of Fouling Control Systems on “In-Service” Ship Performance. GMO Journal of Ship and Marine Technology, 24 (213).pp.5-36.ISSN 1300-1973.
- Baier, R. E. (1984). Initial events in microbial film formation. Marine biodeterioration: an interdisciplinary study, 1, 57-62.

- Bandyopadhyay, P. R. (1987). Rough-wall turbulent boundary layers in the transition regime. *Journal of Fluid Mechanics*, 180, 231-266.
- Bertram, V. (2000). Past, present and prospects of antifouling. 32nd WEGEMT School on Marine Coatings, Plymouth.
- Bijl, P. K., Schouten, S., Sluijs, A., Reichart, G.-J., Zachos, J. C., & Brinkhuis, H. (2009). Early Palaeogene temperature evolution of the southwest Pacific Ocean. *Nature*, 461(7265), 776.
- Bixler, G. D., & Bhushan, B. (2012). Biofouling: lessons from nature. *Philosophical Transactions of the Royal Society A: Mathematical, Physical and Engineering Sciences*, 370(1967), 2381-2417.
- Bott, T. R., & Pinheiro, M. M. V. P. S. (1977). Biological fouling — velocity and temperature effects. *The Canadian Journal of Chemical Engineering*, 55(4), 473-474. doi:10.1002/cjce.5450550420
- Branch, A. E. (2008). *Global supply chain management and international logistics*: Routledge.
- Braun-Blanquet, J. (1932). *Plant sociology. The study of plant communities. Plant sociology. The study of plant communities. First ed.*
- Breur, H. J. A. (2003). Fouling and bioprotection of metals: Monitoring and control of deposition processes in aqueous environments.
- Buma, A. G., Sjollema, S. B., van de Poll, W. H., Klamer, H. J., & Bakker, J. F. (2009). Impact of the antifouling agent Irgarol 1051 on marine phytoplankton species. *Journal of Sea Research*, 61(3), 133-139.
- Burgess, J. G., Boyd, K. G., Armstrong, E., Jiang, Z., Yan, L., Berggren, M., Adams, D. R. (2003). The development of a marine natural product-based antifouling paint. *Biofouling*, 19(S1), 197-205.
- Callow, J., & Callow, M. (2006). Biofilms. In *Antifouling Compounds* (pp. 141-169): Springer.
- Callow, J. A., Stanley, M. S., Wetherbee, R., & Callow, M. E. (2000). Cellular and molecular approaches to understanding primary adhesion in Enteromorpha: an overview. *Biofouling*, 16(2-4), 141-150. doi:10.1080/08927010009378439
- Callow, M. (1990). Ship fouling: problems and solutions. *Chemistry and Industry London*, 123-127.
- Callow, M. E., & Callow, J. A. (2002). Marine biofouling: a sticky problem. *Biologist*, 49(1), 1-5.
- Candries, M. (2001). Drag, boundary-layer and roughness characteristics of marine surfaces coated with antifouling. The University of Newcastle upon Tyne Newcastle upon Tyne, UK,

- Candries, M., & Atlar, M. (2005). Experimental investigation of the turbulent boundary layer of surfaces coated with marine antifouling. *Journal of Fluids Engineering*, 127(2), 219-232.
- Cao, Y., Cai, Y., Hirakubo, T., Fukui, H., & Matsuyama, H. (2011). Fermentation characteristics and microorganism composition of total mixed ration silage with local food by-products in different seasons. *Animal Science Journal*, 82(2), 259-266.
- Cassie, A., & Baxter, S. (1944). Wettability of porous surfaces. *Transactions of the Faraday society*, 40, 546-551.
- Castle, E. S. (1951). Electrical control of marine fouling. *Industrial & Engineering Chemistry*, 43(4), 901-904.
- Castro, M. (2014). International Maritime Organization (IMO) Guidelines for the control and management of ships' biofouling to minimize the transfer of invasive aquatic species. X BIOINC, Instituto de Estudos do Mar Almirante Paulo Moreira, Arraial do Cabo, RJ.
- Cebeci, T., & Chang, K. (1978). Calculation of incompressible rough-wall boundary-layer flows. *AIAA Journal*, 16(7), 730-735.
- CEPE (1999). Utilisation of more environmentally friendly antifouling coatings. Brussels, CEPE: 101.
- Chambers, L. D., Stokes, K. R., Walsh, F. C., & Wood, R. J. (2006). Modern approaches to marine antifouling coatings. *Surface and Coatings Technology*, 201(6), 3642-3652.
- Champ, M. A. (2003). Economic and environmental impacts on ports and harbors from the convention to ban harmful marine anti-fouling systems. *Marine Pollution Bulletin*, 46, 935-940.
- Clauser, F. H. (1954). Turbulent boundary layers in adverse pressure gradients. *Journal of the Aeronautical Sciences*, 21(2), 91-108.
- Coles, D. (1956). The law of the wake in the turbulent boundary layer. *Journal of Fluid Mechanics*, 1(2), 191-226.
- Conn, J., Lackenby, C., & Walker, W. (1953). BSRA Resistance Experiments on the 'Lucy Ashton', Part II: The Ship-Model Correlation for the Naked Hull Conditions. *Trans. Inst. Naval Arch*, 95, 350-436.
- Coraddu, A., Gaggero, S., Villa, D., & Figari, M. (2011a). A new approach in engine-propeller matching. In *Sustainable Maritime Transportation and Exploitation of Sea Resources* (Vol. 631, pp. 631-637): ROUTLEDGE in association with GSE Research.
- Coraddu, A., Gualeni, P., & Villa, D. (2011b). Investigation about wave profile effects on ship stability. In *Sustainable Maritime Transportation and Exploitation of*

Sea Resources (Vol. 143, pp. 143-149): ROUTLEDGE in association with GSE Research.

- Coraddu, A., Oneto, L., Baldi, F., & Anguita, D. (2017). Vessels fuel consumption forecast and trim optimisation: a data analytics perspective. *Ocean Engineering*, 130, 351-370.
- Cowle, M. W., Babatunde, A. O., & Bockelmann-Evans, B. N. (2017). The frictional resistance induced by bacterial based biofouling in drainage pipelines. *Journal of Hydraulic Research*, 55(2), 269-283.
- Crisp, D. (1973). The role of the biologist in antifouling research R.F. Acker, Brown, J.R. De Palma, W.P. Iveson (Eds.), *Proceedings of the Third I.C.M.C.F.*, Northwestern University Press, Evanston, IL (1973), p. 88
- Crisp, D., & Bourget, E. (1985). Growth in barnacles. In *Advances in marine biology* (Vol. 22, pp. 199-244): Elsevier.
- Crisp, D., & Ritz, D. (1973). Responses of cirripede larvae to light. I. Experiments with white light. *Marine Biology*, 23(4), 327-335.
- Cronin, E., Cheshire, A., Clarke, S., & Melville, A. (1999). An investigation into the composition, biomass and oxygen budget of the fouling community on a tuna aquaculture farm. *Biofouling*, 13(4), 279-299.
- Cullimore, D. R. (1999). *Microbiology of Well Biofouling* (Vol. 3): CRC Press.
- Dafforn, K. A., Lewis, J. A., & Johnston, E. L. (2011). Antifouling strategies: history and regulation, ecological impacts and mitigation. *Marine pollution bulletin*, 62(3), 453-465.
- Darvehei, P., Bahri, P. A., & Moheimani, N. R. (2018). Model development for the growth of microalgae: A review. *Renewable and Sustainable Energy Reviews*, 97, 233-258.
- Darwin, C. (1854). *A monograph on the sub-class Cirripedia*: The Ray Society.
- Dean, T., & Hurd, L. (1980). Development in an estuarine fouling community: the influence of early colonists on later arrivals. *Oecologia*, 46(3), 295-301.
- Decker, J. T., Kirschner, C. M., Long, C. J., Finlay, J. A., Callow, M. E., Callow, J. A., & Brennan, A. B. (2013). Engineered antifouling microtopographies: an energetic model that predicts cell attachment. *Langmuir*, 29(42), 13023-13030.
- Del Amo, B., Giudice, C., & Rascio, V. (1984). Influence of binder dissolution rate on the bioactivity of antifouling paints. *JCT, Journal of coatings technology*, 56(719), 63-69.
- Demirel, Y.K (2015). *Modelling the Roughness Effects of Marine Coatings and Biofouling on Ship Frictional Resistance*, PhD thesis, University of Strathclyde.

- Demirel, Y. K., Song, S., Turan, O., & Incecik, A. (2019). Practical added resistance diagrams to predict fouling impact on ship performance. *Ocean Engineering*, 186, 106112.
- Demirel, Y. K., Turan, O., & Incecik, A. (2017). Predicting the effect of biofouling on ship resistance using CFD. *Applied Ocean Research*, 62, 100-118.
- Demirel, Y. K., Turan, O., Incecik, A., Day, S., Fang, H., Downie, S., & Olsen, S. (2015). Experimental determination of the roughness functions of marine coatings. Paper presented at the International Conference on Shipping in Changing Climates.
- Demirel, Y. K., Uzun, D., Zhang, Y., Fang, H.C., Day, A. H., & Turan, O. (2017). Effect of barnacle fouling on ship resistance and powering. *Biofouling*, 33(10), 819-834.
- Dobretsov, S., Xiong, H., Xu, Y., Levin, L. A., & Qian, P.-Y. (2007). Novel antifoulants: inhibition of larval attachment by proteases. *Marine Biotechnology*, 9(3), 388-397.
- Donlan, R. M. (2002). Biofilms: microbial life on surfaces. *Emerging infectious diseases*, 8(9), 881-890. doi:10.3201/eid0809.020063
- Epelbaum, A., Herborg, L., Therriault, T., & Pearce, C. (2009). Temperature and salinity effects on growth, survival, reproduction, and potential distribution of two non-indigenous botryllid ascidians in British Columbia. *Journal of Experimental Marine Biology and Ecology*, 369(1), 43-52.
- Farhat, N., Vrouwenvelder, J. S., Van Loosdrecht, M., Bucs, S. S., & Staal, M. (2016). Effect of water temperature on biofouling development in reverse osmosis membrane systems. *Water research*, 103, 149-159.
- Fingerman, M. (1997). *Endocrinology and Reproduction: Recent Advances in Marine Biotechnology*: CRC Press.
- Flack, K. A., & Schultz, M. P. (2010). Review of hydraulic roughness scales in the fully rough regime. *Journal of Fluids Engineering*, 132(4), 041203.
- Gaggero, S., Villa, D., & Brizzolara, S. (2010). RANS and PANEL method for unsteady flow propeller analysis. *Journal of Hydrodynamics, Ser. B*, 22(5), 564-569.
- Gerliczy, C., & Betz, R. (1986). New Technical Developments in PVDF Piezoelectric Devices in Europe and in the USA. Paper presented at the Sixth IEEE International Symposium on Applications of Ferroelectrics.
- Gitlitz, M. (1981). Recent developments in marine antifouling coatings. M. H. Gitlitz, M & T chemicals, Incorporated. *J. Coating Tech.*, 53(678).
- Gordon, D. P., & Mawatari, S. F. (1992). Atlas of marine-fouling Bryozoa of New-Zealand ports and harbours. Miscellaneous Publication New Zealand Oceanographic Institute.

- Graham, D. (1947). Use of Plastic Ship Bottom Paints. *Trans. Soc. Nav. Archit. Marine Eng.(SNAME)*, 55, 202-243.
- Granville, P. (1982). Drag-characterization method for arbitrarily rough surfaces by means of rotating disks. *Journal of Fluids Engineering*, 104(3), 373-377.
- Granville, P. S. (1958). The frictional resistance and turbulent boundary layer of rough surfaces. *Journal of ship research*, 2(04), 52-74.
- Granville, P. S. (1978). Similarity-Law Characterization Methods for Arbitrary Hydrodynamic Roughnesses. Retrieved from
- Granville, P. S. (1986). Eddy viscosities and mixing lengths for turbulent boundary layers on flat plates, smooth or rough: David W. Taylor Naval Ship Research and Development Center.
- Granville, P. S. (1987). Three indirect methods for the drag characterization of arbitrarily rough surfaces on flat plates. Paper presented at the Proceedings of the Twenty-first American Towing Tank Conference.
- Grigson, C. (1992). Drag losses of new ships caused by hull finish. *Journal of ship research*, 36(02), 182-196.
- Guenther, J., Misimi, E., & Sunde, L. M. (2010). The development of biofouling, particularly the hydroid *Ectopleura larynx*, on commercial salmon cage nets in Mid-Norway. *Aquaculture*, 300(1-4), 120-127.
- Guldhammer, H., & Harvald, S. A. (1974). SHIP RESISTANCE-Effect of form and principal dimensions.(Revised). Danish Technical Press, Danmark, Danmarks Tekniske Hojskole, kademisk Forlag, St. kannikestrade 8, DK 1169 Copenhagen.
- Hama, F. R. (1954). Boundary layer characteristics for smooth and rough surfaces. *Trans. Soc. Nav. Arch. Marine Engrs.*, 62, 333-358.
- Haslbeck, E. G., & Bohlander, G. S. (1992). Microbial biofilm effects on drag-lab and field. Retrieved from
- Hellio, C., & Yebra, D. (2009). *Advances in marine antifouling coatings and technologies*: Elsevier.
- Hirdaris, S. E. (2014). *Global Marine Fuel Trends 2030*.
- Holland, R., Dugdale, T., Wetherbee, R., Brennan, A., Finlay, J., Callow, J., & Callow, M. E. (2004). Adhesion and motility of fouling diatoms on a silicone elastomer. *Biofouling*, 20(6), 323-329.
- Holm, E., Schultz, M., Haslbeck, E., Talbott, W., & Field, A. (2004). Evaluation of hydrodynamic drag on experimental fouling-release surfaces, using rotating disks. *Biofouling*, 20(4-5), 219-226.

- Howell, D., & Behrends, B. (2006). A review of surface roughness in antifouling coatings illustrating the importance of cutoff length. *Biofouling*, 22(6), 401-410.
- Huijs, F., Klijnstra, J., & van Zanten, J. (2006). Antifouling coating comprising a polymer with functional groups bonded to an enzyme. European patent application EP1661955A1.
- Hundley, L. L., & Tate Sr, C. (1980). Hull-fouling studies and ship powering trial results on seven FF 1052 class ships. Retrieved from
- IMO (2003). The Effect Of Legislation And Regulation On Tributyltin Risk In The Marine And Estuarine Environments Of The United States. Peter F. Seligman, Aldis O. Valkirs and Harry D. Johnson, Environmental Sciences Division, U.S. Navy, SSC SD (3601), San Diego CA 92152-6335 http://environ.nosc.mil/Other/seligman_980327.htm
- IMO (2011). Amendments To Marpol Annex VI on Regulations for the Prevention of Air Pollution From Ships by Inclusion Of New Regulations on Energy Efficiency for Ships. Annex 19 Resolution MEPC.203(62).
- Woods. Hole. Oceanographic Institution, (1952). Marine fouling and its prevention: United States Naval Institute, Annapolis, Maryland.
- ITTC (1978) – Recommended Procedures 7.5 – 02 03 – 01.4, Performance, Propulsion 1978 ITTC Performance Prediction Method
- ITTC (2002b) ITTC 2002b. Uncertainty Analysis, Example for Resistance Test. ITTC Recommended Procedures and Guidelines, Procedure 7.5-02-02-02, Revision 01.
- ITTC. (2011). Specialist Committee on Surface Treatment - Final report and recommendations to the 26th ITTC. Retrieved from
- Izubuchi, T. (1934). Increase in Hull Resistance Through Ship Bottom Fouling. *Zosen Kyokai*, 55.
- Johansen, C., Falholt, P., & Gram, L. (1997). Enzymatic removal and disinfection of bacterial biofilms. *Appl. Environ. Microbiol.*, 63(9), 3724-3728.
- Kempf, G. (1937). On the effect of roughness on the resistance of ships. *Trans INA*, 79, 109-119.
- Kiil, S., Weinell, C. E., Pedersen, M. S., & Dam-Johansen, K. (2001). Analysis of self-polishing antifouling paints using rotary experiments and mathematical modeling. *Industrial & engineering chemistry research*, 40(18), 3906-3920.
- Kiil, S., & Yebra, D. (2009). Modelling the design and optimization of chemically active marine antifouling coatings. In *Advances in marine antifouling coatings and technologies* (pp. 334-364): Elsevier.

- Klebanoff, P. (1954). S. and Diehl, W. " Some Features of Artificially Thickened Fully Developed Turbulent Boundary Layers with Zero Pressure Gradient," Rept, 1110.
- Kline, S.J., Morkovin, M.V., Sovran, G., and Cockrell, D.J. editors (1969). Proceedings of the Computer of Turbulent Boundary Layers – 1968 AFOSR-IFP-Stanford Conference, Vol. 1.
- Koopmans, M., & Wijffels, R. H. (2008). Seasonal growth rate of the sponge *Haliclona oculata* (Demospongiae: Haplosclerida). *Marine Biotechnology*, 10(5), 502-510.
- Krishnan, S., Wang, N., Ober, C. K., Finlay, J. A., Callow, M. E., Callow, J. A., Fischer, D. A. (2006). Comparison of the Fouling Release Properties of Hydrophobic Fluorinated and Hydrophilic PEGylated Block Copolymer Surfaces: Attachment Strength of the Diatom *Navicula* and the Green Alga *Ulva*. *Biomacromolecules*, 7(5), 1449-1462. doi:10.1021/bm0509826
- Kristensen, J. B., Meyer, R. L., Laursen, B. S., Shipovskov, S., Besenbacher, F., & Poulsen, C. H. (2008). Antifouling enzymes and the biochemistry of marine settlement. *Biotechnology advances*, 26(5), 471-481.
- Kroeker, K. J., Kordas, R. L., Crim, R., Hendriks, I. E., Ramajo, L., Singh, G. S., Gattuso, J. P. (2013). Impacts of ocean acidification on marine organisms: quantifying sensitivities and interaction with warming. *Global change biology*, 19(6), 1884-1896.
- Krogstad, P.-Å., Antonia, R., & Browne, L. (1992). Comparison between rough-and smooth-wall turbulent boundary layers. *Journal of Fluid Mechanics*, 245, 599-617.
- Krug, P. (2006). Defense of benthic invertebrates against surface colonization by larvae: a chemical arms race. In *Antifouling compounds* (pp. 1-53): Springer.
- Lehaitre, M., Delauney, L., & Compère, C. (2008). Biofouling and underwater measurements. Real-time observation systems for ecosystem dynamics and harmful algal blooms: Theory, instrumentation and modelling. *Oceanographic Methodology Series*. UNESCO, Paris, 463-493.
- Lejars, M. n., Margailan, A., & Bressy, C. (2012). Fouling release coatings: a nontoxic alternative to biocidal antifouling coatings. *Chemical reviews*, 112(8), 4347-4390.
- Leroy, C., Delbarre, C., Ghillebaert, F., Compere, C., & Combes, D. (2008). Effects of commercial enzymes on the adhesion of a marine biofilm-forming bacterium. *Biofouling*, 24(1), 11-22.
- Lewin, R. (1984). Microbial adhesion is a sticky problem. *Science*, 224, 375-378.
- Lewthwaite, J., Molland, A., & Thomas, K. (1985). An investigation into the variation of ship skin frictional resistance with fouling. *Royal Institution of Naval Architects Transactions*, 127.

- Ligrani, P. M. (1989). Structure of turbulent boundary layers. In *Encyclopedia of fluid mechanics* (Vol. 8, pp. 111-189): Gulf Houston, TX.
- Ligrani, P. M., & Moffat, R. J. (1986). Structure of transitionally rough and fully rough turbulent boundary layers. *Journal of Fluid Mechanics*, 162, 69-98.
- Lindholdt, A., Dam-Johansen, K., Yebra, D., Olsen, S., & Kiil, S. (2015). Estimation of long-term drag performance of fouling control coatings using an ocean-placed raft with multiple dynamic rotors. *Journal of Coatings Technology and Research*, 12(6), 975-995.
- Loeb, G., Laster, D., & Gracik, T. (1984). The influence of microbial fouling films on hydrodynamic drag of rotating discs. *Marine Biodeterioration, An Interdisciplinary Study*, 88-94.
- Loeb, G. I., & Neihof, R. A. (1975). Marine Conditioning Films. In *Applied Chemistry at Protein Interfaces* (Vol. 145, pp. 319-335): AMERICAN CHEMICAL SOCIETY.
- Lord, J. P. (2017). Impact of seawater temperature on growth and recruitment of invasive fouling species at the global scale. *Marine ecology*, 38(2), e12404.
- Lunn, I. (1974). *Antifouling: BCA*.
- Lützen, M., & Kristensen, H. O. H. (2012). A model for prediction of propulsion power and emissions—tankers and bulk carriers. Paper presented at the World maritime technology conference.
- Macdonald, R. (2000). Modelling the mean velocity profile in the urban canopy layer. *Boundary-Layer Meteorology*, 97(1), 25-45.
- Manyak, D., Weiner, R., Carlson, P., & Quintero, E. (2005). Preparation and use of biofilm-degrading, multiple-specificity, hydrolytic enzyme mixtures. In: *Google Patents*.
- Marshall, D., Schoenbach, K. H., Abou-Ghazala, A., & Smythe, A. G. (1998). *Conference Record of the 23rd International Power Modulator Symposium*.
- Marson, F. (1969). Anti-fouling paints. I. Theoretical approach to leaching of soluble pigments from insoluble paint vehicles. *Journal of Applied Chemistry*, 19(4), 93-99.
- McDonald, M. R., McClintock, J. B., Amsler, C. D., Rittschof, D., Angus, R. A., Orihuela, B., & Lutostanski, K. (2009). Effects of ocean acidification over the life history of the barnacle *Amphibalanus amphitrite*. *Marine Ecology Progress Series*, 385, 179-187.
- McDougall, K. D. (1943). Sessile marine invertebrates of Beaufort, North Carolina: a study of settlement, growth, and seasonal fluctuations among pile-dwelling organisms. *Ecological Monographs*, 13(3), 321-374.

- McEntee, W. (1916). Variation Of Frictional Resistance Of Ships With Condition Of Wetted Surface. *Journal of the American Society of Naval Engineers*, 28(1), 311-314.
- Melo, L. F., & Bott, T. R. (1997). Biofouling in water systems. *Experimental Thermal and Fluid Science*, 14(4), 375-381. doi:[https://doi.org/10.1016/S0894-1777\(96\)00139-2](https://doi.org/10.1016/S0894-1777(96)00139-2)
- Miller, M. B., & Bassler, B. L. (2001). Quorum sensing in bacteria. *Annual Reviews in Microbiology*, 55(1), 165-199.
- Milne, A. (1990). Roughness and drag from the marine paint chemist's viewpoint. Paper presented at the Marine Roughness and Drag Workshop, Paper.
- Milne, A. (1991). Ablation and after: the law and the profits. *The Institute of Marine Engineers(UK)*, 139-144.
- Milne, A., & Hails, G. (1977). Marine paint. In: Google Patents.
- Mol, V. L., Raveendran, T., & Parameswaran, P. (2009). Antifouling activity exhibited by secondary metabolites of the marine sponge, *Haliclona exigua* (Kirkpatrick). *International Biodeterioration & Biodegradation*, 63(1), 67-72.
- Monty, J., Dogan, E., Hanson, R., Scardino, A., Ganapathisubramani, B., & Hutchins, N. (2016). An assessment of the ship drag penalty arising from light calcareous tubeworm fouling. *Biofouling*, 32(4), 451-464.
- Moss G. Enzyme nomenclature — recommendations of the Nomenclature Committee of the International Union of Biochemistry and Molecular Biology on the nomenclature and classification of enzymes by the reactions they catalyse. Online edition. International Union of Biochemistry and Molecular Biology (NC-IUBMB). Tipton, KF and Boyce, S editors. Department of Chemistry, Queen Mary University of London, Mile End Road, London, E1 4NS, UK. <http://www.chem.qmul.ac.uk/iubmb/enzyme/index.html>. 2006. Accessed 01-27-2008.
- Munk, T., Kane, D., & Yebra, D. (2009). The effects of corrosion and fouling on the performance of ocean-going vessels: a naval architectural perspective. In *Advances in marine antifouling coatings and technologies* (pp. 148-176): Elsevier.
- Murphy, P. V., & Latour, M. J. (1979). Preventing marine fouling. In: Google Patents.
- Nakasono, S., Burgess, J. G., Takahashi, K., Koike, M., Murayama, C., Nakamura, S., & Matsunaga, T. (1993). Electrochemical prevention of marine biofouling with a carbon-chloroprene sheet. *Appl. Environ. Microbiol.*, 59(11), 3757-3762.
- Nikuradse, J. (1933). Laws of flow in rough pipes. National Advisory Committee for Aeronautics. NACA Technical Memorandum, NACA Technical Memorandum, 1292, 60-68.

- Okochi, M., & Matsunaga, T. (1997). Electrochemical sterilization of bacteria using a graphite electrode modified with adsorbed ferrocene. *Electrochimica acta*, 42(20-22), 3247-3250.
- Oliveira, D., & Granhag, L. (2016). Matching forces applied in underwater hull cleaning with adhesion strength of marine organisms. *Journal of Marine Science and Engineering*, 4(4), 66.
- Omae, I. (2003). Organotin antifouling paints and their alternatives. *Applied organometallic chemistry*, 17(2), 81-105.
- Organization, I. M. (2012). *Guidelines for the Control and Management of Ships' Biofouling to Minimize the Transfer of Invasive Aquatic Species: International Maritime Organization*.
- Owen, D., Demirel, Y. K., Oguz, E., Tezdogan, T., & Incecik, A. (2018). Investigating the effect of biofouling on propeller characteristics using CFD. *Ocean Engineering*, 159, 505-516.
- Pansch, C., Schlegel, P., & Havenhand, J. (2013). Larval development of the barnacle *Amphibalanus improvisus* responds variably but robustly to near-future ocean acidification. *ICES Journal of Marine Science*, 70(4), 805-811.
- Perry, A. E., Schofield, W. H., & Joubert, P. N. (1969). Rough wall turbulent boundary layers. *Journal of Fluid Mechanics*, 37(2), 383-413.
- Pettitt, M., Henry, S., Callow, M., Callow, J., & Clare, A. (2004). Activity of commercial enzymes on settlement and adhesion of cypris larvae of the barnacle *Balanus amphitrite*, spores of the green alga *Ulva linza*, and the diatom *Navicula perminuta*. *Biofouling*, 20(6), 299-311.
- Pielke R.A. (2012) *Sea Surface Temperature Trends as A Function of Latitude Bands* by Roger A. Pielke Sr. And Bob Tisdale, Climate Science.
- Propulsion Dynamics. Casper Report, (*Personel communication*,2015).
- Qiu, J.-W., & Qian, P.-Y. (1998). Combined effects of salinity and temperature on juvenile survival, growth and maturation in the polychaete *Hydroides elegans*. *Marine Ecology Progress Series*, 168, 127-134.
- Rahmoune, M., & Latour, M. (1995). Application of mechanical waves induced by piezofilms to marine fouling protection of oceanographic sensors. *Smart Materials and Structures*, 4(3), 195.
- Railkin, A. I. (2003). *Marine biofouling: colonization processes and defenses: CRC press*.
- Rascio, V. J. (2000). Antifouling coatings: where do we go from here. *Corrosion Reviews*, 18(2-3), 133-154.
- Rawlings, N. D., Morton, F. R., & Barrett, A. J. (2006). MEROPS: the peptidase database. *Nucleic acids research*, 34(suppl_1), D270-D272.

- Reading, N. C., & Sperandio, V. (2006). Quorum sensing: the many languages of bacteria. *FEMS microbiology letters*, 254(1), 1-11.
- Rosenhahn, A., Schilp, S., Kreuzer, H. J., & Grunze, M. (2010). The role of “inert” surface chemistry in marine biofouling prevention. *Physical chemistry chemical physics*, 12(17), 4275-4286.
- Sanchez, A., & Yebra, D. (2009). Ageing tests and long-term performance of marine antifouling coatings. In *Advances in marine antifouling coatings and technologies* (pp. 393-421): Elsevier.
- Sarkar (2005). Sarkar, Sahotra, "Ecology", *The Stanford Encyclopedia of Philosophy* (Winter 2016 Edition), Edward N. Zalta (ed.), URL =<<https://plato.stanford.edu/archives/win2016/entries/ecology/>>.
- Scardino, A., Guenther, J., & De Nys, R. (2008). Attachment point theory revisited: the fouling response to a microtextured matrix. *Biofouling*, 24(1), 45-53.
- Scardino, A. J., Harvey, E., & De Nys, R. (2006). Testing attachment point theory: diatom attachment on microtextured polyimide biomimics. *Biofouling*, 22(1), 55-60. doi:10.1080/08927010500506094
- Schetz, J. (1993). *Boundary Layer Theory*. In: Prentice Hall, Englewood Cliffs, NJ.
- Schlichting, H., & Gersten, K. (2016). *Boundary-layer theory*: Springer.
- Schoenherr, K. E. (1932). Resistance of flat surfaces moving through a fluid. *Trans. Soc. Nav. Archit. Mar. Eng.*, 40, 279-313.
- Schultz, M., & Flack, K. (2007). The rough-wall turbulent boundary layer from the hydraulically smooth to the fully rough regime. *Journal of Fluid Mechanics*, 580, 381-405.
- Schultz, M. P. (2000). Turbulent boundary layers on surfaces covered with filamentous algae. *Journal of Fluids Engineering*, 122(2), 357-363.
- Schultz, M. P. (2002). The relationship between frictional resistance and roughness for surfaces smoothed by sanding. *Journal of Fluids Engineering*, 124(2), 492-499.
- Schultz, M. P. (2004). Frictional resistance of antifouling coating systems. *Transactions of the ASME-I-Journal of Fluids Engineering*, 126(6), 1039-1047.
- Schultz, M. P. (2007). Effects of coating roughness and biofouling on ship resistance and powering. *Biofouling*, 23(5), 331-341.
- Schultz, M. P., Bendick, J. A., Holm, E. R., & Hertel, W. M. (2011). Economic impact of biofouling on a naval surface ship. *Biofouling*, 27(1), 87-98. doi:10.1080/08927014.2010.542809
- Schultz, M. P., & Flack, K. A. (2013). Reynolds-number scaling of turbulent channel flow. *Physics of Fluids*, 25(2), 025104.

- Schultz, M. P., & Swain, G. W. (2000). The influence of biofilms on skin friction drag. *Biofouling*, 15(1-3), 129-139.
- Schumacher, J. F., Carman, M. L., Estes, T. G., Feinberg, A. W., Wilson, L. H., Callow, M. E., . . . Brennan, A. B. (2007). Engineered antifouling microtopographies—effect of feature size, geometry, and roughness on settlement of zoospores of the green alga *Ulva*. *Biofouling*, 23(1), 55-62.
- Shapiro, T. A. (2004). The effect of surface roughness on hydrodynamic drag and turbulence.
- Shockling, M., Allen, J., & Smits, A. (2006). Roughness effects in turbulent pipe flow. *Journal of Fluid Mechanics*, 564, 267-285.
- Shtykova, L., Fant, C., Handa, P., Larsson, A., Berntsson, K., Blanck, H., Härelind, H. I. (2009). Adsorption of antifouling booster biocides on metal oxide nanoparticles: effect of different metal oxides and solvents. *Progress in Organic coatings*, 64(1), 20-26.
- Silva-Aciaras, F., & Riquelme, C. (2008). Inhibition of attachment of some fouling diatoms and settlement of *Ulva lactuca* zoospores by film-forming bacterium and their extracellular products isolated from biofouled substrata in Northern Chile. *Electronic Journal of Biotechnology*, 11(1), 60-70.
- Silva, E., Ferreira, O., Ramalho, P., Azevedo, N., Bayón, R., Igartua, A., Calhorda, M. (2019). Eco-friendly non-biocide-release coatings for marine biofouling prevention. *Science of the Total Environment*, 650, 2499-2511.
- Smith, F. W. (1946). Effect of water currents upon the attachment and growth of barnacles. *The Biological Bulletin*, 90(1), 51-70.
- Song, S., Demirel, Y. K., & Atlar, M. (2019). An investigation into the effect of biofouling on full-scale propeller performance using CFD. Paper presented at the ASME 2019 38th International Conference on Ocean, Offshore and Arctic Engineering.
- Stachowicz, J. J., Terwin, J. R., Whitlatch, R. B., & Osman, R. W. (2002). Linking climate change and biological invasions: ocean warming facilitates nonindigenous species invasions. *Proceedings of the National Academy of Sciences*, 99(24), 15497-15500.
- Swain, G. (1998, 22–23 July 1998). Biofouling control: A critical component of drag reduction. Paper presented at the In Proceedings of the International Symposium on Sea Water Drag Reduction, Newport, RI, USA.
- Swain, G., & Touzot, A. (2008). Techniques for dynamically testing and evaluating materials and coatings in moving solutions. In: Google Patents.
- Swain, G. W., Kovach, B., Touzot, A., Casse, F., & Kavanagh, C. J. (2007). Measuring the performance of today's antifouling coatings. *Journal of Ship Production*, 23(3), 164-170.

- Takahashi, T., Sutherland, S. C., Chipman, D. W., Goddard, J. G., Ho, C., Newberger, T., Munro, D. (2014). Climatological distributions of pH, pCO₂, total CO₂, alkalinity, and CaCO₃ saturation in the global surface ocean, and temporal changes at selected locations. *Marine Chemistry*, 164, 95-125.
- Taylor, R. J., Richardson, L. B., & Burton, D. T. (1983). *Ultrasonics International 83, Conference Proceedings*.
- Tezdogan, T., & Demirel, Y. K. (2014). An overview of marine corrosion protection with a focus on cathodic protection and coatings. *Brodogradnja: Teorija i praksa brodogradnje i pomorske tehnike*, 65(2), 49-59.
- Tezdogan, T., Demirel, Y. K., Kellett, P., Khorasanchi, M., Incecik, A., & Turan, O. (2015). Full-scale unsteady RANS CFD simulations of ship behaviour and performance in head seas due to slow steaming. *Ocean Engineering*, 97, 186-206.
- Thiyagarajan, V., Harder, T., & Qian, P.-Y. (2003). Combined effects of temperature and salinity on larval development and attachment of the subtidal barnacle *Balanus trigonus* Darwin. *Journal of Experimental Marine Biology and Ecology*, 287(2), 223-236.
- Townsin, R. (2003). The ship hull fouling penalty. *Biofouling*, 19(S1), 9-15.
- Trindade de Castro, M., Vance, T., Yunnice, A. L., Fileman, T. W., & Hall-Spencer, J. M. (2018). Low salinity as a biosecurity tool for minimizing biofouling on ship sea chests. *Ocean Science*, 14(4), 661-667.
- Turan, O., Demirel, Y. K., Day, S., & Tezdogan, T. (2016). Experimental determination of added hydrodynamic resistance caused by marine biofouling on ships. Paper presented at the 6th European Transport Research Conference.
- UNCTAD. (2017). *Review of Maritime Transport 2017*. Retrieved from
- Uzun, D., Demirel, Y. K., Coraddu, A., & Turan, O. (2019). Time-dependent biofouling growth model for predicting the effects of biofouling on ship resistance and powering. *Ocean Engineering*, 191, 106432.
- Uzun, D., Zhang, Y., Demirel, Y. K., & Turan, O. (2017). Experimental determination of added resistance due to barnacle fouling on ships by using 3D printed barnacles.
- Van der Stap, T., Coolen, J. W., & Lindeboom, H. J. (2016). Marine fouling assemblages on offshore gas platforms in the southern North Sea: Effects of depth and distance from shore on biodiversity. *PloS one*, 11(1), e0146324.
- VI, A. 2012 guidelines for the development of a ship energy efficiency management plan (SEEMP).
- Villanueva, V. D., Font, J., Schwartz, T., & Romani, A. M. (2011). Biofilm formation at warming temperature: acceleration of microbial colonization and microbial interactive effects. *Biofouling*, 27(1), 59-71.

- Von Oertzen, J., Scharf, E., Arndt, E., Sandrock, S., Dettmann, L., Holzapfel, H., Günther, R. (1989). Spezialstudie 'Alternative Antifouling Systeme'. Fachbereich Biologie, Universität Rostock.
- Wang, H., Oguz, E., Jeong, B., & Zhou, P. (2018). Life cycle cost and environmental impact analysis of ship hull maintenance strategies for a short route hybrid ferry. *Ocean Engineering*, 161, 20-28.
- Watanabe, S., Nagamatsu, N., Yokoo, K., & Kawakami, Y. (1969). The augmentation in frictional resistance due to slime. *J. Kansai Society of Naval Architects*, 131, 45-51.
- Waters, C. M., & Bassler, B. L. (2005). Quorum sensing: cell-to-cell communication in bacteria. *Annu. Rev. Cell Dev. Biol.*, 21, 319-346.
- Weinell, C. E., Olsen, K. N., Christoffersen, M. W., & Kiil, S. (2003). Experimental study of drag resistance using a laboratory scale rotary set-up. *Biofouling*, 19(S1), 45-51.
- Wenzel, R. N. (1936). Resistance of Solid Surfaces to Wetting By Water. *Industrial & Engineering Chemistry*, 28(8), 988-994. doi:10.1021/ie50320a024
- Wever, R., Dekker, H., Van Schijndel, J., & Vollenbroek, E. (1995). Antifouling Paint Containing Haloperoxidase and Method to Determine Halide. Retrieved from
- Wojtowicz, J. A. (2000). Dichlorine monoxide, Hypochlorous acid, and Hypochlorites. *Kirk-Othmer Encyclopedia of Chemical Technology*.
- Xavier, J. d. B., Picioreanu, C., & van Loosdrecht, M. C. (2005). A general description of detachment for multidimensional modelling of biofilms. *Biotechnology and bioengineering*, 91(6), 651-669.
- Xiao, L. (2014). Influence of Surface Topography on Marine Biofouling.
- Xiong, H., Qi, S., Xu, Y., Miao, L., & Qian, P.-Y. (2009). Antibiotic and antifouling compound production by the marine-derived fungus *Cladosporium* sp. F14. *Journal of Hydro-environment Research*, 2(4), 264-270.
- Yeber, D. M., Kiil, S., & Dam-Johansen, K. (2004). Antifouling technology—past, present and future steps towards efficient and environmentally friendly antifouling coatings. *Progress in Organic coatings*, 50(2), 75-104.
- Yeginbayeva, I. A., Granhag, L., & Chernoray, V. (2019). Review and historical overview of experimental facilities used in hull coating hydrodynamic tests. *Proceedings of the Institution of Mechanical Engineers, Part M: Journal of Engineering for the Maritime Environment*, 233(4), 1240–1259. <https://doi.org/10.1177/1475090218814132>

Research Outputs

The following publications were generated throughout the timespan of the PhD studies related to this thesis.

Journal papers (SCI / SCI Expanded):

1. **Uzun, D.**, Ozyurt R., Demirel Y.K., Turan, O. (2019) Does the barnacle settlement pattern affect ship resistance and powering? *Applied Ocean Research*, Volume 95,2020,102020, ISSN 0141-1187, <https://doi.org/10.1016/j.apor.2019.102020>
2. **Uzun, D.**, Demirel Y.K., Coraddu, A., & Turan, O. (2019) Time-dependent biofouling growth model for predicting the effects of biofouling on ship resistance and powering, *Ocean Engineering*, Volume 191,106432, ISSN 0029-8018, <https://doi.org/10.1016/j.oceaneng.2019.106432>
3. Demirel Y.K., **Uzun, D.**, Zhang, Y. Fang, H., Day, A.H. & Turan, O. (2017) Effect of barnacle fouling on ship resistance and powering, *Biofouling*, 33:10, 819-834, <https://doi.org/10.1080/08927014.2017.1373279>

Conference papers:

1. **Uzun, D.**, Demirel, Y. K., Coraddu, A., Turan, O. (2019). Life cycle assessment of an antifouling coating based on time-dependent biofouling model. In *18th Conference on Computer Applications and Information Technology in the Maritime Industries*.
2. **Uzun, D.**, Ozyurt, R., Demirel, Y. K., Turan, O. (2018). Time based ship added resistance prediction model for biofouling. In *13th International Marine Design Conference*.

3. **Uzun, D.**, Zhang, Y., Demirel, Y. K. & Turan, O. (2017). Experimental determination of added resistance due to barnacle fouling on ships by using 3D printed barnacles. In The 5th International Conference on Advanced Model Measurement Technology for The Maritime Industry (AMT'17)

4. Demirel, Y. K., **Uzun, D.**, Zhang, Y., & Turan, O. (2018). Life cycle assessment of marine coatings applied to ship hulls. In *Trends and Challenges in Maritime Energy Management* (pp. 325-339). Springer, Cham.